

VOLUME 37

MAY 1959

NUMBER 5

# Canadian Journal of Physics

**Editor:** H. E. DUCKWORTH

**Associate Editors:**

L. G. ELLIOTT, *Atomic Energy of Canada, Ltd., Chalk River*  
J. S. FOSTER, *McGill University*  
G. HERZBERG, *National Research Council of Canada*  
L. LEPRINCE-RINGUET, *Ecole Polytechnique, Paris*  
B. W. SARGENT, *Queen's University*  
G. M. VOLKOFF, *University of British Columbia*  
W. H. WATSON, *University of Toronto*  
G. A. WOONTON, *McGill University*

**Published by THE NATIONAL RESEARCH COUNCIL**  
**OTTAWA** **CANADA**

## CANADIAN JOURNAL OF PHYSICS

Under the authority of the Chairman of the Committee of the Privy Council on Scientific and Industrial Research, the National Research Council issues **THE CANADIAN JOURNAL OF PHYSICS** and five other journals devoted to the publication, in English or French, of the results of original scientific research. Matters of general policy concerning these journals are the responsibility of a joint Editorial Board consisting of: members representing the National Research Council of Canada; the Editors of the Journals; and members representing the Royal Society of Canada and four other scientific societies.

### EDITORIAL BOARD

#### Representatives of the National Research Council

I. McT. Cowan, *University of British Columbia*  
A. Gauthier, *University of Montreal*

H. G. Thode (Chairman), *McMaster University*  
D. L. Thomson, *McGill University*

#### Editors of the Journals

D. L. Bailey, *University of Toronto*  
T. W. M. Cameron, *Macdonald College*  
H. E. Duckworth, *McMaster University*

K. A. C. Elliott, *Montreal Neurological Institute*  
Léo Marion, *National Research Council*  
R. G. E. Murray, *University of Western Ontario*

#### Representatives of Societies

D. L. Bailey, *University of Toronto*  
Royal Society of Canada  
T. W. M. Cameron, *Macdonald College*  
Royal Society of Canada  
H. E. Duckworth, *McMaster University*  
Royal Society of Canada  
Canadian Association of Physicists

K. A. C. Elliott, *Montreal Neurological Institute*  
Canadian Physiological Society  
P. R. Gendron, *University of Ottawa*  
Chemical Institute of Canada  
R. G. E. Murray, *University of Western Ontario*  
Canadian Society of Microbiologists  
T. Thorvaldson, *University of Saskatchewan*  
Royal Society of Canada

#### Ex officio

Léo Marion (Editor-in-Chief), *National Research Council*  
J. B. Marshall (Administration and Awards), *National Research Council*

---

*Manuscripts* for publication should be submitted to Dr. H. E. Duckworth, Editor, Canadian Journal of Physics, Hamilton College, McMaster University, Hamilton, Ontario.

For instructions on preparation of copy, see **NOTES TO CONTRIBUTORS** (back cover).

*Proof, correspondence concerning proof, and orders for reprints* should be sent to the Manager, Editorial Office (Research Journals), Division of Administration and Awards, National Research Council, Ottawa 2, Canada.

*Subscriptions, renewals, requests for single or back numbers, and all remittances* should be sent to Division of Administration and Awards, National Research Council, Ottawa 2, Canada. Remittances should be made payable to the Receiver General of Canada, credit National Research Council.

The journals published, frequency of publication, and prices are:

Canadian Journal of Biochemistry and Physiology	Monthly	\$9.00 a year
Canadian Journal of Botany	Bimonthly	\$6.00 a year
Canadian Journal of Chemistry	Monthly	\$12.00 a year
Canadian Journal of Microbiology	Bimonthly	\$6.00 a year
Canadian Journal of Physics	Monthly	\$9.00 a year
Canadian Journal of Zoology	Bimonthly	\$5.00 a year

The price of regular single numbers of all journals is \$2.00.







# Canadian Journal of Physics

Issued by THE NATIONAL RESEARCH COUNCIL OF CANADA

VOLUME 37

MAY 1959

NUMBER 5

## THERMAL NEUTRON ABSORPTION CROSS SECTION OF $\text{Xe}^{135}$ <sup>1</sup>

H. R. FICKEL<sup>2</sup> AND R. H. TOMLINSON

### ABSTRACT

The effective neutron absorption cross section of  $\text{Xe}^{135}$  has been measured with a mass spectrometer by observing the variation in the  $\text{Cs}^{135}/\text{Cs}^{137}$  fission yield ratio obtained at various thermal neutron fluxes. Values of  $3.15 \pm 0.06$  megabarns and  $3.27 \pm 0.11$  megabarns have been determined for neutron temperatures of  $120^\circ\text{C}$  and  $137^\circ\text{C}$  respectively.

### INTRODUCTION

No fission product requires more consideration in reactor operations than  $\text{Xe}^{135}$  since it is formed in relatively high yield and possesses an abnormally high thermal neutron absorption cross section. It is important to obtain the best possible value for its cross section as well as for its absolute yield. Measurements of the total cross section of  $\text{Xe}^{135}$  have been made at Oak Ridge National Laboratories by Bernstein (1956) using a crystal spectrometer, and by Smith (unpublished) using a fast chopper. Differences of about 10% exist in results of the two methods, and at present there is no basis for favoring the data of either one or the other.

Westcott (1958) has tabulated both sets of data along with calculated values of the effective absorption cross section. The values depend on the choice between the possible values of  $g = 5/8$  and  $g = 3/8$  for the statistical weight factor and hence the total cross-section measurements leave considerable uncertainty in the value of the effective absorption cross section.

The effective neutron cross section has been measured by Petruska *et al.* (1955) and Ivanov *et al.* (1957) using mass spectrometric techniques. Since  $\text{Cs}^{135}$  is the daughter of the short-lived  $\text{Xe}^{135}$  nuclide, it is possible to evaluate the neutron absorption cross section of  $\text{Xe}^{135}$  by comparison of the ratios of  $\text{Cs}^{135}/\text{Cs}^{137}$  from fission product samples obtained at high and low neutron fluxes. Values of the neutron temperature were not determined for either of the effective neutron absorption cross-section measurements made by Petruska *et al.* (1955) or Ivanov *et al.* (1957) and hence comparison of them either with each other or with the total cross-section values is not possible. In the present work the effective cross section of  $\text{Xe}^{135}$  has been measured at

<sup>1</sup>Manuscript received December 30, 1958.

<sup>2</sup>Contribution from Chemistry Department, McMaster University, Hamilton, Ontario.

<sup>3</sup>Holder of Canadian Industries Limited Fellowship.

two temperatures and compared with the total cross-section values of both Bernstein and Smith.

### EXPERIMENTAL

Block assemblies containing five equally spaced holes were prepared using superpure magnesium. Pins of uranium-aluminum alloy (0.108 cm diameter and 0.965 cm in length containing 1 mg  $U^{235}$ ) crimped in superpure aluminum tubing were located in positions on either side of the central hole. Cobalt flux monitors (.005 in. diameter and 1 cm in length weighing approximately 1.15 mg) sheathed in aluminum tubing were placed in the outside positions. Two such assemblies were simultaneously installed at positions S-3-5 and S-6-3 in the graphite reflector of the N.R.X. reactor, Chalk River, and irradiated for 87.83 hours without shutdowns or serious power fluctuations. This time at the flux of these positions was more than that required to ensure 2% precision in the measured values of the effective neutron cross sections. During the irradiation the reactor power was constant within 0.5%, 8-hour power checks showing random fluctuations about 40.4 megawatts, not exceeding 0.3 megawatt at any time.

The  $U^{235}$ -Al alloy pins from the two samples A and B were dissolved separately in vycor crucibles using HCl and  $HNO_3$ . The aluminum sheaths were dissolved along with the pins in order to include the recoil fission fragments. Each solution was evaporated to dryness and the residue redissolved in 10 ml of deionized distilled water. The aluminum was precipitated as  $Al(OH)_3$  using  $NH_4OH$ . The ammonium salts in the supernatant liquid were destroyed by repeated evaporations with aqua regia. The resulting sample was then transferred to the ion source filament of a  $90^\circ$  sector mass spectrometer as described by Inghram (1953).

The  $Co^{60}$  content of the individual cobalt flux monitors after irradiation was compared with standards of known activity by means of a well-type ionization chamber filled with argon at 30-atmosphere pressure. The ion currents from the ionization chamber were determined with a vibrating-reed electrometer. The cobalt standards were calibrated both by coincidence and  $4\pi$  counting techniques.

### RESULTS

The ratio of the number of atoms of  $Cs^{135}$  found after a neutron irradiation of  $U^{235}$  to the total number of atoms of mass 135 produced may be determined by solution of the following differential equations:

$$\begin{aligned}\frac{dU^{235}}{dt} &= -U^{235} {}_{92}\sigma_a^{235} \phi \\ \frac{dI^{135}}{dt} &= 0.95 U^{235} {}_{92}\sigma_f^{235} \phi y^{135} - I^{135} {}_{53}\lambda^{135} \\ \frac{dXe^{135}}{dt} &= I^{135} {}_{53}\lambda^{135} - Xe^{135} ({}_{54}\lambda^{135} + {}_{54}\sigma^{135} \phi) + 0.05 U^{235} {}_{92}\sigma_f^{235} \phi y^{135} \\ \frac{dCs^{135}}{dt} &= Xe^{135} {}_{54}\lambda^{135}\end{aligned}$$

where  $y^{135}$  is the per cent cumulative yield of mass 135 chain, and  $\phi$  is the 2200 meters/second neutron flux,  $\sigma$  and  $\lambda$  are the effective neutron cross section and decay constant for the nuclides indicated by the appropriate subscripts and superscripts.

In these equations it is assumed that there is a 5% primary yield of Xe<sup>135</sup> which is the amount estimated from the Glendenin hypothesis of equal charge displacement (Glendenin and Steinberg 1955). It is also assumed that the remaining 95% of this mass chain is produced directly as I<sup>135</sup> since the half-lives of the precursors are short compared with the irradiation times for which solutions to these equations are required.

Equation (1) may be derived from these differential equations for the conditions that all the I<sup>135</sup> and Xe<sup>135</sup> present at the end of the irradiation have decayed to Cs<sup>135</sup> and that there is a negligible depletion of U<sup>235</sup> during the irradiation.

$$(1) \quad \frac{Cs^{135}}{Y^{135}} = \frac{{}_{54}\lambda^{135}}{K} - \frac{\sigma\phi}{t} \left[ \frac{e^{-Kt} - 1}{K^2} + \frac{0.95(e^{-{}_{53}\lambda^{135}t} - 1)}{{}_{53}\lambda^{135}(K - {}_{53}\lambda^{135})} - \frac{0.95(e^{-Kt} - 1)}{K(K - {}_{53}\lambda^{135})} \right]$$

where  $Y^{135}$  is total number of atoms of mass 135 produced, and  $K$  is equal to:

$${}_{54}\lambda^{135} + {}_{54}\sigma^{135}\phi.$$

The experimental values of Cs<sup>135</sup>/Cs<sup>137</sup> divided by the fission yield ratio of 1.043±0.002 previously obtained by Petruska *et al.* (1955) give the quantity Cs<sup>135</sup>/Y<sup>135</sup> for each of the four simultaneously irradiated samples. The values of  ${}_{54}\sigma^{135}\phi$  shown in Table I have been calculated from the ratios of Cs<sup>135</sup>/Y<sup>135</sup> using equation (1) with values of  ${}_{53}\lambda^{135} = 0.1034 \text{ hr}^{-1}$ ,  ${}_{54}\lambda^{135} = 0.752 \text{ hr}^{-1}$ , and  $t = 87.83 \text{ hours}$ .

TABLE I  
Neutron absorption rates in Xe<sup>135</sup>

Sample	Cs <sup>135</sup> /Cs <sup>137</sup> corrected for decay $\tau_{1/2} = 30 \text{ years}$	Cs <sup>135</sup> /Y <sup>135</sup>	${}_{54}\sigma^{135}\phi$ , hr <sup>-1</sup>
A—Top	0.4868±0.0021	0.4667±0.0022	0.1308±0.0014
Bottom	0.4793±0.0027	0.4595±0.0028	0.1355±0.0018
B—Top	0.7649±0.0057	0.7334±0.0057	0.03801±0.0011
Bottom	0.7632±0.0039	0.7317±0.0040	0.03830±0.00075

The value of the flux  $\phi$  for the positions of each of the cobalt monitors can be obtained from its disintegration rate  $dCo^{60}/dt$  with the following relation:

$$\phi = -\frac{dCo^{60}}{dt} \times \frac{1}{\lambda Co^{60} \hat{\sigma} S t}$$

where  $\lambda$  is the decay constant of Co<sup>60</sup> ( $4.18 \times 10^{-9} \text{ sec}^{-1}$ ),  $\hat{\sigma}$  the effective absorption cross section, and  $S$  the self-shielding correction.

In Table II are shown the values of the disintegration rates and weights of the cobalt monitors. The effective absorption cross sections of the cobalt shown in column 6 of Table II were calculated (assuming 2200 meters/second absorption cross section of 36.5 barns) in the manner described by Westcott (1958).

The values of the neutron temperature and the epithermal indices required for this evaluation have been determined by Bigham (1958) in connection with this present work. The flux depression or self-shielding in the cobalt was calculated as described by Petruska *et al.* (1955). The final column of Table II gives the calculated values of the flux using the irradiation time of 87.83 hours.

TABLE II  
Cobalt monitors data

Sample	Self-serve position	Weight Co <sup>59</sup> , mg	Disintegration rate, counts/sec $\times 10^7$	Neutron* temp., °C	$\hat{\sigma}$ , barns*	Epithermal index, r	$\phi \times 10^{13}$ , n/cm <sup>2</sup> sec†
A—Top	S-3-5	1.163	0.6904 $\pm$ 0.0018	120	36.33	0.018	1.141 $\pm$ 0.003
Bottom		1.151	0.8123 $\pm$ 0.0027				1.238 $\pm$ 0.005
B—Top	S-6-3	1.134	0.1585 $\pm$ 0.0012	137	36.89	0.0098	0.3265 $\pm$ 0.0022
Bottom		1.163	0.1591 $\pm$ 0.0010				0.3286 $\pm$ 0.0015

\*Epithermal indices defined by Westcott (1958) and neutron temperatures both measured by Bigham (1958).

†Corrected by factor of 0.977 for self-shielding (Case *et al.* 1953).

In order to obtain the absorption cross section of Xe<sup>135</sup> from  ${}_{54}\sigma^{135}\phi$  given in Table I, it was necessary to know the flux in each uranium sample. The flux at each of the uranium positions was interpolated from the values at the cobalt positions given in Table II assuming a linear flux gradient between the monitors in each block assembly. These values corrected for a 0.988 self-shielding factor in the uranium pins are given in Table III.

TABLE III  
Effective neutron absorption cross section of Xe<sup>135</sup>

Sample	Self-serve position	Neutron temp., °C	Flux ( $\phi$ ) $\times 10^{13}$ , n/cm <sup>2</sup> sec	$\hat{\sigma}_{Xe^{135}}$ , megabarns	Average $\hat{\sigma}_{Xe^{135}}$ , megabarns
A—Top	S-3-5	120	1.151 $\pm$ 0.0040	3.154 $\pm$ 0.034	3.15 $\pm$ 0.06
Bottom			1.198 $\pm$ 0.0044	3.138 $\pm$ 0.042	
B—Top	S-6-3	137	0.3243 $\pm$ 0.0022	3.264 $\pm$ 0.095	3.27 $\pm$ 0.11
Bottom			0.3244 $\pm$ 0.0019	3.278 $\pm$ 0.068	

The effective neutron absorption cross sections in Table III were obtained by dividing  ${}_{54}\sigma^{135}\phi$  given in column 4, Table I, by these fluxes.

#### DISCUSSION

The precision of the values for the effective absorption cross section of Xe<sup>135</sup> shown in Table III includes only the standard deviation of the observations carried out in this work. No estimate of the absolute accuracy of the values is possible without including the accuracy of the 36.5-barn value used for the 2200 meters/second absorption cross section of the Co<sup>59</sup> and the 9.20-hour half-life used for Xe<sup>135</sup>. To a lesser extent values given in Table III would depend on the accuracy of other quantities such as the resonance integral for Co<sup>59</sup> and the half-life of I<sup>135</sup>. The precision of the cross sections obtained from the samples in assembly B are not as good as those from

assembly A. This arises from the relatively smaller amount of capture by the  $\text{Xe}^{135}$  at the lower flux rather than from the precision of the measurements.

Previous determinations of the effective absorption cross section of  $\text{Xe}^{135}$  have been made by essentially the same method as in this work. Ivanov *et al.* (1957) have found a value of  $3.2 \pm 1.0$  megabarns and Petruska *et al.* (1955) 3.47 megabarns. Direct comparison of these with each other or with the values given in Table III is difficult as neutron temperatures were not measured. The precision of the 3.47-megabarn value obtained by Petruska *et al.* was difficult to estimate in view of flux variations during the irradiation, a factor which was not inherent in the present work. Although the neutron temperature was not determined by Petruska *et al.*, the irradiation position in the N.R.X. reactor for this sample was similar to that of assembly B. If the neutron temperature at the time of this irradiation was essentially the same as for the irradiation in the present work, the agreement of the values is very good.

The total cross-section measurements of Smith (unpublished) and Bernstein (1952) have been used by Westcott (1958) to evaluate the effective neutron absorption cross section of  $\text{Xe}^{135}$  at various temperatures. The calculated values for temperatures corresponding to this work are given in Table IV.

TABLE IV  
Effective absorption cross sections of  $\text{Xe}^{135}$  calculated from total cross sections

	$\sigma_{\text{Xe}^{135}} (g = 3/8) \times 10^5, \text{ barns}$		$\sigma_{\text{Xe}^{135}} (g = 5/8) \times 10^5, \text{ barns}$	
	120° C	137° C	120° C	137° C
Smith	29.78	29.96	33.78	33.98
Bernstein	26.95	27.12	30.19	30.45

These values are not strictly comparable with those obtained in this work since they represent the effective absorption for a pure Maxwellian spectrum of neutrons. The contribution of absorption by epithermal neutrons cannot be estimated until the resonance integral for  $\text{Xe}^{135}$  is known. The values comparable with this work would be slightly less than those given in Table IV, the greater reduction applying to the 120° values for which the epithermal flux is greater. Comparison of the possible values for the effective cross section of  $\text{Xe}^{135}$  given in Table IV with the values obtained in this work given in Table III suggests, however, that the values calculated from the data of Bernstein with the statistical weight factor of  $g = 5/8$  are most consistent with the present work.

#### ACKNOWLEDGMENTS

We wish to thank the Atomic Energy of Canada Limited for supplying the  $\text{U}^{235}$ -Al alloy and carrying out the irradiations. Special acknowledgment should be given to Dr. R. Jervis for preparing the necessary samples and flux monitors, Dr. C. B. Biggam for his determinations of the neutron temperature, and Mr. A. G. Ward for his helpful discussions.

## REFERENCES

- BERNSTEIN, S. 1956. *Phys. Rev.* **102** (3), 823.
- BIGHAM, C. B. 1958. Thermal neutron temperature in NRX self-serve positions S-3-5 and S-6-3. Atomic Energy of Canada Limited Report C.R.R.P. 765.
- CASE, K. M., DE HOFFMANN, F., and PLACZEK, G. 1953. Introduction of the theory of neutron diffusion. Vol. 1 (U.S. Government Printing Office, Washington, D.C.).
- GLEDENIN, L. E. and STEINBERG, E. P. 1955. Proceedings of the International Conference on the Peaceful Uses of Atomic Energy, Vol. 7, paper 614.
- INGHRAM, M. G. and CHUPKA, W. A. 1953. *Rev. Sci. Instr.* **24** (7), 518.
- IVANOV, R. N., GORSHKOV, V. K., ANIKINA, M. P., KUKAVDZE, G. M., and ERSHLER, B. V. 1957. *The Soviet Journal of Atomic Energy* **3** (12), 1436.
- PETRUSKA, J. A., MELAIKA, E. A., and TOMLINSON, R. H. 1955. *Can. J. Phys.* **33**, 640.
- SMITH, E. C., DESMUKE, N., and ATTA. Unpublished.
- WESTCOTT, C. H. 1958. Effective cross section values for well-moderated thermal reactor spectra. Atomic Energy of Canada Limited Report 670.

## A ${}^6\Sigma-{}^6\Sigma$ TRANSITION IN CrH<sup>1</sup>

BENGT KLEMAN<sup>2</sup> AND ULLA UHLER

### ABSTRACT

The infrared band system of CrH has been photographed at high dispersion. Rotational analyses of the 0-0 and 0-1 bands are given. The transition is shown to be a  ${}^6\Sigma^+-{}^6\Sigma^+$ . The upper  ${}^6\Sigma$ -state shows an extended perturbation. Rotational and vibrational constants for the two states are given. The application of theoretical expressions for the fine structure splitting in  ${}^6\Sigma$ -states is discussed and approximate values of the splitting constants in the observed states have been derived. The corresponding system of the isotope molecule CrD was also photographed and a vibrational analysis has been carried out. Finally the electronic configurations of the molecular states and the nature of the perturbing state are discussed. The ultraviolet systems of CrH are briefly mentioned.

### INTRODUCTION

In the band spectrum of CrH one infrared and two ultraviolet systems are known (Kleman and Liljeqvist 1955; Gaydon and Pearse 1937). These systems have now been photographed in emission from a King furnace with the 21-ft grating at the National Research Council of Canada, Ottawa. As expected the infrared system shows a simpler structure than the ultraviolet ones. A rotational analysis of the 0-0 band of the infrared system was undertaken and it is shown in the present paper to be due to a  ${}^6\Sigma^+-{}^6\Sigma^+$  transition. It was not possible at the time, due to a temporary lack of suitable plates, to obtain useful plates of the 0-1 band. This band was later photographed with a plane grating of somewhat smaller dimensions at the Physics Department, University of Stockholm. The accuracy of the measurements of the lines in the 0-1 band is slightly less than in the 0-0 band. Thus the analysis of the 0-1 band does not contribute essentially to the study of the fine structure of the  ${}^6\Sigma$ -terms other than to serve as a useful check on the assignment of the lines in the perturbed regions of the 0-0 band.

There have been comparatively few studies of the fine structure splittings in high multiplicity  $\Sigma$ -terms. The most thoroughly studied ones are probably the  ${}^7\Sigma$ -term in MnH (Nevin 1942, 1945) and the  ${}^4\Sigma$ -terms in  $O_2^+$  (Nevin 1938, 1940) and GeH (Kleman and Werhagen 1953).

In a  $\Sigma-\Sigma$  transition generally only the lines in the main branches can be observed. In the CrH bands no satellite branches were observed and consequently the differences between the sublevels of a rotational state cannot be directly measured. Such a transition does not seem specially suited for a study of the fine structure. In the present case, however, the splittings are rather large. This makes it possible to determine the splitting constants in an indirect way. Experimentally one obtains differences ( $\Delta_2F$ -values) between rotational levels within one and the same substate. Comparing the observed differences with the corresponding theoretical expressions one obtains approximate values of the splitting constants.

<sup>1</sup>Manuscript received January 19, 1959.

Contribution from the Department of Physics, University of Stockholm, Stockholm, Sweden.

<sup>2</sup>National Research Council Postdoctorate Fellow, 1954-1956.

## EXPERIMENTAL

The CrH bands were photographed in emission from a King furnace. The furnace was filled with hydrogen to a pressure of about 1/3 atm. A few grams of chromium were placed in a separate graphite tube in order to prevent the heating tube from being too quickly destroyed. The temperature of the furnace was kept in the range of 2150° to 2250° C. The 0-0 band of the red system was photographed at Ottawa in the first order of a 21-ft concave grating at a dispersion of 2.5 Å/mm. The plates used were Kodak I-N, I-M, and I-Z and the exposure time ranged between 10 minutes and 1 hour. In the third order of the same spectrograph the ultraviolet systems of CrH were photographed on Kodak III-O plates with an exposure time of about 5 minutes. In order to study the vibrational isotopic effect of the red system the furnace was filled with a mixture of helium and deuterium to a pressure of 1/3 atm and the region of the 0-0, 1-0, and 2-0 bands was photographed on I-N plates with an exposure time of 10 minutes. As reference lines for the spectra mentioned above high-order lines from an iron arc spectrum were used.

The 0-1 band was photographed in the first order of a plane grating in Littrow mounting at a dispersion of about 4 Å/mm. The pressure was 2/3 atm and the exposure time 20 minutes on sensitized Kodak I-Z plates. First-order lines of the arc spectra of barium, strontium, and chromium served as comparison spectrum.

*Structure of the Bands*

As can be seen from a comparison between Figs. 1a and 1b, the structure of the infrared system of CrH is simpler than that of the ultraviolet one. A thorough study of the infrared 0-0 band showed 12 branches of approximately the same intensity. No strong lines remained after picking out these branches. The branches form six pairs of associated *R*- and *P*-branches. The straightforward assumption, which is also supported by the further analysis, is that they constitute a  ${}^6\Sigma-{}^6\Sigma$  transition. As is apparent from the intensity formulae for  ${}^6\Sigma-{}^6\Sigma$  transitions given by Premaswarup (1953) only the 12 main branches will be of any appreciable strength. In the present case we have not been able to trace any of the satellite branches. All the branches show one big perturbation and some branches, in addition, show smaller ones. The perturbations originate in the upper state.

The exposures of the 0-1 band are not as good as those of the 0-0 band. Here, too, six *R*- and six *P*-branches are found. The agreement of the combination differences and the presence of the same perturbation pattern confirm the analysis of the 0-0 band.

The CrD plates show a rather dense structure. The systems of both CrH and CrD are present and we were only able to measure the CrD heads of the 0-0, 1-0, and 2-0 bands.

The ultraviolet bands have, as is seen from Fig. 1a, a very complicated structure. No attempt has been made to analyze these bands rotationally.

*Vibrational Analysis of CrH and CrD*

As only two bands have been analyzed rotationally, the vibrational constants



# PLATE I

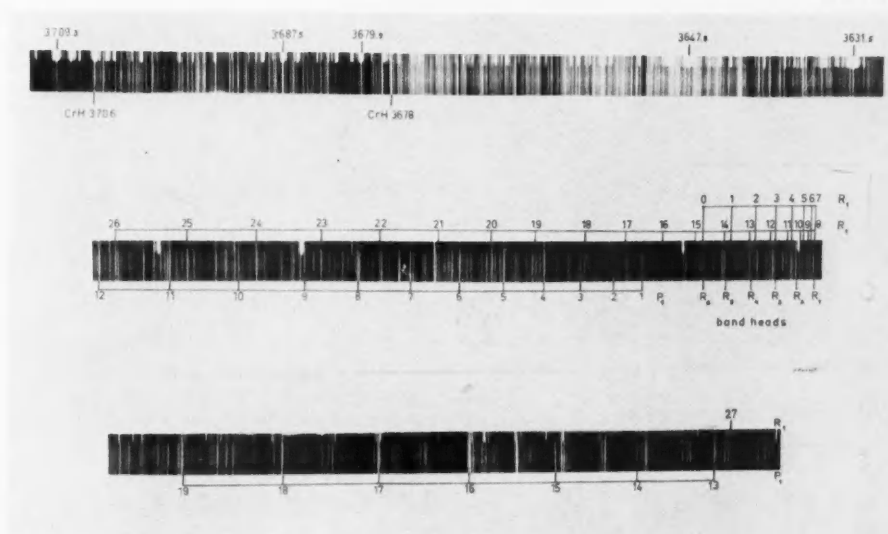
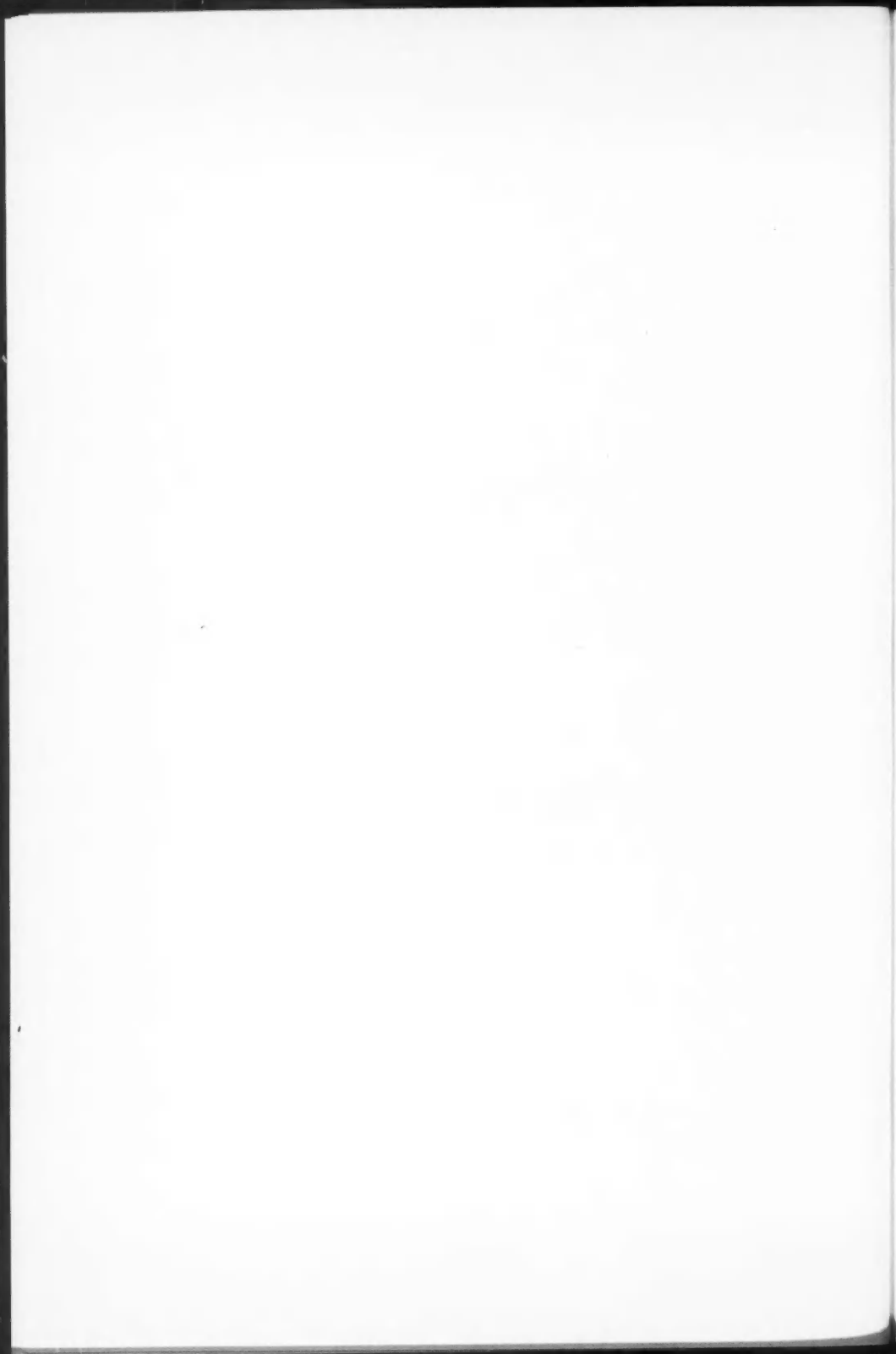


FIG. 1. CrH bands. (a) Upper band. The 3600-Å system. (b) The 0-0 band of the infrared system. Part of the analysis is shown in the figure.



had to be derived from measurements of the band heads. The heads measured are listed in Table I.

TABLE I  
Band heads

CrH				CrD			
Band	$\lambda$ , Å	Int.	$\text{cm}^{-1}$	Band	$\lambda$ , Å	Int.	$\text{cm}^{-1}$
0-1	9968.5	3	10029				
0-0	8611.1	10	11610	0-0	8626.6	10	11589
1-0	7641.7	4	13082	1-0	7901.8	3	12652
2-0	6889.6	1	14511	2-0	7302.9	1	13689

Using the simple isotope formulae the  $\omega'_0$  value of CrD can be calculated from the vibrational constants of the hydride. The value obtained is  $\omega'_0 = 1083 \text{ cm}^{-1}$  in good agreement with the observed value  $1089 \text{ cm}^{-1}$ . In the lower electronic state it is only possible to obtain the interval between the first two vibrational levels.

$$\text{CrH: } \Delta G''_1 = 1581 \text{ cm}^{-1}.$$

The vibrational constants are summarized in Table V.

#### Rotational Analysis

The 0-0 and 0-1 bands were analyzed. The wave numbers of the lines of the 12 main branches in each band are given in Tables II and III.

As mentioned before, the measurements of the lines in the 0-1 band are less accurate than those of the 0-0 band and only the combination differences of the 0-0 band were used for the determination of the rotational constants of the upper state.

A general procedure for obtaining the rotational energy levels of a  $\Sigma$ -state has been developed by van Vleck (1929). It leads in the case of a  $\sigma\Sigma$ -state to a secular determinant of the sixth order. The energy levels  $W_1 \dots W_6$  are the roots of the following equation:

$$\begin{vmatrix} a-W & a_1 & 0 & 0 & 0 & 0 \\ a_1 & b-W & b_1 & 0 & 0 & 0 \\ 0 & b_1 & c-W & c_1 & 0 & 0 \\ 0 & 0 & c_1 & c-W & b_1 & 0 \\ 0 & 0 & 0 & b_1 & b-W & a_1 \\ 0 & 0 & 0 & 0 & a_1 & a-W \end{vmatrix} = 0$$

where

$$a = B[J(J+1) - (15/4)] + 10\epsilon; \quad b = B[J(J+1) + (17/4)] - 2\epsilon;$$

$$c = B[J(J+1) + (33/4)] - 8\epsilon$$

$$a_1 = \sqrt{5}B[J(J+1) - (15/4)]^{1/2}; \quad b_1 = 2\sqrt{2}B[J(J+1) - (3/4)]^{1/2}; \quad c_1 = 3B[J + \frac{1}{2}].$$

The magnetic interaction between  $N$  and  $S$  can to a first approximation be taken into account by adding the expression  $(\gamma/2)[J(J+1) - N(N+1) - S(S+1)]$  where  $\gamma$  is a constant.

TABLE II  
The 0-0 band of CrH

N	$R_1(N)$	$P_1(N)$	$R_2(N)$	$P_2(N)$	$R_3(N)$	$P_3(N)$
0	11563.43*					
1	575.13	11538.63*	11576.13	11530.21	11572.82*	11525.81
2	585.12	526.96*	584.59	515.62*	580.29	510.88
3	593.44	513.81*	591.48	499.05	586.22*	494.23*
4	600.14	499.22*	596.71	481.40	590.30	475.84
5	605.02	483.18*	600.25	462.24	592.68	455.81
6	608.26	465.46*	602.20	441.56	593.44	434.04
7	609.74*	446.14*	602.33	419.33	592.55	410.65
8	609.74*	425.25	600.90	395.53	589.79	385.72
9	607.08	402.80	596.98		584.02	
10	603.71	378.89	592.55	370.19	579.27	359.14
11	598.44	352.55*	586.05	342.57	571.60*	329.68
12	591.48	325.65*	577.78	314.62	562.15	301.47
13	582.87	297.07	567.92	284.79	551.19	270.39*
14	572.51*	266.99	556.49	253.42	538.63*	237.90
15	560.68	235.47	543.46	220.68	524.50	203.99
16	547.21	202.50	528.89	186.50	508.92	168.72
17	532.23*	168.17	512.90	151.04	492.05	132.20
18	515.62*	132.56	495.72*	114.33	474.33	99.44
19	495.72*	99.63	479.51*	076.42	459.02	055.67
20	478.05*	057.45	452.15	037.69	425.75	016.36*
21	457.04	016.36*	431.25	11000.20	404.35	10379.75
22	434.67	10977.58	408.12	10951.81	380.54	925.47
23	410.94	935.91	383.47	910.31	354.98	883.52
24	385.81	893.29	357.41	866.87	328.01	839.31
25	359.55	849.56	330.07	822.20	299.78	793.81
26	331.97	804.93*	301.47	776.59	270.39*	747.23
27	303.28	759.42	271.73	730.01		699.78
28		713.07	240.74	682.64		651.43
29		665.93	208.87*	634.48		602.33
30		618.05		585.63		552.49
31		569.47		536.04		

\*Overlapped.

TABLE II (Concluded)  
The 0-0 band of CrH

$N$	$R_d(N)$	$P_d(N)$	$R_s(N)$	$P_s(N)$	$R_e(N)$	$P_e(N)$
0						
1	11572.82*			11497.54		
2	578.41	11500.80	11572.51*	479.51*	11563.43	11472.72
3	581.78	486.74	572.82*	459.65	562.75	452.58
4	583.22	468.07	571.60*	437.92	560.08	429.35
5	582.87	447.23	568.30	414.21	555.63*	404.35
6	580.87	424.54	563.43*	388.77	549.56	377.47
7	577.09	400.20	556.80	361.66	541.75	349.12
8	571.60*	374.10				
9						
10	564.41*	346.50	548.52	332.93	532.23*	319.18
11	555.63*	317.33	538.63*	302.67	521.21	287.73
12	545.09	286.66	526.96*	270.85	508.49	254.68
13	532.97	254.48	513.81*	237.59	494.23*	220.32
14	519.36	220.83	499.22*	202.86	478.03*	184.45
15	504.21	185.88	483.18*	166.79	460.87	147.21
16	487.59	149.56	465.46*	129.35	441.92	108.66
17	469.70	111.93	446.14*	90.71	421.49	68.83
18	451.26	73.19	426.18	50.85	399.62	27.73
19	435.09	33.45	407.71	9.87	376.32	10985.36
20	399.25	10993.23	373.63	10968.34	350.65*	941.85
21	377.47	955.90	350.65	928.60	325.65*	897.28
22	352.55*	899.02	324.86	873.45	298.27*	850.42
23	326.07		297.48		269.69	804.93*
24	298.27*	856.41	268.69	829.91	239.70	757.29
25	269.00	811.37	238.66*	783.82	208.87*	708.68
26	238.66*	764.98	207.71	736.44	176.61	659.30
27	207.18	717.53	174.86	688.04		609.06
28		669.13		638.73		558.07
29		619.92		588.66		
		569.94		537.82		

\*Overlapped.

TABLE III  
The 0-1 band of CrH

N	R <sub>1</sub> (N)	P <sub>1</sub> (N)	R <sub>2</sub> (N)	P <sub>2</sub> (N)	R <sub>3</sub> (N)	P <sub>3</sub> (N)	R <sub>4</sub> (N)	P <sub>4</sub> (N)	R <sub>5</sub> (N)	P <sub>5</sub> (N)	R <sub>6</sub> (N)	P <sub>6</sub> (N)
0												
1	9991.17	9992.83		9923.09								
2	10000.10	9979.92		9907.80								
3	10008.63	9977.80		891.77								
4	015.46	893.48	10005.25		9999.05	9902.99	9990.65	9895.79	9981.47*	9888.79		
5	015.46	893.48	010.62		10003.06	886.39	993.55	878.45	983.17*	870.37	9873.12*	
6	020.59	877.99	014.80	874.84	006.09	868.43	995.36	859.71	983.94	850.35	973.12*	9819.30
7	024.86	861.20	017.40	856.72	007.64*	849.13	995.92	839.51	983.17*	829.18	970.73	976.23
8	027.67	843.22	018.90	837.31	007.64*	828.02	994.96	828.02	983.17*	818.04	957.26	957.26
9	028.22	824.01	018.26	816.73	006.25	806.87	992.70	795.10	973.13	782.74	963.20	743.77
10	028.55	803.65	017.40	795.10								
11	027.27	781.34	014.80	771.25	004.13	783.92	989.10	771.16	973.12*	757.56	956.86	716.40
12	024.66	758.91	010.95	747.69	000.46	758.42	984.21	746.04	967.32	731.32	950.13	687.70
13	020.59	734.95	005.86	722.59	9994.98	734.49	978.13	719.69	960.06	703.92	941.48	657.93
14	015.46	709.92	001.74	698.09	989.10	708.17	970.73	692.15	951.58	675.19	931.82	627.27
15	011.41	683.14	001.74	666.01	973.84	650.70	952.37	634.02	930.96	614.88	909.00	562.44
16	001.22	656.61	983.17	640.54	972.84	622.70	941.48	603.50	919.57	583.25	895.79	538.70
17	9992.35	628.37	973.12	611.22	952.09	592.34	929.80	572.04	906.23*	550.67	881.43	494.04
18	982.37	599.26	962.36	581.01	940.86	561.06	917.89	539.70	892.64	517.26	865.93	458.48
19	969.42	569.20	953.48	550.01	931.82	528.70	907.80	506.33	890.91	483.18	849.61	422.23
20	958.81	538.17	932.83	518.40								
21	945.40	504.78	904.49	488.32	906.23*	497.00	879.87	473.77	853.92	448.78	830.82	385.05
22	930.96	473.77	887.34	447.99	892.64	467.83	865.43	443.85				
23	915.28	440.36	870.37	414.60								
24	898.88	406.15		379.73								

\*Overlapped.

The splitting constants do not occur in the expression

$$\sum_{r=1}^6 \Delta_2 F_r(J).$$

Thus by plotting

$$\left[ \sum_{r=1}^6 \Delta_2 F_r(J) \right] / (J + \frac{1}{2})$$

against  $(J + \frac{1}{2})^2$  the rotational constants  $B$  and  $D$  can be derived. The values obtained are given in Table V.

#### *Determination of the Splitting Constants*

The secular determinant of the sixth order mentioned above reduces to two of the third order. A first-order development of the roots of these equations leads to the following expressions for the energy levels (Rao 1952).

$$F_1(N) = B \left[ N(N+1) - 10\lambda \frac{N}{2N+3} \right] \quad \text{where} \quad N = J - 5/2$$

$$F_2(N) = B \left[ N(N+1) + \lambda \left( 1 + \frac{27}{2N+3} \right) \right] \quad N = J - 3/2$$

$$F_3(N) = B \left[ N(N+1) + \lambda \left( 4 + \frac{27}{2N+3} - \frac{15}{2N-1} \right) \right] \quad N = J - 1/2$$

$$F_4(N) = B \left[ N(N+1) + \lambda \left( 4 + \frac{15}{2N+3} - \frac{27}{2N-1} \right) \right] \quad N = J + 1/2$$

$$F_5(N) = B \left[ N(N+1) + \lambda \left( 1 - \frac{27}{2N-1} \right) \right] \quad N = J + 3/2$$

$$F_6(N) = B \left[ N(N+1) - 10\lambda \frac{N+1}{2N-1} \right] \quad N = J + 5/2$$

The parameter  $\lambda$  is equal to the spin splitting constant  $\epsilon$  divided by  $B$  ( $\lambda = \epsilon/B$ ).

In order to study the influence of the neglected high-order terms of  $\lambda$  the equations have been solved numerically for the four values  $\lambda = \pm 1.0, \pm 0.1$ . The result, compared with the first-order solution is seen in Fig. 2. The discrepancies between the two solutions are small for  $\lambda = \pm 0.1$ , but quite important for  $\lambda = \pm 1.0$ . It is to be observed that the exact solutions are not, in contrast to the approximate ones, symmetric with respect to a change of sign of  $\lambda$ . A rough calculation showed that the values of  $\lambda$  to be expected in the present case are of the magnitude  $+0.1$  and  $+0.01$  in the upper and lower state respectively. Thus the approximate energy expressions of the rotational sublevels can be assumed to be sufficiently accurate for the determination of the splitting constants in the present case.

In the absence of satellite branches it is impossible to obtain experimental values of differences between any two of the sublevels in a rotational state.

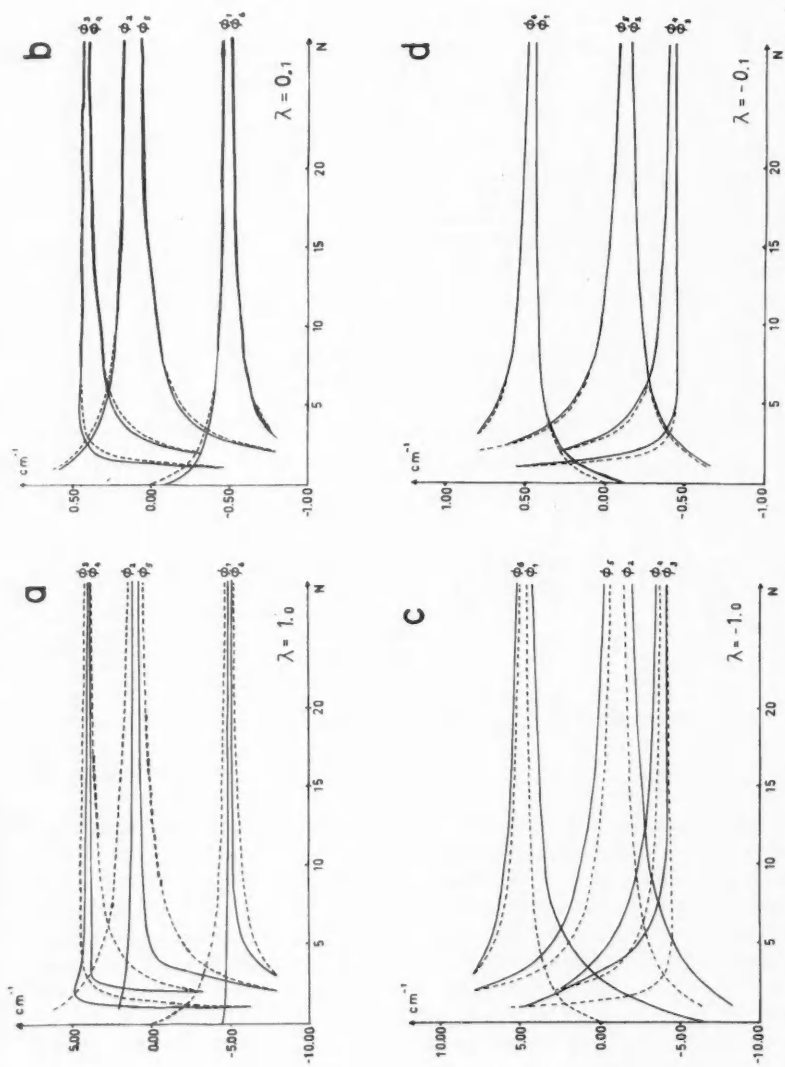


FIG. 2. Sublevel energies of a  $\sigma_2$ -state as a function of  $N$  for different values of the spin splitting constant  $\lambda$ . The broken line curves show Rao's approximate solutions and the full line curves represent the exact solutions.  $B_N(N+1)$  has been subtracted from the sublevel energies, i.e.  $\phi_i = F_i(N) - B_N(N+1)$ . The  $\gamma$ -correction is omitted here.



The only observational data convenient for the determination of the splitting constants are the second differences:

$$\begin{aligned}\Delta_2 F_1(N) &= B \left[ 4(N + \tfrac{1}{2}) - \frac{60\lambda}{(2N+5)(4N+1)} \right] & +5\gamma \\ \Delta_2 F_2(N) &= B \left[ 4(N + \tfrac{1}{2}) - \frac{108\lambda}{(2N+5)(2N+1)} \right] & +3\gamma \\ \Delta_2 F_3(N) &= B \left[ 4(N + \tfrac{1}{2}) - \frac{48\lambda(2N-13)}{(2N+5)(2N+1)(2N-3)} \right] & +\gamma \\ \Delta_2 F_4(N) &= B \left[ 4(N + \tfrac{1}{2}) + \frac{48\lambda(2N+15)}{(2N+5)(2N+1)(2N-3)} \right] & -\gamma \\ \Delta_2 F_5(N) &= B \left[ 4(N + \tfrac{1}{2}) + \frac{108\lambda}{(2N+1)(2N-3)} \right] & -3\gamma \\ \Delta_2 F_6(N) &= B \left[ 4(N + \tfrac{1}{2}) + \frac{60\lambda}{(2N+1)(2N-3)} \right] & -5\gamma\end{aligned}$$

In the expressions above, the term due to  $N, S$  interaction

$$\left[ +\frac{5}{2}\gamma N, +\frac{\gamma}{2}(3N-5), +\frac{\gamma}{2}(N-8), -\frac{\gamma}{2}(N+9), -\frac{\gamma}{2}(3N+8), \text{ and } -\frac{5\gamma}{2}(N+1) \right]$$

in  $F_1(N), F_2(N), F_3(N), F_4(N), F_5(N)$ , and  $F_6(N)$  respectively has been added.

The constants  $\lambda$  and  $\gamma$  are derived graphically by a linear representation of expressions of the type

$$\Delta_2 F_m(N) - \Delta_2 F_n(N) \quad (\text{where } m = 1, 2 \dots 6, n = 1, 2 \dots 6 \text{ and } m \neq n).$$

Every combination of  $m$  and  $n$  has been examined. The scattering of the individual determinations is considerable, however, and the accuracy in the  $\gamma''$ -,  $\lambda''$ -, and  $\lambda'$ -values obtained is roughly 30%. The magnitude of  $\gamma'$  is much larger than that of  $\gamma''$  which reduces the relative error to about 5%. For the upper state some of the curves were slightly bent indicating that the approximate expressions are not quite sufficient. Mean values of the constants derived from the diagrams are given in Table V.

### The Perturbations

As mentioned before, large irregularities in all main branches have been found.

The displacements of the lines from their expected positions, which in some cases amount to  $7 \text{ cm}^{-1}$ , are explained as perturbations in all six sublevels of  $v' = 0$ . This is checked by the analysis of the 0-1 band which shows exactly the same perturbation picture as the 0-0 band. The perturbation maximum occurs at  $N = 20, 21$  in the levels  $F_2\text{-}F_6$  and at  $N = 19, 20$  in the  $F_1$ -level.

In addition to the main perturbations smaller ones have been found at  $N = 9$ , 10 in the  $F_1$ ,  $F_2$ , and  $F_3$  levels. The perturbations are illustrated in Fig. 3.

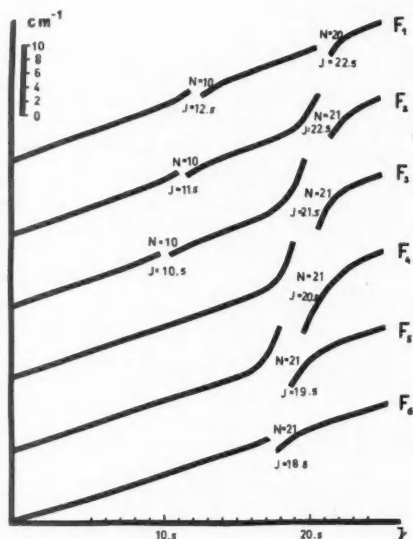


FIG. 3. The perturbations in the level  $v' = 0$ . The unperturbed parts of the sublevel energy functions have been schematically illustrated as straight lines. The magnitude of the perturbations has been represented on a scale given on the ordinate axis. The separations of the lines in the figure are not significant.

A  $^6\Sigma$ -state necessarily belongs to Hund's case *b*. The occurrence of the perturbations at the same  $N$ -number in all the sublevels indicates that the perturbing state also belongs to Hund's case *b* and that its multiplicity must be at least six. For reasons which are given below the perturbing term is assumed to be an  $^8\Sigma$ -state.

Budó and Kovács have treated the case of perturbations between  $\Sigma$ -terms of equal multiplicity (Kovács 1938) and perturbations between  $\Sigma$ -terms of different multiplicity (Budó and Kovács 1938). A necessary condition among others for a perturbation is that the  $J$ -values are equal in the perturbed and the perturbing states. In the case of multiplet terms the  $N$ -values must be equal or differ by an even number.

In the present case it is natural to assume that the large perturbation at  $N = 21$  occurs when both  $J$  and  $N$  are equal for the perturbed and the perturbing state. The smaller perturbations at  $N = 10$ , which have only been partially traced, may represent the case, when the  $N$ -numbers differ by 2 units. From these assumptions and assuming the rotational energy to be roughly  $BN(N+1)$ , we are now able to calculate an approximate  $B^*$ -value of the unknown perturbing state. The value obtained is  $B^* \sim 6.0 \text{ cm}^{-1}$ .

*Expected Electronic States*

In general the low-lying electronic states in diatomic hydrides can be predicted on the basis of the electron configurations in the "united atom". When, however, there are several electron configurations in the "united atom" giving rise to electronic states of approximately equal energy, there will be difficulties in predicting the order of the states in the corresponding hydride molecule. This is the case for CrH as well as for the neighboring molecules as for example MnH.

It therefore does not seem feasible to predict the expected states simply by trying to consider the relative order of excitation of all possible electron configurations. Instead we proceed in the following manner. First, accepting the experimental evidence of the two low-lying  $\Sigma$ -states, we will try to relate these to the proper electron configurations, and then discuss the reason for the assumption that the lowest of these observed states is the ground state of the molecule ( $X \Sigma$ ), and finally we will compare the result with the related molecule MnH. We only need now to consider those electron configurations which can give rise to sextet and higher states and shall assume that of all molecular states arising from one electron configuration the one with the highest spin will be lowest and that, when there are several with the same spin, the one with the highest  $\Lambda$ -value will lie lowest. In Table IV those electron configurations which can give rise to low-lying sextet and octet states are shown.

TABLE IV  
Electron configurations of CrH and MnH

	KL	3d $\sigma$	3d $\pi$	3d $\delta$	4s $\sigma$	4p $\sigma$	4p $\pi$	Lowest state*	Other states
CrH	KL	$\sigma^2$	$\pi^2$	$\delta^2$	$\sigma$			${}^6\Sigma^+ \dots$	Quartets, doublets
	KL	$\sigma^2$	$\pi^2$	$\delta^2$		$\sigma$		${}^6\Sigma^+ \dots$	Quartets, doublets
	KL	$\sigma^2$	$\pi^2$	$\delta^2$			$\pi$	( ${}^6\Pi$ ) $\dots$	Quartets, doublets
	KL	$\sigma$	$\pi^2$	$\delta^2$	$\sigma$	$\sigma$		${}^8\Sigma^+ \dots$	Sextets, quartets, doublets
MnH	KL	$\sigma^2$	$\pi^2$	$\delta^2$	$\sigma$	$\sigma$		${}^7\Sigma^+ \dots$	Quintets, triplets, singlets
	KL	$\sigma^2$	$\pi^2$	$\delta^2$	$\sigma$		$\pi$	${}^7\Pi \dots$	Quintets, triplets, singlets

\*This is the lowest predicted state of the given electron configuration and is (with the exception of the ( ${}^6\Pi$ )-state) assumed to be identical with an observed state.

The two observed  ${}^6\Sigma$ -states in CrH are interpreted as being the  ${}^6\Sigma^+$ -states derived from the electron configurations  $(3d\sigma)^2(3d\pi)^2(3d\delta)^2(4s\sigma)$  and  $(3d\sigma)^2(3d\pi)^2(3d\delta)^2(4p\sigma)$  respectively. Both these states are the only sextet states which can be derived from these electron configurations. Although it cannot be rigorously proved from the present observations, there are many indications in favor of the assumption that the observed  $X \Sigma^+$ -state is the ground state of the CrH molecule. From the experimental point of view the strength of the  $A \Sigma^+ - X \Sigma^+$  system, considering the observed behavior of other hydride spectra in a low-energy light source of this type supports the above

assumption. The ground state of Mn is a  ${}^6S$ -state and this has to be correlated with the ground state  ${}^7S+{}^2S$  of  $\text{Cr}+\text{H}$  via the lowest  ${}^6\Sigma^+$ -state in the  $\text{CrH}$  molecule. By the assumption that this  ${}^6\Sigma^+$  is the ground state we avoid a two-fold-crossing of this potential curve by another presumed ground state curve in the molecule. The above assumptions also look very reasonable in view of the electron configurations which one is forced to assume in  $\text{MnH}$  to explain the two lowest observed states  ${}^7\Sigma^+$  and  ${}^7\Pi$ , viz.  $(3d\sigma)^2(3d\pi)^2(3d\delta)^2(4s\sigma)(4p\sigma)$  and  $(3d\sigma)^2(3d\pi)^2(3d\delta)^2(4s\sigma)(4p\pi)$  (Herzberg 1957). From the appearance of the perturbation in the  $A$   ${}^6\Sigma^+$ -state it is evident that the perturbing state, which has to be a sextet or an octet, is very near to a case  $b$  state. Except for  $\Sigma$ -states pure case  $b$  states are very rare in molecules containing a relatively heavy atom like Cr and, therefore, the perturbing state is in all likelihood a  $\Sigma$ -state. If this is true, it has to be the  ${}^8\Sigma^+$ -state indicated in Fig. 4. The perturbation is rather weak which also fits with the relatively weak interaction between

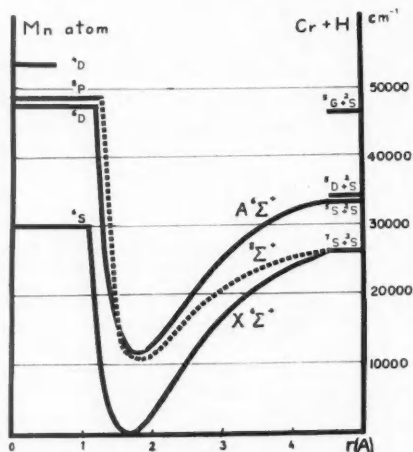


FIG. 4. Potential curves of  $\text{CrH}$ .

states of different multiplicities. The  ${}^8\Sigma^+$ -state can only be derived by breaking up the  $(3d\sigma)^2$  electron pair, and it seems likely that it corresponds to the electron configuration  $(3d\sigma)(3d\pi)^2(3d\delta)^2(4s\sigma)(4p\sigma)$ .

The lowest octet term in the united atom Mn is an  ${}^8P^0$  term, which via the perturbing  ${}^8\Sigma^+$  is to be correlated with  ${}^7S(\text{Cr}) + {}^2S(\text{H})$ . The upper  $A$   ${}^6\Sigma^+$ -state of the infrared system may be correlated with the  ${}^5S(\text{Cr}) + {}^2S(\text{H})$  level of the separated atoms. The suggested term scheme is given in Fig. 4.

An extrapolation of the vibrational levels of the upper  ${}^6\Sigma^+$ -state ( $A$   ${}^6\Sigma$ ) in  $\text{CrH}$  and  $\text{CrD}$  points to a dissociation energy  $D_0'$  for this state of around 23000  $\text{cm}^{-1}$ . This gives for the dissociation energy of the ground state ( $X$   ${}^6\Sigma^+$ )  $D_0'' = 26000 \text{ cm}^{-1}$ . The shapes of the potential curves of  $A$   ${}^6\Sigma^+$  and  $X$   ${}^6\Sigma^+$  (Fig. 4) have been based on these figures.

### The Ultraviolet Systems

The complex structure of the ultraviolet bands rules out the possibility that they are of the  $\Sigma \rightarrow \Sigma$  type. The strength of the 3600-Å system probably implies a transition which is in accordance with the selection rules for an allowed transition. Assuming the ground state to be involved in this transition, the term scheme in Fig. 4 would suggest the upper state to be a  ${}^4\Pi$ -state probably correlated with the  ${}^4D(\text{Cr}) + {}^2S(\text{H})$  dissociation limit.

TABLE V  
Summary of constants of the  $A \ {}^4\Sigma - X \ {}^4\Sigma$  system

	$B_0'' = 6.125 \text{ cm}^{-1}$	$B_0' = 5.268 \text{ cm}^{-1}$
	$D_0'' = 3.38 \times 10^{-4}$	$D_0' = 2.42 \times 10^{-4}$
CrH:	$B_1'' = 5.945$	$\nu_{00} = 11542.88$
	$D_1'' = 3.40 \times 10^{-4}$	$\omega_0' = 1515$
	$\alpha'' = 0.180$	$\omega_0'x_0' = 21.5$
	$\Delta G_{\frac{1}{2}}'' = 1581$	
	$\gamma'' = 0.15 \pm 0.01$	$\gamma' = 1.20 \pm 0.05$
	$\lambda'' = 0.03 \pm 0.01$	$\lambda' = 0.12 \pm 0.04$
	$\epsilon'' = 0.18 \pm 0.06$	$\epsilon' = 0.66 \pm 0.20$

NOTE: For CrD the constants obtained are:

$$\omega_0' = 1089$$

$$\omega_0'x_0' = 13$$

The vibrational constants are derived from band heads.

### ACKNOWLEDGMENTS

Our thanks are due to Drs. A. E. Douglas and G. Herzberg for many helpful suggestions during the course of this work. We are also indebted to Dr. Lars Åkerlind for experimental help with the exposures made in Stockholm.

### REFERENCES

- BUDÓ, A. and KOVÁCS, I. 1938. *Z. Physik*, **111**, 633.  
 GAYDON, A. G. and PEARSE, R. W. B. 1937. *Nature*, **140**, 110.  
 HERZBERG, G. 1957. *Molecular spectra and molecular structure* (D. Van Nostrand, Company, Inc.), p. 341.  
 KLEMAN, B. and WERHAGEN, E. 1953. *Arkiv Fysik*, **6**, 399.  
 KLEMAN, B. and LILJEQVIST, B. 1955. *Arkiv Fysik*, **9**, 345.  
 KOVÁCS, I. 1938. *Z. Physik*, **111**, 640.  
 NEVIN, T. E. 1938. *Phil. Trans. Roy. Soc. London, A*, **237**, 471.  
 ——— 1940. *Proc. Roy. Soc. (London), A*, **174**, 371.  
 ——— 1942. *Proc. Roy. Irish Acad.* **48**, 1.  
 ——— 1945. *Proc. Roy. Irish Acad.* **50**, 123.  
 PREMASWARUP, D. 1953. *Indian J. Phys.* **27**, 415.  
 RAO, K. S. 1952. *Indian J. Phys.* **26**, 47.  
 VAN VLECK, J. H. 1929. *Phys. Rev.* **33**, 467.

# ABSOLUTE STANDARDIZATION OF RADIOACTIVE NEUTRON SOURCES

## II. THE USE OF THE $F^{19}(\alpha, n)Na^{22}$ REACTION<sup>1</sup>

K. W. GEIGER

### ABSTRACT

Fluorine has only one stable isotope,  $F^{19}$ . If neutrons are produced by the  $F^{19}(\alpha, n)Na^{22}$  reaction the neutron output can be calculated from the yield of the resulting radioactive  $Na^{22}$ . The growth of  $Na^{22}$  (half-life, 2.58 years) has been measured in a neutron source consisting originally of 1.6 curies  $Po^{210}$  mixed with  $CaF_2$  powder. Since  $Na^{22}$  is a positron emitter, discrimination against  $\gamma$ -rays from  $Po^{210}$  and from nuclear reactions could be achieved by detecting the two positron annihilation quanta in coincidence. The  $Na^{22}$  growth has been followed over 20 months and is in agreement with the theoretical growth curve. Comparison with a calibrated  $Na^{22}$  source yielded a neutron emission rate of  $(10.70 \pm 0.25) \times 10^6 \text{ sec}^{-1}$ . This resulted in a neutron emission rate of  $(3.16 \pm 0.10) \times 10^6 \text{ sec}^{-1}$  for the Ra- $\alpha$ -Be source of the National Research Council, in good agreement with  $(3.22 \pm 0.05) \times 10^6 \text{ sec}^{-1}$  obtained by a neutron thermalization method.

### INTRODUCTION

In a previous publication (Part I, Geiger and Whyte 1959) the principal methods for the determination of the neutron emission rate,  $Q$ , from a radioactive neutron source have been discussed and an experimental determination of the output of the N.R.C. standard neutron source has been made. This was carried out by using a method where substantially all neutrons were thermalized and captured in an aqueous  $MnSO_4$  bath. Since the proportion of captures in manganese can be calculated the neutron emission rate of the source can be determined by the absolute activity of the produced radioactive manganese-56.

An alternative for the determination of a neutron yield is to use a reaction in the source where the (recoil) particle which is produced simultaneously with the neutron can be detected (associated particle method). This has the advantage that no knowledge of neutron cross sections is required. Accelerator-induced reactions lend themselves easily to the associated particle method; however, the comparison of their neutron yield with that of a radioactive source is difficult. It is therefore more desirable to use an associated particle method within a radioactive neutron source. This principle seems to have been used only on photoneutron sources. Glückauf and Paneth (1938) used the  $Be^9(\gamma, n)2He^4$  reaction and analyzed for the amount of helium produced in the beryllium. Martin, Bishop, and Halban (1955) counted the photoprotons of the  $H^2(\gamma, n)H^1$  reaction in an ionization chamber. The deuterium gas was then replaced by heavy water to obtain a reasonable yield. Such standardizations are very difficult to carry out experimentally.

<sup>1</sup>Manuscript received January 26, 1959.

Contribution from the Division of Applied Physics, National Research Council, Ottawa, Canada.

Issued as N.R.C. No. 5151.

However, the associated particle method could also be used in the more convenient ( $\alpha, n$ ) source when the product nucleus is radioactive. This, as far as the author knows, had not been done previously. The following requirements would have to be met by such a source:

- (1) The neutron-producing reaction should give a high yield.
- (2) All neutrons should originate from the same reaction.
- (3) Other possibly concurrent reactions (e.g.  $\alpha, p$ ) should not produce radioactive nuclides.
- (4) Measurement of the growth of the radioactive product should be possible without destruction of the source.
- (5) The source should be of small size.

The



reaction is probably the only one which fulfills the above requirements well. The neutron yield from fluorine is only excelled by beryllium and boron (e.g. Feld 1953) and fluorine has only one isotope; hence for every neutron formed a  $\text{Na}^{22}$  nuclide is produced. To meet requirements (4) and (5) polonium-210 may be chosen as  $\alpha$ -emitter because of the small number of  $\gamma$ -quanta emitted and its high specific activity. Such a source has been prepared and the neutron emission determined absolutely.

#### THE Po- $\alpha$ -F NEUTRON SOURCE

The source consisted of a nickel cylinder, 8 by 18 mm high and filled with 1 g of  $\text{CaF}_2$  powder; 1.6 curies of  $\text{Po}^{210}$  were distributed by heat through the fluorine.<sup>2</sup> Calcium has higher reaction thresholds than fluorine and has not been found to react with polonium  $\alpha$ -particles (Odeblad 1954; Saha 1938). Besides reaction 1 and inelastic scattering of  $\alpha$ -particles only the following additional reaction is expected to occur



To be useful as a standard the source has to be physically stable with time. This has been checked by comparing its neutron emission rate with that of a Ra- $\alpha$ -Be source over a period of 20 months, using a  $\text{BF}_3$  proportional counter in paraffin. As expected, the neutron emission rate of the Po-F source followed, within the uncertainty of the measurements ( $\pm 0.2\%$ ), the well-established  $\text{Po}^{210}$  half-life of 138.4 days.

The  $\gamma$ -spectrum of the source has been studied with a scintillation spectrometer, using a  $1\frac{1}{2} \times 1$  in. sodium iodide crystal. The spectrum (Fig. 1) of the 30-day-old source is in general agreement with the spectrum obtained by Breen and Hertz (1955) and shows mainly the 0.80-Mev  $\gamma$ -peak of  $\text{Po}^{210}$  and a further photoppeak at 1.28 Mev. This peak is due to de-excitation of the

<sup>2</sup>The source was manufactured by Mound Laboratory, Monsanto Chemical Company, Miamisburg, Ohio.

first-excited state of  $\text{Ne}^{22}$ , reached by reaction 2. Although the identical state is reached by the 2.58-year decay of  $\text{Na}^{22}$ , the  $\gamma$ -ray cannot be assigned to this decay, since after only 30 days very little  $\text{Na}^{22}$  has been produced. In addition,

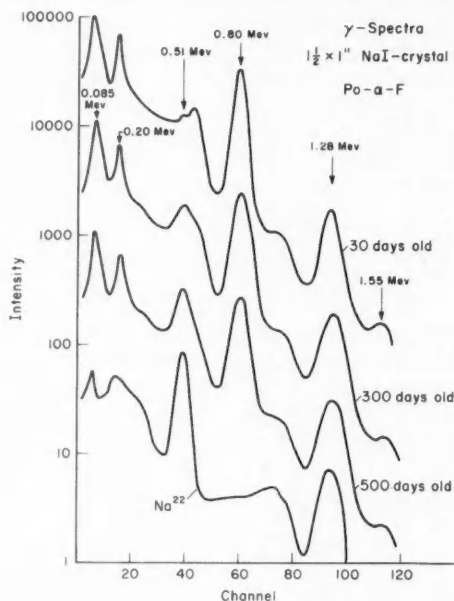


FIG. 1.  $\gamma$ -Spectra from Po- $\alpha$ -F source at various times after preparation. The intensity relations between the spectra are arbitrary. Also shown is the spectrum of pure  $\text{Na}^{22}$ .

the expected 0.51-Mev photopeak from positron annihilation is not apparent; the peak just above 0.51 Mev corresponds to the Compton edge of the 0.80-Mev  $\gamma$ -ray. The peak at 1.55 Mev is probably identical with a  $\gamma$ -ray of the same energy observed by Temmer and Heydenburg (1958), who assigned it to a transition in  $\text{Na}^{22}$ . The photopeaks at 0.21 Mev and part of the 0.085-Mev peak can be attributed to inelastic scattering of  $\alpha$ -particles on  $\text{F}^{19}$  which produces gamma transitions of 0.197 and 0.109 Mev (Temmer and Heydenburg 1958). Part of the 0.085-Mev peak is from polonium X-rays and from fluorescence radiation of a lead shield surrounding the detector.

With increasing age of the source the growth of  $\text{Na}^{22}$  becomes noticeable by the appearance of the 0.51-Mev photopeak (Fig. 1). For comparison the scintillation spectrum of pure  $\text{Na}^{22}$  is also given on this figure.

#### DETERMINATION OF $\text{Na}^{22}$ CONTENT IN THE Po-F SOURCE

The number of  $\text{Na}^{22}$  nuclei present at the time  $t$  after source preparation is:

$$(3) \quad N_2 = \frac{k\lambda_1 N_{1,0}}{\lambda_1 - \lambda_2} [\exp(-\lambda_2 t) - \exp(-\lambda_1 t)]$$



where

$\lambda$  is the decay constant, the subscripts 1 and 2 referring to  $\text{Po}^{210}$  and  $\text{Na}^{22}$ ,  $N_{1,0}$  is the number of  $\text{Po}^{210}$  nuclei present at  $t = 0$  (time of source preparation),

$k$  is the number of  $\text{Na}^{22}$  nuclei produced per  $\text{Po}^{210}$  disintegration. This is, according to reaction 1, equal to the number of neutrons produced.

The neutron emission rate at the time of source preparation therefore is

$$Q_0 = k\lambda_1 N_{1,0}.$$

It is more convenient to express the  $\text{Na}^{22}$  content as a disintegration rate. The equation for the growth of the  $\text{Na}^{22}$  activity then becomes:

$$(4) \quad \lambda_2 N_2 = \frac{Q_0 \lambda_2}{\lambda_1 - \lambda_2} [\exp(-\lambda_2 t) - \exp(-\lambda_1 t)].$$

Hence the initial neutron yield of the source can be calculated once the absolute decay rate of the  $\text{Na}^{22}$  is determined at a time  $t$  after source preparation. It is of course preferable to establish a substantial part of the growth curve experimentally.

Since it is virtually impossible to obtain the  $\text{Na}^{22}$  content from the scintillation spectra of Fig. 1 to the required accuracy, some other method had to be chosen to discriminate against the gamma radiation not belonging to  $\text{Na}^{22}$ . This nuclide is essentially a positron emitter, the positrons being absorbed within the source. By a coincidence arrangement, use has been made of the detection of the two 0.51-Mev annihilation quanta which are emitted simultaneously in opposite directions. Only a negligible fraction of positrons originate from another cause: pair production of neutron capture  $\gamma$ -rays within the source and its surroundings.

Two scintillation counters with  $1\frac{1}{2} \times 1$  in. NaI crystals were used and comparisons carried out to an originally uncalibrated  $\text{Na}^{22}$  reference source. The scintillation counter bias was set such as to accept  $\gamma$ -radiation above either 250 kev or 380 kev. The results agreed within the statistical accuracy which is to be expected since the effect of backscattering is negligible even at 250 kev. The counters were placed at a  $180^\circ$  angle for the measurement of the annihilation radiation and at  $90^\circ$  for background and accidentals. A source-to-crystal distance of 13 cm resulted in a convenient counting rate. The positron emission from the Po-F source as a function of time is shown in Fig. 2. The experimental points follow well the calculated growth curve of  $\text{Na}^{22}$  as given by equation 4. This again strengthens the assumption that the source was physically stable and that the contribution of positrons from other causes than reaction 1 must be negligible.

The coincidence method is very sensitive to source position and to  $\gamma$ -absorption within the source. Therefore, for the absolute  $\text{Na}^{22}$  determination a capsule, identical with that of a source, was made. This was filled with  $\text{CaF}_2$  powder and an aliquot of  $\text{Na}^{22}$  standard solution, dried in the capsule. The  $\text{Na}^{22}$  solution was standardized by the  $4\pi$   $\beta$ -counter method as described for  $\text{Mn}^{56}$

in Part I. In addition, the self-absorption of  $\beta^+$ -particles for one of the counting samples was determined by the  $4\pi \beta\text{-}\gamma$  coincidence method (Campion 1958);  $(97.5 \pm 0.5)\%$  of the emitted  $\beta^+$ -particles were counted. For the calculation

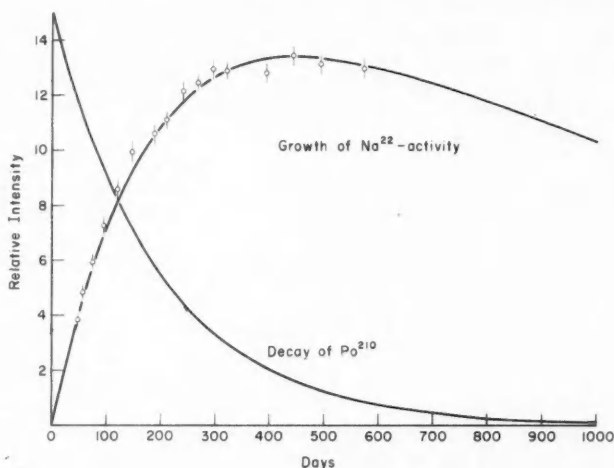


FIG. 2. Positron emission of Po- $\alpha$ -F source as a function of time, based on comparison with a Na<sup>22</sup> reference source. The growth curve (equation 4) is fitted to the experimental points. Also shown for comparison is the decay of Po<sup>210</sup> which is identical with the decrease in neutron emission from the source.

of the Na<sup>22</sup> disintegration rate a branching ratio for electron capture of  $(10.2 \pm 0.5)\%$  has been assumed. This is the theoretical value for an allowed transition with the error estimated from the more recent experimental determinations (e.g. Hagedoorn and Konijn 1957, who also give previous references).

The Na<sup>22</sup> disintegration rate in the neutron source was  $(1.108 \pm 0.020) \times 10^4 \text{ sec}^{-1}$ , 560 days after source preparation. With equation 4 and a Na<sup>22</sup> half-life of  $(2.58 \pm 0.03)$  years (Merritt, Campion, and Hawkings 1957) the resulting emission at the time of source preparation (25 January, 1957) is

$$Q_0 = (10.70 \pm 0.25) \times 10^4 \text{ neutrons per second.}$$

#### COMPARISON WITH THE N.R.C. Ra- $\alpha$ -Be NEUTRON STANDARD AND CONCLUSIONS

Because of its short half-life a Po- $\alpha$ -F source itself is only of limited value as a neutron standard. Therefore, the Ra- $\alpha$ -Be standard of the National Research Council has been calibrated in terms of the Po-F source. The neutron spectra of these two sources are very different; the maximum energy is 12 Mev for Ra- $\alpha$ -Be compared with 3 Mev for Po- $\alpha$ -F (Szilvasi, Geiger, and Dixon 1959). The measurements were carried out by thermalization and capture of nearly all source neutrons in the MnSO<sub>4</sub> as described in Part I. In this case no

absolute activity determination is necessary. After removal of the source and thorough mixing of the bath the  $\text{Mn}^{56}$  activity was measured with a scintillation dip counter ( $1\frac{1}{2} \times 1$  in. NaI Crystal). Some difficulties were experienced with this counter in that the stability was rather poor. This was mainly attributed to temperature variations. The rate due to  $\text{Mn}^{56}$  had to be frequently normalized to the rate from a pitchblende reference source. At the particular discriminator bias used (0.25 Mev) it was found that a sensitivity change of 1% on the pitchblende source corresponded to a change of 1.5% in the  $\text{MnSO}_4$  bath and the normalization had to be carried out accordingly.

During the first 6 months after source preparation three comparisons, each consisting of five bath activations, were carried out and the strength of the N.R.C. neutron standard was found to be  $(28.1 \pm 0.4)$  times that of the Po-F source for the day of its preparation. Corrections have to be applied for fast neutron capture in the bath ( $2.8 \pm 0.4\%$ ) and escape from the tank ( $1.4 \pm 0.4\%$ ) as discussed in Part I. The losses only apply to the Ra- $\alpha$ -Be neutrons since there is virtually no fast neutron loss in the bath from the Po- $\alpha$ -F source. Absorption of thermal neutrons in the Ra- $\alpha$ -Be source amounts to  $(0.4 \pm 0.2)\%$ . For the Po- $\alpha$ -F source, with a total thermal absorption cross section of only  $0.15 \text{ cm}^2$ , this is estimated to be less than 0.1%. Hence the corrected ratio becomes

$$[Q_0(\text{Ra Be})]/[Q_0(\text{Po F})] = 29.4 \pm 0.5.$$

With the neutron emission rate for the Po- $\alpha$ -F source as found in the previous section the rate from the N.R.C. standard becomes  $29.4 \times 10.70 \times 10^4 = 3.15 \times 10^6 \text{ sec}^{-1}$  as of January 1957, or when corrected for growth of  $\text{Po}^{210}$  (de Troyer and Tavernier 1954):

$$Q = (3.16 \pm 0.10) \times 10^6 \text{ neutrons per second as of July 1958.}$$

This may be compared with the rate as determined by the manganese bath method (Part I) of  $(3.22 \pm 0.05) \text{ sec}^{-1}$  as of July 1958. The agreement between the two entirely different standardization approaches is satisfactory and makes the occurrence of a major systematic error unlikely. Although the accuracy of the present method is not quite as high, its main advantage lies in the fact that no cross-section data are required, in contrast to the majority of the standardization work carried out until the present.

#### ACKNOWLEDGMENTS

The author wishes to thank Dr. G. N. Whyte, now at Queen's University, for discussions on various parts of the experiment. Thanks are due to Mr. H. Gladney and Mr. J. Stinson for assistance on the measurements, and also to Dr. P. J. Campion, Atomic Energy of Canada Limited, for the  $\beta$ -self-absorption determination on a  $\text{Na}^{22}$  source.

#### REFERENCES

- BREEN, R. J. and HERTZ, M. R. 1955. *Phys. Rev.* **98**, 599.  
 CAMPION, P. J. 1959. *Intern. J. Appl. Radiation and Isotopes*, **4**, 232.

- FELD, B. T. 1953. The neutron. *In* Experimental nuclear physics, Vol. II, *edited by* E. Segrè (John Wiley & Sons, Inc., New York).
- GEIGER, K. W. and WHYTE, G. N. 1959. *Can. J. Phys.* **37**, 256.
- GLÜCKAUF, E. and PANETH, F. A. 1938. *Proc. Roy. Soc. A*, **165**, 229.
- HAGEDOORN, H. L. and KONIJN, J. 1957. *Physica*, **23**, 1069.
- MARTIN, P., BISHOP, G. R., and HALBAN, H. 1955. *As quoted by* Richmond, R. 1958. *Progress in nuclear energy series 1—Physics and mathematics*, **2**, 165.
- MERRITT, W. F., CAMPION, P. J., and HAWKINGS, R. C. 1957. *Can. J. Phys.* **35**, 16.
- ODEBLAD, E. 1954. *Acta Radiol.* **42**, 391.
- SAHA, N. K. 1938. *Z. Physik*, **110**, 473.
- SZILVASI, A., GEIGER, K. W., and DIXON, W. R. 1959. To be published.
- TEMMER, G. M. and HEYDENBURG, N. P. 1958. *Phys. Rev.* **111**, 1303.
- DE TROYER, A. and TAVERNIER, G. C. 1954. *Acad. roy. Belg., Bull. Classe Sci.* **40**, 150.

# SIZE OF IRREGULARITIES IN THE *E* REGION OF THE IONOSPHERE<sup>1</sup>

M. SRIRAMA RAO<sup>2</sup>

## ABSTRACT

Three-station fading records taken at Ottawa on frequencies ranging between 2.0 and 2.6 Mc/s have been analyzed to determine the *E* region wind velocities (*V*) and frequencies of fading (*N*) for the period June 1953 to April 1955. An empirical relation  $V = 2.41 N\lambda$  has been deduced, on a statistical basis, to represent the above observations. In this equation,  $\lambda$  represents the wavelength of operation. The constant of proportionality (*K*) in this relation has been studied comparatively for three different locations in the northern hemisphere. This constant has been related to a characteristic length *L* which specifies the horizontal size of the irregularities in the *E* region of the ionosphere by the equation:  $L = (1/2)K\lambda$ . Variation of this size with latitude is discussed.

## 1. INTRODUCTION

Systematic measurements have been made, in recent years, on the determination of horizontal drifts in the *E* region of the ionosphere, using the spaced receiver method developed by Mitra (1949). The basic assumption in this method is that the lower portion of the *E* region acts as an irregular reflector and forms a diffraction pattern on the ground when illuminated by a point source of radio waves on the ground. It can be easily seen that the irregularities of the diffraction pattern on the ground would be twice as large as those in the diffracting screen itself. As the ionospheric irregularities drift horizontally, with a velocity *V*, the diffraction pattern on the ground drifts past the receiver with a velocity 2*V* and the received signal exhibits random fading. It has been shown by Rao and Rao (1958), from a statistical study of three-station fading records at Waltair, that for any operating frequency, the average frequency of fading (*N*) is proportional to the ionospheric drift velocity (*V*). This is only statistically true, as there may be a wide scatter of individual observations about the mean straight line of the *N* vs. *V* graph. This means that the size of the ionospheric irregularities at Waltair varies with time around a statistical average value, as will be shown later in this paper. A plot of the individual observations of *N* and *V* for Kjeller, given by Harang and Pedersen (1956), shows such a wide scatter. Their graph also indicates an average increase of the frequency of fading with wind velocity. The aim of the present investigation is to verify this result for Ottawa and to see how the constant of proportionality (*K*) between *V* and *N* $\lambda$  varies with the geographical position of the recording station.

<sup>1</sup>Manuscript received December 19, 1958.

Contribution from the Division of Radio and Electrical Engineering, National Research Council, Ottawa, Canada.

Issued as N.R.C. No. 5152.

<sup>2</sup>National Research Council Postdoctorate Fellow on leave from Andhra University, Waltair, India.

## 2. EXPERIMENTAL DETAILS AND RESULTS FOR OTTAWA

The three-station fading records, used in the present investigation, were taken at the Radio Physics Laboratory, Defence Research Telecommunications Establishment, Ottawa, using the equipment described by Chapman (1953). These records were taken on various frequencies ranging between 2.0 and 2.6 Mc/s in the daytime hours between 0800 and 1600 hours E.S.T. during the period June, 1953, to April, 1955. They have been analyzed to determine the horizontal drift velocities in the *E* region by the method outlined by Rao and Rao (1957), using median values of time delays. Average frequency of fading has also been determined in each case by the simple method given by Rice (1945). The 237 observations, thus obtained, have been divided into five frequency groups: 2.0, 2.2, 2.3, 2.4, and 2.6 Mc/s, respectively, according to the operating frequency. In each frequency group, the various values of drift velocities have been separated into subgroups falling in the ranges 1-10, 11-20, 21-30, etc., meters/second and the average values of drift velocities and fading frequencies in each subgroup estimated. The average values of *V* and *N*, thus obtained, have been presented in Figs. 1 and 2. Figure 1 contains observations taken on 2.0 and 2.6 Mc/s, respectively. A least-square line passing through the original and the various experimental points is drawn for each of these two frequency groups, as done by Rao and Rao (1958). A similar plot of observations, obtained on 2.2, 2.3, and 2.4 Mc/s, respectively,

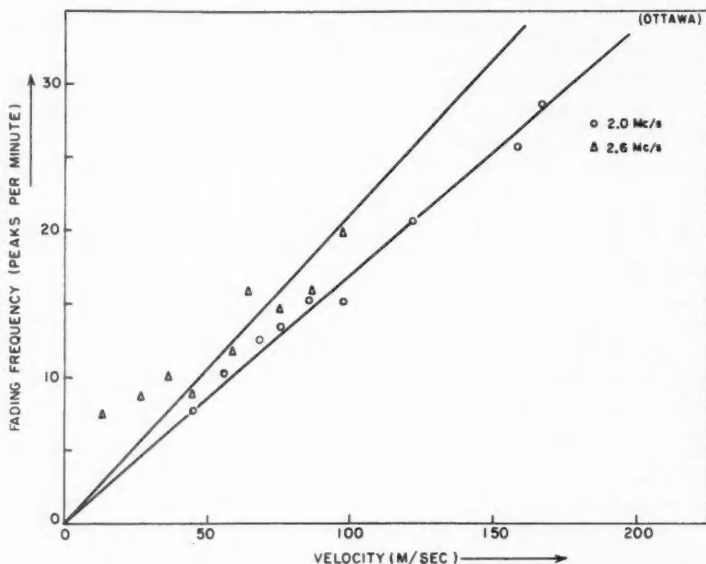


FIG. 1. Plot of average *N* vs. average *V* for observations at Ottawa, on frequencies 2.0 and 2.6 Mc/s. An average straight line is shown passing through the origin and the points of each frequency group.

is shown in Fig. 2. As the total number of observations taken on these three frequencies is smaller than those taken on other frequencies, these points are randomly distributed about a single least-square line passing through the

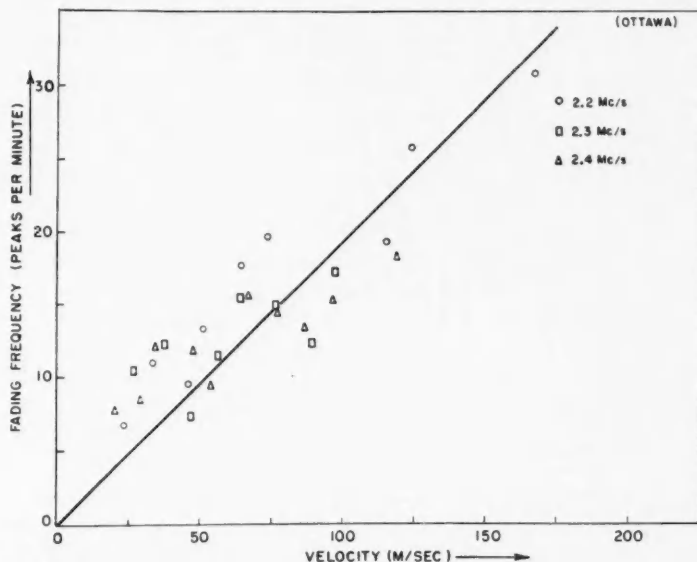


FIG. 2. Plot of average  $N$  vs. average  $V$  for observations at Ottawa, on frequencies 2.2, 2.3, and 2.4 Mc/s. An average straight line passing through the origin and all the points is taken to correspond to an average frequency of 2.3 Mc/s.

origin and all the points. This straight line is taken to correspond to an average frequency of 2.3 Mc/s. These  $N$  vs.  $V$  graphs show a wavelength dependence of the gradient of the average straight lines drawn through the experimental points, as has already been noticed by Rao and Rao (1958). Hence, assuming their general equation

$$(1) \quad V = KN\lambda$$

the value of  $K$ , corresponding to each straight line in Figs. 1 and 2, is estimated and shown in Table I.

TABLE I  
Values of  $K$  for each operating frequency

Operating frequency, Mc/s	$K$
2.0	2.37
2.3	2.37
2.6	2.48
Average	2.41

The standard error of estimate in the values of  $K$  is about 5 to 10%. The values of  $K$  corresponding to all the three frequencies lie within the limits of this error. Using the average  $K$  from Table I, the general equation, similar to (1), for Ottawa may now be written as

$$(2) \quad V = 2.41 N\lambda.$$

### 3. COMPARISON OF RESULTS FOR DIFFERENT LOCATIONS

From a comparison of the value of  $K = 2.41$  for Ottawa with that of  $K = 1.86$  for Waltair, it is obvious that  $K$  varies with the geographic position of the recording station on the earth. In order to get a value of  $K$  for another location, Fig. 16 of the paper by Harang and Pedersen (1956) has been subjected to the type of analysis outlined above and the resultant plot of the average values of  $V$  and  $N$  shown in Fig. 3.

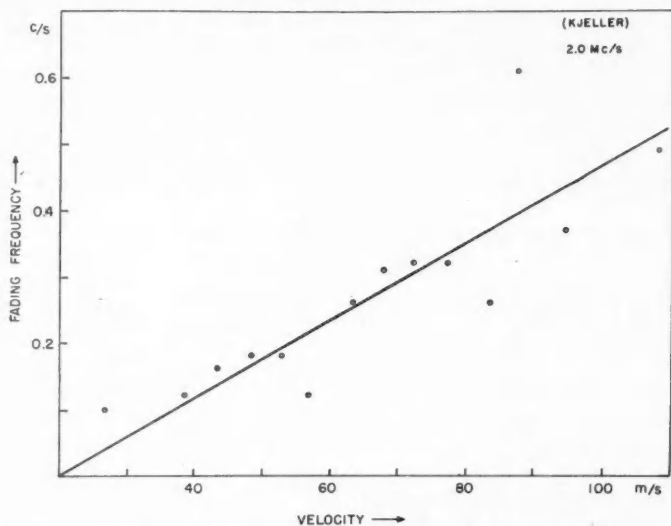


FIG. 3. Plot of average  $N$  vs. average  $V$  for observations at Kjeller, on a frequency 2.0 Mc/s, taken by Harang and Pedersen. An average straight line is shown passing through the origin and the various points.

In preparing this graph, all the points with values of  $N$  greater than 0.75 cycles/second in the original plot have been omitted for the following reason. Harang and Pedersen (1956) have pointed out that higher frequencies of fading correspond to smaller sizes of the diffraction pattern on the ground. Following Rao and Rao (1957), it may be noticed that these cases involve larger curvatures of the lines of maxima of the diffraction pattern, and that wind velocity measurements tend to be inaccurate under such conditions. Further it may be noticed that average frequencies of fading higher than 0.6 cycles/second have not been used in the graphs for Waltair and Ottawa.



A least-square line passing through the origin and the various points in Fig. 3 has been drawn as in the previous cases. It may be noted that those points in Fig. 3 which correspond to a larger number of observations lie close to this straight line. These points which deviate most from this straight line correspond to a smaller number of observations. Using the gradient of this straight line, the following equation for Kjeller may be obtained:

$$(3) \quad V = 2.29 N\lambda.$$

The operating frequency for the observations at Kjeller was 2.0 Mc/s.

It has already been pointed out that for the same velocity of drift, smaller ionospheric irregularities produce higher frequencies of fading. Pawsey (1935) has considered the lower portion of the *E* region as consisting of ion clouds having edges with horizontal dimensions of the order of  $L/2$ , where  $L$  is the least distance on the ground over which the fading is substantially the same. This  $L$  may be taken as a characteristic length which specifies the size of the ionospheric irregularities, following Briggs and Phillips (1950), who have defined it as the distance between two points on the ground for which the fading correlation is 0.5. Again following Pawsey (1935), the period of fading may be approximately given by  $2L/V$ . Now, from a comparison of this with equation (1) we get

$$(4) \quad L = (1/2)K\lambda.$$

It may be noted that the observations presented for Waltair, Ottawa, and Kjeller have all been made by the same method and during the period of minimum solar activity. It would be interesting to compare the results for these three locations, which have been summarized in Table II. Calculated values of geomagnetic latitudes for these locations have been presented in

TABLE II  
Comparison of results for Waltair, Ottawa, and Kjeller

Place	Geographic latitude	Geomagnetic latitude	Magnetic latitude	$L/\lambda$	$\lambda/L$
Waltair	17.8° N.	7.6° N.	7.6° N.	0.93	1.08
Ottawa	45.4° N.	56.8° N.	61.2° N.	1.21	0.83
Kjeller	60.0° N.	60.2° N.	57.5° N.	1.15	0.87

this table. These values have been obtained under the assumption of a uniform dipole field with the geomagnetic north pole situated geographically at 78.5° N., 69.1° W. Calculated values of magnetic latitudes for these three locations have also been presented in Table II. These values have been obtained from the actual magnetic dip angles.\* The statistical average sizes of ionospheric irregularities ( $L$ ) for the three locations have been calculated in terms of the wavelength  $\lambda$  using equation (4), and presented in Table II. It can be seen from this table that the average size of ionospheric irregularities probably increases with the actual magnetic latitude. Thus, there seems to be

\*Note that, in this case, magnetic latitude =  $\tan^{-1} (1/2 \tan \text{magnetic dip})$ .

some geomagnetic control over the size of the ionospheric irregularities in the *E* region and consequently over the fading frequency. The physical significance of this will be discussed in the next section.

Using a different method, Briggs and Phillips (1950) have obtained a histogram of the sizes of ionospheric irregularities observed at Cambridge (geographic latitude: 52.2° N.; geomagnetic latitude: 54.9° N.). From their histogram, the most probable size of ionospheric irregularities is found to be about 170 meters. Using their operating frequency of 2.4 Mc/s for  $\lambda$  in equation (4), it may be found that the most probable *L* for Cambridge is 1.36  $\lambda$  which is high compared with the values in Table II. In fact it is logical to expect this value for Cambridge to be smaller than that for Kjeller in Table II, mostly because the observations of Briggs and Phillips (1950) correspond to the year 1949 where solar activity was much higher than in 1954, the year of minimum solar activity. This discrepancy is probably due to the error in the present estimation of *L* through the approximate equation (4).

#### 4. PROBABLE CAUSE OF VARIATION OF *L* WITH GEOGRAPHIC POSITION ON THE EARTH

It is well known from meteor studies (Rao 1958; Rao and Armstrong 1958) that in the meteoric *M* region, which usually overlaps the lower portion of the *E* region, prevailing winds are normally turbulent. Ionic irregularities at the bottom of the *E* region of the ionosphere are probably caused as a result of such a disturbed or turbulent state. All types of motion in the earth's atmosphere derive their energy directly or indirectly from the sun (Chapman 1953). Hence, it is logical to assume that atmospheric turbulence at the bottom of the *E* region, and hence the size of the irregularities there, are in some way controlled by the energy of the sun's radiation.

Sometimes, turbulence-power *w* per unit mass has been related to the eddy size *L<sub>e</sub>* (Booker 1956) by the equation

$$(5) \quad L_e = v^3/w$$

where *v* is the velocity of the eddy. The systematic drift velocities in the *E* region appear to have the same range of values at various latitudes (Sethuraman 1958). Further, the height of the *E* region above the ground is almost the same at all latitudes, as can be seen from Fig. 4(a). This figure shows a plot of the yearly mean values of the virtual height of the *E* region, for 1954, for various ionospheric stations vs. their geographic latitudes. Hence it may be reasonably assumed that parameters like the diffusion coefficient, which usually vary as a function of height above the ground, are almost the same at all latitudes. These parameters and the wind velocity in the *E* region may influence the eddy velocity *v*. Hence, under the assumption of a constant *v*, we may then consider that

$$(6) \quad L_e \propto 1/w.$$

Now, it may be assumed that the most probable size of irregularities *L* at the bottom of the *E* region at any place is directly related to the most probable

eddy size,  $L_e$ , there. Further, the turbulence-power  $w$  may be directly related to the solar energy absorbed in the  $E$  region. As a simple approximation, it may be considered that the variation with latitude of the solar energy absorbed in the  $E$  region at noon is directly proportional to that of the maximum rate

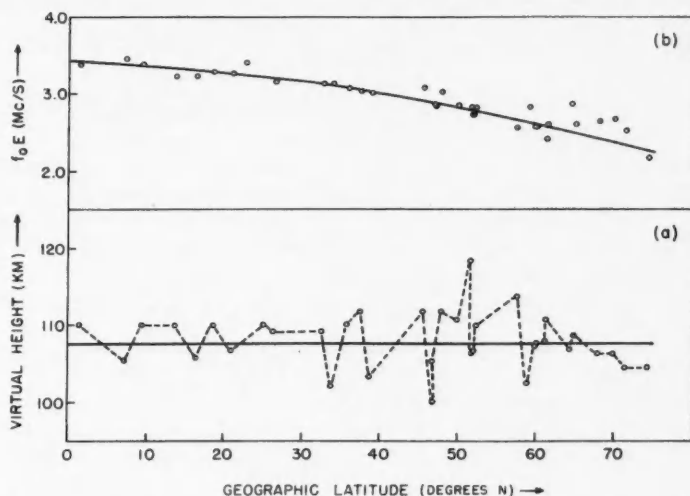


FIG. 4. (a) Plot of yearly mean values of virtual height of the  $E$  region vs. geographic latitude, for the year 1954. (b) Plot of yearly mean values of critical frequency of the  $E$  region vs. geographic latitude, for the year 1954.

of ion production  $q(\chi)$  at the height  $h(\chi)$  of maximum ionization in the  $E$  region ( $\chi$  represents the zenith distance of the sun). This may be taken as a proportionate measure of the variation of  $w$  with latitude. It may be seen from Chapman's derivation (1931) that

$$(7) \quad \frac{q(\chi)}{\alpha} \left( \frac{e^4}{\pi m^2} \right) = f_0^4$$

under equilibrium conditions established at noon. In this equation,  $\alpha$  is the recombination coefficient,  $f_0$  is the noon critical frequency of the  $E$  region, and

$$(8) \quad q(\chi) = \frac{\beta I_0 \cos \chi}{H \exp l}$$

where  $I_0$  is the intensity of the sun's radiation incident upon the  $E$  region,  $\beta$  is the number of ions produced by absorption of unit quantity of the radiation, and  $H$  is the scale height. It has been found by previous workers (Harnischmacher 1951; Scott 1952; Saha 1953) that the critical frequency of the  $E$  region at any hour of the day can be represented by a formula of the type

$$(9) \quad f_c \propto \cos^n \chi$$

where the index  $n$  varies with time and latitude. Hence using the same index  $n$  we may modify equation (7) as

$$(10) \quad q(\chi) \propto f_0^{1/n}$$

because  $q(\chi)$  involves a factor of  $\cos \chi$ . Using the above reasoning, it may be seen that

$$(11) \quad 1/L \propto f_0^{1/n}.$$

In order to verify this relation for the experimental values of  $\lambda/L$  in Table II, the following procedure is followed. The yearly mean values of noon critical frequencies  $f_0 E$  of the  $E$  region, for 1954, for various ionospheric stations have been plotted against the geographic latitudes of those stations in Fig. 4(b). It can be seen from this figure that  $f_0 E$  decreases as latitude increases. Using the mean curve drawn through the various points in this figure, the curve of  $f_0^4$  vs. geographic latitude has been drawn in Fig. 5. As the Chapman's theoretical value of 0.25 has been used for  $n$  in drawing this

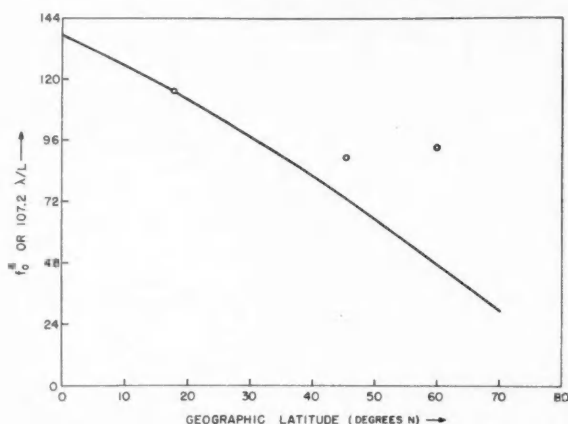


FIG. 5. Graph showing the average curve  $f_0^4$  vs. geographic latitude, obtained from Fig. 4(b). The circles represent values of  $\lambda/L$  from Table II.

curve,  $f_0^4$  is found to drop off very rapidly with increasing latitude.  $\lambda/L$  values from Table II have also been plotted in the same figure. The scale for this plotting has been adjusted proportionately with the previous scale for the  $f_0^4$  curve, in order to get the point for Waltair on this curve. There is not good agreement between the curve and the other two points. This may be due partly to the use of  $n = 0.25$ . Hence the variation of  $n$  with latitude has been considered. As Scott (1952) has pointed out that this variation is a geomagnetic rather than a geographic phenomenon, the yearly mean experimental values of  $n$  for the  $E$  region, for 1954, at various ionospheric stations have been plotted against their corresponding geomagnetic and magnetic latitudes in

Figs. 6(a) and 7(a) respectively. Geomagnetic latitudes in Fig. 6 have been obtained using a uniform dipole magnetic field and magnetic latitudes in Fig. 7 have been obtained using the actual magnetic dip values. Thanks are due to Dr. R. G. Rastogi for furnishing the data, for Figs. 6(a) and 7(a), from his unpublished work. It can be easily seen from these figures that the mean

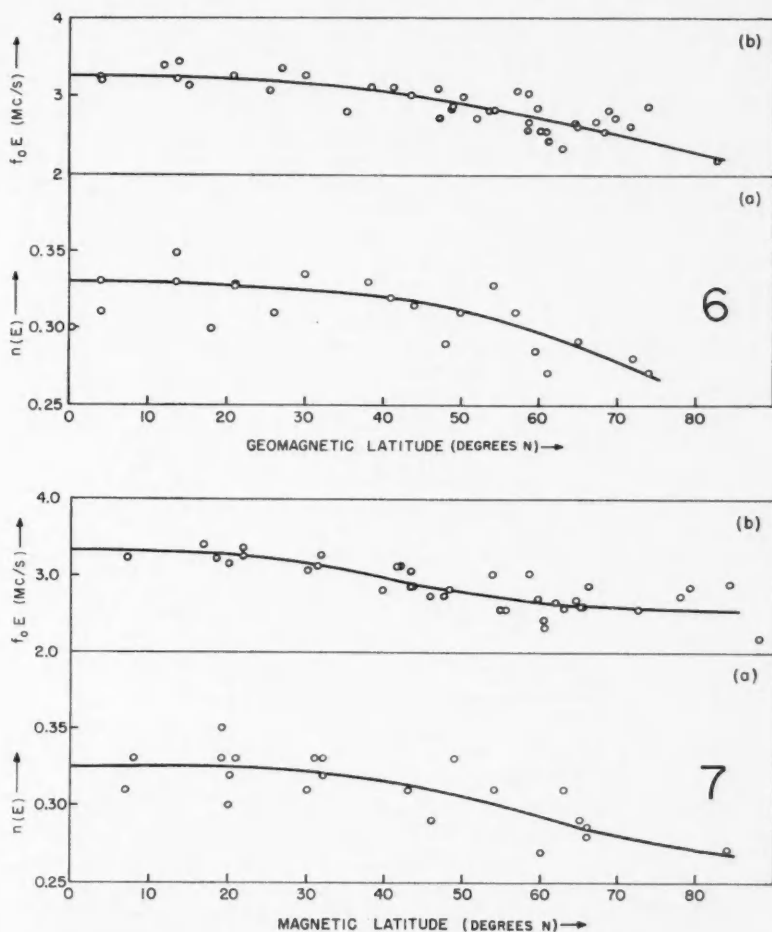


FIG. 6. (a) Plot of yearly mean values of the index  $n$  for the  $E$  region vs. geomagnetic latitude, for the year 1954.

(b) Plot of yearly mean values of critical frequency of the  $E$  region vs. geomagnetic latitude, for the year 1954.

FIG. 7. (a) Plot of yearly mean values for the index  $n$  of the  $E$  region vs. magnetic latitude, for the year 1954.

(b) Plot of yearly mean values of critical frequency of the  $E$  region vs. magnetic latitude, for the year 1954.

curve, through the points, is more flattened at higher latitudes in Fig. 7(a) than in Fig. 6(a). However, it may be said that  $n(E)$  decreases as geomagnetic or magnetic latitude increases. The values of  $f_0E$  for the various ionospheric stations in Fig. 4(b) have been replotted in Figs. 6(b) and 7(b), against geomagnetic and magnetic latitudes respectively. From these figures also, it can be seen that the mean curve through the various points is more flattened at higher latitudes in Fig. 7(b) than in Fig. 6(b). Now, using Figs. 6 and 7, the mean curves of  $f_0^{1/n}$  vs. geomagnetic and magnetic latitudes have been drawn in Figs. 8 and 9, respectively. From a comparison of Figs. 5 and 8 it may be said that the effect of using the experimental values of  $n$  is to cause the value of  $f_0^{1/n}$  to decrease more slowly with increasing latitude than when  $n = 0.25$

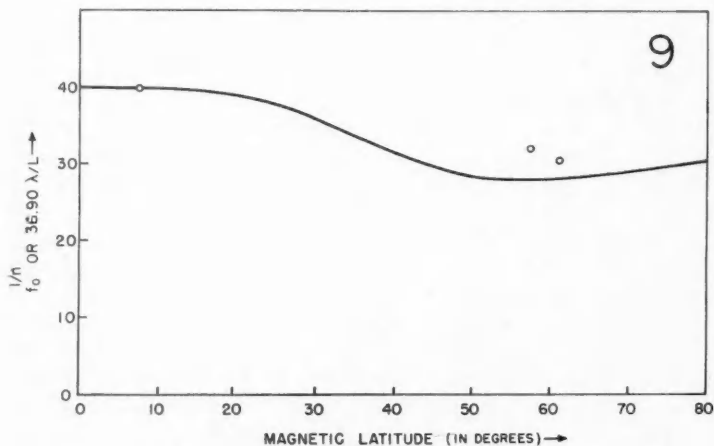
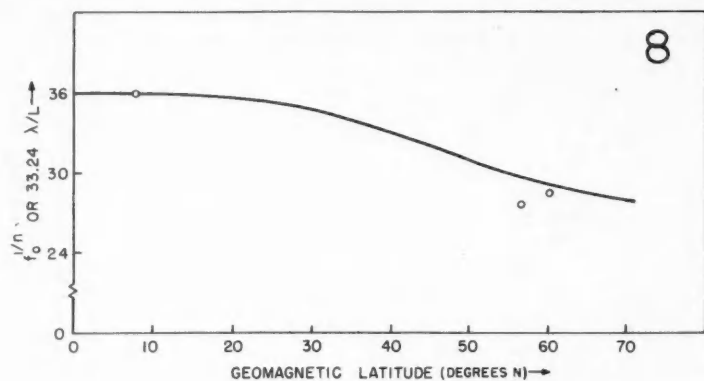


FIG. 8. Graph showing the average curve  $f_0^{1/n}$  vs. geomagnetic latitude, obtained from Fig. 6. The circles represent values of  $\lambda/L$  from Table II.

FIG. 9. Graph showing the average curve  $f_0^{1/n}$  vs. magnetic latitude, obtained from Fig. 7. The circles represent values of  $\lambda/L$  from Table II.

is used. Though the curve in Fig. 8 tends to flatten at higher latitudes, there is a definite increase of  $f_0^{1/n}$  at higher latitudes shown in Fig. 9, where the actual magnetic dip angles are used. This increase is probably due to the ionization produced by charged particles from the sun which are more attracted towards the magnetic poles. This is also in agreement with the observations of Scott (1952), who has pointed out that in the auroral zone ionization by solar radiation is modified by other factors like charged particles. The values of  $\lambda/L$  in Table II have been replotted in Figs. 8 and 9 using the proper geomagnetic and magnetic latitudes respectively. The scales for the *Y*-axis in these figures have been adjusted as in Fig. 5, in order to get the points for Waltair on the curve. From either of these two figures, it may be said that there is reasonable agreement between the curve and the points, within the limits of experimental errors. Thus, in general, we may say that equation (11) is verified to the extent that the size of ionospheric irregularities in the *E* region varies with geomagnetic or magnetic latitude in the same proportion as  $f_0^{1/n}$ . Noon values of  $f_0$  have been taken as representative values for the whole day, whereas values of  $L$  have been obtained using observations distributed over the whole day. No definite conclusions can be drawn with only three points in Figs. 8 and 9. It remains to be seen if observations from other latitudes would also fit into the curves of Figs. 8 and 9. It has to be remembered, however, that the present observations have been confined to the year (1954) of minimum sunspot activity. This is probably a good reason why it has been possible to obtain a definite linear relation between  $V$  and  $N$ . It also remains to be seen if a similar relation could be obtained with observations during the maximum of sunspot activity. It may be expected that during periods of higher sunspot activity, the bottom of the *E* region would be more disturbed and turbulent, resulting in smaller values of the average size of ionospheric irregularities at each place. Further, as geomagnetic storms are more frequent during the year of maximum sunspot activity, there may be a wider scatter of points in the  $N$  vs.  $V$  scatter diagram more towards the higher frequencies of fading (Harang and Pedersen 1956). Actually, the scatter of points may be so wide that the average size of the irregularity at any place may lose the significance given to it in this paper.

Physically, the effect of a strong geomagnetic storm on  $N$  may be envisaged as follows. A strong geomagnetic storm may be expected to disturb the eddy currents in the *E* region. As a strong geomagnetic storm is always accompanied by a greater amount of solar energy input than normal, into the *E* region, it is logical to believe, from equation (6), that the most probable eddy size should decrease. Hence a decrease in the size of ionospheric irregularities in the *E* region may be expected. This, in turn, would increase the frequency of fading. Chapman (1953) has found that during geomagnetically disturbed conditions, there was an indication of great increase in the drift velocity, observed mainly through sporadic *E* echoes. It is generally known that drifts of the sporadic *E* layer are different from those of the normal *E* layer, and further wind velocity determinations under disturbed conditions are relatively unreliable. Hence, no definite conclusions could be drawn about the effect of a geomagnetic storm on wind velocity in the *E* region. Even if this

effect is to increase the drift velocity, it would add to the effect of decreased ionospheric irregularities in enormously increasing the frequency of fading. This is in agreement with Harang and Pedersen's (1956) important observation that the frequency of fading is unusually high during periods of strong geomagnetic storms. It would be interesting if more light could be thrown upon this problem of relating ionospheric irregularities with atmospheric turbulence in the  $E$  region by future investigators. In conclusion, it is suggested that the average size of the ionospheric irregularities varies in some smooth manner with geomagnetic or magnetic latitude.

#### ACKNOWLEDGMENTS

Monthly mean values of  $f_oE$  and virtual heights, at noon, in the  $E$  region at various locations in the northern hemisphere for the period January to December, 1954, have been taken from the F-Bulletins of the Central Radio Propagation Laboratory, U.S.A.

The author is grateful to Dr. J. H. Chapman of the Radio Physics Laboratory, Defence Research Telecommunications Establishment, Ottawa, for providing the three-station fading records used in the present investigation.

The author is deeply indebted to the National Research Council for the award of a Postdoctorate Fellowship which enabled this investigation to be carried out. He is grateful to Dr. P. M. Millman for his personal interest in this work.

#### REFERENCES

- BOOKER, H. G. 1956. *J. Geophys. Research*, **61**, 673.  
 BRIGGS, B. H. and PHILLIPS, G. J. 1950. *Proc. Phys. Soc. B*, **63**, 907.  
 CHAPMAN, J. H. 1953. *Can. J. Phys.* **31**, 120.  
 CHAPMAN, S. 1931. *Proc. Phys. Soc.* **43**, 26, 433.  
 ——— 1953. *Proceedings Conference on Motions in the Upper Atmosphere held at the University of New Mexico, Albuquerque, Sept.*, p. 5.  
 HARANG, L. and PEDERSEN, K. 1956. *Geofys. Publikasjoner*, **19** (10).  
 HARNISCHMACHER, E. 1951. *Compt. rend. acad. sci. (Paris)*, **230**, 1301.  
 MITRA, S. N. 1949. *Proc. Inst. Elec. Engrs.* **96** (III), 441.  
 PAWSEY, J. L. 1935. *Proc. Cambridge Phil. Soc.* **31**, 125.  
 RAO, B. R. and RAO, M. S. 1958. *J. Brit. Inst. Radio Engrs.* **18**, 493.  
 RAO, M. S. 1958. *Can. J. Phys.* **36**, 840.  
 RAO, M. S. and ARMSTRONG, R. L. 1958. *Can. J. Phys.* **36**, 1601.  
 RAO, M. S. and RAO, B. R. 1957. *J. Atmospheric and Terrest. Phys.* **10**, 307.  
 RICE, S. O. 1945. *Bell System. Tech. J.* **23**, 282.  
 SAHA, A. K. 1953. *Indian J. Phys.* **27**, 431.  
 SCOTT, J. C. W. 1952. *J. Geophys. Research*, **57**, 362.  
 SETHURAMAN, R. 1958. *Proc. Indian Acad. Sci. A*, **48**, 84.



## TRANSIENT DECREASES IN COSMIC RAY INTENSITY DURING THE PERIOD OCTOBER 1956 TO JANUARY 1958<sup>1</sup>

A. G. FENTON,<sup>2</sup> K. G. McCracken,<sup>3</sup> D. C. ROSE, AND B. G. WILSON<sup>4</sup>

### ABSTRACT

Recent nucleon intensity data obtained from high counting rate recorders at Ottawa and Hobart, and subsidiary stations, have been examined for evidence for the superposition of transient decreases. It is concluded that, with the statistical accuracy now available due to the high counting rates, it is possible to distinguish two types of transient decreases in the observed variations, superimposed upon the slower 11-year intensity changes. One of these is an almost symmetrical event lasting up to 2 weeks and exhibiting a recurrence tendency of about 27 days, while the other is the more abrupt Forbush decrease which recovers over a period of several days. The evidence indicates that the intensity-controlling mechanism responsible for these short-term transient changes is able to influence the cosmic ray flux at the earth independently of other events that may be in progress at the time. There is also evidence that the physical process controlling the Forbush type of decrease operates over a volume large compared with the earth because the intensity changes at places as far apart as Ottawa, Canada, and Hobart, Tasmania, show changes that are the same within the accuracy of the measurements.

### INTRODUCTION

In a recent paper (Fenton, Fenton, and Rose 1958) it was shown that after correction for atmospheric effects the monthly mean intensity recorded by cubical meson telescopes and neutron monitors at Ottawa and Resolute decreased appreciably between 1954 and 1957, a period during which the solar activity increased from an exceptionally low level in 1954 to an unusually high level in 1957. It was also shown that the short-term transient decreases observed from time to time in the daily mean intensities are not themselves the cause of this longer term decrease, but that they are superimposed upon it. It is the purpose of the present report to consider the question of superposition of decreases in greater detail in an attempt to determine some of the important features of the mechanisms controlling the level of the cosmic ray intensity at the earth during the period October 1956 to January 1958. To do this a separation of the intensity changes into well-known types has been carried out and some comparisons made between corresponding intensity changes at two stations, one in the northern and the other in the southern hemispheres, both above the latitude knee.

### APPARATUS AND LOCATION OF STATIONS

During the period considered in this paper, high counting rate neutron monitors and meson telescopes were operated at Ottawa and Hobart and at

<sup>1</sup>Manuscript received February 6, 1959.

Contribution from the Division of Pure Physics, National Research Council, Ottawa, Canada.

Issued as N.R.C. No. 5160.

<sup>2</sup>Visiting scientist from the Department of Physics, University of Tasmania.

<sup>3</sup>Department of Physics, University of Tasmania.

<sup>4</sup>National Research Council Sulphur Mountain Laboratory, Banff, Alberta.

several other stations in both the northern and southern hemispheres by the National Research Council and the University of Tasmania respectively. These recorders were developed for use during the International Geophysical Year and results from them are considered to be directly comparable, since no significant differences in response or cone of acceptance are expected to arise as a result of the slight differences in design and construction. The location of recording equipment operated at the present time by the two groups is set out in Table I. A complete list of the stations is given for reference purposes, although not all of these are involved in the present analysis. All equipment is operated near sea level except in the case of Sulphur Mountain (2283 meters) and the Hobart neutron monitor (725 meters).

TABLE I

Station	Geographic co-ordinates	Geomagnetic latitude
Sulphur Mountain	51.1° N., 115.6° W.	58° N.
Churchill	58.8° N., 94.2° W.	69° N.
Hobart	42.8° S., 147.5° E.	52° S.
Lae (New Guinea)	6.7° S., 147° E.	16° S.
Macquarie Island	54.5° S., 158.9° E.	61° S.
Mawson (Antarctica)	67.6° S., 62.9° E.	73° S.
Ottawa	45.4° N., 75.6° W.	57° N.
Resolute	74.7° N., 94.9° W.	83° N.

#### NUCLEON INTENSITY VARIATIONS AT OTTAWA AND HOBART

The Ottawa and Hobart daily mean, pressure corrected, nucleon intensities have been compared for the period October 1956 to January 1958 (Fig. 1) in order to illustrate the world-wide nature of the intensity variations. Nucleon

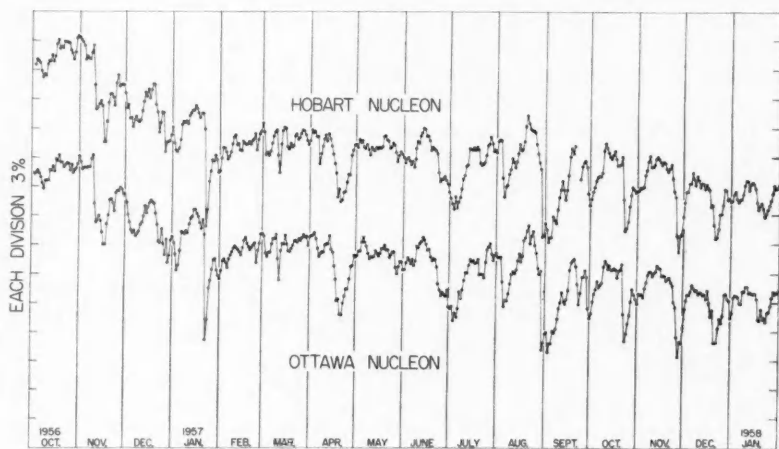


FIG. 1. Daily mean nucleon intensities at Ottawa and Hobart, October 1956 to January 1958. Intensity scales arbitrarily displaced to avoid overlapping.

intensities are considered to be more suitable for the present study than meson data, since the variations are much larger in the nucleon than in the meson component, and because of the atmospheric influence remaining in the meson data after correction for pressure alone. The energy dependence of the intensity variations will not be considered at this time. In the figure the scales have been chosen so that the intensities are comparable on a percentage basis, and the horizontal lines carrying the time scale provide a constant reference level. The Ottawa data have been arbitrarily separated from the Hobart data to avoid overlapping. Throughout this paper Greenwich mean time will be used, the daily mean intensity referring to the mean hourly intensity over a 24-hour period from 00 to 24 hours G.M.T.

Reference to Fig. 1 shows that there is a close correlation between the two sets of data, both in the over-all change of intensity from the beginning to the end of the period, and in the short-term fluctuations. The intensity on January 31, 1958, at both stations was approximately 15% lower than the high point reached at the end of October 1956. (A more detailed comparison is presented in the next section.) The slow over-all intensity decrease was fairly rapid from the beginning of November 1956 to January 1957, then it appears to have recovered slightly before a further general decrease from August 1957 onwards. This over-all decrease is identified with the 11-year solar cycle intensity changes reported originally by Forbush (1954) and discussed recently in relation to the present cycle of solar activity (Fenton, Fenton, and Rose 1958; Neher and Anderson 1958; and Lockwood 1958). Close inspection of Fig. 1 reveals that there are relatively small differences between the daily mean intensities observed at the two stations (the standard deviation for 1 day, calculated from the counting rate, is 0.15% and 0.11% at Ottawa and Hobart respectively). An examination of the hourly intensities at these and other stations has revealed obvious differences in response to transient decreases from station to station. These appear to be at least partly due to primary anisotropies which are detected at somewhat different times and directions in space as the earth rotates. This aspect of the variations has been investigated, and the results will be reported later.

The relatively short-term intensity changes shown in Fig. 1 seem to be more satisfactorily explained in terms of a succession of transient decreases below the prevailing level determined by the 11-year intensity cycle than by a series of temporary increases above a lower level. Thus while the maxima of the intensity-time plot lie on a smooth curve, indicating that a decrease was usually followed by a return to near the predecrease intensity, the minimum values show no such systematic behavior. Furthermore, as is clearly evident for the months October 1956 to January 1958 (Fig. 1), the maxima tend to be broad and relatively free from rapid intensity changes, whereas the minima are short-lived and involve appreciable rates of change of intensity. These observations suggest that the decreases represent the disturbed condition. This view is supported by reference to geomagnetic disturbance data, which shows that sudden commencements of magnetic storms often occur near the beginning of sudden decreases in the cosmic ray intensity, suggesting that

the cosmic ray effect is due to a screening or deceleration process at these times rather than to a source or acceleration process occurring at other times. Additional arguments have been presented by others (e.g. Van Heerden and Thambyahpillai 1955; Neher 1957) to show that decreases rather than increases are involved, except in the rare cases of solar flare increases, which represent injection of additional particles into the solar system by the sun. Other evidence supporting the view that the variations during the period under discussion consisted only of superimposed transient decreases is provided by the correlation of these events with the central meridian passage of active solar regions (Venkatesan 1959).

#### SUPERPOSITION OF INTENSITY DECREASES

The Hobart section of Fig. 1 corresponding to the months of November 1956 to February 1957 has been reproduced in Fig. 2, A. Three classes of intensity change are apparent as shown by the straight lines from maxima to maxima, the smooth curved lines showing more or less symmetrical dips in intensity and the residual smaller variations. This division is somewhat arbitrary but it can be repeated in a consistent way at different stations. The first class is the slow 11-year cyclic change in intensity; the second is a succession of loops of intensity change, which for this series of data appears to be almost periodic and may be associated with solar rotation. The third class consists of the residual short-period changes lasting a few days, and the large Forbush events.

The earlier work of Fenton *et al.* (1958) and Venkatesan (1959) suggests that, of the above classes, two and three may be due to the same basic phenomena but are quite different from the 11-year variation because they have a different spectral sensitivity. In Fig. 2, B, both the 11-year variation and the variations of duration about a month have been removed and the residual variations probably represent small and large Forbush events. Figure 3, A and B, show the same analysis covering the same period at Ottawa. It is, of course, quite possible to continue this analysis for longer periods.

The similarity between the curves 2B and 3B is strong evidence for the world-wide nature of the modulating mechanism. Attention is directed to the close correspondence in all but the smallest variations. On the other hand, there are differences and if these are significant they are very important in assessing the value of theories about the modulating mechanism causing the variation.

Let us look first for differences in the 11-year cyclic change at the two stations. A careful examination makes it apparent that the straight lines joining the points of maxima have not exactly the same slope and the intensity drop may not have the same ratio at the two stations. A quantitative comparison has been made in two ways. First, the monthly means can be compared but these might be affected by differences in the magnitude of decreases in the Forbush events during the month. Alternatively, we may make a comparison of the mean level of the straight lines joining the maxima as shown in Figs. 2 and 3. This was done by picking three periods in Fig. 1 (the straight lines representing the 11-year variation are not shown) and examining

the ratios of the mean levels of the lines. Table II shows these normalized to intensities of 100% for the first period chosen.

TABLE II  
Intensity ratios

Period centered on:	Hobart	Ottawa
November 18, 1956	100%	100%
July 3, 1957	92.2%	91.8%
December 21, 1957	87.0%	87.3%

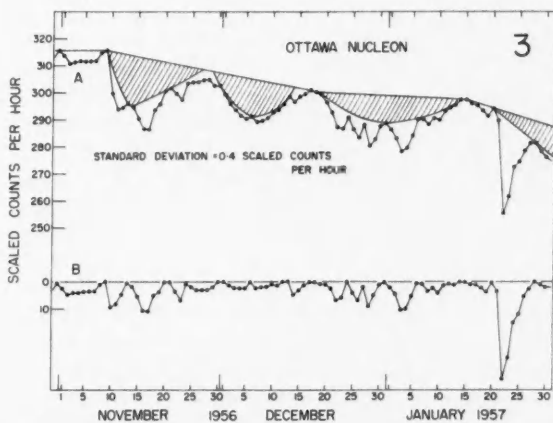
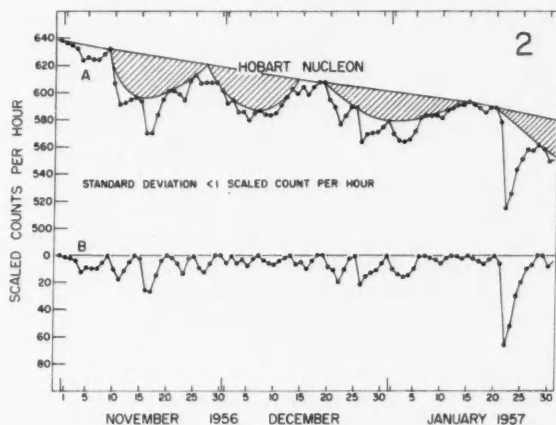


FIG. 2. (A) Daily mean nucleon intensities at Hobart, November 1956 to January 1957 inclusive, shaded to indicate division into three types of decreases. (B) A section of (A) with the slower changes removed.

FIG. 3. (A) Daily mean nucleon intensities at Ottawa, November 1956 to January 1957 inclusive, shaded to indicate division into three types of decreases. (B) A section of (A) with the slower changes removed.

Monthly means treated in the same way are shown in Table III.

TABLE III  
Intensity ratios

Month	Hobart	Ottawa
October 1956	100%	100%
June 1957	89.4%	89.6%
January 1958	85.3%	85.8%

The decrease in intensity is very nearly the same at both stations. It is considered that the differences in columns 2 and 3 are not significant in either table even though they are somewhat greater than the statistical differences that might be expected from a Poisson distribution in counting rate. For 1 month of data the statistical difference due to counting rate should be about .03% but the stability of neutron monitors with their amplifiers and discriminators and the accuracy of barometer correction are also involved. Although calibrations are carried out regularly, an over-all confidence of better than 0.5% over a year is difficult to achieve. There will be a further discussion of accuracies in the following paragraphs. Our conclusion here is that the fractional long-term intensity change is the same at the two stations within the order of accuracy of the measurements.

The depth of the Forbush events or the deepest point in the more symmetrical decreases is a measure that might be used in looking for differences between the two stations. A technique for comparison of these is shown in Fig. 4. The quantity  $\delta I/I$  can be compared for similar events at the two

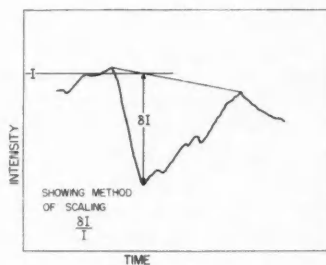


FIG. 4. An idealized Forbush type of decrease showing how  $\delta I/I$  was measured.

stations. The ratio  $(\delta I/I)_{\text{Ottawa}}/(\delta I/I)_{\text{Hobart}}$  should be a constant if the modulating effect is truly world-wide in each event. This is particularly so since both stations are near or above the geomagnetic knee. Table IV shows a series of events all of which are included in Fig. 1. Before considering these let us examine the expected accuracy of such a comparison. The quantity  $\delta I/I$  is estimated as in Fig. 4 from the position of the straight line and the depth of the lowest point representing a daily average. Its statistical accuracy, there-

fore, can be derived from that of the daily averages. This was stated earlier to be 0.11% for Hobart and 0.15% for Ottawa.

TABLE IV  
The magnitude of 11 Forbush decreases at Ottawa and Hobart and the ratio between them

Date	Ottawa, $\delta I/I$	Hobart, $\delta I/I$	Ratio
November 17, 1956	.079	.082	.96
December 8, 1956	.043	.041	1.05
January 3, 1957	.069	.061	1.13
January 22, 1957	.123	.113	1.08
April 20, 1957	.088	.075	1.17
July 3, 1957	.080	.081	.99
August 5, 1957	.061	.070	.87
October 23, 1957	.088	.094	.93
November 27, 1957	.089	.100	.89
December 22, 1957	.061	.062	.99
January 22, 1958	.038	.041	.94

This was based on the total counts for 24 hours and a Poisson distribution. There has always been some uncertainty about the validity of using this to estimate accuracy for a number of reasons. These include the fact that there are errors in barometric readings and possibly in the correction coefficients used, and because in the neutron monitor an appreciable number of events result in collection and counting of more than one neutron per incoming nucleon.

A simple examination of the latter effect was carried out using data from the Ottawa neutron monitor during February and March 1957. The Ottawa neutron has three roughly equivalent recording channels. The final figure used is the sum of the three labelled A, B, and C. The procedure of data handling makes it quite easy to obtain the ratio of the daily averages of say  $I_A/I_C$  before barometer correction. On the assumption that the same flux goes through the two parts of the pile, and no experimental changes occurred during the period, the ratio of  $I_A/I_C$  should be constant except for random fluctuations. A and C were chosen rather than A and B or B and C since A and C are farther apart. The standard deviation of  $I_A/I_C$ , that is, the r.m.s. value of deviations from the mean was calculated from the actual data. Since  $I_A$  and  $I_C$  are practically the same and  $I_B$  is only slightly higher, it is easy to show that the quantity  $\{\sigma(I_A/I_C)\}/(\sqrt{2} \sqrt{3})$  is a fair value for the standard deviation of the sum of the three channels. Using 2 months' data of February and March for 1957, selected because fluctuations during those 2 months were relatively less than for other parts of the period studied, the derived value of  $\sigma$  is 0.22%. This is slightly higher than the 0.15% derived from the counting rate. Added to this there is a barometric error estimated at 0.1 mb and a lack of certainty about the best barometer coefficient. These we estimate to represent an additional random error of 0.1%; thus, we may take the best estimate of our error in the nucleon intensity as being 0.24%. The average value of  $\delta I/I$  in Table IV is 7.4% and assuming that the error in Hobart is

the same as that at Ottawa a simple calculation of the combination of errors gives a standard deviation for column 3 in Table IV of 6.4%. The actual r.m.s. deviation from the mean of the ratio is 9.3%. This is not significantly different from 6.4%, the best estimate we can make of the expected deviation. One can conclude, therefore, that the modulating effect on the cosmic ray flux is so nearly the same at Ottawa and Hobart that measurements of this type cannot show differences. In support of this conclusion it has recently been shown (McCracken 1959) from analysis of the data from Hobart and Mawson that radiation arriving from directions close to the equatorial plane is affected to the same extent as that arriving from large angles to this plane. This is also confirmed by an examination of the curves B in Figs. 2 and 3. The small variations are as closely in agreement as could be expected in view of the statistical accuracies involved and the rather arbitrary method of separating the types of variation. On the other hand, a more detailed analysis must show differences in the decreases because it is well known that Forbush decreases are sometimes followed by an enhanced diurnal variation which follows local time. This alone would be expected to result in differences at different stations. For a preliminary examination of some of these we should look at a more detailed analysis of some of the Forbush-type decreases using hourly values.

In this case we use data from Sulphur Mountain since it is the one in our group with the best statistics, having a counting rate of about 100,000 per hour. As an example, the hourly intensities observed at Sulphur Mountain during the period August 3 to 10, 1957, are plotted in Fig. 5, (a). It is evident

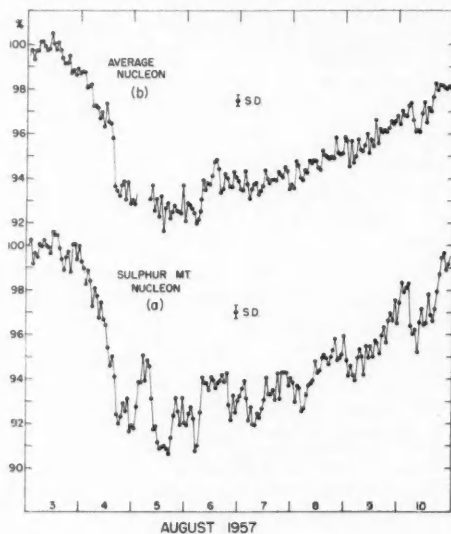


FIG. 5. Hourly nucleon intensities, August 3 to 10, 1957.  
(a) Sulphur Mountain.  
(b) Average of Hobart, Ottawa, Mawson, and Sulphur Mountain.



that the variations are significantly greater and more regular than expected from statistical fluctuations. This event appears to have a different form from station to station, and in order to obtain an approximation to the effect that would be observed with an omnidirectional ( $4\pi$ ) detector at the position of the earth (i.e. independent of the earth's rotation) the mean hourly data from four stations widely spaced in longitude are presented in Fig. 5, (b). In the averaging process each station was given equal weight so that percentage changes would be comparable. It is clear that, after averaging, most of the fluctuations apparent in the record from a single station have been removed, leaving a rather smooth transient decrease on which is superimposed another decrease beginning abruptly on August 4 and ending on August 6. It seems likely that variations of the type shown in Fig. 5, (a), are to be identified with the enhanced daily variations discussed by others (Elliot 1952).

#### DISCUSSION

The evidence presented above supports the view that the cosmic ray intensity observed at the earth is controlled by separate events and that the main controlling influence acts in the same manner over great distances. In other words the scale of the modulating effect must be larger than the earth's dimensions because at stations separated as far as Ottawa and Hobart the effect is the same within the accuracy limits of current measurements. This applies both to the 11-year cyclic change and the magnitude of short-term decreases of the Forbush or cosmic ray storm type. It is significant that the individual short-period events appear to be completely independent and not very closely related to the over-all 11-year cyclic change, though the controlling mechanism of the two may differ only in scale as suggested by Parker (1958). It is difficult to classify the short-term decreases lasting from a few hours to perhaps 2 weeks or 1 month on the basis of their magnitude or shape since the shape is extremely variable and it is uncertain whether the more symmetrical decreases taking several days to reach a minimum are substantially different from those which last from a few hours to 2 or 3 days and show substantially greater gradients. The former may be just a number of smaller decreases so close together that they appear to be one of gentler slope. This is in agreement with the analysis of Venkatesan (1959) in comparing Forbush decreases with the central meridian passage of active regions on the sun.

An analysis by one of us on the energy dependence and correlation with geomagnetic effect (McCracken 1958) suggests that both are produced by a common (probably geocentric) process and the difference in appearance of the events is due to the differences in the extent or speed of the cloud or stream responsible for setting up the process.

The location of the intensity-reducing agencies relative to the earth is important in any theory of the process responsible for cosmic ray intensity variations. The rapid onset and brief duration of the Forbush decreases, the correlation with active solar regions crossing the central meridian, and the association with concurrent geophysical phenomena suggest that these events

are produced by a process acting relatively closely to the earth. On the other hand the similarity in effect over great distances on the earth's surface suggest that the scale is large compared with the earth's dimensions. Individual isolated examples of the rapid decreases which might give a time scale either of the rate of decrease or recovery, practically do not exist, that is, there is no unique obvious characteristic shape on which to base a theory.

The slow changes that make up the 11-year variation may be due to the cumulative effect of solar matter streaming into the whole solar system from active regions on the sun. This would agree with the observation (Fenton, Fenton, and Rose 1958) that, although the long-term intensity is clearly controlled by the general level of solar activity, there is not a close correlation with changes in this activity from month to month. A possible mechanism through which the long-term cosmic ray intensity at the earth may be controlled by matter streaming outward from the sun has been put forward recently by Parker (1958). Whatever the mechanism may be, it is quite effective during the present phase of solar activity in reducing the intensity below the 1954 level and maintaining it without breaks. Between October 1956 and January 1958 the over-all intensity level fell by about 15% (Tables II and III) which is a larger decrease than observed in any of the transients during this period. As reported previously (Fenton, Fenton, and Rose 1958) the over-all decrease in nucleon intensity from April 1954 to December 1957 was 22%, making the slow 11-year cycle changes the most substantial of the three types of events discussed in this paper.

#### ACKNOWLEDGMENTS

The authors wish to express appreciation of those operating the equipment at the various stations from which data were used. The establishment of these stations and their maintenance has been a large undertaking to which several members of the cosmic ray research groups at the University of Tasmania and the National Research Council have contributed. A. G. Fenton acknowledges the award of a travel grant by the Committee of the Royal Society and Nuffield Foundation Bursaries Scheme. K. G. McCracken is grateful to the Australian Atomic Energy Commission for the award of a postgraduate scholarship at the University of Tasmania. Analysis of the data at Hobart was assisted by the Australian Academy of Science.

#### REFERENCES

- ELLIOT, H. 1952. Progress in cosmic ray physics, Vol. 1, *edited by* J. G. Wilson (North-Holland Publishing Co., Amsterdam).  
FENTON, A. G., FENTON, K. B., and ROSE, D. C. 1958. *Can. J. Phys.* **36**, 824.  
FORBUSH, S. E. 1954. *J. Geophys. Research*, **59**, 525.  
LOCKWOOD, J. A. 1958. *Bull. Am. Phys. Soc. Ser. II*, **3**, 220.  
MCCRACKEN, K. G. 1958. Ph.D. Thesis, University of Tasmania, Hobart, Tasmania.  
——— 1959. *Phys. Rev.* **113**, 343.  
NEHER, H. V. 1957. *Phys. Rev.* **107**, 588.  
NEHER, H. V. and ANDERSON, H. 1958. *Phys. Rev.* **109**, 608.  
PARKER, E. N. 1958. *Phys. Rev.* **110**, 1445.  
VAN HEERDEN, I. J. and THAMBYAPILLAI, T. 1955. *Phil. Mag.* **46**, 1238.  
VENKATESAN, D. 1959. *J. Geophys. Research* (in press).

# INVESTIGATION OF DEFORMATION PROCESSES IN ARMCO IRON BY MEANS OF INTERNAL FRICTION AT MEGACYCLE FREQUENCIES<sup>1</sup>

W. J. BRATINA<sup>2</sup>

## ABSTRACT

Internal friction, employing frequencies in the megacycle range, has been used in order to study the characteristics of elastic and plastic deformation in Armco iron. Tensile stresses only were applied in the present investigation.

Among the characteristic features observed three were investigated in detail. (1) A decrease in ultrasonic attenuation at external static stresses within the elastic range, which appears to be related to the ordering effect of the stress on magnetic domains, was investigated. (2) An initial increase in attenuation values regularly observed in cold-worked specimens upon the application of an external load was shown to be associated with the internal stresses. (3) The changes in attenuation resulting from plastic deformation were found to be insignificant in some instances and large in others. An explanation employing the magnetic domain theory and dislocation mechanisms is suggested.

## INTRODUCTION

Attention has been focused recently on the phenomena associated with the elastic deformation of metals and the early stages of plastic deformation including the relaxation processes related to them. To study the fine details of deformation characteristics in metals, high-frequency internal friction methods appear to be particularly well suited. In one of these methods, a beam of ultrasonic energy is sent through the specimen, and the attenuation is studied as a function of a static strain or stress. The experimental data reported in the present paper were obtained by this particular technique applied to Armco iron specimens. Static tensile strains employed were small, mostly in the range of a few tenths of 1%.

## MATERIAL AND EXPERIMENTAL PROCEDURE

Armco iron used in all investigations was in the form of cylindrical specimens with a diameter of  $0.560 \pm 0.001$  inch. The length of the specimens was 10 or 12 inches. The end faces were machined and polished afterwards to a high degree.

The annealing was done in all cases in a hydrogen atmosphere. Details of the annealing procedure are described later.

A standard Sperry Reflectoscope with some modifications was employed for the ultrasonic measurements, and frequencies of a few megacycles (2.2 megacycles in most cases) were used. At the time of the experiments, the Sperry Ultrasonic Attenuation Comparator, which allows the attenuation values to be read directly, was not available. The observations of back reflections on the reflectoscope screen were recorded by means of a 35-mm camera

<sup>1</sup>Manuscript received September 30, 1958.

Contribution from the Department of Engineering and Metallurgy, Ontario Research Foundation, Toronto, Ontario.

<sup>2</sup>Ontario Research Foundation, Toronto, Ontario.

with exposure times of 1/10th of a second or less. The quartz crystal which acts as a transmitter and as a receiver was attached to one end face of the specimen. Dow Corning 200 fluid with a viscosity of 12,500 centistokes at 25° C, as used also by Hutchinson and Filmer (1956), proved to be a highly satisfactory coupling liquid between the crystal and the specimen. The ultrasonic attenuation obtained cannot, therefore, be regarded as an absolute value; the losses due to coupling liquid are included in the observed attenuation magnitude.

The external tensile stresses were applied by means of Riehle Universal Screw Power machine using specially designed auxiliary grips in order to prevent excessive indentations. The rate of loading and unloading was kept constant through the entire elastic region.

The strains were measured and recorded continuously by an MA-5P Microformer-type recorder in conjunction with a T-1M Extensometer.

The standard practice followed in the experiments was to strain the specimen up to a predetermined strain value; the specimen was then kept in this strained condition for 10 minutes and unloaded afterwards. Measurements of ultrasonic attenuation were made at intervals during these operations and were continued at zero load for 60 minutes after unloading.

#### EXPERIMENTAL DATA

Internal friction, of which ultrasonic attenuation is a particular case, can be defined by the equation,

$$\tan \delta = \log \text{dec.} / \pi,$$

where the logarithmic decrement is equal to the difference between the natural logarithms of the amplitude of successive swings. The ultrasonic

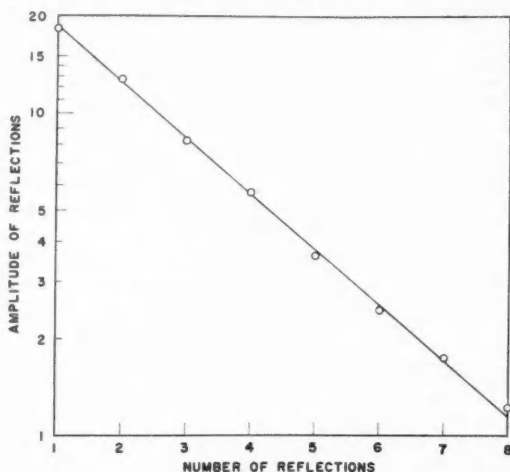


FIG. 1. Logarithm of the amplitudes of successive reflections plotted versus their number for an Armco iron specimen.

attenuation values shown in the present work were derived simply from the difference between the natural logarithms of the amplitude of successive back reflections. Figure 1 corresponds to an actual case; the amplitudes of the successive back reflections are plotted on semilogarithmic scale. The value of the slope representing attenuation value was taken directly from the graph or, as a refinement, it was calculated by the method of least squares.

The ultrasonic technique has been analyzed by Seki, Granato, and Truell (1956) and by Redwood (1957). Our technique corresponds closely to that discussed by Redwood, the diameter of the quartz crystal being larger than that of the specimen. Therefore, the end face of the specimen is completely covered by the crystal. Furthermore, the specimen being in the form of a cylinder of circular cross section acts as a solid "wave-guide", which accounts for an unusually regular attenuation pattern. Dispersion effects cannot be avoided completely, however, and the decay pattern is not ideally exponential. The deviations are not large and a relatively good straight line could be drawn through the experimental points in all cases (cf. Fig. 1).

The attenuation values are shown in all graphs plotted against the tensile strain. The corresponding stress-strain curves are also included in all cases.

The data for three specimens—which seem to show characteristic features—are dealt with in this paper. These actually represent the three prototype experiments, and the data shown are supported by a large number of observations made on many similar specimens. All the specimens in question were annealed in hydrogen for 2 hours at 850° C. Specimen No. 1 was cooled slowly in the furnace, Nos. 2 and 3 slightly more rapidly. Microphotographs show a structure of relatively regular grains with an average grain diameter of 0.08 mm.

*Specimen No. 1* was strained in four steps, the strains 0.04, 0.10, 0.33, and 1.9% being applied in succession. In the first step (Fig. 2(a)), the metal, on

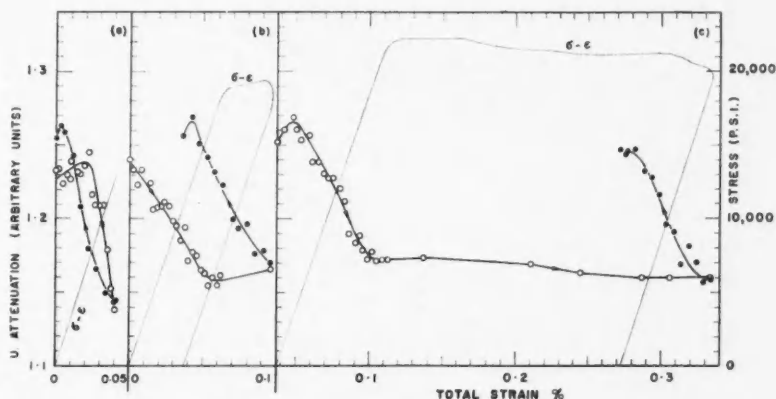


FIG. 2. Ultrasonic attenuation as a function of elastic and plastic strain for specimen No. 1 for the first three stress cycles. Stress-strain curves also shown.

the basis of stress-strain data, still behaves elastically. As the strain is continuously increased from zero value, a rapid decline in the attenuation magnitude—preceded by a slight initial increase—is experienced. A different path is followed on unloading\* and a kind of hysteresis results.

During the second and the third stages of straining up to 0.10 and 0.33 strain per cent respectively (Figs. 2(b) and 2(c)), the characteristic decline of attenuation-strain curve in the elastic region ceases, as soon as plastic deformation starts to occur. Surprisingly enough, the phenomena taking place during this deformation do not seem to have any significant effect on the attenuation values. Neither does the shape of the unloading curve differ from the curve obtained on loading in the elastic region.

Finally, a much higher strain of 1.9% was employed (Fig. 3). A gradual rise in the attenuation associated with irregular fluctuations is observed as the strain increases progressively. The unloading curve assumes also a different, characteristic shape.

In Fig. 4 the data for *specimen No. 2* are shown. In contrast to the previous case, this specimen was strained beyond the elastic region in one step. Quite different results were obtained as compared with Fig. 2. The initial loading causes the attenuation to rise at first and only after a certain stress has been reached does it start to decrease rapidly. Further stressing beyond the elastic limit causes large changes to occur, and the unloading curve obtained after a total strain of only 0.30% assumes a character somewhat similar to that of the unloading curve shown in Fig. 3.

TABLE I

Specimen No.	Anneal	Total strain (%) and type of deformation	Fig. No.	Attenuation characteristics
1	850° C, 2 hr in H <sub>2</sub> , cooled in furnace	(1) 0.04, elastic	2(a)	Decrease on loading; increase on unloading
		(2) 0.10, plastic	2(b)	Decrease on loading, constant during plastic deformation; increase on unloading
		(3) 0.33, plastic	2(c)	The same as strain cycle 2
		(4) 1.90, plastic	3	Decrease on loading, fluctuations during plastic deformation; increase followed by decrease on unloading
2	The same as specimen 1 except for faster cooling	(1) 0.3, plastic	4	Increase followed by decrease on loading, increase and fluctuations during plastic deformation; increase followed by decrease on unloading
3	The same as specimen 2	(1) 0.18, plastic	6	Increase followed by decrease on loading, large increase during plastic deformation; decrease on unloading
		(2) 0.35, plastic	7	Increase followed by decrease on loading, little change during plastic deformation; increase on unloading

\*The terms "loading and unloading curves" are used to denote ultrasonic attenuation-strain relationship throughout.

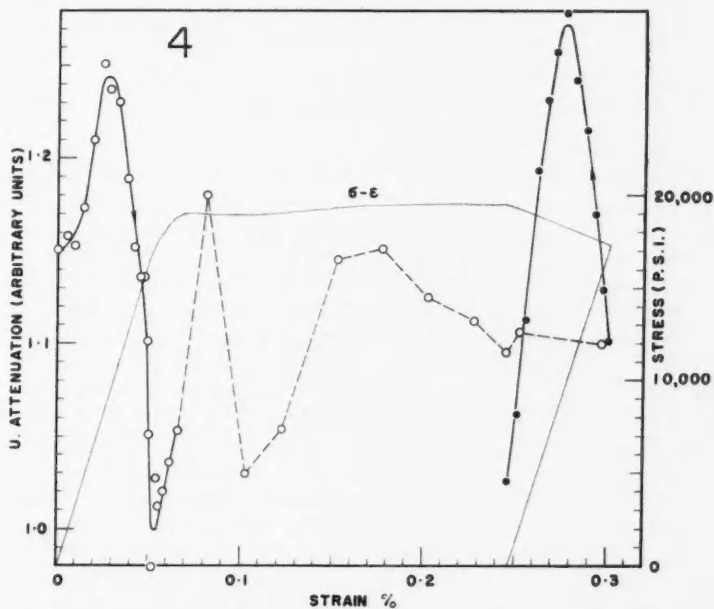
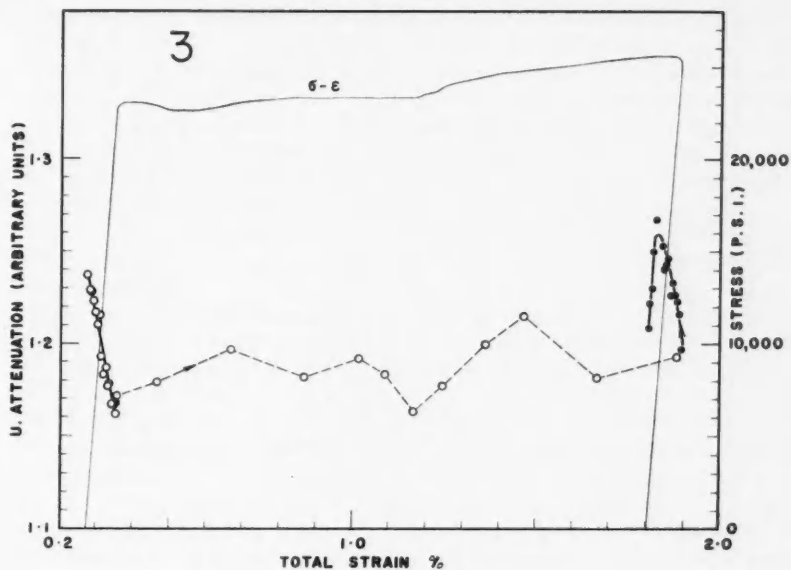


FIG. 3. Ultrasonic attenuation plotted versus large plastic strain for specimen No. 1. The data corresponding to the fourth stress cycle are shown. Stress-strain curve included.

FIG. 4. Ultrasonic attenuation versus strain for the first stress cycle of specimen No. 2. Separate stress-strain curve shown.

Further experiments, on *specimen No. 3*, were done partly in order to test the suggested explanations, and partly in order to obtain additional information. The respective experimental data (Figs. 6 and 7) are for these reasons shown and discussed separately at the end of the paper.

No significant changes in the attenuation were observed during the 10-minute period with the specimens at maximum load. The same happened during the 60-minute period with the specimens at zero load. This applies to all the specimens and the strains employed in the present investigation. Detailed information on these stages is not, therefore, presented.

Plastic deformation was in some instances still progressing after the movement of the tensile machine was stopped. The load was dropping continuously as the elongation increased. This accounts for the break in the end of the stress-strain curve noticed on some of the graphs.

The experimental observations are summarized in the above table.

#### ANALYSIS OF RESULTS

The following experimental observations will require an explanation:

1. An initial decline in attenuation is observed, in annealed specimens as a rule, as the strain is continuously increased within the elastic limit.
2. In cold-worked (plastically strained) specimens, however, a characteristic feature of elastic deformation appears to be an increase in attenuation, followed by a decrease afterwards (the unloading curves in Figs. 3 and 4).
3. A significant rise in the attenuation occurs at the yield stress region in some cases.
4. A change in the initial attenuation (at zero load) is observed in specimens after a plastic or sometimes even after an elastic deformation.

##### (a) Elastic Deformation

The gradual decline in the attenuation associated with an elastic tensile strain (Figs. 2, 3, and 4) appears to be determined mainly by the magnetic characteristics of the material. The ferromagnetic under investigation is subjected to the ultrasonic vibrations of megacycle frequency. There is a loss in internal energy associated with mechanical vibrations of any material. The internal losses in ferromagnetics are much higher than in non-ferromagnetic materials for the reasons of phenomena of magnetic nature. The most significant of these are manifested by magnetomechanical hysteresis, macroeddy and microeddy currents. Since our specimens were demagnetized and high-frequency ultrasonic waves were employed in these experiments, it is likely that microeddy currents comprise the main source of energy loss. These currents are generated between the adjacent domains due to the domain wall motion, induced in our case by ultrasonic strain. Any change in domain configuration, in the number of domains or domain walls, and in their relative mobility will be reflected on the ultrasonic attenuation magnitude.

According to the domain theory of ferromagnetism, a ferromagnetic crystal consists of magnetic domains, which should be distributed at random in an annealed and unmagnetized material. A static stress, applied in our technique by means of a tensile machine, would tend to orient the domains parallel to or



perpendicular to the direction of stress, depending on whether the magnetostriction of the material is positive or negative. At low stresses the reorientation is achieved by the growth of the more favorable oriented domains at the expense of those less favorably oriented. (Higher stresses might induce domain rotation.) The domain dimensions increase under stress and the number of existing domains and the domain walls is reduced accordingly; the domain wall motion as induced by ultrasonic strain is reduced also. As a consequence, a decrease should be experienced in the losses associated with the domain walls and their mobility. The microeddy current losses and the ultrasonic attenuation should, therefore, decline upon the application of static elastic strain.

In order to test the proposed mechanism, the effects of an external magnetic field were studied. A magnetic field plays a role similar to that of stress and the application of a field to a ferromagnetic specimen produces redistributions and rotations of domains similar to those produced by the stress. The data shown in Fig. 5, curve *b*, where an external magnetic field was applied—its axis coinciding with the longitudinal axis of the specimen—furnishes

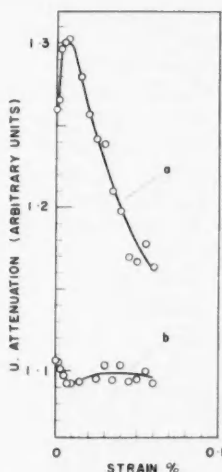


FIG. 5. The effect of an external magnetic field on the ultrasonic attenuation versus strain values: (a) without a magnetic field, (b) with a magnetic field.

support to the previous interpretation. The attenuation at zero load in the presence of an external field is already reduced to a value below the minimum achieved in the absence of a field by the highest elastic strain employed (Fig. 5, curve *a*). This indicates the magnitude of the magnetic contribution. It is reasonable to expect that only insignificant changes in attenuation would occur on the application of the load, i.e. by purely non-magnetic phenomena, as confirmed by the data in Fig. 5, curve *b*.

(b) *Plastic Deformation*

It has been shown (Granato and Lücke 1956) that significant changes in internal friction at megacycle frequencies occurring in non-ferromagnetic materials strained within the elastic limit are associated with dislocation characteristics. On the basis of the same mechanism an increase in the ultrasonic attenuation would be expected in specimens undergoing plastic deformation for the reasons of increased dislocation density. An eventual decrease might follow at larger deformations where, due to high dislocation density, a significant interaction between the dislocations can be expected (Hikata *et al.* 1956).

In a ferromagnetic, however, the changes in attenuation in the elastic strain region appear to be determined mainly by magnetic phenomena, as shown before. In the plastic range, however, both the increase in the number of dislocations and the influence of this increase on the ferromagnetic properties should be taken into consideration. The increase in dislocation density will cause an increase in the internal friction part associated with dislocation mechanisms. The mobility of the domain wall, however, will be reduced due to the effect of the increase in dislocation density. The contribution of the domain mechanisms to the internal loss is, therefore, expected to decrease, as the material is plastically deformed progressively, so that the attenuation related to this source should decrease also.

The observed value of attenuation might be considered as the sum of the two above-mentioned effects. The "magnetic" part seems to be predominant in elastic straining. The "dislocation" part appears to be active in the behavior of attenuation at the yield stress region, in the sometimes erratic pattern of attenuation during plastic deformation, and in the increase in the initial attenuation value (at zero load) in heavily deformed ferromagnetics (not considered in this paper, but to be published separately) as compared with annealed material.

In the actual experiments, straining beyond the elastic limit sometimes did not seem to change the attenuation value at all (specimen 1, Figs. 2(b) and 2(c)), but in other cases caused appreciable variations (specimen 2, Fig. 4). Specimen No. 1, however, was strained in steps, and it is reasonable to expect a certain degree of work hardening; this would render the subsequent deformation less effective. The difference in the behavior of the different specimens is, however, still remarkable.

The data on specimen 1 (Figs. 2(b) and 2(c)) suggests that the resulting plastic deformation was unable to affect the properties of the material as far as these are revealed by ultrasonic methods. The character of the attenuation changes on unloading seems to be in accordance with this and can be explained by the same domain mechanism employed in discussing the curves in Fig. 2(a). The initial attenuation value (at zero load) remained nearly unchanged, as expected, considering the insignificant changes in the attenuation during the plastic deformation.

A radical increase in strain (as used on specimen 2) was always found to produce substantial changes in attenuation, as indicated by Fig. 3. But similar

or even larger effects were also obtained at smaller strains (specimen 2, Fig. 4). Relatively large fluctuations in the attenuation observed during plastic deformation very likely correspond to violent changes occurring within the metal. More consistent variations might be detected employing high-speed photographic technique. As before, the trend in attenuation changes during plastic deformation seems to determine the behavior of strained material. The unloading curves assume in both cases (Figs. 3 and 4) a characteristic shape. As the load is gradually removed, the attenuation starts to rise at first and after passing through a maximum, it decreases to a low value at zero load. The difference in the values at zero load before and after the stress cycle might not be convincing for the case in Fig. 3, but little doubt exists about the difference in Fig. 4. This drop in ultrasonic attenuation is very likely related to the reduced mobility of domain walls due to a higher dislocation density. The contribution of the "dislocation" part of attenuation is apparently less significant under these conditions than the effect of dislocation density on the domain wall mobility.

(c) *Effective Internal Stress*

A characteristic shape of the attenuation-strain curve obtained in sufficiently deformed specimens (the unloading curves in Figs. 3 and 4) was observed also in annealed specimens at very low strains (Figs. 4 and 6). Indications of a similar trend might be found in Figs. 2(a) and 2(c), at the very beginning. In all cases, the characteristic feature is an initial increase in the attenuation as the load is increased.

In aluminum a similar increase was noted at low strains and it was explained in terms of dislocation loop mechanism (Hikata *et al.* 1956). In Armco iron, however, this kind of mechanism does not seem to be probable at the low stresses employed. The dislocation loops are believed to be more effectively pinned by interstitial atoms (cf. the relatively weak pinning produced by substitutional atoms in annealed aluminum).

A simple explanation in terms of internal stresses and their effect on domain configuration is considered here; it appears to account for the observed attenuation characteristics. It is assumed that the specimen at zero load is not ideally stress-free but contains internal stresses. These internal stresses might be either the deformation stresses in plastically strained material, or the residual stresses in annealed specimens. A strong directionality in the internal stress (compression) is expected in the specimens which underwent plastic deformation by tensile loading. Therefore, a pronounced order in the domain configuration is to be expected in these specimens at zero load. As pointed out before, a conclusion about the degree of this order in a specimen in annealed and deformed state cannot be made solely on the basis of initial attenuation (at zero load) data. The observed attenuation is the sum of a "dislocation" and a "magnetic" component. It is, however, possible to obtain an indication of the initial configuration by studying the specimen under low external stresses. The external stress will counteract the pronounced order, produced by the internal stress; the resulting less ordered configuration will manifest itself by

higher losses. As the external stress is increased a point will be reached where the respective components of the internal and the external stress will be equal and opposite. This point should correspond to a maximum in attenuation. A further increase in the external stress will cause a decrease in losses by renewed domain ordering.

#### ADDITIONAL EXPERIMENTAL WORK

The various characteristics found previously on specimens 1 and 2 were also obtained on a further specimen, *specimen No. 3*, which was strained in two steps (Figs. 6 and 7). The observed initial attenuation increase (Fig. 6) seems to be associated with the residual internal stresses. The sharp drop afterwards is caused by the renewed domain ordering discussed above and the similarly

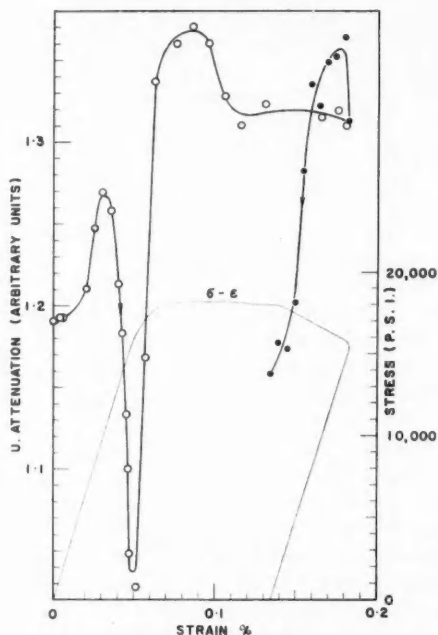


FIG. 6. Ultrasonic attenuation versus strain for specimen No. 3. The data correspond to the first stress cycle. Stress-strain curve included.

sharp rise which follows is related to an efficient plastic deformation. The character of the unloading curve most certainly indicates internal stresses in the deformed material, the attenuation falling continuously as the load is decreased. The value at zero load is lower if compared with the initial attenuation in the annealed material.

The second loading (Fig. 7) after a rest of 15 minutes at zero load followed in reverse the previous unloading curve very closely. With the external and

internal stresses equal, a maximum in the attenuation value is observed. A sharp decline which follows appears to be related to the ordering effect of external stress on the magnetic domains. The plastic deformation taking place

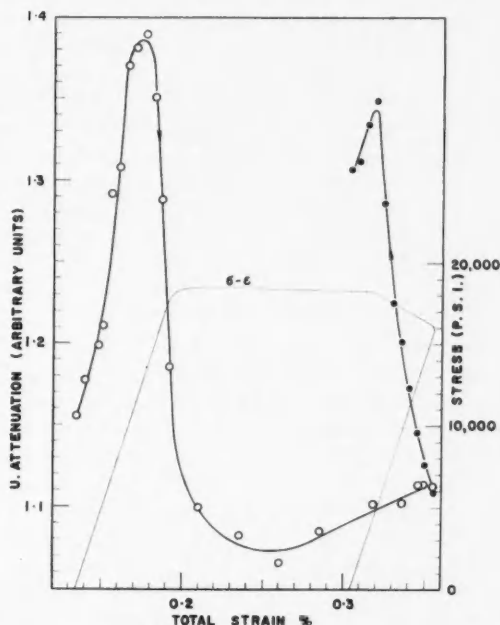


FIG. 7. Ultrasonic attenuation versus strain for the second stress cycle of specimen No. 3. Stress-strain curve also shown.

in this stress cycle shows, however, a surprisingly small effect as far as attenuation is concerned. A similarity with Fig. 2 exists in this respect, and the character of the curve obtained on unloading would actually correspond to a specimen with low effective internal stresses. No satisfactory explanation for this behavior can be offered at present. An increase in the attenuation at zero load might be noted also.

#### SUMMARY

An ultrasonic technique employing megacycle frequencies was used in order to study the changes in Armco iron on straining.

The observed changes seem to be accounted for by magnetic domain theory and dislocation mechanisms. Three features which appear to be characteristic were more closely studied.

1. In the region where the material behaves elastically, an increase in the external stress is accompanied by a decrease in ultrasonic attenuation. The effect was shown to be related to the rearrangement of magnetic domains by

the externally applied stress. The application of an external magnetic field seems to confirm this explanation.

2. An initial increase in attenuation occurring in the elastic region with some annealed and with most strain-hardened specimens appears to be associated with internal stresses, i.e. residual stresses left after annealing or stresses introduced into the material by plastic deformation. These are relieved upon the application of an external tensile stress and the result is a magnetic domain configuration exhibiting higher internal loss.

3. The changes in ultrasonic attenuation accompanying plastic deformation varied widely among individual specimens—large changes occurred in some cases and small changes in others. The difference appears to be related to the difference in straining history. The degree of strain hardening as registered by ultrasonic attenuation seems to correspond to the behavior manifested by the material during the plastic deformation.

#### ACKNOWLEDGMENTS

The work described in this paper forms a part of the program undertaken at the Ontario Research Foundation on the magnetic and mechanical changes in the metals on static and cyclic stressing. The author is indebted to Dr. K. Winterton for numerous discussions, to Dr. U. Martius for most valuable critical comments on the manuscript, and to Mr. P. E. Cavanagh, Director of the Department of Engineering and Metallurgy, for his helpful advice and constant interest.

#### REFERENCES

- GRANATO, A. and LÜCKE, K. 1956. *J. Appl. Phys.* **27**, 583.  
HIKATA, A. *et al.* 1956. *J. Appl. Phys.* **27**, 396.  
HUTCHINSON, T. and FILMER, A. J. 1956. *Can. J. Phys.* **34**, 159.  
REDWOOD, M. 1957. *Proc. Phys. Soc. B*, **70**, 721.  
SEKI, H., GRANATO, A., and TRUELL, R. 1956. *J. Acoust. Soc. Am.* **28**, 230.

# THE IMPEDANCE, RECTIFICATION, AND ELECTROLUMINESCENCE OF ANODIC OXIDE FILMS ON ALUMINUM<sup>1</sup>

ARCHIBALD W. SMITH

## ABSTRACT

An experimental investigation was made of the impedance, rectification, and electroluminescence of anodic oxide films formed on aluminum, in an electrolyte of boric acid and ammonium hydroxide. These properties were studied, where appropriate, as a function of the surface condition before anodization, the formation voltage, the conductivity of the electrolyte, and the frequency. A constant-voltage formation technique was used. The interpretation of the results suggests that the oxide itself is a good dielectric, but that the film contains defects whose number and form depend on the conditions of formation. The defects appear to control the rectification and electroluminescence and have an appreciable influence on the impedance. The frequency dependence of the capacitance was much smaller than that found by previous workers although there was an appreciable contribution arising from geometrical effects in the electrolytic cell. The zero-thickness potential for the film was found to be in agreement with a theoretical estimate.

## 1. INTRODUCTION

Anodic oxide films on aluminum play an important technological role, especially in the construction of capacitors, and have received considerable study in the last 60 years. Although many features of their structure and properties are now understood, there is still a need for further fundamental investigation. The present paper is concerned with the impedance, rectification, and electroluminescence of films formed in an electrolyte which does not dissolve the oxide. At the present time, the origins of the rectification and electroluminescence have not been established, although a number of theories exist. There are many features of the impedance which require further elucidation, particularly the large frequency dependence of the capacitance found by previous workers, and the behavior at low formation voltages. In the work described here measurements of these properties have been made as a function of the formation voltage for two surface conditions, one rough, the other smooth. The impedance was further investigated as a function of the frequency and the conductivity of the electrolyte. The interpretation of the results suggests that the oxide itself behaves as a good dielectric, but that the continuity of the film is disturbed by defects which have an appreciable influence on film properties. This is in agreement with recent work on oxide films on tantalum and zirconium.

## 2. EXPERIMENTAL

### 2.1 Preparation of Samples for Anodization. Electrolytes

The experiments were carried out on aluminum foil of minimum purity 99.99%. Square samples of nominal area 10 cm<sup>2</sup> were cut from the foil, which

<sup>1</sup>Manuscript received January 29, 1959.

Contribution from the Electronics Laboratory of the Defence Research Telecommunications Establishment, Ottawa, Ontario. This work was carried out under Project No. D48-55-50-05.

was  $7.5 \times 10^{-3}$  cm thick, leaving a tab 0.16 cm wide and 1.5 cm long projecting from the center of one side. The tab was used to make electrical connection to the sample and to suspend it in the electrolyte. In order to define the area anodized, and to eliminate undesirable reactions at the air-metal-solution boundary, the tab was coated with wax. The surface of the aluminum was prepared for anodization in two ways: (1) washed for 2 minutes in a 5% solution of sodium hydroxide at 35° C; (2) etched for 45 seconds in a mixture of 45% sulphuric acid (by weight), 43% phosphoric acid, and 12% water at 100° C, and electropolished (Tegart 1956) in the same mixture for 4 minutes at a current density of 100 ma/cm<sup>2</sup>. The first method gave a superficial cleaning only, leaving the surface contours of the aluminum essentially unchanged. The second method removed an appreciable amount of aluminum and left the surface microscopically smooth. Samples treated by these methods will be referred to as 'washed' and 'electropolished', respectively. Photomicrographs of the washed and electropolished surfaces are shown in Fig. 1.

The electrolyte used for anodization was a 5% solution of boric acid with sufficient ammonium hydroxide added to obtain the desired conductivity. Solutions with conductivities between  $0.8 \times 10^{-3}$  and  $2.5 \times 10^{-3}$  mho/cm were used, corresponding to pH values between 5.1 and 5.8. The chemicals were of reagent grade, with a maximum stated chloride content of 2 parts in 10<sup>6</sup>. Water purified with an ion-exchange resin was used throughout for making up solutions and washing samples.

### 2.2 The Electrolytic Cell. Formation Technique

The formation of the oxide films and the measurements, with the exception of the electroluminescent brightness (Section 2.4), were carried out in a cell fitted with a platinized-platinum counterelectrode (the cathode during formation), a calomel reference electrode, and a stirrer. The platinum electrode took the form of a rectangular box (1½ in. long, 1/2 in. wide, and 1¼ in. high) with the top and bottom open. The aluminum samples were suspended in the center of this box, parallel to the long side. The reference electrode was introduced by means of a liquid bridge filled with the same electrolyte as the cell. A thin tube (0.08 in. outer diameter) on the end of the bridge passed through the platinum electrode and ended about 0.05 inch from the sample. In order to prevent the diffusion of chloride ions from the calomel electrode into the cell, asbestos plugs were inserted into the tip of the calomel electrode and into the bridge. The temperature of the cell was not controlled but all work was done in the range  $(26 \pm 2)^{\circ}$  C. The cell was open to the atmosphere.

The measured capacitance of the cell includes the capacitance of the platinum electrode in series with that of the oxide film. The capacitance of this electrode was determined to be about 3100  $\mu$ f at 2 kc/s and 1200  $\mu$ f at 20 kc/s in the solution of lowest conductivity, and larger in the other solutions. The maximum measured capacitance was 6.2  $\mu$ f at 2 kc/s and 4.5  $\mu$ f at 20 kc/s. Thus the error was only 0.2 or 0.3% in the most unfavorable case. The change in series resistance of the platinum electrode between 0.1 and 20 kc/s was determined to be less than 0.1 ohm. The absolute value of this resistance



PLATE I

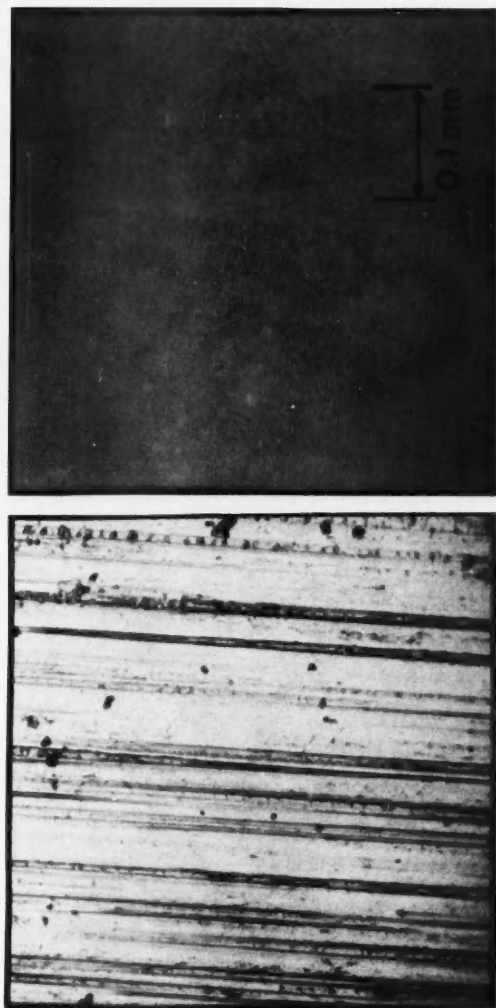


Fig. 1. Photomicrographs of aluminum surface before anodization. Sample on left is washed; on right, electro-polished. See text for details of treatments.



was of little significance because the body of the electrolyte added a relatively large, unknown series resistance.

The formation of the oxide films was carried out by applying a constant voltage to the cell through a series resistor. This resistor limited the initial current density to about 20 ma/cm<sup>2</sup>, and was reduced as formation proceeded in such a way as to keep the current density equal to the above value for as long as possible. Below a formation voltage ( $V_t$ ) of about 15 volts, the resistance of the cell itself resulted in an initial current density of less than 20 ma/cm<sup>2</sup>. The time of formation was increased gradually from 15 minutes at low voltages ( $V_t < 10$ ) to 60 minutes at high voltages ( $V_t > 200$ ). The final current density varied between 1 and 50  $\mu$ a/cm<sup>2</sup>, depending on the surface treatment and the applied voltage, as shown in Table I. Just before stopping formation, the voltage between the platinum and reference electrodes was read on a vacuum tube voltmeter. The sum of this voltage and the applied voltage gave the total formation voltage with respect to the reference electrode.

TABLE I  
Average cell current at the end of film formation

Surface treatment	Formation voltage, $V_t$						
	10	20	50	100	200	300	400
Electropolished	2.0	1.8	1.3	2.5	4.3	6.0	6.4
Washed	2.2	3.0	2.2	3.9	5.1	7.6	35.0

NOTE: Current is in units of  $10^{-4}$  amp/cm<sup>2</sup>.

### 2.3 Impedance Bridge

The impedance of the cell described above was measured on a series resistance-capacitance bridge designed to measure capacitance from 0.1 to 10  $\mu$ f, and resistance from 10 to 1000 ohms, over the frequency range 0.1 to 20 kc/s. Provision was made for applying d-c. potentials up to 200 volts to the cell during measurements. The bridge was equipped with a Wagner ground circuit to balance stray capacitance to ground. The maximum a-c. signal applied to the cell was 50 millivolts. At frequencies of 5 kc/s and below, the measured capacitance was accurate to  $\pm 0.2\%$  or better. Above 5 kc/s, the errors were larger than this, depending on the magnitude of the capacitance, and the resistance in series with it. For the measurements reported here, the upper limit of error was about  $\pm 2\%$  at 20 kc/s. The resistance values were accurate to  $\pm 1\%$  or better at all frequencies.

### 2.4 Electroluminescence Measurements

The electroluminescence of the oxide film was detected with a type 931-A photomultiplier. The electrolytic cell was essentially the same as in the impedance measurements, except that the reference electrode was omitted, and the platinum counterelectrode expanded in size to  $3\frac{1}{2}$  in. by 3 in. by  $1\frac{1}{2}$  in. The samples were correspondingly increased in size to 3 in. square, in order to obtain a higher photocurrent. One of the large sides of the counterelectrode

was a screen of platinum wire, consisting of 0.010-in. diameter wires placed 0.25 inch apart. The light output was observed through this screen and a plane window in the cell container. The photocathode-to-sample distance was about 3 inches. With the particular photomultiplier tube used, the smallest detectable photocurrent was judged to be about  $1.0 \times 10^{-10}$  amp. This figure was determined chiefly by the noise in the photomultiplier.

### 3. RESULTS

#### 3.1 Impedance

The a-c. impedance measurements were carried out in order to investigate the relationship of the equivalent series capacitance ( $C_s$ ) and resistance ( $R_s$ ) of the oxide film to the formation voltage ( $V_f$ ) and frequency of measurement ( $f$ ). It was also desired to know whether the surface treatment before anodization and the conductivity of the electrolyte had any significant effect. To achieve these aims, measurements were performed on four groups of samples, which covered preparation by washing and by electropolishing, and anodization in high- and low-conductivity solutions. Each sample in a group was anodized at a series of successively increasing  $V_f$ , and at each  $V_f$ ,  $C_s$  and  $R_s$  were measured at 0.1, 0.2, 0.5, 1, 2, 5, 10, and 20 kc/s. The series of  $V_f$  for each sample usually extended over the range 10 to 400 volts. The measurements were made about 10 minutes after ceasing formation, because the capacitance dropped about 1% in the first few minutes.

Some measurements were also made on samples anodized over the range 2 to 10 volts. The general program of the measurements was the same as above. The area of the samples was reduced by one-half to 5 cm<sup>2</sup> for these measurements, the readings at 0.1 and 20 kc/s were omitted, and the conductivities of the solutions increased somewhat. The measurements were again made 10 minutes after ceasing formation.

The capacitance results will be considered first. Apart from certain exceptions noted below, the reproducibility between samples varied from 0.1 to 4%, but was usually about 1%. The relationship between  $1/C_s$  and  $V_f$  (at a fixed frequency) was nearly linear, except for washed samples above  $V_f = 200$ . The slopes and intercepts on the  $1/C_s$  axis of the straight lines fitting the data both increased slightly with frequency. These results are illustrated for electropolished samples ( $2.5 \times 10^{-3}$  mho/cm electrolyte) in Fig. 2. The situation near the  $1/C_s$  axis is shown in more detail in the lower insert of this figure. The formation voltage was referred to the potential of the saturated calomel electrode in all the data. The results for washed and electropolished samples were much the same below  $V_f = 200$ . The behavior of washed samples at  $V_f = 300$  and 400 was not very reproducible, but typical measurements are shown by the dashed lines in Fig. 2. It will be seen that they deviate considerably from the straight line established at lower voltages. Decreasing the conductivity of the solution caused the intercepts on the  $1/C_s$  axis to increase more rapidly with frequency, and reduced the deviations from the straight line for washed samples above  $V_f = 200$ . Straight lines have been fitted to the data at 0.2 and 10 kc/s by a least squares procedure, and the resulting constants for the

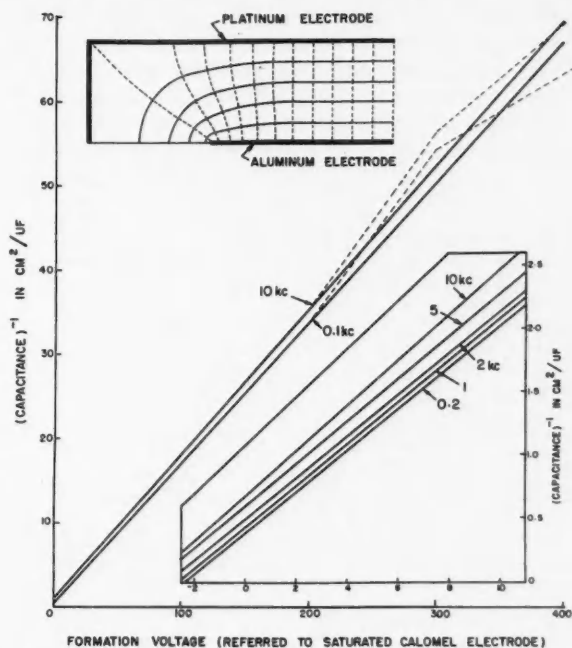


FIG. 2. Reciprocal capacitance plotted against formation voltage. Solid lines: electropolished samples ( $2.5 \times 10^{-3}$  mho/cm electrolyte). Dashed lines: washed samples at  $V_f = 200$ , 300, and 400 ( $1.6 \times 10^{-3}$  mho/cm electrolyte). Upper insert: equipotential (solid) and field (dashed) lines for one quadrant of horizontal plane through center of electrode system.

equation  $1/C_s = a + bV_f$  are shown in Table II. By comparing the various cases, it will be seen that extrapolation of high formation voltage data does not always yield accurate values of the intercept  $a$ .

TABLE II  
Constants of the equation  $1/C_s = a + bV_f$

Surface treatment	Range of $V_f$	Conductivity of electrolyte	Frequency			
			0.2 kc/s		10 kc/s	
			$a$	$b$	$a$	$b$
Electropolished	2-10	$1.6 \times 10^{-3}$	0.423	0.175	0.803	0.208
		2.5	0.402	0.169	0.675	0.188
	10-400	0.83	0.88	0.171	2.41	0.174
		2.5	0.70	0.169	1.20	0.173
Washed	2-10	2.5	0.382	0.164	0.675	0.179
	10-200	0.83	0.41	0.167	1.56	0.174
		1.6	0.37	0.167	1.02	0.171

NOTE: Units— $a$  in  $\text{cm}^2/\mu\text{f}$ ,  $b$  in  $\text{cm}^2/\mu\text{f-volt}$ ,  $V_f$  in volts, conductivity in mho/cm.

The equivalent series resistance results will be discussed next. In general, these were less reproducible than the capacitance results because the resistance of the electrolyte ( $R_e$ ) appeared to vary slightly between anodizations and between samples. The results for electropolished samples in  $2.5 \times 10^{-3}$  mho/cm electrolyte are plotted against the reciprocal of the frequency ( $1/f$ ) in Fig. 3. It will be seen that at frequencies below 2 kc/s,  $R_s$  was proportional to  $1/f$ . At

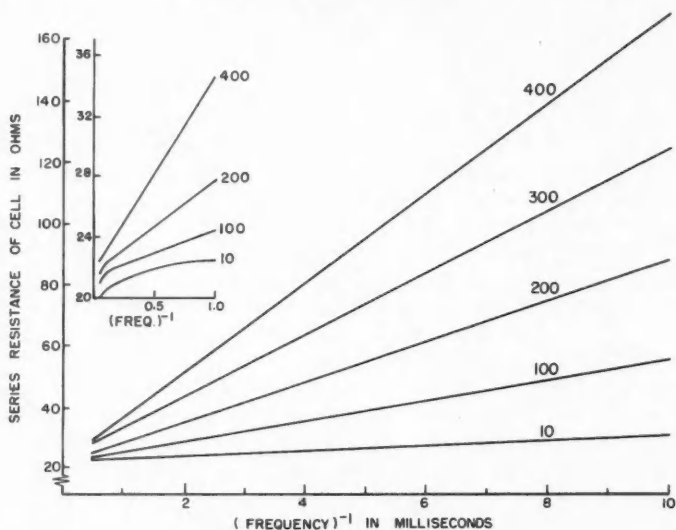


FIG. 3. Series resistance of the electrolytic cell plotted against reciprocal frequency for electropolished samples in  $2.5 \times 10^{-3}$  mho/cm electrolyte.

frequencies above 2 kc/s, there was an appreciable curvature, which made it impossible to determine  $R_e$  by extrapolation to  $1/f = 0$ . This curvature increased as the conductivity of the electrolyte was decreased. For  $V_t$  less than about 10 volts,  $R_s$  was found to be independent of  $V_t$ , except perhaps at 0.1 kc/s. The results for washed samples were very similar except that the slope of the linear portion for  $V_t = 400$  was about three times as great.

Three special runs were made to determine the change in impedance when the formation voltage was reapplied after having ceased formation for a short time. The procedure was as follows: Films were formed to successively higher voltages in the same manner as before. At each formation voltage, the impedance was measured at 0.2, 2, and 20 kc/s, 20 minutes after ceasing formation. The capacitance and resistance values so obtained have been designated  $C_1$  and  $R_1$ , respectively. The formation voltage was then reapplied and 10 minutes later, the impedance measured at the same frequencies, yielding  $C_2$  and  $R_2$ . Finally, the voltage was shut off again and 20 minutes later, the impedance remeasured, yielding  $C_3$  and  $R_3$ . The quantities  $\Delta C_1 = (C_2 - C_1)/C_2$ ,  $\Delta C_3 = (C_2 - C_3)/C_2$ , and  $\Delta R_1 = (R_2 - R_1)/(R_2 - R_e)$  are tabulated in Table III.

The entries in the table are average values of the quantities over the range of  $V_t$  shown in column 2. There was no significant difference between  $R_1$  and  $R_2$ , and  $\Delta C$  did not show any significant trend with the change in thickness. It will be seen that the application of the formation voltage increased the capacitance by a small percentage, which decreased with increasing frequency. The resistance was increased by a much larger factor, which also decreased with increasing frequency.

TABLE III  
The change in impedance upon reapplication of the formation voltage

Quantity	Range of $V_t$	Frequency in kc/s		
		0.2	2	20
$\Delta C_1$	5-250	.034	.025	.018
$\Delta C_2$	5-250	.027	.018	.015
$\Delta R$	5-25	.27	—	—
	30-75	.69	.11	—
	100-250	1.05	.30	—

NOTE: See text for definitions of  $\Delta C_1$ ,  $\Delta C_2$ , and  $\Delta R$ .

### 3.2 Current-Voltage Characteristics

The purpose of the measurements described here was to investigate the effect of the surface treatment before anodization on the d-c. current-voltage characteristics. To obtain these, a sample was successively anodized for 1 hour at  $V_t = 100, 200, 300$ , and 400 in a  $1.6 \times 10^{-3}$  mho/cm electrolyte. At each  $V_t$ , a current-voltage curve was taken by decreasing the applied voltage in steps, starting at the formation voltage, passing through zero current, and then increasing the voltage with the opposite polarity. Current readings were taken about 1 minute after the voltage was set, except at low anodic voltages, where about 5 minutes were allowed. The reproducibility between samples was rather poor, but certain general trends became evident, as illustrated in Fig. 4, for  $V_t = 100$  and 400. Before the results were plotted, the zero-current (i.e. open-circuit) voltage of the system (usually in the range  $\pm 1$  volt) was subtracted from the applied voltage.

It will be seen from Fig. 4 that on a log-log plot, each curve in the anodic or reverse direction consisted of a rapidly falling curved section just below the formation voltage, followed by a more or less linear section at lower voltages (cf. Charlesby 1953; Smith 1957). The experimental points deviated least from the straight line for the 300- and 400-volt cases. There was no unique relation between the current and the thickness at a given voltage along the linear section. However, the current was usually a minimum for  $V_t = 100$  or 200, and a maximum for  $V_t = 300$  or 400. For a given  $V_t$ , the main variation between samples was a displacement of the linear section parallel to the current axis. For instance, at  $V_t = 200$ , the current varied from  $2 \times 10^{-10}$  to  $2 \times 10^{-8}$  amp/cm<sup>2</sup>, with 10 volts applied.

The cathodic or forward curves were steeply rising and, at higher voltages,

the current consistently decreased with increasing thickness. At lower voltages, the curves often crossed over.

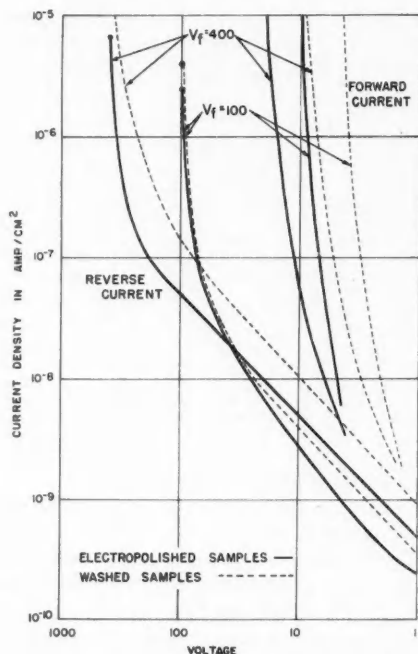


FIG. 4. Current-voltage characteristics for washed and electropolished samples.

It is evident that the washed and electropolished samples behaved in much the same way, but there were two pronounced differences. First, the anodic current for washed samples with  $V_t = 400$  was very erratic when the applied voltage was close to  $V_t$ , and was greater by a factor of 5 to 10. Second, above 5 volts, the cathodic current for washed samples was greater by a factor of about 100.

The determination of the current-voltage curves was not entirely straightforward due to drift of the current. The drift was investigated in a few samples by measuring the current at 1-, 2-, 5-, and 10-minute intervals after the voltage was set, with the following results: After a decrease in the reverse voltage in the range  $V_t > V \gtrsim 0.8 V_t$ , the current drifted downward by amounts up to 40% in 10 minutes. In the range  $0.8 V_t \gtrsim V \gtrsim 0.02 V_t$ , the drift was less than 5% in 10 minutes. In the range  $0.02 V_t \gtrsim V > 0$ , a decrease in voltage often caused a reversal in current, but the current always drifted back to the anodic direction, so that the reversal was temporary. A rough equilibrium was usually established within 10 minutes. This effect prevented the measurement of the zero-current voltage to better than 0.1 or 0.2 volt. In the forward



direction, there was little drift up to 3 or 4 volts. Beyond this, the current drifted rapidly upward after an increase in voltage, without appearing to reach an equilibrium.

### 3.3 Electroluminescence

A study was made of the dependence of the electroluminescence (abbreviated EL) on the surface treatment before anodization and on the formation voltage. At each formation voltage, both the photocurrent, which is proportional to the electroluminescent brightness, and the cell current were measured as a function of the applied voltage, in the same way as the cell current in the previous section. Observation of the EL in the forward direction is very difficult because of the streams of hydrogen gas coming off the surface, and no results for this case will be given here. The results in the reverse direction for washed and electropolished samples are shown in Fig. 5. The ratio of the photocurrent to the cell current ( $I_p/I_c$ ) has been plotted against the field in the film for

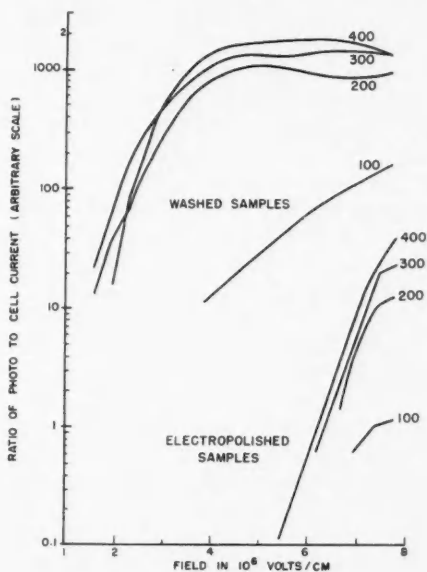


FIG. 5. Ratio of the electroluminescent brightness to the electrolytic cell current plotted against the approximate field in the film. The curves are labelled with the formation voltages.

$V_f = 100, 200, 300,$  and  $400$ . The field was computed approximately by assuming that the thickness  $d$  of a film formed to a voltage  $V_f$  was  $d = 1.3 \times 10^{-7} V_f$  cm. For washed samples at high fields, both the photocurrent and cell current were rather erratic, and the larger fluctuations in these currents were correlated. Under these conditions  $I_p/I_c$  was nearly constant and therefore  $I_p$  was approximately proportional to  $I_c$ . This is in agreement with the results of van Geel, Pistorius, and Bouma (1957) for EL at the formation voltage with

a constant film thickness, although their measurements were made in a somewhat different way. At low fields  $I_p$  fell much more rapidly than  $I_c$ . The ratio  $I_p/I_c$  was much smaller for the electropolished samples, and as  $I_c$  was about the same (cf. Fig. 4),  $I_p$  itself was also much smaller.

#### 4. DISCUSSION AND INTERPRETATION OF RESULTS

##### 4.1 Impedance

In this section, an attempt is made to relate the measurements of the equivalent series capacitance and resistance to phenomena within the electrolytic cell. A simple circuit representation of the cell is first proposed on the basis of a few simple assumptions. By comparing the predicted and observed values of the impedance, it is shown that this simple circuit is inadequate due to certain geometrical effects in the cell. Taking these into account, the section is concluded with a discussion of the relation of the impedance measurements to the properties of the oxide film itself.

The simplest circuit representation of an electrolytic cell containing an anodized electrode consists of a capacitor, representing the effect of the oxide film, in series with a resistor equal to the resistance of the electrolyte. (It is assumed that the impedance of the counterelectrode has been made negligible.) If the oxide has a thickness  $d$  and a complex dielectric constant  $\epsilon^* = \epsilon(1 + iD)$ , its capacitance per unit area will be given by  $C_1 = \epsilon/d$ , in rationalized units. The loss tangent  $D$  for the oxide turns out to be sufficiently small that  $C_1$  may be equated directly to the equivalent series capacitance of the circuit  $C_s = C_1 = \epsilon/d$ . The equivalent series resistance of the oxide is given by  $R_1 = D/\omega C_1$  and thus the series resistance of the circuit is  $R_s = R_0 + D/\omega C_1$ . If the oxide behaves as a good dielectric,  $\epsilon$  and  $D$  will vary only slightly with frequency, generally decreasing as the frequency is increased from 0.1 to 20 kc/s (cf. von Hippel 1954). The linear relation which holds between  $1/C_s$  and  $V_t$ , at least over limited ranges of  $V_t$ , implies that  $d = kV_t$ , where  $k$  is a constant.

This circuit gives a good representation of the frequency and thickness dependence of the impedance of cells containing tantalum and niobium (cf. Young 1955). However, it is not adequate for the present results for aluminum, because extrapolation of the data of Fig. 2 to  $1/C_s = 0$  would give a zero-thickness voltage ( $V_0$ ) which was frequency dependent. This is, of course, impossible. The curvature in the  $R_s$  vs.  $1/f$  plots (Fig. 3) at frequencies below 2 kc/s is also inconsistent with the above circuit.

These discrepancies can be explained by taking into account the frequency dependence arising from the geometry of the electrolytic cell. Suppose that the electrolyte joining the two electrodes is divided into conducting paths of equal resistance. For alternating currents, the electrical circuit from each path to the anodized electrode is completed through a capacitance due to the oxide film. Thus the cell may be effectively represented by a number of circuits in parallel, each consisting of a resistance and capacitance in series. If any of the capacitances are different, the resistances all being taken equal by definition, the impedance of the network will have a different frequency

dependence from a single resistance and capacitance in series. Whether or not the capacitances are equal is determined by the areas on which the conducting paths terminate at the anodized electrode, assuming that the film has a perfectly uniform structure and thickness. The areas are determined by the solution of Laplace's equation for the electrode geometry of the particular cell. The frequency dependence increases with increasing series resistances. Thus it will be larger with the low-conductivity solutions which must be used with aluminum than with the high-conductivity solutions normally used with tantalum and niobium.

Equipotentials and field (or current) lines have been obtained for the horizontal plane through the center of the present electrode system by a graphical solution of Laplace's equation. These are shown for one quadrant in the upper insert of Fig. 2. The regions between the field lines represent conducting paths of equal resistance. It will be seen that paths near the end of the aluminum terminate on smaller areas, and hence on smaller capacitances, than those near the center. The situation is very similar even if the end of the platinum electrode is not closed. Therefore the resultant impedance of the complete electrode may be evaluated approximately by considering only the quadrant shown in Fig. 2. If the capacitance associated with the  $n$ th path is  $C_n$ , and the resistance of each path is  $R$ , the equivalent series capacitance and resistance of the system are given by:

$$\frac{1}{C_s} = \frac{\omega B}{G^2 + Y^2} \quad \text{and} \quad R_s = \frac{G}{G^2 + Y^2},$$

where

$$B = \sum_n \frac{1/\omega C_n}{R^2 + (1/\omega C_n)^2} \quad \text{and} \quad G = \sum_n \frac{R}{R^2 + (1/\omega C_n)^2}.$$

There are two limiting cases: (1) At low frequency and/or capacitance  $\omega C_n R \ll 1$ ,  $C_s = \sum C_n$ , and  $R_s = R \sum C_n^2 / (\sum C_n)^2$ . This approximation is adequate at 0.1 and 0.2 kc/s under the conditions of the present experiments, except perhaps for  $V_t \leq 4$ . (2) At high frequency and/or capacitance  $\omega C_n R \gg 1$ ,  $1/C_s = (1/n^2) \sum (1/C_n)$ , and  $R_s = R/n$ . This approximation is not valid at all under the present conditions. Calculations of  $1/C_s$  and  $R_s$  were made at a number of frequencies and formation voltages, using the upper insert of Fig. 2, and observed  $C_s$  at 0.1 kc/s to determine the capacitances  $C_n$ .  $R$  was estimated from observed  $R_s$  at 20 kc/s. The details of these calculations will not be given here, but it was found that the observed frequency dependence of the intercepts on the  $V_t$  axis, and of the  $R_s$  values for  $V_t < 10$ , was approximately reproduced. The  $1/C_s$  vs.  $V_t$  plots at the higher frequencies were curved, with the second derivative  $d^2(1/C_s)/dV_t^2$  negative and increasing in magnitude with frequency. For instance, the slope at 10 kc/s was 12% larger than that at 0.1 kc/s over the range  $V_t = 4$  to 10, but was 1.2% smaller over the range  $V_t = 50$  to 100. This curvature explains the extraordinarily high slopes obtained at 10 kc/s for the low formation voltage cases of Table II.

The relation of the impedance measurements to actual properties of the oxide film can now be discussed. First, the question of the zero-thickness voltage  $V_0$  will be reconsidered. Experimentally, it is given most accurately by extrapolation of the low formation voltage data at 0.2 kc/s to  $1/C_s = 0$ . An average value of  $V_0 = (-2.4 \pm 0.1)$  volts is obtained from the three cases in Table II for which  $2 \leq V_t \leq 10$ . The frequency dependence arising from the cell geometry will cause this value to be about 0.1 volt too low algebraically, and thus the best experimental value is  $V_0 = (-2.3 \pm 0.1)$  volts. If certain simplifying assumptions are made,  $V_0$  may be calculated theoretically (Vermilyea 1954b; Young 1957a). When oxide-free aluminum is placed in the electrolyte, oxide immediately grows until  $d = k\phi$ , where  $\phi$  is the relative oxidation potential associated with the reaction for the production of oxide:



If the aluminum is anodically biased (by introducing a counterelectrode and an external voltage), more oxide grows on top of the initial layer. Using the free-energy data for bulk  $\text{Al}_2\text{O}_3$ , the value of  $\phi$  may be estimated as +1.50 volts, under standard conditions (Latimer 1952). The electrolytes used in this work had a hydrogen-ion concentration of about  $\text{pH} = 5.2$ . When this is taken into account, and potentials are referred to the saturated calomel electrode, the value  $-2.05$  volts is found for  $V_0$ , in fair agreement with the experimental value of  $(-2.3 \pm 0.1)$  volts.

The slope  $b$  of the  $1/C_s$  vs.  $V_t$  plots will now be briefly discussed. The relation  $b = k/\epsilon$  may be easily derived on the basis of the simple circuit representation. The slopes in Table II may be compared with previous measurements of  $k$  and  $\epsilon$ . These quantities have been measured by many workers under various conditions;  $k = 13 \times 10^{-8}$  cm/volt (Dekker and van Geel 1947; Hass 1949) and  $\epsilon/\epsilon_0 = 8.7$  (van Geel and Schelen 1957) may be taken as representative values. The value of  $b$  derived from these is 0.17 cm/ $\mu\text{f}$ -volt, which is in satisfactory agreement with the values in Table II. The increase in  $b$  with frequency for the data in this table means that  $\epsilon$  decreases slightly, as expected.

The loss tangent  $D$  for thick films ( $V_t \geq 100$ ) has been evaluated using the formula  $D = \omega C_1 R_1$ , with  $C_1$  equal to  $C_s$  for 0.1 kc/s and  $R_1$  determined approximately as  $R_s(V_t \geq 100) - R_s(V_t < 10)$ . Subtraction of the resistance  $R_s(V_t < 10)$  for thin films corrects for the resistance of the electrolyte, and approximately for the frequency dependence arising from the cell geometry. The values obtained are shown in Table IV for  $V_t = 200$  and 400. The values for  $V_t = 100$  and 300 volts were much the same as for  $V_t = 200$ . At high frequencies  $R_1$  is the small difference of large numbers so the uncertainty in  $D$  is quite large. Therefore,  $D$  is given at low frequencies only in Table IV. For each surface treatment,  $D$  tends to be lower in the solution of lower conductivity. For washed samples at  $V_t = 400$ , in the  $2.5 \times 10^{-3}$  mho/cm electrolyte,  $D$  is about three times greater than average, and this fact appears to be related to the higher currents at the end of formation for the same conditions (Table I).

TABLE IV  
The dielectric loss tangent  $D$  for the oxide film

Surface treatment	Formation voltage, $V_f$	Conductivity of electrolyte	Frequency in kc/s			
			0.1	0.2	0.5	1.0
Electropolished	200	0.83 $\times 10^{-3}$	6.8	7.9	6.3	6.1
		2.5	9.6	9.1	8.0	6.9
	400	0.83	10.0	12.6	8.7	7.8
		2.5	12.6	12.0	10.6	10.1
Washed	200	0.83	9.5	9.7	8.2	8.9
		1.6	9.9	9.7	8.1	7.3
	400	0.83	12.5	10.8	11.3	13.0
		1.6	32	31	30	30

NOTE: Entries give the loss tangent in units of  $10^{-3}$ . Conductivity is in units of mho/cm.

The increase in capacitance (or  $\epsilon$ ) which results from the application of the d-c. formation voltage (Table III) appears to be related to effects in the body of the oxide film, because percentagewise it is independent of thickness. The corresponding percentage increase in resistance increases with thickness. This implies an increase in  $D$  which tends to be independent of thickness. These changes are probably due to the introduction of extra carriers through the action of the applied field. The decrease in the change of  $\epsilon$  and  $D$  with increasing frequency suggests that these carriers have a relaxation time of  $10^{-8}$  or  $10^{-4}$  seconds, and therefore are ions. The extra ions could be injected into the oxide itself or into defects in the film opened up by the d-c. field.

The impedance of electrolytic cells containing anodized aluminum electrodes has previously been measured as a function of formation voltage and frequency by van Geel and Scholte (1951), Scholte and van Geel (1953), and Lilienfeld and Miller (1953). Although valid comparisons are difficult to make because of the differing conditions, their results are qualitatively similar to those reported here. One point worth discussing in some detail is the frequency dependence of the capacitance. The situation is illustrated in Fig. 6, in which the reciprocal capacitance, normalized at 1 kc/s, is plotted against frequency on a log scale. It will be seen that the frequency dependence of the present results is considerably smaller, even if the extra dependence caused by the geometry of the cell and by the application of a d-c. field is included. Neither pair of authors considered explicitly the possibility of frequency-dependent effects due to the geometry of their cells, although the conductivity of their electrolytes was low enough to make such effects important. However, such effects alone cannot account for the difference in the frequency dependence, and it appears that actual differences in the structure of the film are involved. An important factor here may be the number and form of defects in films produced under different conditions (see Section 4.2).

Both pairs of authors found non-zero intercepts on the  $1/C_s$  axis and interpreted these as evidence of interfacial effects between the oxide and the electrolyte. However, in neither case was a reference electrode employed, nor was any attempt made to calculate the theoretical voltage at which the

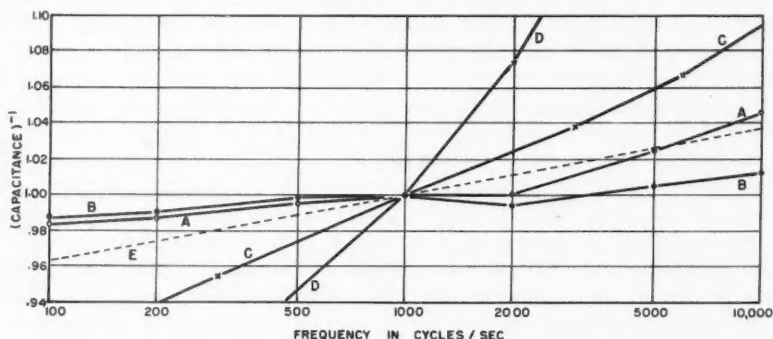


FIG. 6. Reciprocal capacitance, normalized at 1 kc/s, plotted against frequency, on a log scale. Curve A: results of this paper for washed samples with  $V_t = 100$ , and  $1.6 \times 10^{-2}$  mho/cm electrolyte. Curve B: same as curve A, but corrected approximately for frequency dependence of the cell. Curve C: results of Scholte and van Geel (1953, Table V) for  $V_t = 100$ . Curve D: results of Lilienfeld and Miller (1953, Fig. 5) for  $V_t = 180$ . Curve E: typical frequency dependence of a niobium film (Young 1955, Table I).

thickness would be zero. Lilienfeld and Miller used an aluminum cathode and extrapolated to  $V_t = 0$  using data over the range  $V_t = 100$  to 400. It is unlikely that meaningful intercepts can be obtained under these conditions. Unfortunately, van Geel and Scholte analyzed their results by a method which is sensitive to systematic errors in the high-frequency measurements (such as would be caused by geometrical effects in the cell). For these reasons, the evidence for interfacial effects appears to be of questionable validity.

#### 4.2 The Role of Defects in the Oxide Film

Oxide films formed on tantalum and zirconium appear to have defects whose number and size depend on the roughness of the surface and on the thickness of the film (Vermilyea 1954a; Young 1957b and 1958). The defects have an observable effect on the capacitance and loss tangent, and on the rectification. Young (1957b) has suggested that they arise from compressional stresses building up due to preferential oxidation of sharp projections of metal, and that they might take the form of cracks filled with electrolyte or gas. However, many of the defects would probably take less violent forms, ranging in size down to minute pores containing only a few water molecules. Impurities in the metal might cause similar defects by interfering with the normal formation of oxide.

The present experimental results for aluminum are consistent with the concept of defects in the film. This is brought out most clearly by the difference in the capacitance (Fig. 2), the loss tangent (Table IV), and the current at the end of formation (Table I) for washed and electropolished samples. It is evident from this data that the defects become more serious as the formation voltage and the conductivity of the electrolyte are increased. If it is assumed that most of the d-c. current passes through defects, rather than the oxide, two aspects of the current-voltage characteristics of Fig. 4 can

be more easily understood, namely the increase in the reverse current with increasing thickness, and the relatively greater forward current for washed samples. Young (1958) has concluded that the observed current-voltage characteristics for the tantalum are chiefly determined by defects. The present results for aluminum appear to be more consistent with this view than with a previous theory (Smith 1957) in which rectification arose from the difference in the behavior of holes and electrons at the oxide/electrolyte interface. However, the mechanism by which the defects rectify still remains to be determined.

The influence of the defects on film properties will be more extensive if it is possible for electronic breakdown to occur at a defect. It is well known that penetration of water vapor into pores lowers the breakdown strength of insulators (e.g. Inuishi and Powers 1957). The extra conduction due to the water probably leads to a local heating which causes breakdown in the surrounding insulator. A similar type of breakdown would be expected to occur at pores in anodic oxide films, but in this case the breakdown would be partially blocked off by the formation of new oxide and/or a gas bubble. If new oxide were formed, it would probably be thicker than normal because of the local temperature rise. By this mechanism, minute pores having little or no effect at low voltages could give rise to more serious defects and changes in film properties when the formation voltage was raised. Other, though less probable, types of breakdown are also possible. For instance, the intrinsic "high temperature" type of breakdown (Frohlich and Simpson 1950) could occur in regions of oxide containing a large number of electron traps.

Two further experimental observations can be more easily understood on the basis of electronic breakdown. First, the erratic nature of the cell and photocurrents for washed samples (Section 3.3) could be due to the random occurrence of breakdown. Second, the conductivity of the electrolyte could influence the film properties through its effect on breakdown. This may be seen as follows: The overvoltage necessary to drive a given current through a pore will be a function of the conductivity of the electrolyte. In general, it would be expected that the overvoltage would be higher for a solution of lower conductivity. This was found to be true experimentally at a platinum electrode in the electrolytes used to anodize the aluminum in the present work. If this is true for the oxide electrode also, it would be expected that a higher applied voltage would be required to cause breakdown with the solution of lower conductivity. This is consistent with the observed effect of the conductivity on the impedance.

#### 4.3 Electroluminescence

There are two principal explanations for the steady EL in the anodic direction: (1) Collisions of electrons with impurity atoms which act as luminescent activators. This mechanism has been discussed previously (Smith 1957; van Geel *et al.* 1957). (2) Breakdown effects in the oxide. The emission of visible radiation would be expected from a region of breakdown. The well-known scintillations which become visible at high formation voltages are a



striking example of this. When these occur, the damage to the film is extensive enough to be seen under the microscope (Vermilyea 1954a).

The relative importance of the first and second mechanisms will depend on conditions in the particular film under study. For the present results (Fig. 5) it is possible that the EL for the electropolished samples is determined chiefly by the first mechanism. But the difference between the electropolished and washed samples in the magnitude and field dependence of  $I_p/I_0$  can be most easily understood in terms of an increasing number of defects, and hence an increasing amount of breakdown. The erratic nature of the EL for washed samples, under conditions previously noted, also follows more naturally on the breakdown mechanism. On the collision mechanism, the decrease in brightness upon polishing can only be understood by making the more special assumption that the activating impurity is concentrated at the surface.

### 5. CONCLUSIONS

The chief conclusions may be summarized as follows:

- (1) Under the conditions of formation used here, the oxide behaves as a good dielectric.
- (2) The observed voltage corresponding to zero thickness of the film is in reasonable agreement with the theoretical value.
- (3) The films contain defects whose number and size increase with increasing surface roughness before anodization, and with increasing thickness. The presence of the defects probably leads to a randomly occurring breakdown of the oxide in the regions surrounding them.
- (4) The characteristics of the rectification and electroluminescence are probably determined by the defects.

### REFERENCES

- CHARLESBY, A. 1953. *Proc. Phys. Soc. B*, **66**, 533.  
 DEKKER, A. J. and VAN GEEL, W. CH. 1947. *Philips Research Repts.* **2**, 313.  
 FROHLICH, H. and SIMPSON, J. H. 1950. Intrinsic dielectric breakdown in solids, in *Advances in electronics*, Vol. II (Academic Press, Inc., New York).  
 VAN GEEL, W. CH., PISTORIUS, C. A., and BOUMA, B. C. 1957. *Philips Research Repts.* **12**, 465.  
 VAN GEEL, W. CH. and SCHELEN, B. J. J. 1957. *Philips Research Repts.* **12**, 240.  
 VAN GEEL, W. CH. and SCHOLTE, J. W. A. 1951. *Philips Research Repts.* **6**, 54.  
 HASS, G. 1949. *J. Opt. Soc. Am.* **39**, 532.  
 VON HIPPEL, A. R. 1954. *Dielectric materials and applications* (John Wiley & Sons, Inc., New York).  
 INUSHI, Y. and POWERS, D. A. 1957. *J. Appl. Phys.* **28**, 1017.  
 LATIMER, W. M. 1952. *The oxidation states of the elements* (Prentice-Hall, Inc., New York).  
 LILIENTHAL, J. E. and MILLER, C. 1953. *J. Electrochem. Soc.* **100**, 222.  
 SCHOLTE, J. W. A. and VAN GEEL, W. CH. 1953. *Philips Research Repts.* **8**, 47.  
 SMITH, A. W. 1957. *Can. J. Phys.* **35**, 1151.  
 TEGART, W. J. McG. 1956. *The electrolytic and chemical polishing of metals* (The Pergamon Press, Ltd., London).  
 VERMILYEA, D. A. 1954a. *Acta Met.* **2**, 476.  
 ——— 1954b. *J. Electrochem. Soc.* **101**, 389.  
 YOUNG, L. 1955. *Trans. Faraday Soc.* **51**, 1250.  
 ——— 1957a. *Trans. Faraday Soc.* **53**, 841.  
 ——— 1957b. *Acta Met.* **5**, 711.  
 ——— 1958. *British Columbia Research Council Annual Report for Defence Research Telecommunications Establishment Project No. D48-55-50-05.*



## PHOTONEUTRON CROSS SECTION OF $\text{Ni}^{58}$ <sup>1</sup>

J. P. ROALSVIG, R. N. H. HASLAM, AND D. J. MCKENZIE

### ABSTRACT

The reaction  $\text{Ni}^{58}(\gamma, n)\text{Ni}^{57}$  has been investigated between 12- and 24-Mev maximum photon energy. The absolute yield value at 22 Mev was found to be much lower than reported previously. Also, a shorter half-life of  $\text{Ni}^{57}$  was obtained. The cross section was determined using two different methods.

### 1. RELATIVE ACTIVATION CURVE

The activation curve and the cross-section curve for the reaction  $\text{Ni}^{58}(\gamma, n)\text{Ni}^{57}$  have been determined from threshold (12.0 Mev) up to 24.0 Mev. Nickel disks with diameter 2.5 cm and thickness 0.15 mm were irradiated in the center of the X-ray beam from the University of Saskatchewan 24-Mev betatron at a fixed distance from the target. The disks were irradiated at different maximum betatron energies, the irradiation procedure being the same for all disks.

In order to obtain a relative yield curve, no correction for the finite irradiation time was necessary. However, the relative dose given to each disk was measured by a monitor in connection with an  $R$ - $C$  circuit whose time constant was equal to the mean life of  $\text{Ni}^{57}$ . Also the relative number of roentgens per dose was measured for different energies to find the relative number of roentgens given to each disk. This ratio changes slightly with the energy.

The secondary activity from  $\text{Ni}^{57}$  was followed for several days in a proportional flow counter. The disks were mounted on aluminum of sufficient thickness to obtain saturated backscattering. Since all disks were of the same thickness, no correction for self-absorption and backscattering was necessary in determining a relative activation curve.

The activity in counts/minute,  $N_0$ , at the end of the irradiation was obtained from the decay curve of each sample. After the short-period activities (due largely to  $\text{Ni}^{62}(\gamma, p)\text{Co}^{61}$ ) had disappeared, in about 24 hours, the least squares method was used to obtain the best-fitting straight line relating  $\ln N$  and  $t$ . The  $N_0$  was divided by the dose given to the sample and by the weight of the sample to give a point on the relative activation curve.

The somewhat high yield value at 24-Mev maximum photon energy (see Fig. 2) could be explained by the onset of the reaction  $\text{Ni}^{58}(\gamma, 2n)\text{Ni}^{56}$  with threshold 23.2 Mev and a half-life of 6.4 days. However, the slopes of the decay curves of samples exposed at this energy did not yield any higher half-life than the others; nor did the points show any departure from a straight line even after 120 hours.

Also the half-life of  $\text{Ni}^{57}$  was obtained by this method. It was found to be  $34.1 \pm 1.4$  hours, which is slightly lower than the values reported previously

<sup>1</sup>Manuscript received February 16, 1959.

Contribution from the Physics Department, University of Saskatchewan, Saskatoon, Saskatchewan, Canada.

by Maienschein and Meem (1949), Friedlander *et al.* (1950), and Rudstam (1956). Their values were  $35.7 \pm 1$  hours,  $36.4 \pm 1$  hours, and 37.6 hours respectively.

## 2. ABSOLUTE YIELD VALUE AT 22 MEV

The absolute value of the activation curve was determined at 22-Mev maximum bremsstrahlung. Nickel disks, with the same diameter as before but with thicknesses ranging from 10 to several hundred milligrams per square centimeter were irradiated 54.7 cm from the target, the betatron being operated at a maximum energy of 22 Mev. Recent investigations have shown that the energy stability is very good, so that deviations from 22 Mev were assumed to be less than 20 kev.

A slightly different irradiation procedure was followed: The disks were irradiated for a time,  $t_R$ , and the counting rates were corrected for finite irradiation time by multiplying by the factor  $t_R(1 - e^{-\lambda t_R})^{-1}$ . The relative dose given to the sample was recorded by a monitor connected to a condenser and was given in arbitrary units (see Johns *et al.* (1950)). The disks were counted in a flow counter as before and the counting rates at zero time obtained. These were corrected for self-absorption in the samples, backscattering, absorption of the backscattered  $\beta$ -particles, and geometry of the counter by using a method outlined in another paper (Roalsvig and Haslam 1959).

The corrected number of counts were divided by the dose and by the number of moles\* of  $Ni^{58}$  in the disks to give saturated activity per mole per unit dose.

The peaking effect of the X-ray beam, that is the distribution of intensity as a function of angular distance from the beam axis at the position of the disks, was measured by two different methods: (a) Small copper squares, 1 cm  $\times$  1 cm  $\times$  0.5 mm, were irradiated at the same time at different distances from the center of the beam. They were counted in the flow counter, and the relative counting rates at a fixed time were obtained. (b) A copper disk, 5 cm in diameter and 1 mm thick, was irradiated with its center at the center of the beam. It was then placed on a X-ray film for 1 hour. The film was developed and measured by a microphotometer. The relative intensity distributions  $F(r)$  found by these two methods were in agreement.  $F(r)$  is shown in Fig. 1, by the curve marked "position I". The "effective area" of the disks, defined as  $\int_{r=0}^{r=1.25 \text{ cm}} F(r) 2\pi r dr$ , was calculated, and the ratio of the true area to the "effective area" was found to be 1.104.

The number of roentgens per arbitrary dose unit was obtained by using a "Farmer Sub-Standard Dosimeter", manufactured by the Baldwin Instrument Company, referred to as a Baldwin-Farmer r-meter. The instrument has been calibrated for  $Co^{60}$  radiation, the calibration factor being 1.08. This same factor was applied to obtain the dose in roentgens of the high-energy bremsstrahlung used in the present experiment. The thimble chamber of the Baldwin-Farmer r-meter was placed in the center of a lucite block, 8  $\times$  8  $\times$  8 (cm), and given a dose corresponding to a certain number of arbitrary units.

\*By definition: 1 mole = 1 gram atom.

This was done several times at different distances from the betatron target. A  $1/D^2$  dependence was obtained for the roentgens per unit dose, where  $D$  is the distance from the target to the center of the thimble chamber. The

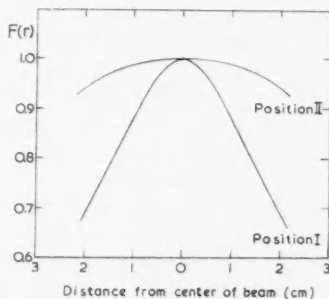


FIG. 1. Spread of the relative intensity of the X-ray beam from its center at two different distances from the target. Position I: 54.7 cm; position II: 182.0 cm.

number of roentgens per unit dose at the position where the nickel disks were irradiated was obtained from this relationship. These values were corrected for differences in pressure and temperature from the values (76 cm Hg and  $22^\circ\text{C}$ ) at which the instrument was calibrated.

Since the Baldwin-Farmer r-meter, however, is placed inside a lucite block, the nickel disks should theoretically also be placed in the center of the lucite block (see Johns *et al.* 1950; Katz and Cameron 1951). This introduces a correction factor,

$$\frac{\int_{\text{threshold}}^{22 \text{ Mev}} \sigma_E(\gamma, n) P(E, 22 \text{ Mev}) e^{\mu(E)x} dE}{\int_{\text{threshold}}^{22 \text{ Mev}} \sigma_E(\gamma, n) P(E, 22 \text{ Mev}) dE},$$

where  $\sigma_E(\gamma, n)$  is the cross section at the energy  $E$  for the reaction  $\text{Ni}^{58}(\gamma, n)\text{Ni}^{57}$ . Since only ratios are involved, relative values can be used.  $P(E, 22 \text{ Mev})$  is the number of photons per  $\text{cm}^2$  per 100 r with energy between  $E+1/2dE$  and  $E-1/2dE$ , when the maximum photon energy is 22 Mev. These values were taken from Katz and Cameron (1951).  $\mu(E)$  is the X-ray attenuation coefficient in the lucite of X rays with energy  $E$ . Lucite was taken as  $\text{C}_5\text{O}_2\text{H}_8$  (i.e. 8% H, 60% C, and 32% O). The values of  $\mu(E)$  were taken from Grodstein (1957);  $x$  is the thickness of 4 cm of lucite ( $4.13 \text{ g/cm}^3$ ). The integrations have to be carried through from threshold to 22 Mev. The correction factor was calculated to be 1.074.

The absolute value obtained in this way is  $3.17 \times 10^7 \text{ n/100 r mole}$ . However, this value has to be corrected due to electron capture. It was found by Friedlander *et al.* (1950) and recently confirmed by Konijn *et al.* (1956, 1958) that the ratio of the probability of electron capture to positron emission in  $\text{Ni}^{57}$  is

very nearly unity. The absolute activation value at 22 Mev is therefore  $0.63 \times 10^8$  n/100 r mole. The absolute activation curve normalized to this value is given in Fig. 2.

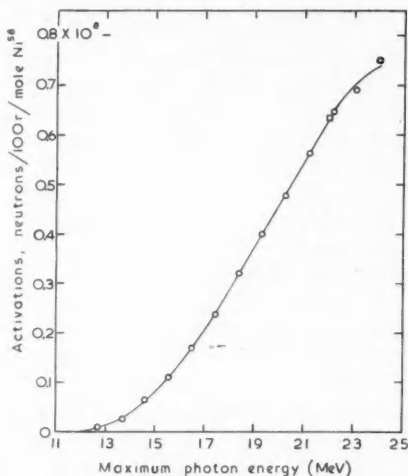


FIG. 2. Activation values for the reaction  $\text{Ni}^{58}(\gamma, n)\text{Ni}^{57}$  as a function of maximum photon energy.

### 3. COMPARISON OF ABSOLUTE YIELD VALUES

The absolute yield value was first measured by Price and Kerst (1950) for the natural element of nickel to be  $1.04 \times 10^8$  n/100 r mole at 22 Mev. Katz *et al.* (1951) obtained the value  $1.12 \times 10^8$  n/100 r mole for the reaction  $\text{Ni}^{58}(\gamma, n)\text{Ni}^{57}$  alone, also at 22 Mev. This value is much higher than the present one. Skarsgard (1955) measured the ratio of the yield of  $\text{Cu}^{63}(\gamma, n)\text{Cu}^{62}$  to the yield of  $\text{Ni}^{58}(\gamma, n)\text{Ni}^{57}$  at 23 Mev to be 3.4.

In order to compare this ratio with the present work, the absolute yield of the reaction  $\text{Cu}^{63}(\gamma, n)\text{Cu}^{62}$  at 22 Mev was redetermined, using the same method as for nickel. The correction factor for the absorption in the lucite block is essentially the same, being 1.075 for this reaction. Also, the copper disks were irradiated at two distances from the target: (I) 54.7 cm as for nickel, and (II) 182.0 cm. The peaking effect was also measured in the second position and is given in Fig. 1 (curve marked "position II"). The correction factor was 1.007 in this position. After these corrections were applied, the two saturated activities showed a  $1/D^2$  attenuation to within 0.4%, where  $D$  is the distance from the target to the disk. The absolute yield value obtained was  $2.25 \times 10^8$  n/mole 100 r, which is somewhat lower than the value  $2.51 \times 10^8$  n/mole 100 r used previously in this laboratory (Katz and Cameron 1951).

The activation curve of the reaction  $\text{Cu}^{63}(\gamma, n)\text{Cu}^{62}$  was also remeasured from 20 to 23 Mev. Excellent agreement was found with the older curve of Johns *et al.* (1950) when the latter was normalized to the present value at 22 Mev.

The half-life of  $\text{Cu}^{62}$  which was obtained from our experiment was (9.72

$\pm 0.03$ ) minutes. This value agrees well with the value of Berman and Brown (1954),  $(9.73 \pm 0.02)$  minutes, but is lower than the value 9.9 minutes as given by the General Electric Chart of the Nuclides 1956.

The ratio of the yield of  $\text{Cu}^{63}(\gamma, n)\text{Cu}^{62}$  to the yield of  $\text{Ni}^{58}(\gamma, n)\text{Ni}^{57}$  was calculated to be 3.5 at 22 Mev, and 3.4 at 23 Mev, in excellent agreement with Skarsgard. Titterton (1958a) has also measured this ratio at 30 Mev to be 3.3. Since the cross-section curve of  $\text{Cu}^{63}(\gamma, n)\text{Cu}^{62}$  has its maximum at a lower energy than that of  $\text{Ni}^{58}(\gamma, n)\text{Ni}^{57}$ , a lower value of the yield ratio is expected at higher energy. Titterton's result is thus in better agreement with the present value of the ratio than with the old one of Katz *et al.* (2.2 at 22 Mev).

The difference between the present activation value and that previously reported from this laboratory may be due to several factors. The calibration of the betatron energy scale is more reliable than it was at the time of the earlier investigation (1951). Longer irradiations and the use of improved counting methods have made better counting statistics possible. The decay curves were also followed for longer times to make sure that short-period activities had died out. It seems probable that some contribution from the  $(\gamma, p)$  reaction in  $\text{Ni}^{62}$  might have been included in the earlier work with a consequent increase in the observed yield. Perhaps the most important factor is an improved knowledge of the corrections to be applied for self-absorption and backscattering.

#### 4. CROSS SECTION

Two different methods were used in calculating the cross-section curve. These were:

- (a) the "photon difference method" of Katz and Cameron (1951), and
- (b) the "modified spectrum method" of Penfold and Leiss (1958).

The two curves are given on Fig. 3 and the characteristic values in Table I.

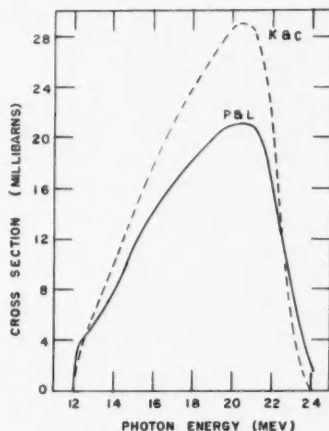


FIG. 3. Cross-section curves for the reaction  $\text{Ni}^{58}(\gamma, n)\text{Ni}^{57}$  as a function of photon energy. Curve marked K and C: photon difference method; curve marked P and L: modified spectrum method.

The general shapes of the two cross-section curves are the same. They both have their maxima at 20.5 Mev, and their half widths are nearly the same. However, the absolute value of  $\sigma_{\max}$  by using the "photon difference method" is about 40% higher than the value obtained by the "modified spectrum method".

TABLE I  
Yield and cross-section data for the reaction  $\text{Ni}^{58}(\gamma, n)\text{Ni}^{57}$

References	Yield at 22 Mev, n/100 r mole	Ratio of yields, $\{\text{Cu}^{63}(\gamma, n)\text{Cu}^{62}\} /$ $\{\text{Ni}^{58}(\gamma, n)\text{Ni}^{57}\}$	$E_m$ , Mev	$\sigma_m$ , mb	$\Gamma_{1/2}$ , Mev	$\int_0^{21 \text{ Mev}} \sigma(\gamma, n) dE$ , Mev-barn
Price and Kerst (1950)	$1.04 \times 10^{8a}$					
Katz <i>et al.</i> (1951)	$1.12 \times 10^8$	2.2 at 22 Mev	18.5	60	4.6	0.33
Katz and Cameron (1951)			18.5	54	5.6	0.34
Katz and Cameron renormalized	$(0.63 \times 10^8)$		18.5	30	5.6	0.18
Skarsgard (1955)		3.4 at 23 Mev				
Titterton (1958a)		3.3 at 30 Mev				
Titterton (1958b)			19.0	32	4.4	0.22 (to 32 Mev)
Present work	$0.63 \times 10^8$	3.5 at 22 Mev	20.5 <sup>b</sup>	29	7.2	0.20
			20.5 <sup>c</sup>	21	8.0	0.16

<sup>a</sup>For natural element.

<sup>b</sup>Katz and Cameron's method.

<sup>c</sup>Penfold and Leiss' method.

A comparison between the present work and that of Katz and Cameron (1951), and of Titterton (1958b), is presented in Table I. This indicates that the cross-section curve in this work is much flatter and has a lower maximum value. Also, this maximum value is found at a higher energy than reported previously. However, good agreement is found for the integrated cross sections.

#### ACKNOWLEDGMENTS

The authors wish to thank Professor L. Katz and Professor D. V. Cormack for valuable discussions; they are indebted to the latter for the loan of Baldwin-Farmer r-meter belonging to the Cancer Clinic at the University Hospital, Saskatoon. We should also like to thank Dr. E. W. Titterton and Dr. Turchinets of the Australian National University, for making their results accessible before publication.

#### REFERENCES

- BERMAN, A. I. and BROWN, K. L. 1954. Phys. Rev. **96**, 83.  
 FRIEDLANDER, G., PERLMAN, M. L., ALBURGER, D., and SUNYAR, A. W. 1950. Phys. Rev. **80**, 30.  
 GRODSTEIN, G. W. 1957. X-ray attenuation coefficients, N.B.S. Circular 583 (U.S. Government Printing Office, Washington, D.C., U.S.A.).  
 JOHNS, H. E., KATZ, L., DOUGLAS, R. A., and HASLAM, R. N. H. 1950. Phys. Rev. **80**, 1062.  
 KATZ, L. and CAMERON, A. G. W. 1951. Can. J. Phys. **29**, 518.  
 KATZ, L., JOHNS, H. E., BAKER, R. G., HASLAM, R. N. H., and DOUGLAS, R. A. 1951. Phys. Rev. **82**, 271.

- KONIJN, F., VAN NOOIJEN, B., MOSTERT, P., and ENDT, P. M. 1956. *Physica*, **22**, 887.  
KONIJN, F., HAGEDORN, H. L., and VAN NOOIJEN, B. 1958. *Physica*, **24**, 129.  
MAIENSCHIN, F. and MEEM, J. L., JR. 1949. *Phys. Rev.* **76**, 899.  
PENFOLD, A. S. and LEISS, J. E. 1958. Analysis of photo cross sections (Physics Research Laboratory, University of Illinois).  
PRICE, G. A. and KERST, D. W. 1950. *Phys. Rev.* **77**, 806.  
ROALSVIG, J. P. and HASLAM, R. N. H. 1959. *Can. J. Phys.* **37**, 499.  
RUDSTAM, G. 1956. Thesis, University of Uppsala, Uppsala, Sweden.  
SKARSGARD, L. D. 1955. Thesis, University of Saskatchewan, Saskatoon, Sask.  
TITTERTON, E. W. 1958a. Conference on Photonuclear Reactions, Washington, D.C., paper A1.  
——— 1958b. Private communication.

# STUDY OF PHASE PROPAGATION IN SUPERCONDUCTING ALUMINUM BY ULTRASONIC ATTENUATION MEASUREMENTS<sup>1</sup>

K. L. CHOPRA AND T. S. HUTCHISON

## ABSTRACT

The phase propagation in superconducting aluminum has been studied by measuring the time rate of change of ultrasonic attenuation. The time taken for the destruction of the superconducting phase in a cylindrical specimen, by means of a magnetic field,  $H$ , greater than the critical field,  $H_c$ , is approximately proportional to  $\{H/(H-H_c)\}$  in agreement with eddy-current theory. In the converse case, where the superconducting phase is restored by switching off the magnetic field  $H$  ( $>H_c$ ), the total time taken is nearly independent of the temperature (or  $H_c$ ) as well as  $H$ . The superconducting phase grows at a non-uniform volume rate which is considerably less than the uniform rate of collapse.

## INTRODUCTION

It is now well known (Bömmel 1954; MacKinnon 1955, 1957; Mason and Bömmel 1956; Morse, Tamarkin, and Bohm 1956; Chopra and Hutchison 1958) that when a metal specimen undergoes a transition from normal to superconducting phase the high-frequency ultrasonic attenuation decreases rapidly. This is shown for polycrystalline aluminum in Fig. 1, which is reproduced from our previous paper (Chopra and Hutchison 1958) where the temperature measurements below 1° K were in error and have been corrected. Thus the change in ultrasonic attenuation provides another tool to detect

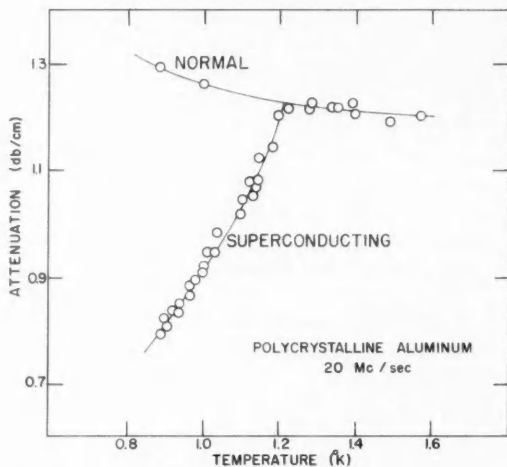


FIG. 1. Ultrasonic attenuation vs. temperature in polycrystalline aluminum.

<sup>1</sup>Manuscript received February 4, 1959.

Contribution from the Department of Physics, Royal Military College of Canada, Kingston, Ontario, Canada.



the superconducting transition. Rates of growth of a phase following a magnetically induced transition are readily followed. It is clear that this method gives a measure of the volume rate of growth of the new phase in a localized region determined by the path of the sound beam in the specimen.

Faber (1952, 1953, 1954) has studied thoroughly the nucleation process which initiates the phase transition and the subsequent growth of the phase in the case of tin. We shall be concerned here with the latter aspect of the phase transition, namely the propagation of the phase. According to the theory of Pippard (1950) and Lifshitz (1950), the rate at which the superconducting phase collapses radially in cylindrical specimens is controlled by an electromagnetic damping associated with the eddy currents. The latter are generated due to the displacement of magnetic lines of force through the normal phase during the movement of the interphase boundary. If the cylindrical core of the superconducting phase is contracting radially and symmetrically in a long rod of radius,  $r$ , under the influence of an external longitudinal field  $H$  ( $> H_c$ ), the time it takes to collapse completely is proportional to  $\sigma r^2 \{H/(H - H_c)\}$  where  $\sigma$  is the effective electrical conductivity of the normal phase. Faber (1953) has checked this result for various tin specimens.

In the converse case, when the superconducting phase is allowed to expand radially, the process is expected to be asymmetrical and the above-mentioned eddy-current theory not valid. Faber has explained this on the basis of the general principle that the closer the boundary is to the outside surface of a specimen, the less difficulty it experiences in displacing flux through the intervening normal phase. Thus the boundary moving inwards will be quite stable while the outward-moving boundary will be composed of a tortuous arrangement of radially expanding superconducting filaments.

This paper presents results on the average volume rate of growth of the superconducting or normal phase in cylindrical specimens of polycrystalline aluminum. Results on a single crystal of different geometry are also mentioned.

#### EXPERIMENTAL DETAILS

Measurements of ultrasonic attenuation are made by the conventional pulse technique. A pulse of 20 Mc/sec longitudinal waves is axially applied to one end of the cylindrical specimen by a  $\frac{1}{2}$ -in. quartz crystal which is also used to receive the reflected pulses. After amplification, the pulse and its echoes are displayed on an oscilloscope and photographed with a 16-mm Cine Kodak Special Movie Camera. The rate of change of the logarithm of the amplitude of one of the decaying echo pulses. A pair of Helmholtz coils (diameter, 12 inches) around the liquid air Dewar provides a variable magnetic field. Temperatures down to 0.88° K are obtained in a booster cryostat (Atkins *et al.* 1955).

The polycrystalline cylindrical specimens are prepared from aluminum of 99.99% purity. They are recrystallized from the cold-rolled condition by annealing at 500° C for 5 hours. This process gives a grain size of  $\sim 3$  mm.

The single crystal specimen is obtained from aluminum of similar purity and is of cubical shape with side 20 mm.

### RESULTS

Two simple cases have been studied. In the first case, the attenuation is measured as a function of time when the superconducting phase of the cylindrical specimen collapses radially under the influence of an applied magnetic field  $H$  ( $>H_c$ ). In the second case the time rate of change of attenuation is measured when the superconductivity of the cylindrical specimen is restored by removing the applied magnetic field  $H$  ( $>H_c$ ).

Figure 2 shows a plot of attenuation coefficient against time for a polycrystalline cylindrical specimen of diameter 20 mm and length 40 mm. The initial time taken for the attenuation to show any change is the time taken for the collapsing process to reach the region traversed by the  $\frac{1}{2}$ -in. cylindrical

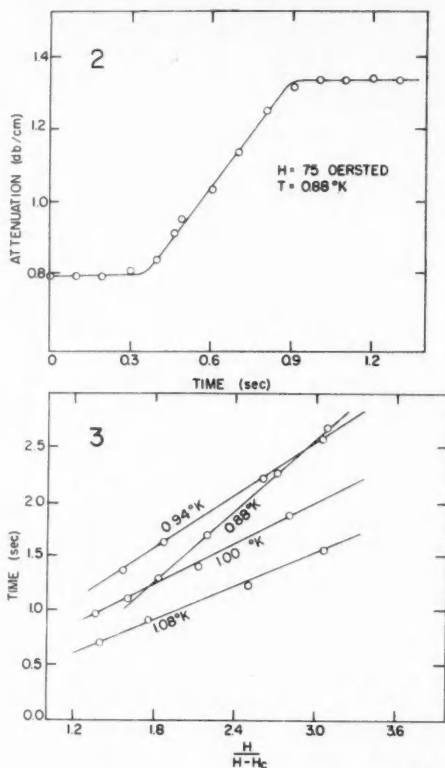


FIG. 2. Ultrasonic attenuation coefficient as a function of time for radially collapsing superconducting phase.

FIG. 3. Total time taken for collapsing of superconducting phase as a function of  $\{H/(H-H_c)\}$ .

sound beam. The linearity of the graph indicates that the gross rate of change of superconducting volume in the  $\frac{1}{2}$ -in. cylinder is constant and that the process is symmetrical. Similar volume rates are obtained with the single crystal which is probably due to the poorer geometry.

The total time taken for the collapse of the superconducting phase is measured as a function of the temperature and applied magnetic field. Figure 3 shows a plot of time against  $\{H/(H-H_c)\}$ . The straight-line relations verify the validity of the eddy-current theory. Marked departures from this relation occur for  $H$  close to  $H_c$ . The dependence of the slopes of the straight lines on temperature indicates that the electrical conductivity  $\sigma$  is a function of temperature.

It is clear that the average volume rate of propagation of the superconducting phase in the above case is a function of both temperature (or  $H_c$ ) and the magnetic field  $H$ . At  $T = 0.88^\circ \text{K}$  and  $H = 97$  oersted, the rate is  $5 \text{ cm}^3/\text{sec}$ .

In the converse case, a plot of attenuation coefficient against time for the same specimen is shown in Fig. 4. The non-linear curve indicates that, as expected, the growth of the superconducting phase is not symmetrical. More-

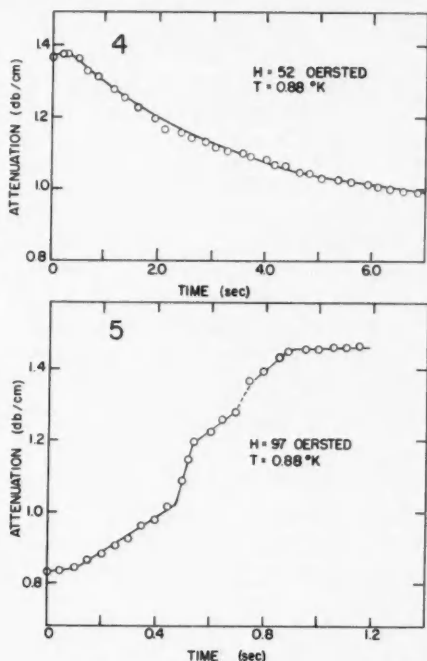


FIG. 4. Ultrasonic attenuation coefficient as a function of time for the growth of superconducting phase.

FIG. 5. Ultrasonic attenuation coefficient as a function of time for radial collapse by steps of superconducting phase.

over, the total time taken for the restoration of the superconducting phase is nearly independent of temperature (or  $H_c$ ) as well as applied magnetic field  $H$ . The average rate of propagation is about  $0.5 \text{ cm}^3/\text{sec}$ . The single crystal gives similar rates—this probably being due to the poorer geometry in the single crystal than in the polycrystalline cylinder.

It should be mentioned that in thicker specimens (for example, one with diameter 30 mm and length 40 mm) the plot of attenuation coefficient against time shows steps as shown in Fig. 5. This seems to indicate the movement of domains at different rates.

### CONCLUSIONS

Measurements of ultrasonic attenuation have been successfully utilized to study the gross rate of propagation of the superconducting or normal phase. The radial collapse of the superconducting phase has been found to be symmetrical and to obey eddy-current theory.

In the converse case, when superconductivity is allowed to expand radially, the process is found to be asymmetrical. In fact, the rate being independent of temperature as well as magnetic field, the transition process appears to be quite devious.

### ACKNOWLEDGMENTS

This work was supported by the Defence Research Board of Canada, Grant No. 7510-14, Project No. D44-75-10-14, whose assistance is gratefully acknowledged.

### REFERENCES

- ATKINS, K. R., EDWARDS, M. H., and PULLAN, G. T. 1955. *Rev. Sci. Instr.* **26**, 49.  
BÖMMEL, H. E. 1954. *Phys. Rev.* **96**, 200.  
CHOPRA, K. L. and HUTCHISON, T. S. 1958. *Can. J. Phys.* **36**, 805.  
FABER, T. E. 1952. *Proc. Roy. Soc. A*, **214**, 392.  
——— 1953. *Proc. Roy. Soc. A*, **219**, 75.  
——— 1954. *Proc. Roy. Soc. A*, **223**, 147.  
LIFSHITZ, E. M. 1950. *J. Exptl. Theoret. Phys. U.S.S.R.* **9**, 834.  
MACKINNON, L. 1955. *Phys. Rev.* **100**, 955.  
——— 1957. *Phys. Rev.* **106**, 70.  
MASON, W. P. and BÖMMEL, H. E. 1956. *J. Acoust. Soc. Am.* **28**, 930.  
MORSE, R. W., TAMARKIN, P., and BOHM, H. V. 1956. *Phys. Rev.* **101**, 1610.  
PIPPARD, A. B. 1950. *Phil. Mag.* **41**, 243.

## ON TOROIDAL FUNCTIONS<sup>1</sup>

S. C. LOH<sup>2</sup>

### ABSTRACT

The general solutions of Laplace's equation in toroidal co-ordinates have been derived, both for the three-dimensional and the axial symmetrical cases. Also, the general theory and properties of toroidal functions have been briefly outlined.

The numerical tables for the zonal and the tesseral toroidal functions were calculated by the I.B.M. 650 Computer at the University of Toronto, and are included in the present paper.

### INTRODUCTION

Toroidal functions, which arise when Laplace's equation is separated in toroidal co-ordinates and are suitable for problems in which the boundary conditions are given over the surfaces of anchor rings, were first investigated by Neumann (1864), Hicks (1881, 1884), Basset (1893), Niven (1892), and others. Although Relton (1931, 1933) and Fock (1932) emphasized the desirability of tabulating the toroidal functions which are essentially the Legendre functions of half odd integral order, and also suggested that the tabulation of the functions should be through the hypergeometric functions, in terms of which they may be expressed, the author has only been able to trace one numerical table of the zonal toroidal functions, namely that published by Fouquet (1937), apart from the numerical table calculated by Carter and the author (1958).

Although toroidal functions were studied many years ago, the lack of numerical tables greatly limited their application to physical problems. There are, however, a number of physical problems where toroidal functions may be found useful, such as the potential of a ring, the electric potential of a tore and its capacity, the velocity potential for a tore moving parallel to its axis, as well as the energy of the motion, and the self-inductance of a tore.

In the present paper, a brief discussion of the general theory of toroidal functions is presented and a complete set of numerical tables for zonal toroidal functions and tesseral toroidal functions has been computed and included. In addition, expressions for the approximate values of  $p_n(u)$  and  $q_n(u)$  are also derived.

### TOROIDAL CO-ORDINATES

Toroidal co-ordinates are a natural co-ordinate system to describe a ring. The relationship between the toroidal co-ordinates ( $u, v, w$ ) and the Cartesian co-ordinates ( $x, y, z$ ) is given by

<sup>1</sup>Manuscript received February 3, 1959.

Contribution from the Radio and Electrical Engineering Division, National Research Council, Ottawa, Canada.

Issued as N.R.C. No. 5171.

<sup>2</sup>National Research Council Postdoctorate Fellow.

$$(1) \quad \begin{cases} x = \frac{a \sinh u \cos w}{\cosh u - \cos v}, \\ y = \frac{a \sinh u \sin w}{\cosh u - \cos v}, \\ z = \frac{a \sin v}{\cosh u - \cos v}, \end{cases}$$

where  $0 \leq u < \infty$ ,  $0 \leq v < 2\pi$ , and  $0 \leq w < 2\pi$ . The surface  $u = u_0$  is an anchor ring with axial circle in the  $x$ - $y$  plane, centered at the origin, of radius  $a \coth u_0$ , having a circular cross section of radius  $a \operatorname{csch} u_0$ . The surface  $v = v_0$  (for  $v_0 < \pi$ ) is that part of the sphere of radius  $a \csc v_0$ , with center at  $x = y = 0$ ,  $z = a \cot v_0$ , which is above the  $x$ - $y$  plane, and the rest of the same sphere below the  $x$ - $y$  plane, is the surface  $v = 2\pi - v_0$  (see Fig. 1). The limiting tore  $u = \infty$  is an infinitely thin ring of radius  $a$ . It is evident that the value of  $a$  can be so chosen that any given anchor ring will be included in the system.

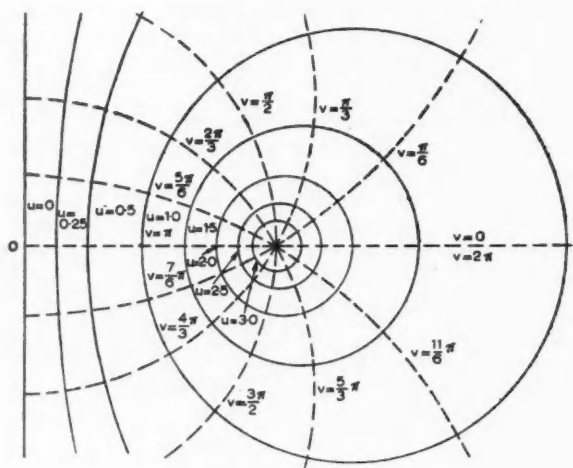


FIG. 1. Toroidal co-ordinates.

For the element of length  $ds$  we have in the new co-ordinates  $u, v, w$ ,

$$(2) \quad (ds)^2 = (h_u du)^2 + (h_v dv)^2 + (h_w dw)^2$$

which is easily found to reduce to

$$(3) \quad (ds)^2 = \frac{a^2}{(\cosh u - \cos v)^2} \{ (du)^2 + (dv)^2 + \sinh^2 u (dw)^2 \}.$$

Expressed in terms of the toroidal co-ordinates, Laplace's equation becomes

$$(4) \quad \frac{\partial}{\partial u} \left( \frac{\sinh u}{\cosh u - \cos v} \frac{\partial \phi}{\partial u} \right) + \frac{\partial}{\partial v} \left( \frac{\sinh u}{\cosh u - \cos v} \frac{\partial \phi}{\partial v} \right) + \frac{1}{(\cosh u - \cos v) \sinh u} \frac{\partial^2 \phi}{\partial w^2} = 0.$$

## TESSERAL TOROIDAL FUNCTIONS

In order to reduce equation (4) to a form for which integrals can be obtained, let  $\phi = \psi \sqrt{(\cosh u - \cos v)}$ ; Laplace's equation then becomes

$$(5) \quad \frac{\partial^2 \psi}{\partial u^2} + \frac{\partial^2 \psi}{\partial v^2} + \frac{1}{\sinh^2 u} \frac{\partial^2 \psi}{\partial w^2} + \coth u \frac{\partial \psi}{\partial u} + \frac{1}{4} \psi = 0.$$

Let us endeavor to satisfy the equation by means of a function  $\psi = U \cdot V \cdot W$ , where  $U$  is a function of  $u$  only,  $V$  of  $v$  only, and  $W$  of  $w$  only; substituting in the differential equation and dividing throughout by  $U \cdot V \cdot W$ , we have

$$(6) \quad \frac{1}{U} \left( \frac{d^2 U}{du^2} + \coth u \frac{dU}{du} + \frac{1}{4} U \right) + \frac{1}{V} \frac{d^2 V}{dv^2} + \frac{1}{W} \frac{1}{\sinh^2 u} \frac{d^2 W}{dw^2} = 0.$$

In this equation the first term involves  $u$  only, the second  $v$  only, and the third  $w$  only; it is consequently obvious that the only case in which it can be satisfied is when each term is equal to a constant, the sum of the three constants being equal to zero. We thus obtain three ordinary differential equations

$$(7) \quad \frac{d^2 W}{dw^2} + m^2 W = 0,$$

$$(8) \quad \frac{d^2 V}{dv^2} + n^2 V = 0,$$

and

$$(9) \quad \frac{d^2 U}{du^2} + \coth u \frac{dU}{du} - \left( n^2 - \frac{1}{4} + \frac{m^2}{\sinh^2 u} \right) U = 0.$$

The independent solution of the equation (7) is

$$(10) \quad W = a_m \cos mw + b_m \sin mw$$

where  $a_m$  and  $b_m$  are arbitrary constants.

Similarly, the solution of the equation (8) is

$$(11) \quad V = c_n \cos nv + d_n \sin nv$$

where  $c_n$  and  $d_n$  are arbitrary constants.

In the theory of toroidal functions,  $n$  is any positive integer, and  $m$  is any positive integer which is not greater than  $n$ , the value zero being included.

The differential equation (9) is satisfied by

$$(12) \quad \begin{aligned} p_n^m(u) &= \frac{1}{\pi} \frac{(-1)^m \Gamma(n + \frac{1}{2})}{\Gamma(n - m + \frac{1}{2})} \int_0^\pi \frac{\cos m\theta d\theta}{(\cosh u + \sinh u \cos \theta)^{n+1}} \\ q_n^m(u) &= \frac{(-1)^m \Gamma(n + \frac{1}{2})}{\Gamma(n - m + \frac{1}{2})} \int_0^\pi \frac{\cosh m\theta d\theta}{(\cosh u + \sinh u \cosh \theta)^{n+1}} \end{aligned}$$

where  $p_n^m(u)$  and  $q_n^m(u)$  are known as "tesseral or associated toroidal functions" of first and second kinds of degree  $n$  and order  $m$ .

Using equation (12) the following tables (I and II) of values for both kinds up to the fourth order have been worked out by the I.B.M. 650 Computer at the University of Toronto. The numbers in parentheses in the tables indicate the power of 10 by which tabulated values are to be multiplied, i.e.,  $p_2^2(1.0) = 0.95216$ .

TABLE I  
Tesseral toroidal functions of the first kind

$m$	$\rho^1(u)$	$\rho^2_1(u)$	$\rho^2_2(u)$	$\rho^2_3(u)$	$\rho^2_4(u)$	$\rho^2_5(u)$	$\rho^3_1(u)$	$\rho^3_2(u)$	$\rho^3_3(u)$	$\rho^3_4(u)$	$\rho^3_5(u)$	$\rho^4(u)$		
0.0	0	0	0	0	0	0	0	0	0	0	0	0		
0.1	(-2)	3.7505	(-1)	4.4104	(-3)	8.1683	(-2)	7.4162	(-1)	2.7366	(-3)	6.7444		
0.2	7.5032	(-1)	3.8081	0	9.1081	(-2)	3.3001	(-1)	3.0200	(0)*	1.1332	(-2)	3.6909	
0.3	1.1261	5.8221	5.8221	(0)*	1.4353	2.7857	7.4809	(-1)	6.9874	2.6972	(0)*	1.2682	(-1)	1.7705
0.4	1.9707	2.0474	4.1963	(-1)	1.3436	(0)*	1.2911	8.9199	2.2719	3.1626	(0)*	5.6420	(-1)	1.7705
0.5	1.8803	(0)*	1.0304	2.7849	6.0943	2.1274	8.9199	2.2719	3.1626	6.5873	(0)*	5.6420	(-1)	1.7705
0.6	2.9504	1.9874	3.6933	8.7054	3.1138	3.3770	(1)	1.4419	8.1360	1.2902	(0)*	5.6420	(-1)	1.7705
0.7	2.6405	1.5741	4.8287	(1)	7.2342	4.3218	3.7218	2.3410	(0)*	2.3324	2.3324	3.1466	(0)	3.1466
0.8	3.0240	1.8971	5.7145	1.7444	5.7718	6.0687	3.3944	2.0068	3.1412	5.6480	(1)	1.9524	(1)	1.9524
0.9	3.4106	2.2635	8.0819	2.4028	7.4941	9.2065	5.0526	3.1412	4.5609	8.7836	3.2439	5.2203	(2)	5.2203
1.0	3.8009	2.6819	1.0402	3.4769	9.5216	(1)	1.2501	7.4301	6.4639	2.0119	(2)	1.9137	(2)	1.9137
1.1	4.1957	3.1616	1.3368	4.9105	1.6765	2.9383	3.2516	4.6600	2.2331	4.3956	2.8657	4.2487	(3)	4.2487
1.2	4.5902	3.5024	1.6365	6.3817	2.9383	3.8547	3.2516	4.6600	2.2331	4.3956	2.8657	4.2487	(3)	4.2487
1.3	4.9846	3.8969	1.9372	7.8578	4.2520	4.8546	6.6649	2.9684	3.9232	5.7301	2.7673	3.9782	(4)	3.9782
1.4	5.3783	4.2916	2.2380	9.3411	5.5777	8.5099	9.5172	6.7190	4.8026	6.8269	4.8177	6.8269	(4)	6.8269
1.5	5.7719	4.6861	2.5387	10.8292	6.8370	1.8416	2.7533	8.8026	4.0048	7.9036	8.1073	7.9036	(4)	7.9036
1.6	6.1658	5.0800	2.8394	12.3163	8.1622	3.0962	3.9174	(2)	1.1449	5.7301	2.7673	5.7301	(4)	5.7301
1.7	6.5596	5.4736	3.1404	13.8034	9.5010	7.0859	3.0726	1.4855	3.3752	6.8269	4.8177	6.8269	(4)	6.8269
1.8	6.9533	5.8672	3.4413	15.2905	10.8407	8.3021	3.0726	1.4855	3.3752	7.9036	8.1073	7.9036	(4)	7.9036
1.9	7.3470	6.2608	3.7422	16.7776	12.2800	9.5216	3.0726	1.4855	3.3752	8.9806	9.2886	8.9806	(4)	8.9806
2.0	7.7407	6.6545	4.0431	18.2647	13.7671	10.7578	3.0726	1.4855	3.3752	10.0596	10.4694	10.0596	(4)	10.0596
2.1	8.1344	7.0482	4.3440	19.7518	15.2542	12.0000	3.0726	1.4855	3.3752	11.1386	11.6502	11.1386	(4)	11.1386
2.2	8.5281	7.4419	4.6449	21.2389	16.7413	13.2427	3.0726	1.4855	3.3752	12.2176	12.8310	12.2176	(4)	12.2176
2.3	8.9218	7.8356	4.9458	22.7260	18.2284	14.4850	3.0726	1.4855	3.3752	13.2966	14.0118	13.2966	(4)	13.2966
2.4	9.3155	8.2293	5.2467	24.2131	19.7155	15.7278	3.0726	1.4855	3.3752	14.3756	15.1926	14.3756	(4)	14.3756
2.5	9.7092	8.6230	5.5476	25.7002	21.2026	17.0000	3.0726	1.4855	3.3752	15.4546	16.3734	15.4546	(4)	15.4546
2.6	1.1406	3.1404	5.6497	2.7253	5.6497	9.1343	1.5451	8.4044	2.2709	4.1450	3.3752	1.6660	(5)	1.6660
2.7	1.2035	3.6497	7.2535	1.2059	1.2059	1.8008	(3)	1.0807	3.2251	5.3429	4.8013	2.3755	(5)	2.3755
2.8	1.2664	4.2413	9.3129	1.8386	2.0677	1.3892	4.5795	6.8821	6.8269	8.8211	6.8269	3.3842	(5)	3.3842
2.9	1.3293	4.8330	11.3721	2.4713	2.8426	2.8426	6.5019	8.8098	9.7036	11.6502	8.1073	4.8177	(5)	4.8177
3.0	1.3922	5.4246	13.4314	3.1014	3.7014	2.8426	2.2942	11.6502	13.4314	14.5000	10.0596	6.8269	(5)	6.8269
3.1	1.4551	6.0161	15.4907	3.7311	4.5711	3.0726	2.9477	1.3103	1.4064	1.9588	9.7178	8.1073	(5)	8.1073
3.2	1.5180	6.6076	17.5499	4.3608	5.4408	3.8471	3.7868	1.8599	1.8599	2.7822	10.0596	8.0141	(5)	8.0141
3.3	1.5809	7.2001	19.6091	4.9505	6.3105	4.4740	4.8644	2.4239	2.4239	3.9510	10.0596	8.0141	(5)	8.0141
3.4	1.6438	7.7916	21.6683	5.5402	7.1732	5.2022	5.4408	3.1154	3.1154	5.6100	10.0596	8.0141	(5)	8.0141
3.5	1.7067	8.3831	23.7275	6.1300	8.0360	6.0480	6.0480	4.0033	4.0033	7.9649	10.0596	8.0141	(5)	8.0141
3.6	1.7696	8.9746	25.7867	6.7197	8.9006	7.0306	7.0306	5.1437	5.1437	1.1307	1.1307	5.6438	(6)	5.6438
3.7	1.8325	9.5661	27.8459	7.3094	9.7653	8.1719	8.1719	6.6081	6.6081	1.6051	1.6051	8.0141	(6)	8.0141
3.8	1.8954	1.0194	29.9051	7.9001	10.6300	9.3426	9.3426	8.2836	8.2836	2.1319	2.1319	1.1319	(6)	1.1319
3.9	1.9583	1.0823	31.9643	8.4908	11.5000	10.5138	10.5138	9.0903	9.0903	2.7239	2.7239	2.2390	(6)	2.2390
4.0	2.0212	1.1452	34.0235	9.0815	12.3700	11.3971	11.3971	1.4904	1.4904	4.5899	4.5899	2.2932	(6)	2.2932



TABLE II  
Tesseral toroidal functions of the second kind

$n$	$q_1^0(u)$	$q_1^1(u)$	$q_1^2(u)$	$q_1^3(u)$	$q_1^4(u)$	$q_1^5(u)$	$q_1^6(u)$	$q_1^7(u)$	$q_1^8(u)$	$q_1^9(u)$	$q_1^{10}(u)$
0.0	$-\infty$	$-\infty$	$-\infty$	$-\infty$	$-\infty$	$-\infty$	$-\infty$	$-\infty$	$-\infty$	$-\infty$	$-\infty$
0.1	-9.8784	-9.5690	-8.7474	(2) 1.9845	(2) 1.9609	(2) 1.9204	(3) -7.9020	(3) -7.8538	(5) 4.6761		
0.2	-4.8023	-4.3815	-3.9147	(1) 4.8550	(1) 4.8417	(1) 4.8301	(2) -9.6702	(2) -9.5502	(4) 2.8839		
0.3	-3.0821	-2.6146	-2.1514	(2) 2.0815	(1) 1.8972	(1) 1.6884	(2) -9.6702	(2) -9.5502	(4) 2.8839		
0.4	-2.2076	-1.7279	-1.3020	(0)* 6.5834	(0)* 6.5834	(0)* 6.5834	(1) -9.6702	(1) -9.5502	(4) 2.8839		
0.5	-1.6755	-1.2040	-0.7874	(0)* 6.7357	5.3995	4.1474	(1) -5.2322	(1) -4.3525	(2) 6.6511		
0.6	-1.3171	-0.8587	-0.4207	4.3657	3.2460	2.2051	-2.7834	-2.1631	2.6399		
0.7	-1.0595	-0.6587	-0.3179	2.9659	2.0350	1.3192	-1.5910	-1.1480	1.2681		
0.8	-0.86615	-0.5336	-0.2466	2.0818	1.3128	(-1) 7.7807	(0)* -9.5504	(0)* -9.5504	(1) 6.5158		
0.9	-0.71633	-0.4061	-0.16701	1.4960	0.86445	4.6736	-5.9545	-3.6529	3.5153		
1.0	-5.9756	-2.6993	-1.1480	1.0940	5.7780	2.8448	-3.8095	-2.1438	1.9061		
1.1	-5.0174	-2.0577	-0.9236	(-1) 8.1061	3.9058	1.7490	-2.4871	-1.2806	1.3092		
1.2	-4.2342	-1.5755	-0.8581	6.0778	2.6630	1.0835	-1.6492	-1.1069	7.7534		
1.3	-3.5873	-1.2104	-0.7591	4.5781	1.8278	(-2) 6.7512	(-1) 1.069	-4.7437	3.9612		
1.4	-3.0486	-0.9324	-0.6721	3.4757	1.2611	4.2260	(-1) -7.5010	-2.9262	2.3951		
1.5	-2.5972	-0.71980	-0.46795	2.6517	(-2) 8.7364	2.6549	-5.1215	-1.8167	1.4631		
1.6	-2.2169	-0.5660	-0.3076	2.0311	6.0778	1.6727	-3.5180	-1.1337	(-1) 9.0109		
1.7	-1.9233	-0.4568	-0.1841	1.5906	4.2317	1.0452	-2.4983	(-2) 7.1035	5.5969		
1.8	-1.6924	-0.3807	-0.1047	1.2021	2.9552	4.2334	-1.1096	-2.8149	3.4815		
1.9	-1.5002	-0.31018	-0.0282	(-2) 9.2792	2.0672	4.2334	-1.1096	-2.8149	2.1790		
2.0	-1.1922	-0.2122	-0.0122	7.1744	1.4480	2.6853	(-2) -8.1505	-1.7781	1.3685		
2.1	-1.0231	-0.15632	-0.0719	5.5544	1.0155	1.7050	-5.6916	-1.1251	(-2) 8.6188		
2.2	-0.7849	-0.11093	-0.0343	3.3395	(-3) 2.1194	1.7050	-5.6916	(-3) -1.5231	3.4406		
2.3	-0.6487	-0.0849	-0.0149	2.5924	5.0064	(-4) 6.8886	-2.7885	-4.5237	2.1791		
2.4	-0.5741	-0.07146	-0.0082	2.0137	3.5186	4.3822	-1.9553	-2.8721	1.3819		
2.5	-0.5231	-0.06320	-0.0053	2.0137	2.4742	2.7860	-1.3723	-1.8251	1.3819		
2.6	-0.47925	-0.05616	-0.0033	1.5649	1.7404	1.7756	(-3) -9.6388	-1.1605	(-3) 8.7717		
2.7	-0.44213	-0.0503	-0.0023	1.2169	1.2237	1.307	-6.7740	(-4) -7.3832	5.5726		
2.8	-0.4092	-0.0456	-0.0016	0.9181	(-4) 8.0686	(-5) 4.5887	-3.3504	-2.9917	2.2535		
2.9	-0.38092	-0.04155	-0.0011	0.73597	4.0686	2.9239	-2.3575	-1.9052	1.4339		
3.0	-0.35632	-0.03820	-0.0008	5.7262	4.2731	3.0062	-1.8653	-1.6593	(-4) 9.1279		
3.1	-0.33499	-0.035670	-0.0006	4.4561	3.0062	1.8653	-1.6593	(-5) -7.7318	5.8124		
3.2	-0.31619	-0.03342	-0.0004	3.4681	2.1194	1.1875	(-6) 7.5092	(-4) -8.2249	3.7021		
3.3	-0.29979	-0.03142	-0.0003	2.6996	1.4929	7.5092	-8.2249	-3.1396	2.3584		
3.4	-0.28579	-0.02966	-0.0002	2.1015	1.0517	4.8248	-5.7921	-2.0010	1.5627		
3.5	-0.27374	-0.02813	-0.0001	1.6361	0.73597	3.0757	-4.0794	-2.0010	1.5627		
3.6	-0.26349	-0.02688	-0.0001	1.2738	5.2196	1.9907	-2.8735	-1.2754	(-5) 9.5757		
3.7	-0.25472	-0.02584	-0.0001	(-4) 9.0181	3.6775	1.2500	-2.0242	(-6) -8.1400	6.1027		
3.8	-0.24725	-0.02494	-0.0001	7.7228	2.5911	(-7) 7.9693	-1.4260	(-6) -8.1400	3.8897		
3.9	-0.24080	-0.02415	-0.0001	6.0135	1.8256	5.0809	-1.0046	-3.3039	2.4794		
4.0	-0.23542	-0.02345	-0.0001	4.6827	1.2864	3.2394	(-5) -7.0780	-2.1063	1.5805		

The tesseral toroidal functions  $p_n^m(u)$  and  $q_n^m(u)$  are essentially the associated Legendre's functions of first and second kinds of degree  $(n - \frac{1}{2})$  and order  $m$  respectively; the relations between  $p_n^m(u)$  and  $q_n^m(u)$ , and the corresponding associated Legendre's functions are

$$(13) \quad \begin{aligned} p_n^m(u) &= P_{n-\frac{1}{2}}^m(\cosh u) \\ q_n^m(u) &= Q_{n-\frac{1}{2}}^m(\cosh u). \end{aligned}$$

The new notations are suggested by Carter and Loh (1958).

The required solutions of Laplace's equation are

$$(14) \quad \begin{aligned} &\sqrt{(\cosh u - \cos v)} p_n^m(u) \frac{\cos}{\sin} nv \frac{\cos}{\sin} mw \\ &\sqrt{(\cosh u - \cos v)} q_n^m(u) \frac{\cos}{\sin} nv \frac{\cos}{\sin} mw. \end{aligned}$$

The spaces interior to and exterior to a tore are not simply connected; and thus the toroidal functions are not always directly applicable to the solution of potential problems for those spaces in which circulation is involved, as the potentials in such cases are not always uniquely determined by their values on the surface of the tore. It may be shown easily that, for the space exterior to the given tore ( $u = u_1$ )—that is,  $0 \leq u \leq u_1$ —the  $p$ -functions must be used as potential functions. Similarly, for the space interior to the given tore—that is,  $u_1 \leq u \leq \infty$ —the  $q$ -functions are chosen as potential functions. Heine (1881) has mistakenly stated that the  $p$ -functions are to be adapted as potential functions to the interior space and the  $q$ -functions to the exterior space.

However, the general solution of Laplace's equation in toroidal co-ordinates ( $u, v, w$ ) may be given by the series,

$$(15) \quad \phi = \sqrt{(\cosh u - \cos v)} \sum_n \sum_m (a_m \cos mw + b_m \sin mw) \times (c_n \cos nv + d_n \sin nv) \times \{A_{mn} p_n^m(u) + B_{mn} q_n^m(u)\},$$

where  $a_m, b_m, c_n, d_n, A_{mn}, B_{mn}$  are arbitrary constants to be determined by the boundary conditions.

#### ZONAL TOROIDAL FUNCTIONS

For the particular problems having cylindrical symmetry, the variable  $w$  becomes irrelevant. Expressed in terms of co-ordinates  $u$  and  $v$ , Laplace's equation becomes

$$(16) \quad \frac{\partial}{\partial u} \left( \frac{\sinh u}{\cosh u - \cos v} \frac{\partial \phi}{\partial u} \right) + \frac{\partial}{\partial v} \left( \frac{\sinh u}{\cosh u - \cos v} \frac{\partial \phi}{\partial v} \right) = 0.$$

Again we substitute,

$$(17) \quad \phi = \psi \sqrt{(\cosh u - \cos v)}.$$

Equation (16) reduces to

$$(18) \quad \frac{\partial^2 \psi}{\partial u^2} + \frac{\partial^2 \psi}{\partial v^2} + \coth u \frac{\partial \psi}{\partial u} + \frac{1}{4} \psi = 0.$$

This is satisfied by a function of the form

$$(19) \quad \psi = F(u) \cdot G(v)$$

if

$$(20) \quad \frac{d^2 G}{dv^2} + n^2 G = 0$$

and

$$\frac{d^2 F}{du^2} + \coth u \frac{dF}{du} + \left( \frac{1}{4} - n^2 \right) F = 0.$$

The first equation is satisfied by  $G = \cos(nv + \alpha_n)$  and the second by  $p_n(u)$  and  $q_n(u)$ ;  $p_n(u)$  and  $q_n(u)$  are known as the zonal toroidal functions of first and second kinds respectively.

The general solutions of Laplace's equation in toroidal co-ordinates having axial symmetry are of the form

$$(21) \quad \phi = \sqrt{(\cosh u - \cos v)} \sum_{n=0}^{\infty} \{A_n p_n(u) + B_n q_n(u)\} \cos(nv + \alpha_n)$$

where  $A_n, B_n, \alpha_n$  are arbitrary constants. The constants are to be chosen so as to fit the given boundary conditions.

The zonal toroidal functions of the two kinds are here denoted by

$$(22) \quad p_n(u) = \frac{1}{\pi} \int_0^\pi \frac{d\theta}{(\cosh u - \sinh u \cos \theta)^{n+1}},$$

$$q_n(u) = \int_0^\infty \frac{d\theta}{(\cosh u + \sinh u \cosh \theta)^{n+1}}.$$

For the particular cases, where  $n = 0$  and  $n = 1$ , it has been shown by Hicks (1881) that

$$(23) \quad p_0(u) = 2\sqrt{k'} F(k) = 2e^{-(u/2)} F(k),$$

$$p_1(u) = \frac{2}{\sqrt{k'}} E(k) = 2e^{u/2} E(k),$$

and

$$(24) \quad q_0(u) = 2\sqrt{k'} F(k') = 2e^{-(u/2)} F(k'),$$

$$(25) \quad q_1(u) = \frac{2}{\sqrt{k'}} [F(k) - E(k)] = 2e^{u/2} [F(k') - E(k')]$$

where

$$k^2 = 1 - e^{-2u},$$

$$k'^2 = e^{-2u}.$$

$F$  and  $E$  are the complete elliptic integrals of the first and second kinds, and  $k^2$ , the square of the modulus.

Starting with the values of  $p_0(u)$ ,  $p_1(u)$ ,  $q_0(u)$ ,  $q_1(u)$ , the zonal toroidal functions of higher order can be derived from the recurrence formulae (Hicks 1881), argument " $u$ " understood:

$$(26) \quad (2n+1) p_{n+1} - 4n \cosh u p_n + (2n-1) p_{n-1} = 0$$

and

$$(27) \quad (2n+1) q_{n+1} - 4n \cosh u q_n + (2n-1) q_{n-1} = 0.$$

Using equations (23), (24), (25), (26), and (27), the numerical tables (III and IV) for the first four functions of each kind have been worked out by Carter and Loh (1958) in connection with their investigation of the electric field between a rod and a concentric ring. These numerical tables have been checked by the I.B.M. 650 Computer at the University of Toronto. There are differences between these figures and those contained in Fouquet's table

TABLE III  
Zonal toroidal functions of the first kind

$u$	$p_0^0(u)$	$p_1^0(u)$	$p_2^0(u)$	$p_3^0(u)$	$p_4^0(u)$
0	1.0000	1.0000	1.0000	1.0000	1.0000
0.1	(-1) 9.9938	1.0019	1.0094	1.0220	1.0397
0.2	9.9751	1.0075	1.0378	1.0893	1.1635
0.3	9.9440	1.0169	1.0858	1.2060	1.3856
0.4	9.9009	1.0300	1.1547	1.3793	1.7314
0.5	9.8460	1.0469	1.2459	1.6196	2.2410
0.6	9.7795	1.0676	1.3615	1.9419	2.9739
0.7	9.7021	1.0921	1.5043	2.3659	4.0161
0.8	9.6141	1.1205	1.6776	2.9176	5.4910
0.9	9.5161	1.1526	1.8852	3.6311	7.5740
1.0	9.4086	1.1887	2.1320	4.5506	(1) 1.0615
1.1	9.2924	1.2287	2.4236	5.7330	1.4667
1.2	9.1679	1.2726	2.7667	7.2518	2.0533
1.3	9.0359	1.3206	3.1692	9.2015	2.8826
1.4	8.8971	1.3727	3.6401	(1) 1.1704	4.0554
1.5	8.7521	1.4289	4.1902	1.4914	5.7151
1.6	8.6015	1.4895	4.8321	1.9033	8.0648
1.7	8.4460	1.5544	5.5802	2.4319	(2) 1.1393
1.8	8.2863	1.6238	6.4515	3.1103	1.6108
1.9	8.1229	1.6978	7.4659	3.9808	2.2790
2.0	7.9565	1.7765	8.6462	5.0980	3.2262
2.1	7.7876	1.8602	(1) 1.0019	6.5320	4.5691
2.2	7.6167	1.9489	1.1616	8.3727	6.4734
2.3	7.4444	2.0429	1.3472	(2) 1.0736	9.1741
2.4	7.2711	2.1423	1.5631	1.3769	(3) 1.3005
2.5	7.0973	2.2474	1.8139	1.7663	1.8438
2.6	6.9234	2.3584	2.1055	2.2662	2.6147
2.7	6.7497	2.4756	2.4444	2.9080	3.7082
2.8	6.5766	2.5992	2.8382	3.7320	5.2597
2.9	6.4045	2.7296	3.2958	4.7900	7.4609
3.0	6.2337	2.8669	3.8276	6.1484	(4) 1.0584
3.1	6.0643	3.0116	4.4455	7.8925	1.5016
3.2	5.8967	3.1639	5.1635	(3) 1.0132	2.1304
3.3	5.7311	3.3243	5.9978	1.3007	3.0226
3.4	5.5677	3.4931	6.9671	1.6609	4.2886
3.5	5.4066	3.6708	8.0934	2.1439	6.0851
3.6	5.2480	3.8578	9.4021	2.7525	8.6344
3.7	5.0920	4.0545	(2) 1.0923	3.5340	(5) 1.2252
3.8	4.9388	4.2614	1.2689	4.5375	1.7385
3.9	4.7884	4.4790	1.4742	5.8259	2.4669
4.0	4.6408	4.7079	1.7126	7.4802	3.5006

TABLE IV  
Zonal toroidal functions of the second kind

$u$	$q_0^0(u)$	$q_1^0(u)$	$q_2^0(u)$	$q_3^0(u)$	$q_4^0(u)$
0	$\infty$	$\infty$	$\infty$	$\infty$	$\infty$
0.1	4.3799	2.3896	1.7421	1.3675	1.1117
0.2	3.6805	1.7124	1.1022	(-1) 7.7142	(-1) 5.6171
0.3	3.2669	1.3295	(-1) 7.6406	4.8023	3.1482
0.4	2.9693	1.0691	5.5122	3.1202	1.8452
0.5	2.7350	(-1) 8.7684	4.0668	2.0763	1.1088
0.6	2.5404	7.2828	3.0433	1.4027	(-2) 6.7680
0.7	2.3733	6.1010	2.2995	(-2) 9.5739	4.1755
0.8	2.2262	5.1425	1.7495	6.5825	2.5956
0.9	2.0947	4.3543	1.3378	4.5501	1.6225
1.0	1.9754	3.6995	1.0270	3.1581	1.0185
1.1	1.8661	3.1515	(-2) 7.9066	2.1987	(-3) 6.4135
1.2	1.7654	2.6902	6.1013	1.5345	4.0489
1.3	1.6719	2.3001	4.7166	1.0729	2.5611
1.4	1.5846	1.9691	3.6515	(-3) 7.5135	1.6225
1.5	1.5030	1.6875	2.8300	5.2679	1.0292
1.6	1.4263	1.4473	2.1954	3.6970	(-4) 6.5344
1.7	1.3542	1.2422	1.7044	2.5965	4.1522
1.8	1.2861	1.0667	1.3239	1.8247	2.6402
1.9	1.2219	(-2) 9.1635	1.0289	1.2830	1.6796
2.0	1.1611	7.8749	(-3) 7.9993	(-4) 9.0250	1.0690
2.1	1.1035	6.7694	6.2211	6.3504	(-5) 6.8058
2.2	1.0490	5.8205	4.8394	4.4697	4.3342
2.3	(-1) 9.9726	5.0055	3.7654	3.1466	2.7608
2.4	9.4819	4.3053	2.9303	2.2156	1.7589
2.5	9.0160	3.7035	2.2807	1.5603	1.1208
2.6	8.5737	3.1862	1.7753	1.0989	(-6) 7.1424
2.7	8.1535	2.7413	1.3820	(-5) 7.7406	4.5521
2.8	7.7542	2.3588	1.0759	5.4528	2.9015
2.9	7.3748	2.0297	(-4) 8.3771	3.8414	1.8495
3.0	7.0142	1.7466	6.5220	2.7063	1.1790
3.1	6.6714	1.5031	5.0789	1.9067	(-7) 7.5162
3.2	6.3454	1.2935	3.9548	1.3434	4.7917
3.3	6.0355	1.1132	3.0796	(-6) 9.4658	3.0549
3.4	5.7408	(-3) 9.5808	2.3982	6.6697	1.9477
3.5	5.4605	8.2456	1.8675	4.6997	1.2418
3.6	5.1940	7.0966	1.4543	3.3116	(-8) 7.9174
3.7	4.9405	6.1078	1.1326	2.3335	5.0481
3.8	4.6994	5.2568	(-5) 8.8201	1.6443	3.2186
3.9	4.4701	4.5244	6.8689	1.1587	2.0522
4.0	4.2520	3.8941	5.3493	(-7) 8.1647	1.3085

in which there are undoubtedly a number of errors. In addition, the numerical table for the first derivative of the zonal toroidal functions  $p_n'(u)$ ,  $q_n'(u)$  has been computed and included in the paper. The relations between  $p_n'(u)$  and  $q_n'(u)$  and the zonal toroidal functions  $p_n(u)$  and  $q_n(u)$  are

$$(28) \quad \frac{dp_n(u)}{du} = \frac{2n+1}{2 \sinh u} (p_{n+1} - \cosh u p_n),$$

$$\frac{dq_n(u)}{du} = \frac{2n+1}{2 \sinh u} (q_{n+1} - \cosh u q_n).$$

Using the above expressions derived, the numerical tables for the first derivative of toroidal functions have been calculated and are shown in Tables V and VI.

TABLE V  
The first derivative of zonal toroidal functions of the first kind

$u$	$p'_0(u)$	$p'_1(u)$	$p'_2(u)$	$p'_3(u)$	$p'_4(u)$
0	0	0	0	0	0
0.1	(-2) -1.2484	(-2) 3.7512	(-1) 1.8824	(-1) 4.4194	(-1) 8.0245
0.2	-2.4886	7.5024	3.8081	9.1081	(0)* 1.6967
0.3	-3.7117	(-1) 1.1261	5.8220	(0)* 1.4353	2.7857
0.4	-4.9097	1.5027	7.9708	2.0474	4.1963
0.5	-6.0753	1.8803	(0)* 1.0304	2.7849	6.0943
0.6	-7.2012	2.2594	1.2874	3.6933	(1) 1.1509
0.7	-8.2813	2.6405	1.5741	4.8287	1.2342
0.8	-9.3101	3.0240	1.8971	6.2619	1.7444
0.9	(-1) -1.0283	3.4106	2.2636	8.0819	2.4628
1.0	-1.1196	3.8009	2.6819	(1) 1.0402	3.4769
1.1	-1.2046	4.1957	3.1616	1.3368	4.9105
1.2	-1.2832	4.5959	3.7136	1.7165	6.9392
1.3	-1.3551	5.0024	4.3502	2.2030	9.8117
1.4	-1.4205	5.4161	5.0860	2.8269	(2) 1.3881
1.5	-1.4791	5.8383	5.9373	3.6272	1.9647
1.6	-1.5313	6.2699	6.9236	4.6543	2.7821
1.7	-1.5770	6.7123	8.0669	5.9724	3.9411
1.8	-1.6165	7.1668	9.3931	7.6643	5.5845
1.9	-1.6499	7.6346	(1) 1.0633	9.8362	7.9152
2.0	-1.6776	8.1171	1.2719	(2) 1.2625	(3) 1.1221
2.1	-1.6998	8.6158	1.4793	1.6204	1.5910
2.2	-1.7168	9.1322	1.7201	2.0800	2.2563
2.3	-1.7289	9.6678	1.9998	2.6702	3.2001
2.4	-1.7363	(0)* 1.0224	2.3247	3.4278	4.5390
2.5	-1.7395	1.0803	2.7021	4.4006	6.4388
2.6	-1.7387	1.1406	3.1404	5.6497	9.1343
2.7	-1.7342	1.2035	3.6497	7.2535	(4) 1.2959
2.8	-1.7263	1.2691	4.2413	9.3128	1.8386
2.9	-1.7153	1.3377	4.9286	(3) 1.1957	2.6087
3.0	-1.7014	1.4095	5.7270	1.5352	3.7014
3.1	-1.6851	1.4845	6.6546	1.9711	5.2519
3.2	-1.6664	1.5631	7.7323	2.5308	7.4521
3.3	-1.6456	1.6455	8.9844	3.2495	(5) 1.0574
3.4	-1.6230	1.7319	(2) 1.0439	4.1724	1.1066
3.5	-1.5987	1.8224	1.2129	5.3573	2.1291
3.6	-1.5730	1.9174	1.4093	6.8787	3.0213
3.7	-1.5461	2.0171	1.6374	8.8324	4.2872
3.8	-1.5181	2.1218	1.9024	(4) 1.1341	6.0838
3.9	-1.4891	2.2316	2.2103	1.4562	8.6331
4.0	-1.4594	2.3470	2.5681	1.8697	(6) 1.2251

For the general properties and a discussion of toroidal functions the reader should consult the articles by Hicks and Basset.

TABLE VI

The first derivative of zonal toroidal functions of the second kind

$n$	$q'_0(u)$	$q'_1(u)$	$q'_2(u)$	$q'_3(u)$	$q'_4(u)$
0	$\infty$	$\infty$	$\infty$	$\infty$	$\infty$
0.1	(1) -1.0044	-9.8756	-9.5660	-9.1781	-8.7448
0.2	(0)* -5.0711	-4.8024	-4.3815	-3.9147	-3.4496
0.3	-3.4243	-3.0821	-2.6146	-2.1514	-1.7371
0.4	-2.6062	-2.2076	-1.7279	-1.3020 (-1)	-9.5895
0.5	-2.1178	-1.6755	-1.2040 (-1)	-8.2784	-5.5481
0.6	-1.7932	-1.3171 (-1)	-8.6586	-5.4208	-3.3005
0.7	-1.5613	-1.0595	-6.3568	-3.6179	-1.9992
0.8	-1.3868 (-1)	-8.6615	-4.7336	-2.4466	-1.2261
0.9	-1.2501	-7.1633	-3.5611	-1.6701 (-2)	-7.5863
1.0	-1.1395	-5.9756	-2.6993	-1.1480	-4.7249
1.1	-1.0476	-5.0174	-2.0577 (-2)	-7.9326	-2.9574
1.2	(-1) -9.6971	-4.2342	-1.5755	-5.5036	-1.8581
1.3	-9.0235	-3.5873	-1.2104	-3.8301	-1.1709
1.4	-8.4321	-3.0486 (-2)	-9.3243	-2.6721 (-3)	-7.3953
1.5	-7.9062	-2.5972	-7.1980	-1.8678	-4.6795
1.6	-7.4331	-2.2169	-5.5660	-1.3076	-2.9654
1.7	-7.0037	-1.8953	-4.3098 (-3)	-9.1659	-1.8814
1.8	-6.6107	-1.6224	-3.3407	-6.4313	-1.1947
1.9	-6.2487	-1.3902	-2.5918	-4.5162 (-4)	-7.5927
2.0	-5.9134	-1.1922	-2.0122	-3.1735	-4.8283
2.1	-5.6015	-1.0231	-1.5632	-2.2311	-3.0719
2.2	-5.3100 (-2)	-8.7849	-1.2149	-1.5693	-1.9552
2.3	-5.0369	-7.5164 (-3)	-9.4454	-1.1041	-1.2449
2.4	-4.7802	-6.4847	-7.3459 (-4)	-7.7708 (-5)	-7.9282
2.5	-4.5386	-5.5741	-5.7140	-5.4703	-5.0503
2.6	-4.3106	-4.7926	-4.4464	-3.8516	-3.2176
2.7	-4.0952	-4.1214	-3.4603	-2.7123	-2.0503
2.8	-3.8915	-3.5447	-2.6932	-1.9103	-1.3066
2.9	-3.6986	-3.0492	-2.0964	-1.3455 (-6)	-8.3279
3.0	-3.5158	-2.6232	-1.6320 (-5)	-9.4780	-5.3082
3.1	-3.3425	-2.2509	-1.2706	-6.6770	-3.3837
3.2	-3.1780	-1.9419 (-4)	-9.8926	-4.7040	-2.1570
3.3	-3.0219	-1.6710	-7.7026	-3.3142	-1.3751
3.4	-2.8736	-1.4379	-5.9977	-2.3350 (-7)	-8.7666
3.5	-2.7327	-1.2374	-4.6703	-1.6453	-5.5890
3.6	-2.5987	-1.0649	-3.6368	-1.1593	-3.5634
3.7	-2.4718 (-3)	-9.1646	-2.8320 (-6)	-8.1684	-2.2719
3.8	-2.3509	-7.8872	-2.2054	-5.7558	-1.4485
3.9	-2.2360	-6.7880	-1.7175	-4.0558 (-8)	-9.2356
4.0	-2.1267	-5.8422	-1.3375	-2.8579	-5.8886

APPROXIMATE EXPRESSIONS FOR  $p_n(u)$ 

The zonal toroidal functions of the first kind may be written as

$$(29) \quad p_n(u) = \frac{1}{\pi} \int_0^{\pi} \frac{d\theta}{(\cosh u - \sinh u \cos \theta)^{n+1}}.$$

Two special cases will now be considered.

(i) *For small values of  $u$  ( $u < 1.0$ )*

If the above integral is expanded as a power series of  $\cos \theta$ , term-by-term integration leads to

$$(30) \quad p_n(u) = \frac{1}{\pi} (\cosh u)^{-n-\frac{1}{2}} \left\{ \pi + \frac{\pi}{4} \left( n + \frac{1}{2} \right) \left( n + \frac{3}{2} \right) \tanh^2 \frac{u}{2} + \dots \right\}.$$

The substitutions

$$\cosh u \doteq (1 + \frac{1}{2} u^2 + \dots)$$

and

$$(31) \quad \tanh u \doteq u + \dots$$

reduce equation (30) to

$$(32) \quad p_n(u) \doteq \left( 1 + \frac{4n^2 - 1}{16} u^2 \right)$$

neglecting the terms of order higher than the second.

$$p_0(u) \doteq \left( 1 - \frac{1}{16} u^2 \right)$$

$$p_1(u) \doteq \left( 1 + \frac{3}{16} u^2 \right)$$

$$p_2(u) \doteq \left( 1 + \frac{15}{16} u^2 \right)$$

The approximate values for  $p_n(u)$  having small arguments given by equation (32) have been calculated and plotted in Fig. 2. This approximate expression derived for  $p_n(u)$  for small values of  $u$  is surprisingly accurate, even beyond the expected range of validity.

(ii) *For large values of  $u$  ( $u > 1.5$ )*

By replacing  $\cosh u$  and  $\sinh u$  with their exponential forms in equation (29), it is seen that

$$(33) \quad p_n(u) = \frac{1}{\pi} \int_0^\pi \left\{ \frac{1}{2} (e^u + e^{-u}) - \frac{1}{2} (e^u - e^{-u}) \cos \theta \right\}^{n+\frac{1}{2}} d\theta.$$

The substitution

$$\theta' = \frac{1}{2}(\pi - \theta)$$

reduces the above integral to

$$(34) \quad p_n(u) = \frac{2}{\pi} e^{-(n+\frac{1}{2})u} \int_0^{\pi/2} \frac{d\theta'}{(\cos^2 \theta' + e^{-2u} \sin^2 \theta')^{n+\frac{1}{2}}}.$$

By comparison with the approximate expression for the complete elliptic integral,

$$(35) \quad \int_0^{\pi/2} \frac{dx}{(\cos^2 x + k^2 \sin^2 x)^{1/2}} \doteq \log(4/k), \quad \text{if } k^2 \text{ is small.}$$



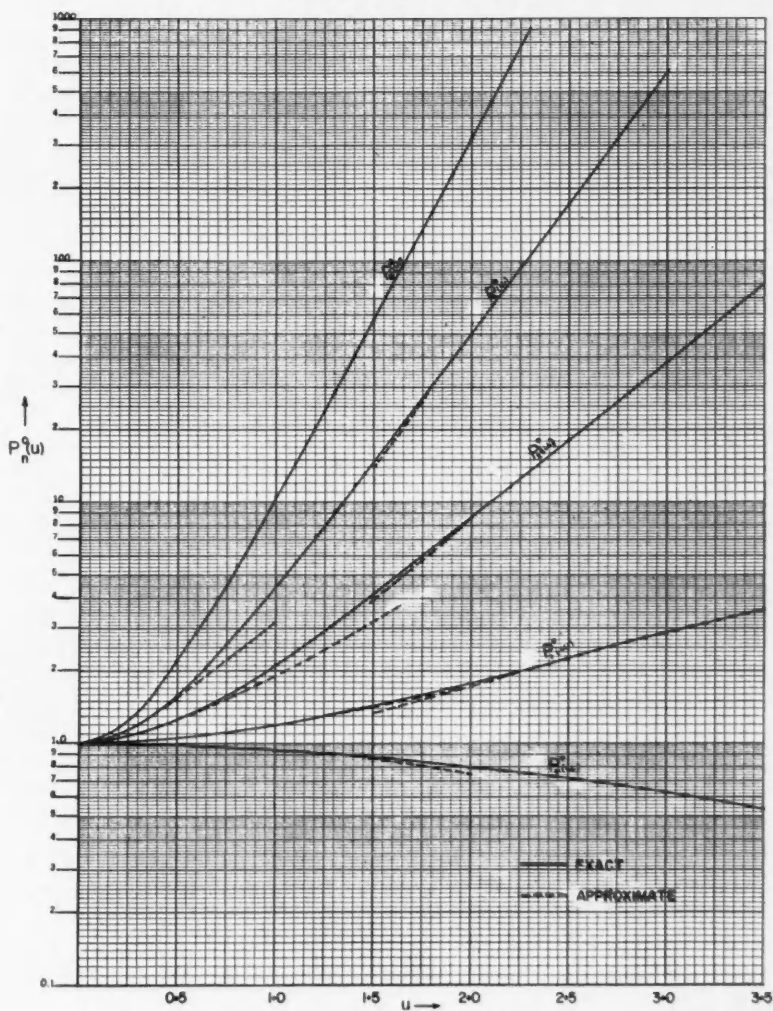


FIG. 2. Zonal toroidal functions of first kind.

We then find

$$\begin{aligned}
 p_0(u) &\doteq \frac{2}{\pi} e^{-1/2 u} (\log_e 4 + u) \doteq \frac{2}{\pi} u e^{-1/2 u} \\
 p_1(u) &\doteq \frac{2}{\pi} e^{1/2 u}, \\
 p_n(u) &\doteq \frac{2}{\pi} \frac{2 \cdot 4 \cdot 6 \dots (2n-2)}{3 \cdot 5 \cdot 7 \dots (2n-1)} e^{(n-1/2)u}.
 \end{aligned}
 \tag{36}$$

The approximate values have been computed and plotted in Fig. 2.

APPROXIMATE EXPRESSIONS FOR  $q_n(u)$ 

The zonal toroidal functions of the second kind,  $q_n(u)$ , are defined as

$$q_n(u) = \int_0^\infty \frac{d\theta}{(\cosh u + \sinh u \cosh \theta)^{n+1}}.$$

Also it may easily be shown that  $q_n(u)$  can be expressed in terms of  $p_n(u)$  in the form

$$(37) \quad q_n(u) = A_n p_n(u) \int_u^\infty \frac{du}{\sinh u [p_n(u)]^2}$$

where  $A_n$  is an arbitrary constant and is found to be unity in the present case.

Two cases are now to be considered separately.

(i) For large values of  $u$ 

Using the approximate expression, equation (36), derived for  $p_n(u)$  in the preceding section, equation (37) yields

$$(38) \quad q_n(u) = \frac{\pi \cdot 3 \cdot 5 \dots (2n-1)}{2 \cdot 4 \dots (2n-2)} e^{(n-\frac{1}{2})u} \int_{+u}^\infty \frac{du}{\sinh u e^{(2n-1)u}}.$$

The integral in equation (38) can be evaluated by expressing  $\sinh u$  in terms of its exponential equivalent; therefore,

$$(39) \quad \begin{aligned} q_n(u) &= \pi \frac{3 \cdot 5 \dots (2n-1)}{2 \cdot 4 \dots (2n-2)} e^{(n-\frac{1}{2})u} \int_{+u}^\infty \frac{du}{e^{(2n-1)u} (e^u - e^{-u})} \\ &= \pi \frac{3 \cdot 5 \dots (2n-1)}{2 \cdot 4 \dots (2n-1)} e^{(n-\frac{1}{2})u} \int_u^\infty e^{-2nu} (1 - e^{-2u})^{-1} du. \end{aligned}$$

For purposes of the analysis, let us expand  $(1 - e^{-2u})^{-1}$  by use of the binomial theorem, and integrate term by term. We have then an approximate expression for  $q_n(u)$  given by:

$$(40) \quad \begin{aligned} q_n(u) &= \pi \frac{1 \cdot 3 \cdot 5 \dots (2n-1)}{2 \cdot 4 \dots (2n)} \left\{ e^{-(n+\frac{1}{2})u} + \frac{n}{n+2} e^{-(n+\frac{5}{2})u} + \dots \right\} \\ &= \pi \frac{1 \cdot 3 \cdot 5 \dots (2n-1)}{2 \cdot 4 \dots (2n)} e^{-nu} \left\{ e^{-\frac{1}{2}u} + \frac{n}{n+2} e^{-\frac{5}{2}u} + \dots \right\}. \end{aligned}$$

For large values of  $u$  ( $u > 2.0$ ), the result with one term is quite satisfactory; that is

$$q_0(u) = \pi e^{-\frac{1}{2}u},$$

$$q_1(u) = \frac{\pi}{2} e^{-\frac{3}{2}u},$$

$$q_2(u) = \frac{3\pi}{8} e^{-\frac{5}{2}u},$$

and

$$(41) \quad q_n(u) = \pi \frac{1 \cdot 3 \cdot 5 \dots (2n-1)}{2 \cdot 4 \cdot 6 \dots 2n} e^{-(n+\frac{1}{2})u}.$$

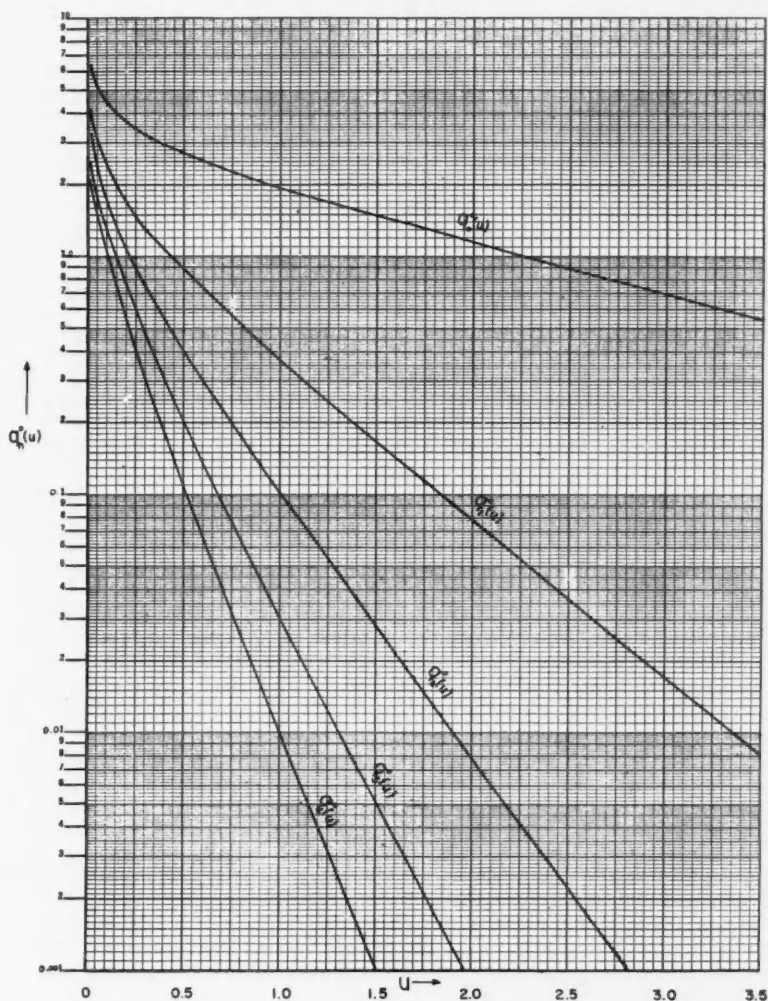


FIG. 3. Zonal toroidal functions of second kind.

*(ii) Series Expression*

A simple but good approximate expression for  $q_n(u)$  with small values of  $u$  is somewhat difficult to achieve. However, the author has derived a series expression for  $q_n(u)$ , which is valid for both large and small values of  $u$ .

By replacing  $\cosh u$  and  $\sinh u$  with their exponential forms, equation (22) yields

$$\begin{aligned}
 (42) \quad q_n(u) &= \int_0^\infty \frac{d\theta}{\left\{ \frac{1}{2}e^u(1+\cosh \theta) + \frac{1}{2}e^{-u}(1-\cosh \theta) \right\}^{n+1}} \\
 &= e^{-(n+\frac{1}{2})u} \int_0^\infty \frac{d\theta}{(\cosh^2 \frac{1}{2}\theta - e^{-2u} \sinh^2 \frac{1}{2}\theta)^{n+1}} \\
 &= e^{-(n+\frac{1}{2})u} \int_0^\infty \cosh^{-(2n+1)} \frac{1}{2}\theta \{1 + (n+\frac{1}{2})e^{-2u} \tanh^2 \frac{1}{2}\theta + \dots\} d\theta \\
 &= e^{-(n+\frac{1}{2})u} \left\{ \int_0^\infty \frac{\cosh \frac{1}{2}\theta d\theta}{(1+\sinh^2 \frac{1}{2}\theta)^{n+1}} + \frac{2n+1}{2} e^{-2u} \int_0^\infty \frac{\cosh \frac{1}{2}\theta \sinh^2 \frac{1}{2}\theta d\theta}{(1+\sinh^2 \frac{1}{2}\theta)^{n+2}} \right. \\
 &\quad \left. + \dots \right\}.
 \end{aligned}$$

If we introduce

$$\sinh \frac{1}{2} \theta = x,$$

then,

$$\frac{1}{2} \cosh \frac{1}{2} \theta d\theta = dx.$$

Equation (42) can be reduced to the following expression:

$$q_n(u) = 2e^{-(n+\frac{1}{2})u} \left\{ \int_0^\infty \frac{dx}{(1+x^2)^{n+1}} + e^{-2u} \left( \frac{2n+1}{2} \right) \int_0^\infty \frac{x^2 dx}{(1+x^2)^{n+2}} + \dots \right\}.$$

The substitution  $x = \tan \phi$  leads to

$$\begin{aligned}
 (43) \quad q_n(u) &= \pi e^{-(n+\frac{1}{2})u} \frac{(2n-1)(2n-3) \dots 1}{2n(2n-2) \dots 2} \left\{ 1 + e^{-2u} \cdot \frac{2n+1}{2} \cdot \frac{1}{2n+2} \right. \\
 &\quad \left. + e^{-4u} \frac{(2n+1)(2n+3) \cdot 1 \cdot 3}{(2n+2)(2n+4) \cdot 2 \cdot 4} + \dots \right\}.
 \end{aligned}$$

Equation (43) is the general expression for  $q_n(u)$ , which is valid for all values of  $u$ .

#### ACKNOWLEDGMENTS

The author wishes gratefully to thank the National Research Council of Canada for the award of a Postdoctorate Fellowship.

Acknowledgment is also due to Professor G. W. Carter of Leeds University for his encouragement and valuable advice, and to Dr. Robert F. Millar of the Radio and Electrical Engineering Division, National Research Council, for many useful discussions and invaluable comments on this manuscript.

#### REFERENCES

- AIREY, J. R. 1935. *Phil. Mag.* **19**, 177.  
 BASSET, A. B. 1893. *Proc. London Math. Soc.* **24**, 180.  
 CARTER, G. W. and LOH, S. C. 1958. *J. Inst. Elect. Engrs. Part IV*, 13.  
 FOCK, V. 1932. *Phys. Z. Sowjetunion*, **1**, 215.  
 FOUQUET, W. 1937. *Z. angew. Math. u. Mech.* **17**, 48.  
 HEINE, E. 1881. *Anwendungen der Kugelfunktionen*, Vol. 2 (Reimer, Berlin), p. 283.  
 HICKS, W. H. 1881. *Phil. Trans. Roy. Soc.* **31**, 609.  
 ——— 1884. *Phil. Trans. Roy. Soc.* **35**, 161.  
 HOBSON, E. W. 1931. *The theory of spherical and ellipsoidal harmonics* (Cambridge University Press, London).

- LOH, S. C. 1957. Ph.D. Thesis, University of Leeds.
- MORSE, P. M. and FESHBACH, H. 1953. Methods of theoretical physics (McGraw-Hill Book Co., Inc.).
- NEUMANN, C. 1864. Allgemeine Lösung des Problems über den stationärer Temperaturzustand eines homogenen Körpers welcher von irgend zwei nichtkonzentrischen kugelflächen begrenzt wird. H. W. Schmitt, Halle.
- NIVEN, W. D. 1892. Proc. London Math. Soc. XXIV, 372.
- RELTON, F. E. 1931. Phil. Mag. 11, 129.
- 1933. Phil. Mag. 15, 840.

# THE LYMAN BANDS OF MOLECULAR HYDROGEN<sup>1</sup>

G. HERZBERG AND L. L. HOWE

## ABSTRACT

The Lyman bands of  $H_2$  have been investigated under high resolution with a view to improving the rotational and vibrational constants of  $H_2$  in its ground state. Precise  $B_v$  and  $\Delta G$  values have been obtained for all vibrational levels of the ground state. One or two of the highest rotational levels of the last vibrational level ( $v = 14$ ) lie above the dissociation limit. Both the  $B'_v$  and  $\Delta G'_v$  curves have a point of inflection at about  $v'' = 3$ . This makes it difficult to represent the whole course of each of these curves by a single formula and therefore makes the resulting equilibrium constants somewhat uncertain. This uncertainty is not very great for the rotational constants for which we find

$$B_e = 60.864 \quad \alpha_e = 3.0764 \text{ cm}^{-1}$$

but is considerable for the vibrational constants  $\omega_e$  and  $\omega_e x_e$ , for which three-, four-, five-, and six-term formulae give results diverging by  $\pm 1 \text{ cm}^{-1}$ . The rotational and vibrational constants for the upper state ( $B'^1\Sigma_u^+$ ) of the Lyman bands are also determined. An appreciable correction to the position of the upper state is found.

## 1. INTRODUCTION

The most precise values at present available for the rotational and vibrational constants of the hydrogen molecule in its ground electronic state are those derived from the quadrupole spectrum in the photographic infrared (Herzberg 1950a) and from Raman data (Stoicheff 1957). However, these constants represent precisely only the lowest vibrational and rotational levels, up to  $v = 3$  and  $J = 5$ . For the higher vibrational and rotational levels one is dependent on the emission spectrum of  $H_2$  in the vacuum ultraviolet. The frequency dispersion in the vacuum ultraviolet is low, and therefore, in the early work of Hyman (1930) and Jeppesen (1933), vibrational and rotational differences were obtained only with rather modest wave number accuracy. As a result there were differences of up to  $4 \text{ cm}^{-1}$  between the predicted and observed wave numbers of the quadrupole infrared bands.

Recent improvements in vacuum ultraviolet spectroscopy have made it possible to measure lines in this region with much greater accuracy. Because of the importance of the  $H_2$  molecule in general and of a precise knowledge of all its energy levels in particular, it was considered to be of interest to remeasure a sufficient part of the far ultraviolet spectrum in order to obtain the constants of all vibrational levels of  $H_2$  in the ground state. The behavior of the levels near the dissociation limit promised to be of particular interest (compare the early work of Beutler 1934).

There are two well-known emission band systems of  $H_2$  in the vacuum ultraviolet; the Lyman bands ( $B-X$ ) representing a  ${}^1\Sigma_u^+ \rightarrow {}^1\Sigma_g^+$  transition and the Werner bands ( $C-X$ ) representing a  ${}^1\Pi_u \rightarrow {}^1\Sigma_g^+$  transition. Since the former

<sup>1</sup>Manuscript received February 23, 1959.

Contribution from the Division of Pure Physics, National Research Council, Ottawa, Canada.

Issued as N.R.C. No. 5170.

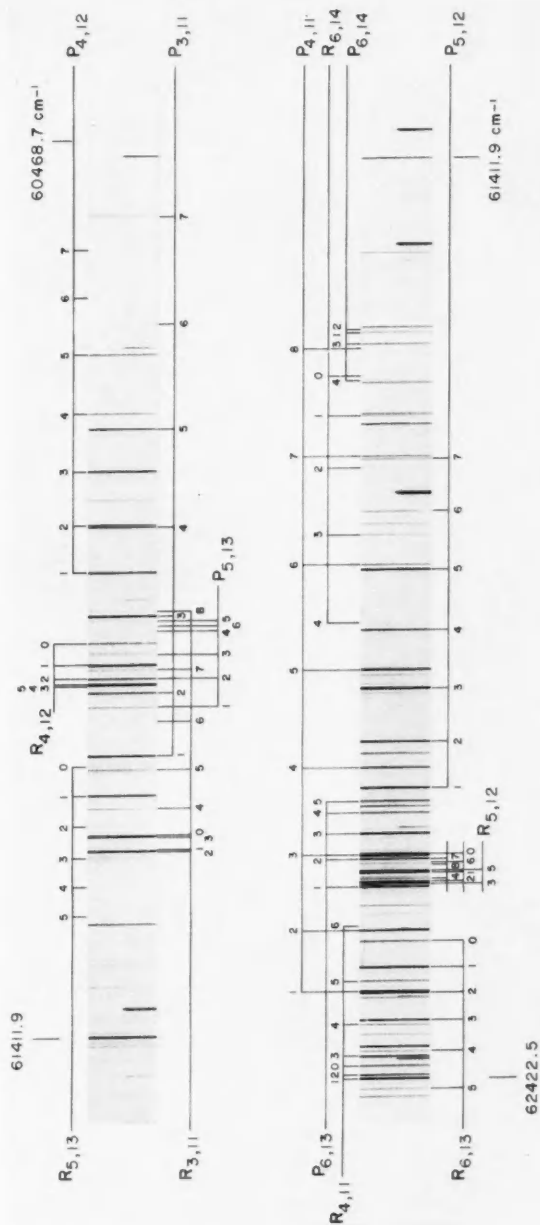


FIG. 1. Section of the spectrum of H<sub>2</sub> extending from 1655 to 1600 Å. Some of the Lyman bands are indicated.





lie at longer wavelengths and therefore allow one to obtain a higher wave number accuracy they were chosen for the present work. Moreover, the higher vibrational levels of the ground state are more favored in this transition than in the Werner bands on account of the Franck-Condon principle.

## 2. EXPERIMENTAL

The Lyman bands of  $H_2$  can be produced in any discharge through hydrogen. In the present work most spectra were obtained by means of an electrodeless discharge tube operated by a high-frequency oscillator (a Raytheon microtherm unit). In order to bring out lines of high rotational quantum number a few spectra were taken with a high-current tube with electrodes of conventional type. The electrodeless tube was also used in some experiments with liquid nitrogen cooling in order to reduce the Doppler width of the lines and to simplify the spectrum by the exclusion of lines with high  $J$ .

The spectra were taken in the fourth and fifth orders of our 3-meter vacuum spectrograph, that is with a dispersion of 0.66 or 0.5 Å/mm. The orders were separated by means of a foregrating as described by Douglas and Herzberg (1957). Standards were supplied by a Fe hollow cathode discharge tube. The light from this source was sent through the  $H_2$  discharge tube onto the slit of the spectrograph. The Fe lines were photographed in second order. No attempt to eliminate the error introduced by the method of overlapping orders was made, that is the absolute accuracy of the wavelengths may only be  $\pm 0.01$  Å corresponding to  $\pm 0.5$  cm<sup>-1</sup> but the relative accuracy (and therefore the accuracy of rotational and vibrational differences) was  $\pm 0.05$  cm<sup>-1</sup> for unblended lines. Lines that were more than 0.5 cm<sup>-1</sup> apart were resolved, that is the attained resolving power was well above 100,000. The measurements were made with a photoelectric comparator built in this laboratory by Dr. B. P. Stoicheff according to the design of Tomkins and Fred (1951).

In Fig. 1 a section of the long wavelength end of the spectrum is reproduced showing some of the bands with the highest  $v''$  values.

## 3. ANALYSIS OF THE SPECTRUM

The Lyman bands represent a typical many-line spectrum (see Fig. 1); individual bands or branches are not at all obvious. However, with the bands analyzed by Hyman and Jeppesen, it was relatively easy to proceed and find other bands. Some difficulty was encountered in assigning the lines of the bands of highest  $v''$  since, because of the high  $D''$  values, the form of the branches is rather unusual and since in addition the branches are very short. However, the use of combination relations has in each case made a reliable analysis possible.

In Table I are listed the wave numbers of the lines of all the bands that have been analyzed. Lines used more than once are indicated by asterisks. There are a considerable number of lines which remain unidentified. These are listed in Table II for the region 1685–1380 Å. It is very difficult to see what their identification may be unless they are "extra lines" of some of the weaker bands with perturbations.

TABLE I  
Vacuum wave numbers of the lines of the Lyman bands of H<sub>2</sub>

J	0-3 band $\nu_0 = 78420.9_s \text{ cm}^{-1}$		0-4 band $\nu_0 = 74952.9_s \text{ cm}^{-1}$		0-5 band $\nu_0 = 71711.4_s \text{ cm}^{-1}$		0-6 band $\nu_0 = 68697.6_s \text{ cm}^{-1}$		0-7 band $\nu_0 = 65915.5_i \text{ cm}^{-1}$	
	P(J)	R(J)	P(J)	R(J)	P(J)	R(J)	P(J)	R(J)	P(J)	R(J)
0		78459.84		74992.03		71750.37		68736.57		65953.59*
1	78319.93	436.16	74857.76	973.88	71621.79	737.96*	68613.71	729.85	65837.40	953.59*
2	157.67	349.94	706.60	898.97	481.84	674.29	485.32	677.80	720.83	913.13
3	77935.62	202.32	501.38	768.14	293.77	560.40	314.14	580.90*	567.13	833.90
4	655.82	77994.53	243.96	582.66	058.70	397.40	101.51*	440.50	378.21	716.92
5	320.81	728.34	73936.79	344.51	70779.47	187.06	67850.78	258.44	156.27	563.88
6			582.91	055.89	459.80	70931.58	563.71*	036.99*		64903.86
7			185.21	73719.74	099.09	633.66	243.13	67777.74		623.79
8			72747.19	336.30	69704.27	296.16†				
9			272.22	72916.92	271.89†	69922.21				
10			71764.28	454.32						
11			225.96							

J	0-8 band $\nu_0 = 63372.3_s \text{ cm}^{-1}$		1-3 band $\nu_0 = 79739.4_s \text{ cm}^{-1}$		1-4 band $\nu_0 = 76271.3_s \text{ cm}^{-1}$		1-5 band $\nu_0 = 73029.8_s \text{ cm}^{-1}$		1-6 band $\nu_0 = 70016.1_s \text{ cm}^{-1}$	
	P(J)	R(J)	P(J)	R(J)	P(J)	R(J)	P(J)	R(J)	P(J)	R(J)
0				79776.47		76308.15		73066.80		70052.99
1	63300.32*	63416.49	79638.50	749.13	76175.98	286.36	72940.14	050.49	69932.01	042.48
2	195.99	388.63	474.13	657.09	022.92	205.68	798.37		801.77	69984.63
3	060.76	327.55	248.19	502.17†	75813.85	067.78	606.27	72860.21	626.72	880.53
4	62896.43	235.35*	78962.84	285.79	550.97*	75873.52	365.68		408.76	731.16
5	704.70	112.42	620.79		236.56	625.36	079.10		150.47	539.65
6			227.84						68854.47	306.48
7					74466.05	74976.15	71380.09		524.11	035.63

J	1-7 band $\nu_0 = 67233.9_s \text{ cm}^{-1}$		1-8 band $\nu_0 = 64690.7_s \text{ cm}^{-1}$		1-9 band $\nu_0 = 62397.8_s \text{ cm}^{-1}$		1-10 band $\nu_0 = 60371.5_s \text{ cm}^{-1}$		2-3 band $\nu_0 = 81020.8_s \text{ cm}^{-1}$	
	P(J)	R(J)	P(J)	R(J)	P(J)	R(J)	P(J)	R(J)	P(J)	R(J)
0		67270.80		64727.89		62434.14		60408.40		
1	67155.85	266.16	64618.70	729.02	62332.28	442.67	60312.92	423.30	80919.91	81025.36
2	037.36*	220.13	512.46	605.33	239.04	422.54*	233.84	416.57		80928.63
3	66879.80	133.60	373.30	627.16	119.34	373.22	135.27	389.14	524.79	
4	685.20	007.89	203.20	525.85	61975.07	298.41*	019.41	342.11		
5	455.94	66844.81	004.28	393.25	808.77	197.94	59888.56	277.45		
6	194.78	646.66	63779.54	231.52	622.98		745.54	197.57		
7	65904.64*	416.10	531.82	043.40	420.89	61930.33	593.42	105.10		
8	588.72	156.21	266.71†	63831.80†			435.51			
9	250.44	65870.02								
10	64890.37									

J	2-4 band $\nu_0 = 77552.8_s \text{ cm}^{-1}$		2-5 band $\nu_0 = 74311.2_s \text{ cm}^{-1}$		2-6 band $\nu_0 = 71297.5_s \text{ cm}^{-1}$		2-7 band $\nu_0 = 68515.3_s \text{ cm}^{-1}$		2-8 band $\nu_0 = 65972.2_s \text{ cm}^{-1}$	
	P(J)	R(J)	P(J)	R(J)	P(J)	R(J)	P(J)	R(J)	P(J)	R(J)
0		77588.08		74346.49		71332.85		68437.24*		66007.47
1	77457.48	563.14*	74221.53	327.12	71213.56	319.06	68437.24*	68542.70	65900.21	005.74
2	302.70	477.65	078.10*	253.02	081.62	256.49	317.02	491.10*	792.24	65967.17
3	090.45	333.02*	73882.73	125.56	70903.32	146.17	156.38		649.85	892.71
4	76822.57	131.76	637.34	73946.19	680.63	70989.51	67956.99		474.93	783.86
5	502.03	76874.63	344.59	717.16	416.14	788.76	721.58		269.92	642.58
6	131.92	565.26	007.56	440.99	112.61	546.20	452.85		037.68	471.11
7	75715.46		72629.38	120.51	69773.44	268.10			64781.24*	272.37
8	256.63								504.08	

\*Blended line.

†Doubtful.

TABLE I (Continued)  
 Vacuum wave numbers of the lines of the Lyman bands of H<sub>2</sub>

2-9 band $\nu_0 = 63679.2_s \text{ cm}^{-1}$			2-10 band $\nu_0 = 61652.9_s \text{ cm}^{-1}$		2-11 band $\nu_0 = 59916.3_s \text{ cm}^{-1}$		3-3 band $\nu_0 = 82267.6_s \text{ cm}^{-1}$		3-4 band $\nu_0 = 78799.5_s \text{ cm}^{-1}$	
J	P(J)	R(J)	P(J)	R(J)	P(J)	R(J)	P(J)	R(J)	P(J)	R(J)
0		63714.45		61688.28*		59951.42				78833.48
1	63613.78	719.20	61594.39	699.82	59865.51	970.98	82267.90		805.41	
2	518.82	693.66	513.62	688.28*	800.39	975.28		78548.18	715.86	
3	395.94	638.74	411.92	654.66	722.29	965.15	81767.27	332.90	566.00*	
4	247.00*	555.90	291.23	600.08	633.41	942.13		061.06*		
5	074.50	447.10	154.20*	526.82	536.04	908.54		77734.66	092.80	
6	62881.22	314.92	003.63	437.12				357.78	77773.77	
7	670.13	161.32	60842.79	334.15				76933.83	406.50	
8	445.08		675.61					465.72		
9								75958.74	76527.53	

3-5 band $\nu_0 = 75558.0_s \text{ cm}^{-1}$			3-6 band $\nu_0 = 72544.3_s \text{ cm}^{-1}$		3-7 band $\nu_0 = 69762.1_s \text{ cm}^{-1}$		3-8 band $\nu_0 = 67218.9_s \text{ cm}^{-1}$		3-9 band $\nu_0 = 64926.0_s \text{ cm}^{-1}$	
J	P(J)	R(J)	P(J)	R(J)	P(J)	R(J)	P(J)	R(J)	P(J)	R(J)
0		75591.80		72578.05		69768.95	67253.20		64959.81	
1	75468.26	569.40	72460.04	561.40	69683.97	785.14	67146.88	248.08	64860.47	961.59
2	323.45	491.12	326.93	494.58	562.35	730.10	037.36*	205.10	764.08	932.02
3	125.17	358.19	145.71	378.75	398.74	631.86	66892.20	125.29	638.30	871.35
4	74875.53	172.13	71918.73		195.10	491.87	713.08	009.50	485.16	781.24*
5	577.23	74935.06	648.41*		68954.18	312.22	502.46	66860.43	307.08	665.09
6	233.59	650.26	338.49		678.28*	095.71	263.90		106.99	521.97*
7	73847.25	320.77	70991.45		371.92	68844.78	65994.66	466.83	63888.28	357.10
8					036.99*				654.33	
9					67679.26*					

3-10 band $\nu_0 = 62899.7_s \text{ cm}^{-1}$			3-11 band $\nu_0 = 61163.1_s \text{ cm}^{-1}$		3-12 band $\nu_0 = 59748.1_s \text{ cm}^{-1}$		4-3 band $\nu_0 = 83480.5_s \text{ cm}^{-1}$		4-4 band $\nu_0 = 80012.5_s \text{ cm}^{-1}$	
J	P(J)	R(J)	P(J)	R(J)	P(J)	R(J)	P(J)	R(J)	P(J)	R(J)
0		62933.49		61197.18		59781.65			80045.25	
1	62841.18	942.35	61112.21*	213.41*	59706.64	807.34	83379.66	83476.86	79917.37	014.55
2	758.88	926.59*	045.70	213.41*			210.94		759.88	79921.12
3	654.25	887.35	60964.73	197.70			82976.29		542.05	
4	529.42	826.05	871.46	168.04					266.09	
5	386.83	744.82	768.68	126.71					78034.86	279.57
6	229.45	645.91	659.62	076.57						
7	060.96	533.92	548.21	021.17	59395.70				120.22	78576.07
8	61884.73	411.49	438.78	60959.67						
9	705.63	281.07		336.50						
10				247.30						
11				179.44						

4-5 band $\nu_0 = 76771.0_s \text{ cm}^{-1}$			4-6 band $\nu_0 = 73757.2_s \text{ cm}^{-1}$		4-7 band $\nu_0 = 70975.1_s \text{ cm}^{-1}$		4-8 band $\nu_0 = 68431.9_s \text{ cm}^{-1}$		4-9 band $\nu_0 = 66139.0_s \text{ cm}^{-1}$	
J	P(J)	R(J)	P(J)	R(J)	P(J)	R(J)	P(J)	R(J)	P(J)	R(J)
0		76803.19		73789.64		71007.65	68464.40		66170.87*	
1	76681.11	778.28	73673.16	770.36	70897.06	70994.22	68359.94	457.12	66073.55	170.87*
2	534.70		538.46	699.66	773.97	935.30	249.26	410.50	65975.81*	137.05
3	334.15		354.68	578.70	607.85	831.94	101.51*	325.46	847.37*	071.51
4	080.61		123.83	409.18	400.39	685.94	67918.29	203.68	690.29	65975.81*
5	76777.17		72848.81	193.34	154.27	498.94	702.71	047.32	507.14	851.81
6	427.21		532.36	72931.78*	69872.46		457.42	67856.51	300.85	702.38
7	034.22		178.21				185.98		074.88	530.06*
8			71789.89†							

\*Blended line.

†Doubtful.

TABLE I (Continued)  
Vacuum wave numbers of the lines of the Lyman bands of H<sub>2</sub>

J	4-10 band $\nu_0 = 64112.7_s \text{ cm}^{-1}$		4-11 band $\nu_0 = 62376.0_s \text{ cm}^{-1}$		4-12 band $\nu_0 = 60961.1_0 \text{ cm}^{-1}$		4-13 band $\nu_0 = 59911.9_z \text{ cm}^{-1}$		5-3 band $\nu_0 = 84660.6_0 \text{ cm}^{-1}$	
	P(J)	R(J)	P(J)	R(J)	P(J)	R(J)	P(J)	R(J)	P(J)	R(J)
0		64145.09		62408.42		60903.38		59944.07		84670.99
1	64054.17	151.38	62325.33	422.54*	60919.21	61016.44	59890.73	977.98	84559.75	653.23
2	63970.54	131.82	257.41	418.62	869.32	030.59*	852.37	60013.80		
3	863.34	087.82	173.79	397.92	812.92	037.02*	828.97	053.14	152.70	
4	734.57	019.98	076.69	362.10	752.48	037.02*	813.24	098.64		
5	586.88*	63931.54	61968.80	313.50	691.13	036.08	809.42	154.15		
6	423.41		853.58	252.26	632.79		823.11	224.73		
7			734.80		582.38		862.13	317.92		
8			617.42		540.24		935.72			

J	5-4 band $\nu_0 = 81192.5_0 \text{ cm}^{-1}$		5-5 band $\nu_0 = 77951.0_s \text{ cm}^{-1}$		5-6 band $\nu_0 = 74937.3_0 \text{ cm}^{-1}$		5-7 band $\nu_0 = 72155.1_z \text{ cm}^{-1}$		5-8 band $\nu_0 = 69611.9_s \text{ cm}^{-1}$	
	P(J)	R(J)	P(J)	R(J)	P(J)	R(J)	P(J)	R(J)	P(J)	R(J)
0				77982.35		74968.39		72186.59*		69643.23
1	81097.32	81190.90	77861.32	954.87	74853.21	946.78	72077.00	170.56	69539.93	633.51*
2	80916.90		713.92	870.15	717.30	872.46	71952.81	108.03	427.99	583.20
3	718.38		510.46	726.27*	530.99	746.85	784.12	71999.93	277.61	493.42
4			254.00	528.28	296.54	571.53	573.02		091.03	365.95
5			76945.25	277.39	016.69	348.82	322.36		68870.71*	202.79
6			589.33		73694.40	081.80	034.97		619.65	006.09*
7			189.52	76630.97		73773.24	70714.27		341.54	68781.18
8			75749.36†						039.55	529.30

J	5-9 band $\nu_0 = 67319.0_z \text{ cm}^{-1}$		5-10 band $\nu_0 = 65292.7_s \text{ cm}^{-1}$		5-11 band $\nu_0 = 63556.1_0 \text{ cm}^{-1}$		5-12 band $\nu_0 = 62141.1_z \text{ cm}^{-1}$		5-13 band $\nu_0 = 61091.9_z \text{ cm}^{-1}$	
	P(J)	R(J)	P(J)	R(J)	P(J)	R(J)	P(J)	R(J)	P(J)	R(J)
0		67350.12		65323.84		63586.88*		62172.33		61122.77
1	67253.20*	346.92	65234.12	327.62	63505.27	598.81	62099.21	192.77	61060.84	154.20*
2			149.28	304.50	435.88*	591.59	048.11	203.32	030.59	186.46
3	023.72		039.65	255.39	350.13	565.91	61989.24	205.05	005.29	221.16
4			64907.34	182.15	249.41	524.14	925.15	200.09		260.94
5	66675.14		754.84	087.05	136.84	468.90	859.06	191.50	60977.49	
6	462.93		585.60	64972.95	015.93		794.98	182.48	982.68	
7	230.45		403.09	842.90	62890.55		738.10	178.75		
8			209.52		765.40		693.55	183.83		
9							669.63			

J	5-14 band $\nu_0 = 60469.9_z \text{ cm}^{-1}$		6-5 band $\nu_0 = 79098.6_1 \text{ cm}^{-1}$		6-6 band $\nu_0 = 76084.8_s \text{ cm}^{-1}$		6-7 band $\nu_0 = 73302.7_z \text{ cm}^{-1}$		6-8 band $\nu_0 = 70759.5_s \text{ cm}^{-1}$	
	P(J)	R(J)	P(J)	R(J)	P(J)	R(J)	P(J)	R(J)	P(J)	R(J)
0		60501.01		79128.74				73332.70		70790.97
1	60452.52	546.10	79008.94	098.94		76090.53	73224.40	314.48	70687.30	777.94
2	451.32	606.30	78860.32		75863.87		099.16	248.56		723.84
3	468.70	684.49	654.62	78862.49	675.49	75882.87	72928.23	136.00	421.91	629.65
4	511.40	786.31	394.08				713.74	72978.54		
5			081.56	401.88			458.51	779.40		
6			77720.17				165.64			
7			314.05				71838.59	262.59		

\*Blended line.

†Doubtful.

TABLE I (Continued)  
 Vacuum wave numbers of the lines of the Lyman bands of H<sub>2</sub>

6-9 band $\nu_0 = 68466.6_0 \text{ cm}^{-1}$			6-10 band $\nu_0 = 66440.3_4 \text{ cm}^{-1}$			6-11 band $\nu_0 = 64703.6_3 \text{ cm}^{-1}$			6-12 band $\nu_0 = 63288.7_0 \text{ cm}^{-1}$			6-13 band $\nu_0 = 62239.5_2 \text{ cm}^{-1}$		
J	P(J)	R(J)	P(J)	R(J)	P(J)	R(J)	P(J)	R(J)	P(J)	R(J)	P(J)	R(J)		
0		68496.63					64733.51		63318.53			62269.34		
1	68401.00*	491.10*	66381.52	66471.78	64652.80	742.85	63247.00*	336.80	62208.32	298.41*				
2	300.93	450.40		445.04	582.50	732.00	194.42	343.94	177.69	327.12				
3	167.78	375.75*			494.17	702.04	133.30	341.23	149.44	357.31				
4	003.68	268.71			389.99	654.94	065.83	330.77	126.68	391.78				
5	67811.37	131.75		211.43	272.98	593.35	62995.38	315.60	113.66*	433.03				
6	593.94				146.52	521.97*	926.59*	300.32*	113.66*					
7	354.73	67777.74			014.86	438.81	862.35	286.89						
8	098.01						810.88							
9							778.93							

6-14 band $\nu_0 = 61617.5_0 \text{ cm}^{-1}$			7-5 band $\nu_0 = 80213.9_7 \text{ cm}^{-1}$			7-6 band $\nu_0 = 77200.2_4 \text{ cm}^{-1}$			7-7 band $\nu_0 = 74418.0_0 \text{ cm}^{-1}$			7-8 band $\nu_0 = 71874.9_2 \text{ cm}^{-1}$		
J	P(J)	R(J)	P(J)	R(J)	P(J)	R(J)	P(J)	R(J)	P(J)	R(J)	P(J)	R(J)		
0		61647.08		80243.15		77229.00		74446.92		71903.82				
1	61600.08*	690.06	80124.38	211.00	77116.12	202.71	74339.87	426.52	71802.90	880.53*				
2	597.46	747.14	79974.71	118.49	76977.79	121.67	213.36	357.25	688.63	832.55				
3	612.74	820.58	766.66	79967.05	786.93*	76987.25	040.01	240.38	533.71	733.79				
4	651.98	916.98	502.17*		545.94	801.15	73822.81*	078.10*	340.41					
5			78986.04		257.31	565.94	562.68*	73871.87	111.32					
6					75924.49		264.79	625.73*	70849.67					
7					550.97*		72931.78*	342.62	559.06					

7-9 band $\nu_0 = 69581.9_4 \text{ cm}^{-1}$			7-10 band $\nu_0 = 67555.7_0 \text{ cm}^{-1}$			7-11 band $\nu_0 = 65819.0_4 \text{ cm}^{-1}$			7-12 band $\nu_0 = 64404.0_0 \text{ cm}^{-1}$			7-13 band $\nu_0 = 63354.8_0 \text{ cm}^{-1}$		
J	P(J)	R(J)	P(J)	R(J)	P(J)	R(J)	P(J)	R(J)	P(J)	R(J)	P(J)	R(J)		
0		69610.88				65847.37*		64432.76		63383.62				
1	69516.45	603.12	67497.09	67583.86	65768.21	854.82	64362.17	448.74	63323.80	410.40				
2	415.19	550.05	409.97	553.86	696.65	840.58	308.65	452.60	291.98	435.88				
3	279.75	480.09	295.73	496.33*	606.13	806.44	245.31	445.61	261.40	461.71				
4	112.38	367.99		412.13		754.19	174.56	430.10	235.35*	490.86				
5	68915.81	224.92	66995.50	304.65	686.54		099.76	408.88	218.25	527.21				
6			815.55						212.94	576.18				
7	448.08		620.51	031.67					230.22					

7-14 band $\nu_0 = 62732.9_2 \text{ cm}^{-1}$			8-6 band $\nu_0 = 78284.2_0 \text{ cm}^{-1}$			8-7 band $\nu_0 = 75502.0_0 \text{ cm}^{-1}$			8-8 band $\nu_0 = 72958.9_4 \text{ cm}^{-1}$			8-10 band $\nu_0 = 68639.7_2 \text{ cm}^{-1}$		
J	P(J)	R(J)	P(J)	R(J)	P(J)	R(J)	P(J)	R(J)	P(J)	R(J)	P(J)	R(J)		
0		62761.61		78312.24		75529.89		72986.90		68667.61				
1	62715.60	802.21	78200.19*	284.08	75423.78	507.66	72886.86	970.83	68580.90*	665.07				
2	711.61	855.68	061.06*	200.19*	296.58	435.83	771.70	911.22	492.92	632.49				
3			77868.42	062.66	121.42	315.65	615.07	809.32	376.84	571.36				
4			624.36	77872.94		149.88	419.07	667.97	235.33					
5			332.88*	632.48			186.59*		070.81	364.03*				
6			76996.70	339.49			71921.60		67887.55					
7									679.26*					

\*Blended line.

TABLE I (Continued)  
Vacuum wave numbers of the lines of the Lyman bands of H<sub>2</sub>

J	8-11 band $\nu_0 = 66903.0_4 \text{ cm}^{-1}$		8-12 band $\nu_0 = 65488.0_8 \text{ cm}^{-1}$		8-13 band $\nu_0 = 64438.9_0 \text{ cm}^{-1}$		8-14 band $\nu_0 = 63816.9_4 \text{ cm}^{-1}$		9-6 band $\nu_0 = 79337.0_2 \text{ cm}^{-1}$	
	P(J)	R(J)	P(J)	R(J)	P(J)	R(J)	P(J)	R(J)	P(J)	R(J)
0		66930.81		65515.74				63844.69		79363.91
1	66852.12	936.15	65446.04	530.06*			63799.52	883.41	79252.98	333.53
2	779.76	919.32	391.95*	530.06*			794.82	934.29	112.64	
3	687.34	881.62		520.85		64536.04	806.06	64000.36	78917.53*	104.37
4	577.25			501.87	64313.92		839.36	087.52*	670.65	
5	452.56			480.42					374.26	
6	317.71									

J	9-7 band $\nu_0 = 76554.8_4 \text{ cm}^{-1}$		9-8 band $\nu_0 = 74011.7_0 \text{ cm}^{-1}$		9-9 band $\nu_0 = 71718.7_4 \text{ cm}^{-1}$		9-10 band $\nu_0 = 69692.4_4 \text{ cm}^{-1}$		9-11 band $\nu_0 = 67955.8_2 \text{ cm}^{-1}$	
	P(J)	R(J)	P(J)	R(J)	P(J)	R(J)	P(J)	R(J)	P(J)	R(J)
0		76581.90		74038.72		71745.41		69719.22		67982.82
1	76476.56	557.06	73939.51	020.09	71653.13	733.79*	69633.51*	714.38	67905.02*	985.57
2	347.98	482.09	822.81*	73957.12	549.85	683.59	545.04	678.42	831.51	965.40
3	170.78	357.36	664.28	850.86*	410.50	596.98	426.20	613.04	736.80	923.43
4	75947.33		464.97	703.19	237.10				623.43	861.76
5	679.70		228.14	516.70	032.76				494.37	782.87
6	372.19				70800.69				353.40	
7	028.10				544.37					
8					264.72					

J	9-12 band $\nu_0 = 66540.8_4 \text{ cm}^{-1}$		9-13 band $\nu_0 = 65491.6_4 \text{ cm}^{-1}$		9-14 band $\nu_0 = 64869.7_0 \text{ cm}^{-1}$		10-6 band $\nu_0 = 80359.2_4 \text{ cm}^{-1}$		10-7 band $\nu_0 = 77577.0_4 \text{ cm}^{-1}$	
	P(J)	R(J)	P(J)	R(J)	P(J)	R(J)	P(J)	R(J)	P(J)	R(J)
0		66567.30		65518.26		64896.36		80385.82		77603.33
1	66498.85	579.36*	65460.43	541.00	64852.32	932.68	80275.22	354.02	77498.79	577.62
2	443.33		426.57	560.61	846.53	980.40	134.26		369.68	500.98
3	375.85	562.01	391.95*	578.59	855.47	65042.00	79938.33		191.28	376.72
4	299.16		359.97	598.26	885.46	123.69			76966.02	195.79
5	216.68	505.08	334.93	623.48	956.20	244.87			609.02	76952.00
6	132.48								382.24	
7	051.88									

J	10-8 band $\nu_0 = 75033.9_2 \text{ cm}^{-1}$		10-9 band $\nu_0 = 72740.9_6 \text{ cm}^{-1}$		10-10 band $\nu_0 = 70714.7_0 \text{ cm}^{-1}$		10-11 band $\nu_0 = 68978.0_4 \text{ cm}^{-1}$		10-12 band $\nu_0 = 67563.0_6 \text{ cm}^{-1}$	
	P(J)	R(J)	P(J)	R(J)	P(J)	R(J)	P(J)	R(J)	P(J)	R(J)
0		75060.17		72767.18				69004.20		67589.05
1	74961.66	040.63	72675.43	754.28			68927.19	006.09*	67521.09	599.97
2	845.08	74076.15	571.52	702.98			853.47	68984.48	465.02	596.38
3	684.95	870.30	431.02	615.85	70446.94		757.35	942.80	396.45	582.06
4		712.74		256.48			642.55		318.34	
5			052.22		131.85		513.22*		236.08	

\*Blended line.

TABLE I (Concluded)  
Vacuum wave numbers of the lines of the Lyman bands of  $H_2$

10-13 band $\nu_0 = 66513.8_s \text{ cm}^{-1}$			10-14 band $\nu_0 = 65891.9_s \text{ cm}^{-1}$		11-7 band $\nu_0 = 78569.1_s \text{ cm}^{-1}$		11-8 band $\nu_0 = 76025.9_s \text{ cm}^{-1}$		11-9 band $\nu_0 = 73733.0_s \text{ cm}^{-1}$	
<i>J</i>	<i>P(J)</i>	<i>R(J)</i>	<i>P(J)</i>	<i>R(J)</i>	<i>P(J)</i>	<i>R(J)</i>	<i>P(J)</i>	<i>R(J)</i>	<i>P(J)</i>	<i>R(J)</i>
0		66539.83		65918.00		78594.16				73758.00
1	66482.61	561.53	65874.59	953.59*	78491.62	566.00*	75954.00		73667.30	742.56
2	448.18	579.36*	868.14	999.76	360.59	485.51	835.72	75960.64	562.68*	687.26
3	412.50	597.96	875.93	66061.41	179.80	354.14			419.26	593.59
4	379.10		904.64*		77950.57	173.54			240.66	
5	354.29				676.42	77946.27*	224.84		029.47	302.18
6	328.29				359.99	672.42				
7	304.99				76992.10†					

11-10 band $\nu_0 = 71706.7_s \text{ cm}^{-1}$		11-12 band $\nu_0 = 68555.1_s \text{ cm}^{-1}$		11-13 band $\nu_0 = 67505.9_s \text{ cm}^{-1}$		11-14 band $\nu_0 = 66883.9_s \text{ cm}^{-1}$		12-7 band $\nu_0 = 79531.5_s \text{ cm}^{-1}$		
<i>J</i>	<i>P(J)</i>	<i>R(J)</i>	<i>P(J)</i>	<i>R(J)</i>	<i>P(J)</i>	<i>R(J)</i>	<i>P(J)</i>	<i>R(J)</i>	<i>P(J)</i>	<i>R(J)</i>
0		71731.95				67530.83		66908.84		79556.56
1	71648.41*	723.32	68513.11*	68588.38	67474.78	549.95	66866.56	941.79	79453.57	529.13
2	557.16	682.14		580.90*	439.16	563.71*	858.96	984.04	323.09	
3	435.36	609.64	384.92	559.27	400.98	575.25	864.34	67038.34	142.70	293.46
4	285.12		302.64		363.65		889.08	111.80		
5	109.15		213.35				925.38			

12-8 band $\nu_0 = 76988.3_s \text{ cm}^{-1}$		12-9 band $\nu_0 = 74695.4_s \text{ cm}^{-1}$		12-10 band $\nu_0 = 72669.1_s \text{ cm}^{-1}$		12-11 band $\nu_0 = 70932.4_s \text{ cm}^{-1}$		12-12 band $\nu_0 = 69517.5_s \text{ cm}^{-1}$		
<i>J</i>	<i>P(J)</i>	<i>R(J)</i>	<i>P(J)</i>	<i>R(J)</i>	<i>P(J)</i>	<i>R(J)</i>	<i>P(J)</i>	<i>R(J)</i>	<i>P(J)</i>	<i>R(J)</i>
0		77013.30		74720.15		72694.19		70957.44*		
1	76916.27	76992.10*	74629.90		72610.67	686.33	70881.73	957.44*	69476.13	69551.23
2	797.97	929.86	525.61	656.59	519.68	651.33	806.52			
3	636.11	786.93*	382.02	532.59	398.31	548.95	708.66	859.33		498.92
4	437.90		209.34		254.49					
5	164.10		73968.65		048.40		430.27			

12-13 band $\nu_0 = 68468.3_s \text{ cm}^{-1}$		12-14 band $\nu_0 = 67846.3_s \text{ cm}^{-1}$		13-7 band $\nu_0 = 80464.9_s \text{ cm}^{-1}$		13-8 band $\nu_0 = 77921.8_s \text{ cm}^{-1}$		13-9 band $\nu_0 = 75628.8_s \text{ cm}^{-1}$		
<i>J</i>	<i>P(J)</i>	<i>R(J)</i>	<i>P(J)</i>	<i>R(J)</i>	<i>P(J)</i>	<i>R(J)</i>	<i>P(J)</i>	<i>R(J)</i>	<i>P(J)</i>	<i>R(J)</i>
0							77946.27*			
1	68437.24*	68513.22*		67905.02*		80457.32	77849.84	920.13	75563.23	
2	401.00*							847.21		75572.55
3	364.03*	514.16*	67827.33	977.97	80070.90		563.58*	726.27*	310.55	
4	332.87						354.95	563.58*		
5	270.01						104.78	351.62		
6							76817.47†			

13-10 band $\nu_0 = 73602.5_s \text{ cm}^{-1}$		13-11 band $\nu_0 = 71865.9_s \text{ cm}^{-1}$		13-12 band $\nu_0 = 70450.9_s \text{ cm}^{-1}$		13-14 band $\nu_0 = 68779.8_s \text{ cm}^{-1}$		
<i>J</i>	<i>P(J)</i>	<i>R(J)</i>	<i>P(J)</i>	<i>R(J)</i>	<i>P(J)</i>	<i>R(J)</i>	<i>P(J)</i>	<i>R(J)</i>
0		73625.73*		71889.53*			68803.24	
1	73544.04	614.32	71815.19	885.56			68762.59	832.96
2	451.36	568.30	737.96*	855.33			753.33	870.71*
3	326.35	489.62	636.78	800.10	70276.40		755.57	918.83
4	171.22	379.65	513.43				775.45	
5	72989.19	242.86	371.19		093.39			

\*Blended line.

†Doubtful.





Most of our assignments were checked by combination differences. The agreement of combination differences formed from unblended lines is within  $\pm 0.1 \text{ cm}^{-1}$ . Table III illustrates this agreement for the level  $v'' = 11$ . Similar tables were set up for all other vibrational levels of the upper and lower state but are not reproduced here in order to save space.

TABLE III  
 $\Delta_2 F''(J)$  values derived from bands with  $v'' = 11$

Band \ J	1	2	3	4	5	6
2-11	151.03	248.69	341.87	429.11		
3-11	(151.48*)	248.68*	341.95*	429.02	508.42	578.50
4-11	151.01	248.75*	341.93	429.12	508.52	(578.64)
5-11	151.00*	248.68	(342.18)	429.07	508.21	(578.35)
6-11	151.01	248.68	342.01	429.06	508.42	578.49
7-11	150.72*	248.69				
8-11	151.05	248.81	342.07	429.06*		
9-11	151.01	248.77	341.97	429.06	508.30	
10-11	150.73	248.74*	341.93	(429.58)		
12-11	150.92*	248.78*		429.06*		
13-11		248.78	341.90	428.91		
Mean	150.94	248.73	341.95	429.05	508.37	578.50

\*From blended lines.

( ) Not included in the mean.

(a) *The Lower State,  $X^1\Sigma_g^+$*

In Fig. 2 the values of  $\{\Delta_2 F''(J)\}/\{4(J+\frac{1}{2})\}$  are plotted against  $(J+\frac{1}{2})^2$  for all vibrational levels of the ground electronic state. As is well known, according to the relation

$$(1) \quad \frac{\Delta_2 F_v(J)}{4(J+\frac{1}{2})} = \left(B_v - \frac{3}{2}D_v + \frac{27}{16}H_v\right) - \left(2D_v - \frac{17}{2}H_v\right)(J+\frac{1}{2})^2 + 3H_v(J+\frac{1}{2})^4 \dots$$

the intercepts of the lines in Fig. 2 give the  $B_v$  values, the slopes the  $D_v$  values, and the curvatures the  $H_v$  values. For the actual determination of these quantities the plots were made for each  $v''$  separately after addition of

$$a(J+\frac{1}{2})^2 - b(J+\frac{1}{2})^4$$

with suitable values of  $a$  and  $b$  to make the resulting line straight and of sufficiently small slope that both the remaining slope and the intercept could be determined accurately. The value of  $b$  is then  $3H_v$  while the slope of the straight line added to  $a$  is  $\{2D_v - (17/2)H_v\}$  and the intercept is  $\{B_v - (3/2)D_v + (27/16)H_v\}$ .

A check on the  $B_v$  and  $D_v$  values is obtained in the process of determining the vibrational differences  $\Delta G''(v+\frac{1}{2})$ . This was done by forming the differences of corresponding lines of bands with the same upper state and differing by  $\Delta v'' = 1$  in the lower state according to the formula

$$(2) \quad R_{v''}(J) - R_{v''+1}(J) = P_{v''}(J) - P_{v''+1}(J) = \Delta G''(v''+\frac{1}{2}) \\ - (B_{v''} - B_{v''+1})J(J+1) + (D_{v''} - D_{v''+1})J^2(J+1)^2 \\ - (H_{v''} - H_{v''+1})J^3(J+1)^3 + \dots$$

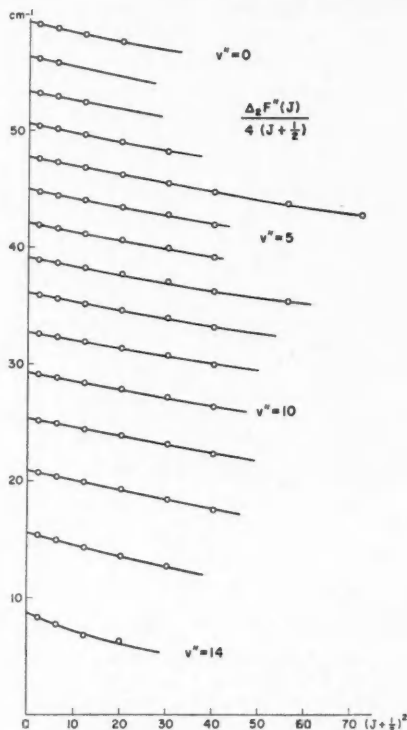


FIG. 2. Values of  $\Delta^2 F''(J)/4(J+\frac{1}{2})$  for all observed vibrational levels of the ground state of  $H_2$ .

If one adds to the numerical value of the left-hand side of this equation the numerical value of the quantity

$$(B_{v''} - B_{v''+1})J(J+1) - (D_{v''} - D_{v''+1})J^2(J+1)^2 + (H_{v''} - H_{v''+1})J^3(J+1)^3$$

with the previously determined  $B_v$ ,  $D_v$ , and  $H_v$  values and plots against  $J(J+1)$  one should obtain a horizontal line if the  $B_v$ ,  $D_v$ , and  $H_v$  values were correct. The slope and curvature of the line actually obtained gives small corrections to these constants. Actually for hydrogen the terms in  $D_v$  and  $H_v$  are relatively much larger than for most other molecules and it is difficult to obtain them with sufficient accuracy from the plots of equation (2). In most cases, therefore, the  $D_v$  and  $H_v$  were taken from the  $\Delta_2 F''$  values and only the  $B_v$  values were slightly adjusted. However, for  $v'' = 13$  and 14 the number of  $\Delta F''$  values available is insufficient and the constants were determined entirely from the  $\Delta G$  plots. The curvature of these last  $\Delta G$  plots is so large that it cannot be satisfactorily represented by (2). Therefore the  $B_{13}$ ,  $D_{13}$ ,  $B_{14}$ ,  $D_{14}$  have much reduced accuracy.

In Table IV all the  $B''$ ,  $D''$ , and  $H''$  values thus obtained are collected. The constants for  $v = 0, 1, 2$  are those of Stoicheff (1957), except that the values for  $v = 1$  have been recalculated from his data using an approximate  $H_1$  value from Fig. 6 below. The level  $v = 3$  is the only one for which our measurements can be compared with Stoicheff's values. Stoicheff found  $B_3 = 50.628_2$  and  $D_3 = 0.0412_5 \text{ cm}^{-1}$  while we find  $B_3 = 50.623_2$  and  $D_3 = 0.0406_9$ . The agreement is quite satisfactory. In Table IV the average of these two sets is listed for  $v = 3$ . For comparison with the new values the earlier  $B_v$  data of Jeppesen are listed in column 3. Experimental  $D_v$  values had previously been determined only for  $v = 0, 2, 3$  while  $H_v$  had only been determined for  $v = 0$  (Stoicheff 1957). In spite of the lower wave number accuracy the present data yield  $D_v$  and  $H_v$  of an accuracy comparable to the Raman work since they extend to higher  $J$  values.

TABLE IV  
Rotational constants of the ground state of  $\text{H}_2$

$v''$	$B_v'', \text{cm}^{-1}$		$D_v'', \text{cm}^{-1}$	$H_v'', \times 10^{-6} \text{cm}^{-1}$
	This paper	Jeppesen		
0	59.3392 <sup>a</sup>	59.373	0.0450 <sup>a</sup>	5.2 <sup>a</sup>
1	56.3685 <sup>b</sup>	56.391	0.0437 <sup>b</sup>	
2	53.4754 <sup>a</sup>	53.508	0.0427 <sup>a</sup>	
3	50.6257 <sup>d</sup>	50.676	0.0409 <sup>d</sup>	3.75
4	47.801 <sub>3</sub>	47.850	0.0397 <sub>1</sub>	3.50
5	44.958 <sub>1</sub>	44.954	0.0385 <sub>1</sub>	3.4 <sub>2</sub>
6	42.096 <sub>1</sub>	42.075	0.0377 <sub>9</sub>	3.3 <sub>3</sub>
7	39.145 <sub>3</sub>	39.116	0.0367 <sub>7</sub>	3.2 <sub>1</sub>
8	36.088 <sub>2</sub>	36.068	0.0365 <sub>3</sub>	3.2 <sub>0</sub>
9	32.833 <sub>0</sub>	32.694	0.0363 <sub>4</sub>	3.0 <sub>9</sub>
10	29.311 <sub>2</sub>		0.0366 <sub>0</sub>	2.5 <sub>0</sub>
11	25.399 <sub>1</sub>		0.0378 <sub>1</sub>	1.8 <sub>1</sub>
12	20.926 <sub>3</sub>		0.0413 <sub>0</sub>	(1.8 <sub>3</sub> ) <sup>e</sup>
13	15.582 <sub>4</sub> <sup>c</sup>		0.0492 <sub>7</sub>	—
14	8.770 <sub>1</sub> <sup>c</sup>		0.0846 <sub>7</sub>	—

<sup>a</sup>Stoicheff's values.

<sup>b</sup>Obtained from Stoicheff's data using an interpolated  $H''$ .

<sup>c</sup>Obtained from  $\Delta G''$  plots.

<sup>d</sup>Average of Stoicheff's and our values.

<sup>e</sup>Assumed value.

The  $\Delta G''$  values obtained from the intercepts of the plots of equation (2) are listed in Table V. The first three values are from Stoicheff. The values of Jeppesen are given in column 3. The fourth column gives  $\Delta_2 G''(v+1)$  and the fifth column  $G_0(v)$  obtained by simply adding up the values in the first column.

In Figs. 3a, 4, 5a, 6, 7a, 8 are plotted the values of  $B_v$ ,  $\Delta B_v$ ,  $D_v$ ,  $H_v$ ,  $\Delta G(v+\frac{1}{2})$ , and  $\Delta^2 G(v+1)$ . The  $B_v$  and  $\Delta G_v$  curves have very similar behavior showing an initial slight positive curvature and toward the end a rapid convergence to zero. The  $D_v$  curve is of a quite different type reaching very high values at the last  $v''$  values.  $H_v$  seems to change sign near  $v = 12$ .

The  $B_v$  and  $\Delta G(v+\frac{1}{2})$  values are much more accurate than can be represented by plots like Figs. 3a and 7a. Even after subtraction of linear terms

TABLE V  
Vibrational differences and vibrational levels in the ground state of H<sub>2</sub>

$v + \frac{1}{2}$	$\Delta G''(v + \frac{1}{2})$		$\Delta^2 G''$		$G_0(v)$	$v$
	This paper	Jeppesen	This paper	This paper		
				0		0
$\frac{1}{2}$	4161.13 <sub>7</sub> *	4160.96				
$1\frac{1}{2}$	3925.97 <sub>8</sub> *	3922.18	235.16 <sub>2</sub>	4161.14		1
$2\frac{1}{2}$	3695.24 <sub>0</sub> *	3693.82	230.73 <sub>8</sub>	8087.11		2
$3\frac{1}{2}$	3468.01	3467.82	227.23 <sub>0</sub>	11782.35		3
$4\frac{1}{2}$	3241.56	3239.51	226.45	15250.36		4
$5\frac{1}{2}$	3013.73	3013.96	227.83	18491.92		5
$6\frac{1}{2}$	2782.18	2782.01	231.54 <sub>8</sub>	21505.65		6
$7\frac{1}{2}$	2543.14	2543.36	239.04 <sub>8</sub>	24287.83		7
$8\frac{1}{2}$	2292.96	2292.55	250.18	26830.97		8
$9\frac{1}{2}$	2026.26	2026.28	266.70	29123.93		9
$10\frac{1}{2}$	1736.66	1737.53	289.60	31150.19		10
$11\frac{1}{2}$	1414.98	1416.92	321.68	32886.85		11
$12\frac{1}{2}$	1049.18		365.80	34301.83		12
$13\frac{1}{2}$	621.96		427.22	35351.01		13
				35972.97		14

\*Stoicheff's values.

as in Figs. 3*b* and 7*b* a very smooth curve remains which in each case shows a point of inflection at about  $v'' = 3$ . The rise of the first few points above the straight line representing the next few points is quite striking (see the initial drop of the  $\Delta B$  and  $\Delta^2 G$  curves) and apparently must be related to a peculiarity of the potential energy curve. A similar point of inflection has been observed for the  $\Delta G$  values of the ground state of the O<sub>2</sub> molecule (Curry and Herzberg 1934). While H<sub>2</sub> and O<sub>2</sub> are the only cases of homonuclear molecules for which this anomaly has been observed in the ground state, it is quite common for polar molecules, for example HF, HCl, and others. It may be due to the contribution of ionic states to the ground state, since for ionic states a  $\Delta G$  curve with positive curvature throughout is expected.

On account of the initial inflection it is difficult to represent the whole  $B_v''$  and  $\Delta G''$  curves by polynomial expressions except by using a very large number of terms. This is shown by Figs. 3*c* and 7*c* where the deviations from the five-term formulae

$$(3) \quad B_v'' = 60.818_6 - 2.9621_1(v + \frac{1}{2}) + 0.00458(v + \frac{1}{2})^2 + 0.004548(v + \frac{1}{2})^3 - 0.0005105(v + \frac{1}{2})^4,$$

$$(4) \quad \Delta G''(v + \frac{1}{2}) = 4278.70_6 - 235.4967(v + \frac{1}{2}) + 0.5886_1(v + \frac{1}{2})^2 + 0.2803_6(v + \frac{1}{2})^3 - 0.03790_8(v + \frac{1}{2})^4$$

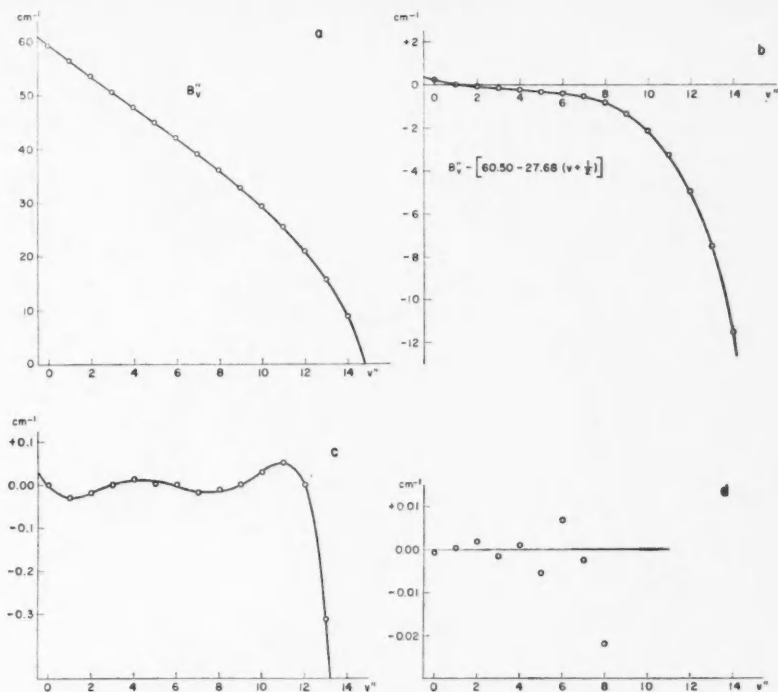


FIG. 3.  $B_v$  curve for the  $X^1\Sigma_g^+$  ground state of  $H_2$ .  
 (a) Plotted directly.  
 (b) Plotted after subtraction of a linear term.  
 (c) Residuals of equation (3).  
 (d) Residuals of equation (9).

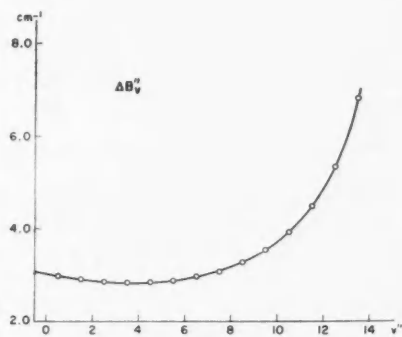


FIG. 4.  $\Delta B_v$  curve for the  $X^1\Sigma_g^+$  ground state of  $H_2$ .

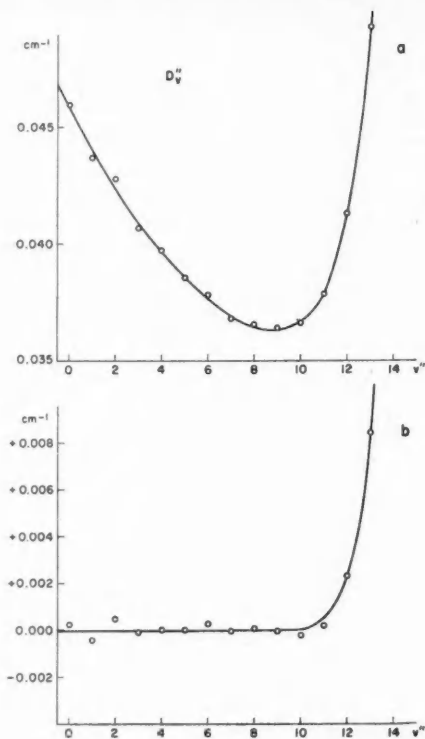


FIG. 5.  $D_v$  curve for the  $X^1\Sigma_g^+$  ground state of  $H_2$ .  
 (a) Plotted directly.  
 (b) Residuals of equation (15).

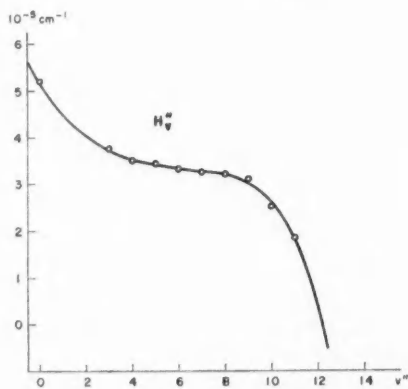


FIG. 6.  $H_v$  curve for the  $X^1\Sigma_g^+$  ground state of  $H_2$ .

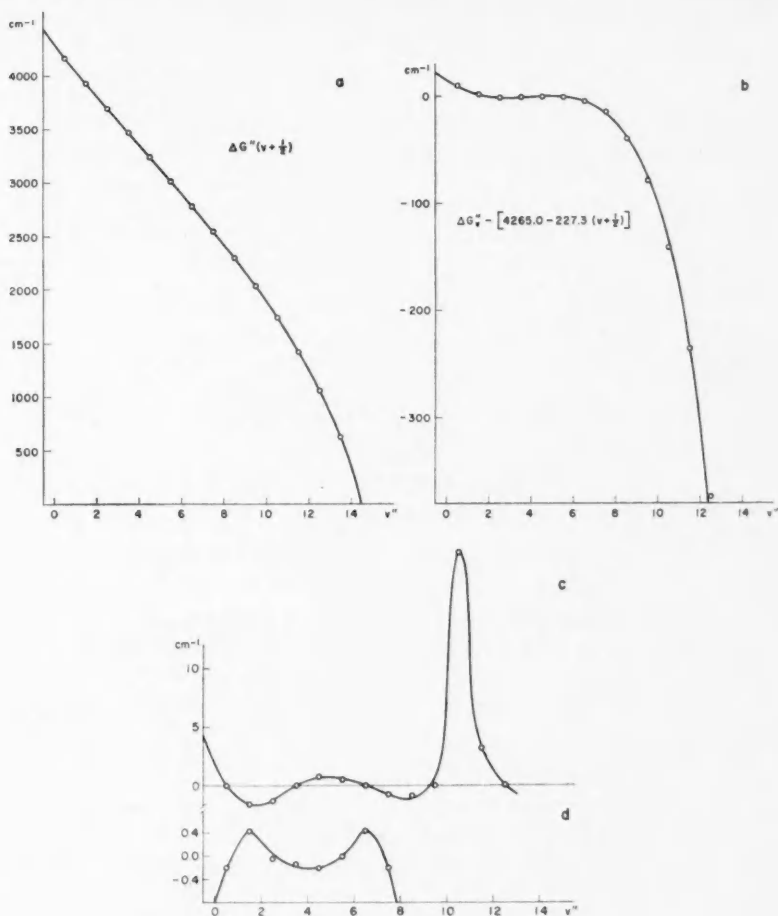


FIG. 7.  $\Delta G(v + \frac{1}{2})$  curve for the  $X^1\Sigma_g^+$  ground state of H.  
 (a) Plotted directly.  
 (b) Plotted after subtraction of a linear term.  
 (c) Residuals of equation (4).  
 (d) Residuals of equation (14).

are shown. These formulae were so chosen that the observed  $B_v$  and  $\Delta G(v + \frac{1}{2})$  for  $v = 0, 3, 6, 9, 12$  are exactly represented. It is seen that there are large systematic deviations which are much larger than the possible error of the individual  $B_v$  and  $\Delta G(v + \frac{1}{2})$  values and which cannot be reduced by a different choice of coefficients in the equations. It is clear from Figs. 3c and 7c that the first term in (3) and (4) does not give the correct  $B_v$  and  $\omega_e$  respectively. Rather,

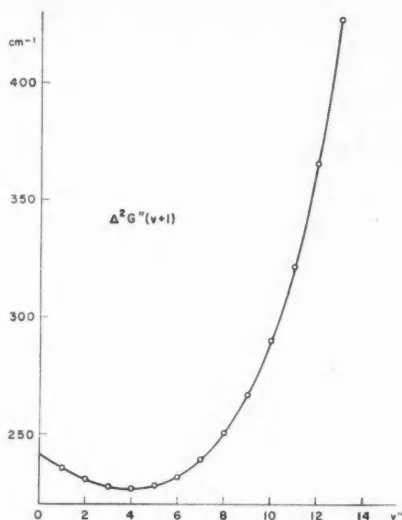


FIG. 8.  $\Delta^2 G''(v+1)$  curve for the  $X^1\Sigma_g^+$  ground state of  $H_2$ .

in order to obtain these constants the curves in Figs. 3c and 7c have to be extrapolated to  $-\frac{1}{2}$ . Such an extrapolation is inherently beset with difficulties when the  $B_v$  and  $\Delta G$  values do not follow a simple formula and, therefore, the  $B_e$  and  $\omega_e$  values derived in the following discussion have appreciably larger limits of error than the individual  $B_v$  and  $\Delta G$  values.

Stoicheff (1957) obtained from his  $B_0, B_1, B_2, B_3$  values, by the method of least squares, the three-term formula

$$(5) \quad B_v'' = 60.840_7 - 3.0177_4(v + \frac{1}{2}) + 0.0285_5(v + \frac{1}{2})^2$$

which, when the slightly revised  $B_1$  and  $B_3$  values of Table IV are used, changes to

$$(6) \quad B_v'' = 60.842_1 - 3.0243_6(v + \frac{1}{2}) + 0.0302_6(v + \frac{1}{2})^2.$$

If the same  $B_v$  values are represented by a four-term formula one obtains

$$(7) \quad B_v'' = 60.864_3 - 3.0810_8(v + \frac{1}{2}) + 0.0644_8(v + \frac{1}{2})^2 - 0.0057_0(v + \frac{1}{2})^3,$$

while a five-term formula for the first five  $B_v$  values is

$$(8) \quad B_v'' = 60.868_7 - 3.0958_3(v + \frac{1}{2}) + 0.0788_7(v + \frac{1}{2})^2 - 0.0110_7(v + \frac{1}{2})^3 + 0.0006_7(v + \frac{1}{2})^4.$$

Finally a least squares four-term formula was developed from the first eight  $B_v$  values ( $B_0 \dots B_7$ ):

$$(9) \quad B_v'' = 60.863_8 - 3.0763_8(v + \frac{1}{2}) + 0.0601_7(v + \frac{1}{2})^2 - 0.0048_1(v + \frac{1}{2})^3.$$



As shown in Fig. 3*d*, the residuals for the first five  $B_e$  values are less than  $0.002 \text{ cm}^{-1}$ . This together with the agreement with  $B_e$  from (7) and (8) suggests that a fairly satisfactory extrapolation to  $-\frac{1}{2}$  has been obtained and that we can put  $B_e = 60.864$ ,  $\alpha_e = 3.076_4$ ,  $\gamma_e = 0.0601_7$ ,  $\delta_e = 0.0048_1 \text{ cm}^{-1}$ . These constants are significantly different from Stoicheff's values which were based on a three-term formula. It is believed that the new  $B_e$  value represents an improvement.

With regard to the vibrational levels the situation is not as satisfactory. Using the first three, four, five, and six  $\Delta G$  values one obtains the following three-, four-, five-, and six-term formulae (the first already given by Stoicheff)

$$(10) \quad \Delta G''(v+\frac{1}{2}) = 4280.299 - 239.457_0(v+\frac{1}{2}) + 2.1725_7(v+\frac{1}{2})^2,$$

$$(11) \quad \Delta G''(v+\frac{1}{2}) = 4280.666 - 240.4725_8(v+\frac{1}{2}) + 2.9050_0(v+\frac{1}{2})^2 \\ - 0.1536_7(v+\frac{1}{2})^3,$$

$$(12) \quad \Delta G''(v+\frac{1}{2}) = 4280.173 - 238.8198_3(v+\frac{1}{2}) + 1.2898_1(v+\frac{1}{2})^2 \\ + 0.4473_3(v+\frac{1}{2})^3 - 0.07512_6(v+\frac{1}{2})^4,$$

$$(13) \quad \Delta G''(v+\frac{1}{2}) = 4279.590 - 236.7367(v+\frac{1}{2}) - 1.0535_2(v+\frac{1}{2})^2 \\ + 1.5820_0(v+\frac{1}{2})^3 - 0.32179_2(v+\frac{1}{2})^4 + 0.019733(v+\frac{1}{2})^5.$$

There is no clear convergence. If one uses the first eight  $\Delta G$  values for a four-term least square solution one finds

$$(14) \quad \Delta G''(v+\frac{1}{2}) = 4282.041_7 - 243.5764_0(v+\frac{1}{2}) + 4.5417_4(v+\frac{1}{2})^2 \\ - 0.3966_7(v+\frac{1}{2})^3.$$

The residuals from this formula are plotted in Fig. 7*d*. The deviation of  $\Delta G(1\frac{1}{2})$  and  $\Delta G(6\frac{1}{2})$  from the formula is far larger than any conceivable error of the observed values. One must assume that the true  $\Delta G$  curve is strongly curved with respect to eq. (14) (see Fig. 7*c*) and therefore  $\omega_e$ ,  $\omega_e x_e$  . . . cannot be obtained from this formula. The  $\omega_e$  values corresponding to the formulae (4), (10), (11), (12), (13), (14) are 4396.55, 4400.39, 4401.39, 4399.80, 4398.30, 4404.59  $\text{cm}^{-1}$  respectively. Both the first and the last of these values are clearly not the true  $\omega_e$  values since the residuals of (4) and (14) plotted in Figs. 7*c* and 7*d* indicate definitely a large deviation for  $v = -\frac{1}{2}$ . It is very difficult to determine which of the remaining four  $\omega_e$  values (if any) is the correct one since there is no convergence. For lack of better information it seems best to retain Stoicheff's original value 4400.39  $\text{cm}^{-1}$  based on the first three  $\Delta G$  values since there is no good reason why the initial part of the curve should depend on the higher terms necessary to account for the higher  $\Delta G$  values. One must, however, realize that while the  $\omega_e$  value in itself is quite accurate, it depends strongly on the method of evaluation (i.e. the number of terms used). This large uncertainty of  $\omega_e$  and the smaller one of  $B_e$  is unfortunate since it is the  $B_e$ ,  $\omega_e$ , . . . values that can be most directly interpreted in terms of internuclear distances and vibrational frequencies and which are required if one wants to predict the constants of the isotopic molecules HD, D<sub>2</sub>, HT, T<sub>2</sub>, etc.

The  $D_v$  values can be represented by a polynomial more easily than the  $B_v$  and  $\Delta G$  values. Figure 5b shows the residuals using the four-term expression

$$(15) \quad D_v'' = 0.04657_3 - 0.001616(v'' + \frac{1}{2}) - 1.43 \times 10^{-5}(v'' + \frac{1}{2})^2 + 7.6 \times 10^{-6}(v'' + \frac{1}{2})^3.$$

As shown by Figs. 3a and 7a, both the  $B_v$  and the  $\Delta G$  curves are likely to go through zero between  $v = 14$  and  $v = 15$  in agreement with the fact that no bands with  $v = 15$  were found in spite of considerable search. The breaking-off of the vibrational structure in the ground state of  $H_2$  does not lead to a very accurate value for the dissociation energy  $D_0^0$  since the last observed interval is still fairly large. However, it is consistent with the precise value  $D_0^0 = 36116 \pm 6 \text{ cm}^{-1}$  obtained by Beutler (1935) from the onset of the far ultraviolet absorption continuum.

The energy of the  $v'' = 14$  level above  $v'' = 0$  (see Table V) is  $35973.0 \text{ cm}^{-1}$ . This is the  $J = 0$  level. The  $J = 1$  level lies  $2B - 4D - 8H = 17.2 \text{ cm}^{-1}$  above this. Adding the observed  $\Delta_2 F$  values successively to the energies of the  $J = 0$  and  $J = 1$  levels, one obtains the following values for the rotational levels of the last vibrational level

$J = 0$	35973.0,	$J = 1$	35990.2,	$J = 2$	36022.8,
$J = 3$	36067.6,	$J = 4$	36117.8,	$J = 5$	36153.4.

The last observed rotational level is definitely above the dissociation limit, while the second last is possibly above it. The existence of sharp rotational levels above the dissociation limit is easily understood since the effective potential energy curves for  $J \neq 0$  have maxima which have to be passed before the molecule can dissociate (see e.g. Herzberg 1950b). Unfortunately it is not readily possible to predict the exact height of these maxima unless the potential curve for  $J = 0$  were very precisely known for large  $r$  values. From the observation that lines with  $J = 5$  are still quite sharp while lines with  $J = 6$  are absent, presumably on account of extreme width, one must conclude that for barriers of more than  $60 \text{ cm}^{-1}$  the H atoms readily pass through. It will be interesting to compare the transmission of D atoms with those of H atoms through these barriers.

(b) *The Upper State,  $B^1\Sigma_u^+$*

The molecular constants of the upper state were determined in substantially the same way as for the ground state. The combination differences  $\Delta_2 F'$  as well as the  $\Delta G'$  values agree very well with the values derived by Richardson and Davidson (1929) for the lower  $v$  values from an analysis of some visible bands of  $H_2$  which have the  $B^1\Sigma$  state as lower state. We have preferred not to mix our data with theirs but have evaluated  $B'_v$ ,  $D'_v$ ,  $\Delta G'$  independently. On account of a number of perturbations the rotational constant  $H'_v$  could be determined only for a few levels. The average of these values  $H'_v = 1.1 \times 10^{-5} \text{ cm}^{-1}$  was assumed to apply to all vibrational levels of the  $B^1\Sigma$  state.

Our final values of  $B'_v$  and  $D'_v$  are given in Table VI and the values of  $\Delta G'$  and  $\nu_{00} + G'_0(v)$  in Table VII. The  $B_v$  values of Jeppesen (1933) which are

partially based on those of Richardson and Davidson (1929) are included in Table VI for comparison. Similarly the  $\nu_{00} + G'(v)$  values given by Dieke (1958) and also based on Jeppesen's data are included in Table VII. The systematic almost constant deviations in the latter case (up to  $9 \text{ cm}^{-1}$ ) are apparently due to lack of adequate standards in Jeppesen's work, which was

TABLE VI  
Rotational constants of the upper state ( $B^1\Sigma_u^+$ )

$v$	$B_v', \text{cm}^{-1}$		$D_v', \text{cm}^{-1}$
	This paper	Jeppesen	
0	19.453 <sub>7</sub>	19.449	0.0154 <sub>1</sub>
1	18.469 <sub>1</sub>	18.475	0.0133 <sub>1</sub>
2	17.653 <sub>8</sub>	17.646	0.0121 <sub>0</sub>
3	16.927 <sub>1</sub>	16.927	0.0111 <sub>1</sub>
4	16.265 <sub>3</sub>	16.260	0.0102 <sub>1</sub>
5	15.650 <sub>7</sub>	15.621	0.0094 <sub>5</sub>
6	15.066 <sub>5</sub>	15.000	0.0085 <sub>7</sub>
7	14.493 <sub>9</sub>	14.406	0.0076 <sub>2</sub>
8	14.027 <sub>2</sub>		0.0060 <sub>9</sub>
9	13.468 <sub>9</sub>		0.0058 <sub>7</sub>
10	13.165 <sub>2</sub>		0.0030 <sub>4</sub>
11	12.554 <sub>4</sub>		0.0042 <sub>1</sub>
12	12.610 <sub>5</sub>		—
13	11.797 <sub>2</sub>		0.0054 <sub>2</sub>

TABLE VII  
Vibrational constants of the upper state ( $B^1\Sigma^+$ )

$v + \frac{1}{2}$	$\Delta G'(v + \frac{1}{2}), \text{cm}^{-1}$	$\nu_{00} + G'(v), \text{cm}^{-1}$		$v$
		This paper	Dieke	
		90203.35	90195.46	0
$\frac{1}{2}$	1318.41	91521.76	91513.80	1
$1\frac{1}{2}$	1281.43	92803.19	92795.28	2
$2\frac{1}{2}$	1246.77	94049.96	94041.99	3
$3\frac{1}{2}$	1212.98	95262.94	95255.00	4
$4\frac{1}{2}$	1180.02	96442.96	96434.95	5
$5\frac{1}{2}$	1147.58	97590.54	97582.45	6
$6\frac{1}{2}$	1115.36	98705.90	98698.0	7
$7\frac{1}{2}$	1084.02	99789.92	99781.2	8
$8\frac{1}{2}$	1052.76	100842.68	100834.0	9
$9\frac{1}{2}$	1022.22	101864.90	101858.0	10
$10\frac{1}{2}$	992.07	102856.97	102852.3	11
$11\frac{1}{2}$	962.37	103819.34	103812.0	12
$12\frac{1}{2}$	933.44	104752.78	104751.3	13

particularly troublesome since he used a grazing incidence instrument. Jeppesen quotes an error of the relative  $\lambda$  values of  $0.05 \text{ \AA}$  corresponding to  $3 \text{ cm}^{-1}$  in the region in which his work overlaps ours. Our wave numbers are believed to be free from such large systematic errors (see Section 2) and, therefore, the values of column 3 are considered to supersede those of Jeppesen.<sup>2</sup>

In Figs. 9a, 10, and 11a the  $B'_v$ ,  $D'_v$ , and  $\Delta G'$  values are plotted. It is seen that the shapes of the curves are very different from those of the ground state. There is a pronounced positive curvature for both  $B'_v$  and  $\Delta G'$ , much greater than the initial positive curvature in the ground state. The  $B^1\Sigma_u^+$  state is generally considered to be an ionic state and the behavior of the  $B'_v$  and  $\Delta G'$  curves can be understood on this basis.

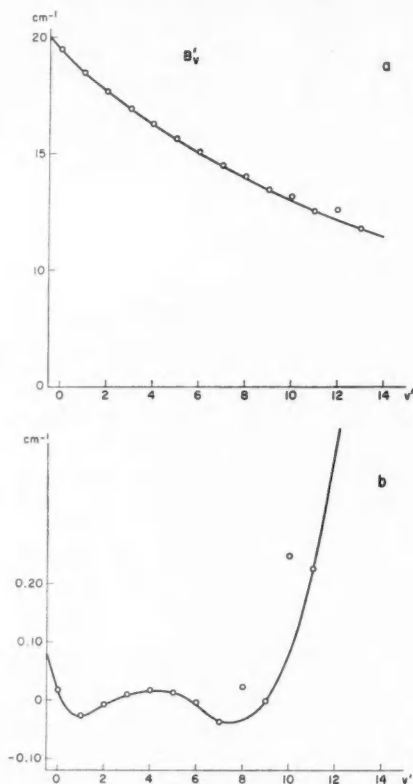
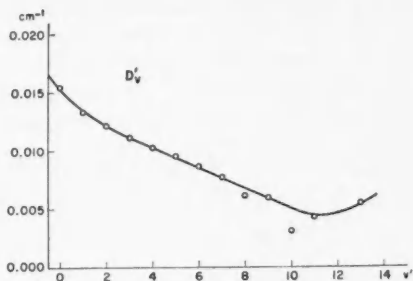
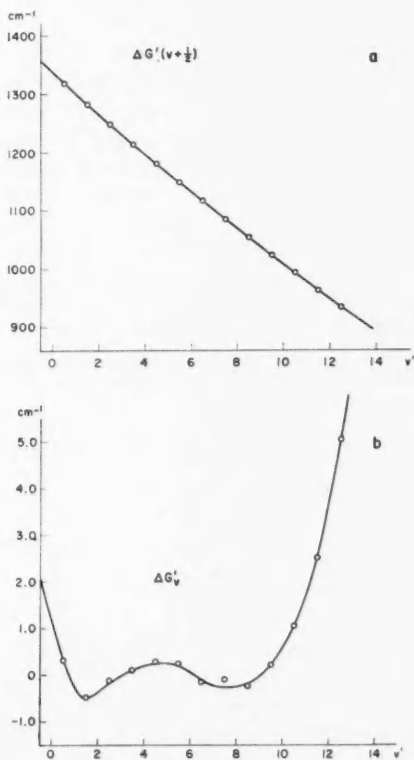


FIG. 9.  $B_v$  curve for the  $B^1\Sigma_u^+$  upper state of the Lyman bands of  $H_2$ .  
(a) Plotted directly.  
(b) Residuals of equation (18).

<sup>2</sup>It must be noted that Jeppesen's band origins  $\nu_0$  are larger by approximately  $\frac{1}{4}(B''-B')$  than Dieke's and ours since he uses the rotational term  $F(J) = B(J+\frac{1}{2})^2$  instead of  $BJ(J+1)$ . His  $\nu_0$  unlike ours is not the wave number of the transition  $J' = 0 \rightarrow J'' = 0$ .

FIG. 10.  $D_v$  curve for the  $B^1\Sigma_u^+$  state of  $H_2$ .FIG. 11.  $\Delta G(v + \frac{1}{2})$  curve for the  $B^1\Sigma_u^+$  state of  $H_2$ .  
(a) Plotted directly.  
(b) Residuals of equation (19).

As in the ground state, a large number of terms would be required to represent all the  $B'$  and  $\Delta G'$  values within the accuracy of the measurements. The following two formulae represent the first four  $B'_v$  and  $\Delta G'_v$  values exactly but the higher values increasingly poorly.

$$(16) \quad B'_v = 20.035 - 1.2312(v + \frac{1}{2}) + 0.14518(v + \frac{1}{2})^2 - 0.013450(v + \frac{1}{2})^3$$

$$(17) \quad \Delta G'(v + \frac{1}{2}) = 1338.22 - 40.690(v + \frac{1}{2}) + 2.2475(v + \frac{1}{2})^2 - 0.24167(v + \frac{1}{2})^3$$

while a least squares representation of the first 10 values yields

$$(18) \quad B'_v = 19.952 - 1.0619(v + \frac{1}{2}) + 0.06494(v + \frac{1}{2})^2 - 0.002628(v + \frac{1}{2})^3,$$

$$(19) \quad \Delta G'(v + \frac{1}{2}) = 1336.68 - 37.503(v + \frac{1}{2}) + 0.6951_6(v + \frac{1}{2})^2 - 0.02464_0(v + \frac{1}{2})^3.$$

There are considerable differences between the coefficients in these two sets of formulae. It would appear that the first set yields more significant values for the equilibrium constants  $B_e$ ,  $\alpha_e$ ,  $\omega_e$ ,  $\omega_e x_e$  . . . and these are therefore chosen as the final values in Table VIII. On the other hand the formulae (18) and (19) give a much better representation for the higher  $v'$  values. As is shown in Figs. 9b and 11b. Nevertheless there are systematic deviations which can be removed only by introducing still higher terms. Such a calculation did not seem worth while.

TABLE VIII

Molecular constants of  $H_2$  in its ground state ( $X^1\Sigma_g^+$ ) and first-excited state ( $B^1\Sigma_u^+$ )

	$X^1\Sigma_g^+$	$B^1\Sigma_u^+$	
$B_0$	59.339 <sub>2</sub>	19.453 <sub>7</sub> cm <sup>-1</sup>	
$B_e$	60.864	20.035	} from equations (8) and (14)
$\alpha_e$	3.0763 <sub>8</sub>	1.2312	
$\gamma_e$	0.0601 <sub>7</sub>	0.1451 <sub>8</sub>	
$r_e$	0.74158	1.29253	
$r_e^*$	0.74116		
$D_e$	0.04657	0.01625	} from equations (12) and (18)
$\beta_e$	-0.00161 <sub>6</sub>	-0.00216 <sub>5</sub>	
$v_{00}$	0	90203.3 <sub>8</sub>	
$T_e$	0	91699.1 <sub>0</sub>	
$\omega_e$	4400.39	1358.9 <sub>1</sub>	} from equations (10) and (17)
$\omega_e x_e$	120.81 <sub>1</sub>	21.52 <sub>9</sub>	
$\omega_e y_e$	0.724 <sub>2</sub>	0.8700 <sub>0</sub>	
$\omega_e z_e$		-0.0604 <sub>2</sub>	

The  $D'_v$  values (Tables VI and Fig. 10) can be represented by

$$(20) \quad D'_v = 0.01625 - 0.00216_5(v + \frac{1}{2}) + 2.28_9 \times 10^{-4}(v + \frac{1}{2})^2 - 1.18_5 \times 10^{-5}(v + \frac{1}{2})^3.$$

Figures 9b and 10 show that the  $B'_v$  and  $D'_v$  values for  $v' = 8, 10$ , and 12 are strongly perturbed. The higher vibrational levels of the  $B^1\Sigma_u^+$  state starting with  $v' = 8$  are in the same energy range as the lower vibrational levels of  $C^1\Pi_u$ . Indeed, if one plots the (unperturbed) total term values of the  $B^1\Sigma_g$  and  $C^1\Pi_u$  against  $J(J+1)$  one finds intersections between  $B^1\Sigma_g$  ( $v = 8$ ) and  $C^1\Pi_u$  ( $v = 0$ ) at  $J \sim 7$ , between  $B^1\Sigma_g$  ( $v = 10$ ) and  $C^1\Pi_u$  ( $v = 1$ ) at  $J \sim 6$ , and between  $B^1\Sigma_g$  ( $v = 12$ ) and  $C^1\Pi_u$  ( $v = 2$ ) at  $J \sim 4$ , and no intersections for  $B^1\Sigma$ ,  $v = 7, 9, 11, 13$ . These intersections of the (unperturbed) term

curves are clearly the reason for the anomalously high  $B$  and low  $D$  values of the levels with  $v = 8, 10, 12$ . Unfortunately no observations are available for high  $J$  values beyond the perturbations, and therefore it is not possible to obtain the true  $B'_v$  values for these levels.

The  $B'_v$  and  $\Delta G'$  curves (Figs. 9b and 11b) also seem to indicate perturbations for  $v' = 0$  or 1, or both, but no perturbing levels are located in this energy region. One must therefore conclude that the apparent irregularities are similar in nature to those found for the ground state at the lowest  $v$  values.

## 6. CONCLUSION

In Table VIII are collected the molecular constants derived from the analysis of the Lyman bands for the equilibrium positions of the upper and lower states. While these constants suffer from the difficulties mentioned earlier, it is believed that they represent improvements over those at present in the literature. It must be emphasized again that these constants represent well only the lower vibrational and rotational levels. For the higher levels the observed  $B_v$ ,  $\Delta G$ , and  $D$  values should be used.

In Table VIII two internuclear distances are given, one ( $r_e$ ) based directly on the observed  $B_v$  and the other ( $r_e^*$ ) after correction for various minor effects described more fully by Stoicheff (1957). With the new  $r_e'$  value of  $H_2$  the agreement of the  $r_e$  values of  $H_2$ , HD,  $D_2$  is no longer quite as good as according to Stoicheff. Improvements similar to the present ones for  $H_2$  in the constants of  $D_2$ ,  $T_2$ , and other isotopes appear desirable in order to find the cause of the apparent small discrepancies of the  $r_e$  values. Such investigations are being planned in this laboratory.

It would be interesting if theoretical work could be carried out which would give a more detailed explanation of the behavior of the  $B_v$  and  $\Delta G$  curves for low  $v$  values. Such work would probably also enable one to derive more reliable equilibrium values,  $B_e$  and  $\omega_e$ , and might remove the discrepancies in the  $r_e$  values.

## ACKNOWLEDGMENTS

We are very much indebted to Mr. J. Shoosmith for taking the spectrograms on which the present analysis is based and to Dr. B. P. Stoicheff and Dr. A. E. Douglas for many helpful remarks during the course of this work.

## REFERENCES

- BEUTLER, H. 1934. *Z. physik. Chem. B*, **27**, 287.  
— 1935. *Z. physik. Chem. B*, **29**, 315.  
CURRY, J. and HERZBERG, G. 1934. *Ann. Physik*, **19** (5) 800.  
DIEKE, G. H. 1958. *J. Mol. Spectroscopy*, **2**, 494.  
DOUGLAS, A. E. and HERZBERG, G. 1957. *J. Opt. Soc. Am.* **47**, 625.  
HERZBERG, G. 1950a. *Can. J. Research, A*, **28**, 144.  
— 1950b. *Spectra of diatomic molecules*, 2nd ed. (D. Van Nostrand Company, Inc., New York).  
HYMAN, H. H. 1930. *Phys. Rev.* **36**, 187.  
JEPPSEN, C. R. 1933. *Phys. Rev.* **44**, 165.  
RICHARDSON, O. W. and DAVIDSON, P. M. 1929. *Proc. Roy. Soc.* **123**, 54.  
STOICHEFF, B. P. 1957. *Can. J. Phys.* **35**, 730.  
TOMKINS, F. S. and FRED, M. 1951. *J. Opt. Soc. Am.* **41**, 641.

## ANALYSIS OF TWO INTERFERING $1/2+$ LEVELS IN THE DISINTEGRATION OF $C^{14}$ BY PROTONS<sup>1</sup>

A. J. FERGUSON AND H. E. GOVE

### ABSTRACT

Two interfering resonances occurring at bombarding energies of 1.32 Mev and 1.51 Mev in the reactions  $C^{14}(pn)N^{14}$  and  $C^{14}(p\gamma)N^{14}$  have been analyzed in terms of Wigner's two-level formula. Resonant energies and reduced widths have been found which give good fits to the shapes of the yield curves for both processes in the neighborhood of the resonances. The absolute cross sections for the  $C^{14}(pn)N^{14}$  and  $N^{14}(np)C^{14}$  reactions are obtained from the analysis without reference to the measured cross sections. The calculated cross sections are found to be about 40% lower than the measured ones.

### INTRODUCTION

The analysis of two interfering resonances of the same spin and parity presents some features not found in a single resonance or in the interference of several levels of different spins and parities. Such a feature is the property discovered by Newton (Newton 1952; Thomas 1955) that the normal compound nucleus formation may not be, and probably generally will not be, obtained in these circumstances. The first study of interfering levels of the same spin and parity appears to be that of Fowler and Thomas (1953). Other studies have been made by Krotkov (1955) and Vogt (1958b). A case bearing some resemblance to the two-level one occurs in the reaction  $C^{12}(p\gamma)N^{12}$  (Woodbury, Tollestrup, and Day 1954) at a bombarding energy of 1.7 Mev where interference between a resonance and a non-resonant background is present. Two preliminary reports of the present work have been given (Ferguson *et al.* 1955; Ferguson and Gove 1956). A complete revision of the calculation has been made since the last of these to remove the rather substantial approximations contained in the earlier work.

Two interfering  $1/2+$  resonances have been observed by Bartholomew *et al.* (1954, 1955) in the reactions  $C^{14}(pn)N^{14}$  and  $C^{14}(p\gamma)N^{14}$ . These are particularly advantageous for the present study because only a single channel spin is involved, so that the cross section is given by a single intensity. One proton channel and two neutron channels are possible in the energy interval. One of the neutron channels involves  $D$  waves and is assumed to be negligible. This assumption is supported by the neutron elastic scattering studies of Johnson, Petree, and Adair (1951). The gamma-ray widths are some orders of magnitude smaller than the particle widths, and their contributions to the total widths are neglected. Only the ground state gamma ray has been studied, which is assumed to be a pure electric dipole transition. Figure 1 gives the yield curves obtained by Bartholomew *et al.* (1955).

<sup>1</sup>Manuscript received February 4, 1959.

Contribution from the Physics Division, Atomic Energy of Canada Limited, Chalk River, Ontario.

Issued as A.E.C.L. No. 782.



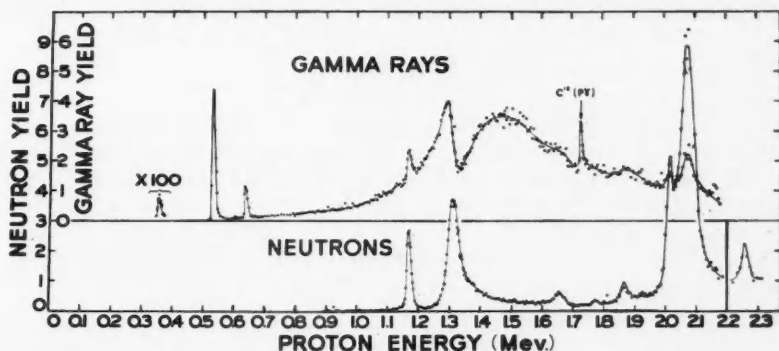


FIG. 1. Yields of ground state gamma rays and of neutrons from  $C^{14}$  bombarded by protons as functions of the bombarding energy in the laboratory system. The yields are in arbitrary units. The gamma-ray yield was measured at  $90^\circ$ . The neutron yield was measured at  $90^\circ$  up to 2.2 Mev and at  $0^\circ$  above this. The resonances concerned in the present study have energies 1.32 Mev and 1.51 Mev.

The two-level formula of Wigner (Wigner 1946; Lane and Thomas 1958; Vogt 1958a) has been used. Fitting was done by the least-squares method, the computations being done on FERUT, the Ferranti electronic computer at the University of Toronto. The Wigner formula can be approximated by two resonance-like terms combined in amplitude, with an arbitrary phase between them. The early work was done on this basis prior to the decision to fit directly in terms of the reduced widths of the resonance theory, and this will be discussed briefly.

### THEORY

It will be convenient to use the comprehensive development recently given by Lane and Thomas (1958). We will adhere to their notation throughout. If only a single spin, parity, and channel spin contribute, then the reaction cross section can be written

$$(1) \quad \sigma_{cc'} = \frac{\pi}{k_c^2} \left| U_{cc'}^{J\pi} \right|^2.$$

The formulae appropriate to the present work are given in Chapter IX, Section 1, of Lane and Thomas. We write for the scattering matrix

$$(2) \quad \begin{aligned} U &= \Omega W \Omega \\ &= \Omega [1 + \mathfrak{B}^{1/2} (1 - \mathbf{R} \mathbf{L}^0)^{-1} \mathbf{R} \mathfrak{B}^{1/2} \mathbf{w}] \Omega. \end{aligned}$$

Here  $\Omega$ ,  $\mathfrak{B}$ ,  $\mathbf{L}^0$ , and  $\mathbf{w}$  are diagonal matrices whose elements are

$$\Omega_{cc'} = \delta_{cc'} \exp i(\omega_c - \phi_c)$$

$$\mathfrak{B}_{cc'} = \delta_{cc'} \rho_c / (F_c^2 + G_c^2)$$

$$\mathbf{L}_{cc'}^0 = \delta_{cc'} [S_c - B_c + i P_c]$$

$$\mathbf{w}_{cc'} = 2i \delta_{cc'}$$

and where  $\omega_c$  is the Coulomb phase shift,

$$\sum_{l=1}^{l_c} \tan^{-1} \eta/l,$$

$\phi_c$  is the hard-sphere phase shift  $\tan^{-1} F_c/G_c$ ;  $F_c$  and  $G_c$  are the regular and irregular solutions for channel  $c$  in the external region;  $P_c$  is the penetrability,  $\rho_c/(F_c^2 + G_c^2)$ ;  $S_c$  is the energy shift term,  $P_c(F_c F'_c + G_c G'_c)$ ; and  $B_c$  is the arbitrary boundary value parameter. The elements of  $\mathbf{W}$  are the Wronskians of the incoming and outgoing solutions for the various channels;  $\rho_c = k_c r_c$  where  $k_c$  is the wave number and  $r_c$  the radial co-ordinate for channel  $c$ . The prime indicates differentiation with respect to  $\rho$ .

$\mathbf{R}$  is the Wigner  $\mathbf{R}$ -matrix given by

$$\mathbf{R} = \sum_{\lambda} \frac{(\gamma_{\lambda} \times \gamma_{\lambda})}{E_{\lambda} - E}$$

where  $\gamma_{\lambda}$  is a vector whose elements,  $\gamma_{\lambda c}$ , are the reduced width amplitudes for the various channels. The  $E_{\lambda}$  are the characteristic energies of the nuclear states;  $(\gamma_{\lambda} \times \gamma_{\lambda})$  is the direct product of the vectors  $\gamma_{\lambda}$  and  $\gamma_{\lambda}$ .

It will be assumed that the entire yield in the energy range considered arises from the two  $1/2+$  resonances. In this case the division of  $\mathbf{R}$ ,

$$\mathbf{R} = \mathbf{R}^0 + \mathbf{R}',$$

given by Lane and Thomas is not useful, so that we put  $\mathbf{R}^0 = 0$  with some simplification of the formulae. The results required are given by the two-level, many-channel form. To find  $\mathbf{U}$  we then have

$$(3) \quad (1 - \mathbf{R}\mathbf{L}^0)^{-1} \mathbf{R} = \sum_{\lambda\mu} (\gamma_{\lambda} \times \gamma_{\mu}) A_{\lambda\mu}$$

(Lane and Thomas 1958, Chapter IX, equation (1.13)). Substitution in equation (2) gives for a non-diagonal element of  $\mathbf{U}$

$$(4) \quad U_{cc'} = 2i \exp i(\omega_c + \omega_{c'} - \phi_c - \phi_{c'}) (P_c P_{c'})^{1/2} \sum_{\lambda\mu} \gamma_{\lambda c} \gamma_{\mu c'} A_{\lambda\mu}.$$

$A_{\lambda\mu}$  is an element of the level matrix  $\mathbf{A}$  given by

$$\mathbf{A} = (\mathbf{e} - \mathbf{E} - \boldsymbol{\xi})^{-1};$$

$\mathbf{e}$  is a diagonal matrix whose elements are the  $E_{\lambda}$ .  $\mathbf{E}$  is the energy,  $E$ , times the unit matrix.  $\boldsymbol{\xi}$  has elements

$$\begin{aligned} \xi_{\lambda\mu} &= \sum_c L_{cc}^0 \gamma_{\lambda c} \gamma_{\mu c} \\ &= \sum_c (S_c - B_c + iP_c) \gamma_{\lambda c} \gamma_{\mu c}. \end{aligned}$$

$\boldsymbol{\xi}$  is separated into its real and imaginary parts

$$\boldsymbol{\xi} = -\boldsymbol{\Delta} + \frac{1}{2}i\boldsymbol{\Gamma}$$

where  $\Delta$  is the shift matrix and  $\Gamma$  the width matrix.  $\Delta$  and  $\Gamma$  have elements

$$\Delta_{\lambda\mu} = - \sum_c (S_c - B_c) \gamma_{\lambda c} \gamma_{\mu c},$$

$$\Gamma_{\lambda\mu} = 2 \sum_c P_c \gamma_{\lambda c} \gamma_{\mu c}.$$

Since  $S_c$  varies only slowly with energy, we have assumed the arbitrary parameters  $B_c$  chosen so that

$$S_c - B_c = 0.*$$

The diagonal elements of  $\Gamma$  are the ordinary widths of the levels familiar from the one-level formula.

For the present two-level case the elements of  $\Delta$  are

$$A_{11} = (E_2 - E - \xi_{22})/D,$$

$$A_{22} = (E_1 - E - \xi_{11})/D,$$

$$A_{12} = A_{21} = \xi_{12}/D.$$

Here  $D = (E_1 - E - \xi_{11})(E_2 - E - \xi_{22}) - \xi_{12}^2$  is the determinant of the matrix  $(\mathbf{e} - \mathbf{E} - \boldsymbol{\xi})$ .  $U_{cc'}$  may now be evaluated by substituting these quantities in equation (4) and finally the cross section,  $\sigma_{cc'}$ , found from equation (1). The explicit formula which results is given by Lane and Thomas, Chapter XII, equation (4.4).

#### DETAILS OF THE COMPUTATION

The two levels involved in the present study occur at proton-bombarding energies of 1.31 Mev and 1.50 Mev. The lower resonance has a total width of about 40 kev, and the proton and neutron widths have comparable magnitudes. The upper one has a total width of approximately .5 Mev which is composed almost entirely of proton width. Figure 1 shows the yields of the  $(p\gamma_0)$  and the  $(pn)$  processes from the work of Bartholomew *et al.* (1955). The gamma-ray curve suggests that most of the gamma yield throughout the range results from the broad resonance at 1.5 Mev and this yield curve gives the best indications available of the width of this resonance. The fit for the gamma rays was made over the region 0.91 Mev to 1.61 Mev. A narrow resonance with spin and parity 1/2- occurs in the range at 1.165 Mev. The points in a 60 kev long region at this resonance were omitted from the fit. The fit to the  $(pn)$  yield was initially made over the same range as for the gamma rays but it was soon found that the neutron yield below 1.28 Mev predicted by the theory was many times smaller than the observed yield here, suggesting a contribution from another process. Thus in subsequent work the fit to the neutron yield was confined to the range 1.28 Mev to 1.61 Mev.

\*This approximation need not have been made. At the time the calculations were performed, the present development was not available to the authors and the one used required this choice. If  $B$  is chosen to obtain this result at 1.1 Mev, then the shift term for the broad resonance will be 50 kev at .85 Mev and 1.50 Mev, the ends of the regions considered. The shift term for the narrow resonance is 1 kev at these points and is negligible where this resonance contributes strongly.

The method of fitting was the least-squares one. However, since the computation of the derivatives required for the usual analytical procedure appeared somewhat complicated, a trial and error method was adopted wherein the fit was computed for a succession of values of one parameter, the value for the best fit was selected, and the procedure repeated for another parameter. About 10 such cycles of adjustment were used, each cycle representing one trial and error adjustment of every parameter. Following this, one final adjustment was made using a set of normal equations derived in a way given later in the discussion of errors. If we let  $Y_M$  be the measured yield and  $Y_C$  the calculated yield, and  $\sigma$  the standard error of the measurement, then the quantity minimized is

$$(5) \quad \Delta = \sum_r \frac{1}{\sigma_r^2} (Y_{Mr} - Y_{Cr})^2.$$

The summation is over all the measured points, including both the neutron and gamma-ray yields. The two yield curves were thus fitted simultaneously.

The formula for the yield was simplified by factoring out the proton and neutron penetrabilities from the  $(pn)$  yield and the proton penetrability from the  $(p\gamma)$  yield and incorporating these in the weight factors. For computing the penetrability, a radius,  $a$ , of  $4.774 \times 10^{-13}$  cm was used, obtained from the formula  $a = 1.4(A^{1/3} + 1) \times 10^{-13}$  cm (Gove 1958). The energies, measured yields, weights, and proton penetrabilities were placed in the computer in tabular form. The absolute yield of the reactions was not well known so that an adjustable normalization factor was placed in the neutron yield. Since the gamma-ray yield is homogeneous in the two gamma-ray widths such a factor is intrinsically contained in these and would be redundant if put in explicitly. Nine parameters were adjusted in all. These were the two resonant energies; six reduced widths representing the proton, neutron, and gamma channels for the two levels; and the normalization factor for the neutron yield.

The variances and covariances of the adjusted quantities are given, as is well known, by the elements of the inverse of the matrix of the normal equations. The normal equations are not obtained directly in the method we have used, but can be derived in the following way. Let us denote the nine parameters by  $\gamma_r$ ,  $r = 1, 2, \dots, 9$ .  $\Delta$  can be expanded as a Taylor series in terms of the  $\gamma$ 's:

$$\Delta = \Delta_0 + \sum_r \frac{\partial \Delta}{\partial \gamma_r} \delta \gamma_r + \frac{1}{2} \sum_{rs} \frac{\partial^2 \Delta}{\partial \gamma_r \partial \gamma_s} \delta \gamma_r \delta \gamma_s + \dots$$

The normal equations are the set given by

$$\frac{\partial \Delta}{\partial \delta \gamma_r} = 0.$$

Stopping the series at the second-order term this gives the set

$$(6) \quad \sum_s \frac{\partial^2 \Delta}{\partial \gamma_r \partial \gamma_s} \delta \gamma_s = - \frac{\partial \Delta}{\partial \gamma_r}; \quad r, s = 1, \dots, 9.$$

The matrix of the normal equations which we require is thus that whose  $r$ sth element is

$$\frac{\partial^2 \Delta}{\partial \gamma_r \partial \gamma_s}.$$

Once the minimum of  $\Delta$ , which it may be noted corresponds to the vanishing of the right-hand sides of equations (6), has been found, these elements can be formed by varying the parameters first one at a time, giving  $\partial^2 \Delta / \partial \gamma_r^2$ , and then two at a time, giving  $\partial^2 \Delta / \partial \gamma_r \partial \gamma_s$ . By using both positive and negative increments of the parameters, both the first and second derivatives can be found if the true minimum has not quite been reached. All the coefficients of the normal equations (6) are then known and a further adjustment can be made by solving them. This was done at the end of the trial and error fitting and produced an appreciable improvement in the fit, demonstrating the accuracy of the normal equations. Inverting the normal matrix gave directly the standard errors of the parameters.

### RESULTS

The fitted yields are shown for the  $(pn)$  case in Fig. 2 and for the  $(p\gamma)$  case in Fig. 3. The abscissae of these graphs are the center of mass energies, which are  $14/15$  times the proton energies in the laboratory system. In both these figures the yield of the 1.165-Mev resonance has been indicated. The regions of energy which were omitted from the fit are indicated by giving the theoretical yield as a dotted curve. The theoretical  $(pn)$  yield vanishes at

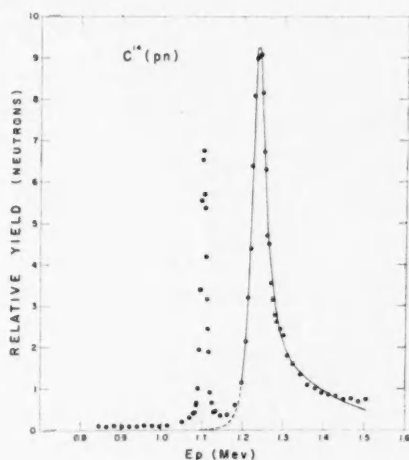


FIG. 2. Theoretical fit to the yield of the  $C^{14}(pn)N^{14}$  reaction. The fit was made only in the region covered by the solid line. The abscissae are the energy of the incident proton in the center of mass system. The yields are in arbitrary units.

1.07 Mev and increases somewhat below this, but does not exceed 1/2% of the observed yield down to where the study was started. This vanishing of the cross section has been noted by Wigner (1946).

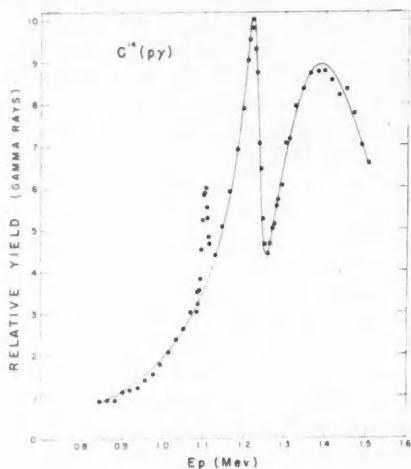


FIG. 3. Theoretical fit to the yield of the  $C^{14}(p\gamma)N^{16}$  reaction. The fit was made only in the region covered by the solid line. The abscissae are the energy of the incident proton in the center of mass system. The yields are in arbitrary units.

The parameters for these curves are given in Table I.  $E_0$  is the resonant energy of the resonance.  $\gamma_p$ ,  $\gamma_n$ , and  $\gamma_\gamma$  are respectively the reduced width

TABLE I

Resonant energies,  $E_0$ , reduced width amplitudes and partial and total widths. The partial and total widths for each resonance are calculated at the resonant energy. The energies and widths are for the center of mass system

	Narrow resonance	Broad resonance
$E_0$ Mev	$1.2302 \pm .0003$	$1.4078 \pm .0035$
$\gamma_p$ (Mev) $^{1/2}$	$.0888 \pm .0035$	$.6084 \pm .0048$
$\gamma_n$ (Mev) $^{1/2}$	$.1482 \pm .0020$	$-.0472 \pm .0013$
$\gamma_\gamma$ (ev) $^{1/2}$	$1.442 \pm .044$	$3.102 \pm .028$
$\Gamma_p$ kev	$6.8 \pm .5$	$400.9 \pm 6.3$
$\Gamma_n$ kev	$34.6 \pm .9$	$4.0 \pm .2$
$\Gamma_\gamma$ ev	$4.2 \pm .7$	$19.2 \pm .4$
$\Gamma$ kev	$41.4 \pm 1.1$	$404.9 \pm 6.3$

amplitudes for the proton, neutron, and ground state gamma-ray channels.  $\Gamma_p$ ,  $\Gamma_n$ , and  $\Gamma_\gamma$  are the corresponding partial widths obtained from

$$\Gamma_{c\lambda\lambda} = 2 P_c \gamma_\lambda^2.$$

$\Gamma$  is the total width given by

$$\Gamma = \sum_c \Gamma_{c\lambda\lambda}.$$

With the exception of the gamma-ray partial width, these quantities are functions of energy by virtue of the penetration factor. The tabulated values are calculated at  $E_0$  for the level concerned. All of the energies refer to the center of mass system.

The minimum value of  $\Delta$  was 509. The expectation value of this quantity is  $(m-r)$  where  $m$  is the number of points and  $r$  the number of adjusted parameters. There were 32 points in the  $(pn)$  curve, 46 in the  $(p\gamma)$  curve, and 9 parameters, giving  $m-r = 69$ .  $\Delta$  is thus sufficiently different from its expectation value to suggest that the fit is not adequate. However, only the errors due to counting statistics were included in the calculation, and it is reasonable to expect that other errors will be present.

With the exception of  $\gamma_\gamma$ , the errors given in Table I have been calculated from the formula

$$\sigma_\lambda = \left( \frac{509}{69} N_{\lambda\lambda}^{-1} \right)^{1/2}$$

where  $N_{\lambda\lambda}^{-1}$  is the diagonal element of the inverse of the normal matrix corresponding to the  $\lambda$ th parameter. The errors in  $\gamma_\gamma$  are derived from the uncertainty in measuring the absolute  $\gamma$ -ray yield.

#### DISCUSSION

A better physical insight into the formula can be obtained by expressing  $W_{cc'}$  as a sum of resonance-like amplitudes, although it is inconvenient to do this for computation. Wigner (1946) has shown how this can be done in general by diagonalizing the matrix  $\mathbf{e}-\xi$ . In the present simple case  $W_{cc'}$  has the form

$$W_{cc'} = i N_{cc'}/D$$

where  $N_{cc'}$  is a complex function explicitly involving  $E$  to the first degree.  $D$  is a second-degree polynomial in  $E$  which can be resolved into its two factors.  $W_{cc'}$  can then be resolved into two resonance amplitudes by the partial fractions rule. Even in this simple case the expressions are somewhat complicated and will not be given explicitly. It is found that there is a relative phase between the two amplitudes which will vary from reaction to reaction. In a case such as the present one where only two dominant channels exist, the ratio of these two complex quantities is limited to a relatively small region of the complex plane by the requirement that reduced widths be real.

If

$$(7) \quad W_{pm} = i \left\{ \frac{Y_1}{E_1' - E - (i\Gamma_1'/2)} + \frac{Y_2}{E_2' - E - (i\Gamma_2'/2)} \right\}$$

where  $Y_1$  and  $Y_2$  are the complex amplitudes for the two levels and

$$E_1' - E - \frac{i\Gamma_1'}{2}$$

and

$$E_2' - E - \frac{i\Gamma_2'}{2}$$

are the factors of  $D$ , then the ratio  $Y_1/Y_2$  is limited to regions of the complex plane determined by the ratio  $\Gamma_{11}/\Gamma_{22}$ .  $W_{pn}$  refers here specifically to the  $(pn)$  process and the subscripts 1 and 2 to the lower and upper resonances. In Fig. 4 is shown the complex plane of  $Y_1/Y_2$ . The region allowed by the requirement of real reduced widths is shaded. The crosses representing unrestricted fits

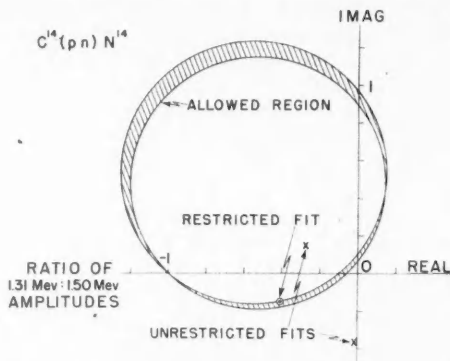


FIG. 4. The complex plane representing the ratio of the amplitudes of the two interfering resonances in the  $C^{14}(pn)N^{14}$  reaction. The allowed region is that for which real reduced widths can be found for the Wigner two-level formula.

were obtained in some earlier work using equation (7) directly. The adjusted quantities were  $|Y_1|$ ,  $|Y_2|$ ,  $\arg Y_1/Y_2$ ,  $E'_1$ ,  $E'_2$ , and  $\Gamma'_1$ .  $\Gamma'_2$  is not well determined by the  $(pn)$  yield and a value taken from the  $(p\gamma)$  yield was used. The energy dependence of  $|Y_1|$ ,  $|Y_2|$ ,  $\Gamma'_1$ , and  $\Gamma'_2$  was included in an approximate way. To this approximation  $Y_1/Y_2$  is independent of energy. The restricted fit was obtained under the requirements that it lie in the allowed region and be compatible with the  $(p\gamma)$  fit.

A necessary and sufficient condition, for a definite  $E$ ,  $J$ , and parity, that the distribution of products in outgoing channels be independent of the incoming channel is that the reduced widths of the levels\* have the form (Newton 1952)

$$\gamma_{\mu i} = \alpha_{\mu} \beta_i$$

where  $\alpha_{\mu}$  does not depend on the channel,  $i$ , and  $\beta_i$  does not depend on the level,  $\mu$ . In the present case this would require

$$\frac{\gamma_{1p}}{\gamma_{2p}} = \frac{\gamma_{1n}}{\gamma_{2n}} = \frac{\gamma_{1\gamma}}{\gamma_{2\gamma}}$$

which is clearly not obtained. We thus do not have compound nucleus formation in the region where the resonances overlap. Newton has shown further that where compound nucleus formation is obtained, then reaction cross sections vanish between resonances† which evidently does not occur here.

\*The levels must overlap. Compound nucleus formation is always obtained at an isolated resonance.

†This should not be confused with the vanishing cross section that is always obtained, either between the resonances or beyond them, when there are only two channels.



Although a knowledge of the absolute yield has not been used in the calculation, the results do provide the absolute ( $pn$ ) and ( $np$ ) cross sections. The reason for this apparent paradox is that we have been able to determine all of the neutron and proton partial widths from the shape of the yield curve through the interference which is present.  $\sigma_{np}$  for the narrow level has been measured by Johnson and Barschall (1950) and  $\sigma_{pn}$  for the same level by Sanders (1956) and Macklin and Gibbons (1958). A comparison is made between these measurements and the values obtained from the theory and is given in Table II.

TABLE II

Comparison of measured and theoretical cross sections for the ( $np$ ) and ( $pn$ ) reactions for the level occurring at proton energy 1.230 Mev in the center of mass system

	$\sigma_{np}$ , millibarns	$\sigma_{pn}$ , millibarns
Measured	200	315
Calculated	131	194
Ratio, measured : calculated	1.53	1.62

The agreement between the theory and experiment is poor, and lies outside the error of 30% given by Sanders. It is of interest that the one-level formula with  $\gamma_{1p}$  and  $\gamma_{1n}$  from Table I gives  $\sigma_{pn} = 309$  millibarns. This shows that the interference from the broad resonance is destructive in the region of the narrow resonance. An attempt to fit the absolute cross sections has not been made, but there is little doubt that the agreement with the shape of the yield curve would be materially spoiled in such an attempt.

The fact that the neutron yield between 0.85 Mev and 1.0 Mev is substantially greater than that calculated from the present fit may be significant. The yield curve of Macklin and Gibbons shows a typical S-wave threshold, so that the yield in this region must be attributed principally to 1/2+ states that have not been included in the calculation. If most of the reaction amplitude not specifically due to the 1.230-Mev resonance throughout the region fitted results from a non-resonant process rather than from the broad 1.408-Mev resonance, then  $\gamma_n$  for the latter may be considerably smaller than quoted. With a non-resonant contribution it is also likely that the absolute cross sections can be fitted adequately.

The ( $np$ ) and ( $n\gamma_0$ ) cross sections for thermal neutron energies computed from the present results are given in Table III. The experimental cross sections are those quoted by Bartholomew *et al.* (1955). The large difference between

TABLE III

( $np$ ) cross section and ( $n\gamma_0$ ) cross section for the ground state gamma ray for thermal neutrons

	Calculated	Measured
$\sigma_{np}$	0.13 barns	1.7 barns
$\sigma_{n\gamma}$	0.45 millibarns	13 millibarns

the calculated  $\sigma_{np}$  of Table III and the value of Bartholomew *et al.* results from a slight reduction in the neutron width of the broad resonance and from destructive interference from the narrow resonance which causes a six-fold reduction of the cross section. This cross section will have a large uncertainty due to this cancellation. The calculated  $\sigma_{n\gamma}$  is the same as the one calculated by Bartholomew *et al.*

The cross sections for the elastic scattering processes  $C^{14}(pp)C^{14}$  and  $N^{14}(nn)N^{14}$  can be predicted from the resonance parameters for the range of excitation energies studied provided the potential scattering phase shifts are known. No measurement of the  $C^{14}(pp)C^{14}$  process has been made. The process  $N^{14}(nn)N^{14}$  has been studied by Johnson, Petree, and Adair (1951) and shows clearly the 1.23-Mev resonance, but no evidence of the broad 1.41-Mev one. The present results predict an extremely small neutron scattering amplitude for the broad resonance so that this process should be essentially a one-level one involving only the 1.23-Mev resonance.

The signs of the reduced widths are arbitrary to a large extent and those given represent only one of several choices. Any change of sign which keeps the signs of the three quantities  $\gamma_{1p}\gamma_{2p}$ ,  $\gamma_{1n}\gamma_{2n}$ , and  $\gamma_{1\gamma}\gamma_{2\gamma}$  unchanged also keeps the cross sections unchanged.

The narrow and broad resonances have isotopic spins 1/2 and 3/2 respectively (Bartholomew *et al.* 1955; Bartholomew *et al.* 1956). In the ordinary case no interference occurs in the total cross section between states of different total angular momentum. Analogously, it might be expected that interference will not be present between states of different total isotopic spin, contrary to what has been found here. However, the absence of interference in the ordinary case requires that the incident beam and the target be unpolarized and that polarization be undetected in the final nucleus and the emergent beam. Here the incident and emergent beams are completely polarized in isotopic spin space so that interference must be expected.

#### NOTE ADDED IN PROOF

A detailed comparison of the  $(pn)$  yields of Bartholomew *et al.*, Sanders (1956), and Macklin and Gibbons (1958) has recently been made. In the range 1.19 Mev to 1.51 Mev (center of mass) differences have been found between the curves as follows: the energy scale of Macklin and Gibbons is 18 kev less than that of the other two studies; the peak of the 1.23-Mev resonance is about 20% lower in the data of Bartholomew *et al.* than in that of Macklin and Gibbons; the yield near 1.45 Mev of Bartholomew *et al.* is about 40% higher than that of Macklin and Gibbons. Correspondence between the yields to better than 10% is otherwise obtained. An error of 18 kev may thus be present in the resonant energies found here. Uncertainties in the reduced width amplitudes revealed by these differences are difficult to estimate, but are probably less than those arising from other sources such as neglect of non-resonant contributions.

Mr. Syurei Iwao (private communication) has recently extended the calculation by including a 1/2+ resonance near an excitation energy of 9 Mev

in the  $N^{15}$  nucleus. This has successfully accounted for the yield below 1.19 Mev and has reduced the disagreement between the measured and calculated cross sections at the peak of the 1.23-Mev resonance.

#### ACKNOWLEDGMENTS

The coding of the program for this calculation has been done by Miss Jean Tucker under the supervision of Dr. H. S. Gellman. We are greatly indebted to Dr. Erich Vogt for extensive comments on the manuscript and for verifying by a detailed calculation that interference is present in the total cross section between states of different total angular momentum in collision processes with polarized particles.

#### REFERENCES

- BARTHOLOMEW, G. A., BROWN, F., GOVE, H. E., LITHERLAND, A. E., and PAUL, E. B. 1954. Phys. Rev. **96**, 1154.  
——— 1955. Can. J. Phys. **33**, 441.  
BARTHOLOMEW, G. A., LITHERLAND, E. A., PAUL, E. B., and GOVE, H. E. 1956. Can. J. Phys. **34**, 147.  
FERGUSON, A. J., BARTHOLOMEW, G. A., GOVE, H. E., LITHERLAND, A. E., and PAUL, E. B. 1955. Proc. Roy. Soc. Canada, **49**, 153.  
FERGUSON, A. J. and GOVE, H. E. 1956. Bull. Am. Phys. Soc. **1**, 180, paper HA4.  
FOWLER, W. A. and THOMAS, R. G. 1953. Phys. Rev. **91**, 473(A).  
GOVE, H. E. 1958. Nuclear reactions, Vol. I (North-Holland Publishing Co.).  
JOHNSON, C. H. and BARSCHALL, H. H. 1950. Phys. Rev. **80**, 818.  
JOHNSON, C. H., PETREE, B., and ADAIR, R. K. 1951. Phys. Rev. **84**, 775.  
KROTKOV, R. 1955. Can. J. Phys. **33**, 622.  
LANE, A. M. and THOMAS, R. G. 1958. Revs. Modern Phys. **30**, 257.  
MACKLIN, R. L. and GIBBONS, J. H. 1958. Private communication to A. G. W. Cameron (to be published).  
NEWTON, T. D. 1952. Can. J. Phys. **30**, 53.  
SANDERS, R. M. 1956. Phys. Rev. **104**, 1434.  
THOMAS, R. G. 1955. Phys. Rev. **97**, 224.  
VOGT, E. 1958a. Nuclear reactions, Vol. I (North-Holland Publishing Co.).  
——— 1958b. Phys. Rev. **112**, 203.  
WIGNER, E. P. 1946. Phys. Rev. **70**, 606.  
WOODBURY, H. H., TOLLESTRUP, A. V., and DAY, R. B. 1954. Phys. Rev. **93**, 1311.

---

## NOTES

---

### RADIATION FROM A SMALL LOOP IMMERSED IN A SEMI-INFINITE CONDUCTING MEDIUM

JAMES R. WAIT\*

It is well known that a circular loop antenna situated in the air and with its axis parallel to the ground will radiate a vertically polarized ground wave. Furthermore, if the electrical constants of the ground are known, the field strength of the ground wave can be readily calculated from convenient curves prepared by Norton (1941). He also discusses in detail the effect of raising the transmitting and receiving antenna above the ground.

In this note the effect of burying one or both of the transmitting and receiving loops in the ground is considered. For purposes of analysis the ground is assumed to be represented by a semi-infinite homogeneous medium of conductivity  $\sigma$ , dielectric constant  $\epsilon$ . The air is assumed to be a semi-infinite insulator with dielectric constant  $\epsilon_0$ . The permeability of the whole space is taken as  $\mu$ , equal to that of free space. At low radio frequencies the insulated loop can be represented as a magnetic dipole oriented in the direction of the loop axis. The fields vary according to the factor  $\exp(i\omega t)$ .

Choosing an  $(x, y, z)$  co-ordinate system, with the insulating medium defined by  $z < 0$  and the conducting medium defined by  $z > 0$ , the dipole is located at  $(0, 0, h)$  and oriented in the  $y$  direction. The electric and magnetic fields in the conductor can be represented in terms of a Hertz vector  $\mathbf{F}$  as follows:

$$(1) \quad \mathbf{E} = -\text{curl } \mathbf{F}$$

$$(2) \quad i\mu\omega\mathbf{H} = -\gamma^2\mathbf{F} + \text{grad div } \mathbf{F}$$

where

$$\gamma^2 = i\sigma\mu\omega - \epsilon\mu\omega^2.$$

A subscript 0 is added to the quantities in order that they shall pertain to the insulating region, so that

$$\gamma_0^2 = -\epsilon_0\mu\omega^2$$

since

$$\mu = \mu_0.$$

The formal solution of the problem can now be obtained in a straightforward manner by matching cylindrical wave functions at the boundary  $z = 0$  (Sommerfeld 1926). The formal result is given by Wait and Campbell (1953).

\*Present address: National Bureau of Standards, Boulder, Colorado.

- (3)  $F_x = 0$   
 (4)  $F_y = C(P_1 - P_2 + Q)$   
 (5)  $F_z = CR$

where

$$Q = 2\gamma_0^2 \int_0^\infty \frac{e^{-u(h+z)} \lambda J_0(\lambda \rho) d\lambda}{u\gamma_0^2 + u_0\gamma^2}$$

$$R = 2(\gamma_0^2 - \gamma^2) \frac{\partial}{\partial y} \int_0^\infty \frac{e^{-u(h+z)} \lambda J_0(\gamma \rho) d\lambda}{(u\gamma_0^2 + u_0\gamma^2)(u_0 + u)}$$

$$P_1 = e^{-\gamma r_1}/r_1, \quad P_2 = e^{-\gamma r_2}/r_2$$

and where

$$\rho = (x^2 + y^2)^{\frac{1}{2}}$$

$$r_1 = [\rho^2 + (z-h)^2]^{\frac{1}{2}}, \quad r_2 = [\rho^2 + (z+h)^2]^{\frac{1}{2}},$$

$$u_0 = (\lambda^2 + \gamma_0^2)^{\frac{1}{2}}, \quad u = (\lambda^2 + \gamma^2)^{\frac{1}{2}}.$$

The constant  $C$  is proportional to the strength of the dipole and is given by

$$C = i\mu\omega IdA/4\pi$$

where  $I$  is the total circulating current in the loop and  $dA$  is the area of the loop. In a previous paper (Wait and Campbell 1953) the integrals were evaluated in closed form with the restriction that  $|\gamma_0\rho| \ll 1$  and certain approximate results were given for other cases. It is the purpose of the present note to show that expressions for the radiation fields can be readily obtained by generalizing Sommerfeld's results for dipoles at the interface.

For a highly conducting ground, it is permissible to make the substitution

$$u = \gamma(1 + \lambda^2/\gamma^2)^{\frac{1}{2}} \cong \gamma(1 + \gamma_0^2/\gamma^2)^{\frac{1}{2}} \cong \gamma$$

since the saddle point of the integrals is near  $\lambda = \gamma_0$  when  $|\gamma^2| \gg |\gamma_0^2|$ . This approximation was used by Sommerfeld (1926) originally in the evaluation of the integrals for the case when the dipole is at the interface. The integrals  $Q$  and  $R$  can then be written

$$Q \cong 2\gamma_0^2 \gamma^{-2} e^{-\gamma(z+h)} \int_0^\infty (u_0 + \gamma_0^2/\gamma)^{-1} \lambda J_0(\lambda \rho) d\lambda$$

and

$$R \cong -2\gamma^{-1} e^{-\gamma(z+h)} \frac{\partial}{\partial y} \int_0^\infty [(u_0 + \gamma_0^2/\gamma)^{-1} - (u_0 + \gamma)^{-1}] \lambda J_0(\lambda \rho) d\lambda.$$

Integrals of this type can be expressed in terms of the error function as shown by Niessen (1948) for the case where  $|\gamma_0\rho| \gg 1$ . Thus  $R$  and  $Q$  are given by

$$Q \cong 2\gamma_0^2 \gamma^{-2} e^{-\gamma(z+h)} e^{-\gamma_0\rho} \rho^{-1} F(p)$$

$$R \cong 2\gamma^{-1} \frac{\partial}{\partial y} e^{-\gamma(z+h)} e^{-\gamma_0\rho} \rho^{-1} [F(p) - F(p')]$$

where

$$p = -\gamma_0^3 \rho / (2\gamma^2) \quad \text{and} \quad p' = -(\gamma_0 \rho / 2)(\gamma^2 / \gamma_0^2)$$

and  $F(p)$  is an attenuation factor given by

$$F(p) = 1 - i(\pi p)^{\frac{1}{2}} e^{-p} \text{erfc.} (ip^{\frac{1}{2}})$$

while for large values of  $p$ ,  $F(p) \cong -1/(2p)$ .

The fields  $H_z$  and  $H_y$  are then given by

$$(6) \quad i\mu\omega H_y \cong -2C\gamma_0^2 e^{-\gamma(z+h)} e^{-\gamma_0 \rho} \rho^{-1} F(p) \sin^2 \phi$$

and

$$(7) \quad i\mu\omega H_z \cong 2C\gamma_0^2 e^{-\gamma(z+h)} e^{-\gamma_0 \rho} \rho^{-1} F(p) \sin \phi \cos \phi$$

where

$$\phi = \cos^{-1} y/\rho.$$

These expressions, which are valid for  $|\gamma_0 \rho| \gg 1$ , were given in a previous paper (Wait and Campbell 1953) without proof.

When  $(z+h)$  tends to zero, the fields are the well-known expressions for the far-zone field intensity of a loop antenna situated on the surface. The effect of burying the transmitting loop and also the receiving loop is to simply modify the magnetic fields for the case of the loops on the surface by a factor  $\exp[-\gamma(z+h)]$ . This conclusion is not modified for distances even when the restriction  $|\gamma_0 \rho| \gg 1$  is violated as long as  $|\gamma \rho| \gg 1$  and  $\rho \gg (z+h)$ .

The additional attenuation  $G$  of the far-zone field, due to the immersion of the loops in the conducting medium, is then simply given by

$$G = (z+h)/\delta \text{ nepers.} = 8.68 (z+h)/\delta \text{ db}$$

where  $\delta$  is the "skin depth" of the radiation in the conducting medium given by

$$\delta = \text{real part of } 1/\gamma \cong [2/(\sigma\mu\omega)]^{\frac{1}{2}}.$$

It is also of interest to note that an  $H_z$  component is present but it varies as  $\rho^{-2}$  in the radiation field and is not of any practical significance.

- NIESSEN, K. F. 1948. *Z. Naturforsch.* **3**(a), 555.  
 NORTON, K. A. 1941. *Proc. Inst. Radio Engrs.* **29**, 623.  
 SOMMERFELD, A. N. 1926. *Ann. Physik*, **81**, 1135.  
 WAIT, J. R. and CAMPBELL, L. L. 1953. *J. Geophys. Research*, **58**, 167.

RECEIVED FEBRUARY 18, 1959.  
 DEPARTMENT OF ELECTRICAL ENGINEERING,  
 UNIVERSITY OF TORONTO,  
 TORONTO, ONTARIO.

## THE NOSE-ON RADAR CROSS SECTIONS OF FINITE CONES\*

H. BRYSK, R. E. HIATT, V. H. WESTON, AND K. M. SIEGEL

Keys and Primich (1959) have completed the most thorough determination of the radar cross sections of perfectly conducting finite cones known to the authors. Certain features of these data are stated to disagree with theoretical predictions (Siegel 1958). The disturbing fact that some of the data of Keys and Primich (1959) do not fall off like  $1/\lambda^4$  at the long wavelength end has led us to examine these results critically and to perform some experimental measurements of our own near the Rayleigh region. Part 1 explains briefly our nose-on Rayleigh predictions for the finite cone. Part 2 discusses the resonance region for the cone. Part 3 describes measurements we have made since obtaining a preprint of Keys and Primich (1959). Our results indicate no need to revise the theoretical discussion of Siegel (1958). At the same time, we find good agreement in the experimental data.

## 1. RAYLEIGH REGION THEORY

The reasoning behind the Rayleigh region theory, as given in Siegel (1958), is as follows: In a scattering experiment the probe measures results which depend upon polarization, wavelength, and properties of the body. Here we are discussing nose-on cross sections from a perfectly conducting body of revolution; the constitutive constants of the scatterer are thus simply fixed, and it is known in this case that the return is independent of polarization. A priori we expect the radar cross section in the Rayleigh region to have an inverse fourth power wavelength dependence. Since dimensionally the cross section is an area, we know this wavelength dependence must be multiplied by a factor of the dimension of length to the sixth power. When the wavelength is large in respect to the dimensions of the body, the body looks like a singularity to the wave. The return must then be insensitive to the fine structure of the body, because a geometric singularity on the body (e.g., a point, a line, a sharp interface) looks to the wave merely as a singular detail superimposed on a singularity. Thus the obvious first choice for a length to the sixth power is the volume squared. Accordingly, we write

$$(1) \quad \sigma = C_1 k^4 (VF)^2,$$

where  $\sigma$  is the nose-on backscattering radar cross section,  $k = 2\pi/\lambda$  where  $\lambda$  is the wavelength.  $C_1$  is a pure number,  $V$  is the volume of the scatterer, and  $F$  is a dimensionless correction factor that takes into account any shape dependence of the cross section. In view of the expected insensitivity of the cross section to fine details of structure, it should be possible to express  $F$  fairly accurately as a function of a length-to-width ratio only.

\*Work carried out under contract with the Rome Air Development Center of the Air Research and Development Command, United States Air Force.

Rayleigh himself has solved exactly the scattering of an electromagnetic wave incident along one of the axes of a spheroid for the case in which the wavelength is large compared with all the dimensions of the spheroid. Thus we know  $C_1 F^2$  for the spheroid. This expression tends to a constant value for very prolate spheroids, and to infinity for very oblate ones (since the disk has a finite cross section despite a vanishing volume). A very simple approximation, which reproduces Rayleigh's complicated formulae to within 1%, is (Siegel 1958):

$$(2) \quad F = 1 + (\pi y)^{-1} e^{-y},$$

$$(3) \quad C_1 = 4/\pi,$$

where  $y$  is the ratio of the principal axis along the direction of incidence to that normal to it.

The proposed extension of this result to shapes for which an exact solution is not available consists of retaining eq. (2), with  $y$  redefined as a constant times the ratio of the maximum dimensions along the direction of incidence and normal to it; the basis for the choice of the constant is that, in the limit as the shape is flattened, the disk cross section should emerge. In this way, a finite cone of base radius  $r$  and height  $h$  is assigned a cross section (Siegel 1958):

$$(4) \quad \sigma = (4/\pi) k^4 V^2 [1 + (\pi y)^{-1} e^{-y}]^2,$$

where

$$V = (1/3)\pi r^2 h, \quad \text{and } y = h/4r.$$

Keys and Primich compare cones of total angle  $8^\circ$  and  $120^\circ$  and point out that the theoretical difference in cross section on a volume-squared basis is 28 db, whereas experimentally they obtained a difference of 4 to 5 db. If the  $F$  factor is taken into account, the theoretical cross sections differ only by 18 db. There remains a discrepancy of the order of 14 db. This is, however, easily explained by the fact that Keys and Primich were using in their comparison cross-section values for the  $8^\circ$  cone at  $kr \sim .45$ , which is not in the Rayleigh region. For a cone with total angle  $\theta$  and base radius  $r$  to be in the Rayleigh region, the following must hold:

$$kr \cot(\theta/2) < 1, \quad \theta < 90^\circ$$

$$kr < 1, \quad \theta > 90^\circ$$

or, for an  $8^\circ$  cone,  $kr < \tan 4^\circ = .07$ .

In our experimental results, we have yet to hit the Rayleigh region for our small angle cones, but we are approaching it. Our large angle cones are already there. Our experimental and theoretical results appear to be consistent.

## 2. RESONANCE REGION THEORY

In Siegel (1958), it was shown that, for small wavelengths, the main contribution to the nose-on cross section of a finite cone is from the ring singularity at the base. The physical optics results were computed by using wedge-like



local fields in evaluating the contribution of the ring singularity. The minor cone resonances (past the first) were predicted to lie at the same locations as for the ring. It was felt that the rise on the small wavelength side of the first resonance could be approximated by the ring. Keys and Primich have shown experimentally that the locations of the resonances (other than the first) agree indeed for rings and cones.

We have pointed out that in the Rayleigh region the backscattering cross section for incidence along the axis of a perfectly conducting body of revolution depends primarily upon the volume of the body, modified by a factor involving the length-to-width ratio. This implies that if the orientation of the body is reversed (front to rear) the Rayleigh return should not change significantly. Siegel has predicted that this should remain true as one enters the resonance region from the Rayleigh side—specifically that, if a cone in this region is turned around, the return should not be much affected. Honda (Honda, Silver, and Clapp 1956) has measured this front-to-rear ratio for several cones. In the small wavelength region, the reversed cone gives a return two orders of magnitude greater than nose-on. (Theoretically, this can be understood as due to the flat plate effect of the base in the reversed position.) For the smallest cone, on the other hand, which is just about at the first resonance (apex angle  $15^\circ$ ,  $kr = 1.5$ ), the rear contribution is larger by only a factor of  $2 \pm .5$ . This suggests that the location of the first resonance for the cone can be approximated by that of the resonance for the cone's base, namely the disk.

Comparing disk, sphere, and prolate spheroid (Siegel *et al.* 1956) results, for incidence along the symmetry axis, it is evident that the location of the first resonant point, as a function of  $kr$ , where  $r$  is the maximum radius of revolution, decreases with elongation. Hence, the disk provides the upper bound for the location of the first resonance for spheroids. Since the disk is a limiting case for the cone too, we expect the disk answer also to be the upper bound for the cone.

The first resonant point is the largest value of  $\lambda$  (or the smallest value of  $1/\lambda$ ) for which  $d\sigma/d\lambda = 0$ . Hence, to exhibit the first resonant point, one must plot  $\sigma$  vs.  $\lambda$  (or  $1/\lambda$ ), or some constant multiples of these quantities such as  $(\sigma/\pi r^2)$  vs.  $kr$ . On the other hand, if the ordinate  $(\sigma/\lambda^2)$  is chosen (as was done in Keys and Primich (1959)), the maxima of the curve obtained are zeros of  $d(\sigma/\lambda^2)/d\lambda$ , which do not necessarily coincide with zeros of  $d\sigma/d\lambda$ . On a  $(\sigma/\pi r^2)$  vs.  $kr$  plot, Keys and Primich's results for the cone show a first resonance at  $kr \approx 1.5$ . This compares with  $kr \approx 1.1$  for the ring (Kouyoumjian 1956; Weston 1957) and  $kr \approx 1.6$  for the disk (Andrejewski 1952).

These results will now allow us to predict the location of the resonance region for other bodies with greater precision than we previously could.

### 3. PRELIMINARY EXPERIMENTAL RESULTS

Measurements have been made at four different frequencies on the nose-on radar cross sections of small cones with apex half angles of  $7.5^\circ$ ,  $9.6^\circ$ ,  $12^\circ$ ,  $45^\circ$ , and  $60^\circ$ . The four frequencies (3020, 3800, 9300, and 9900 Mc/s) were used in

order to provide more experimental points for a given number of models, and also to cross-check results obtained at different frequencies with different equipment. Measurements were also made on a cone with a half angle of  $4^\circ$  at frequencies of 8465 and 9900 Mc/s. Values of  $kr$  for the cones measured ranged from about 0.12 to 4.5.

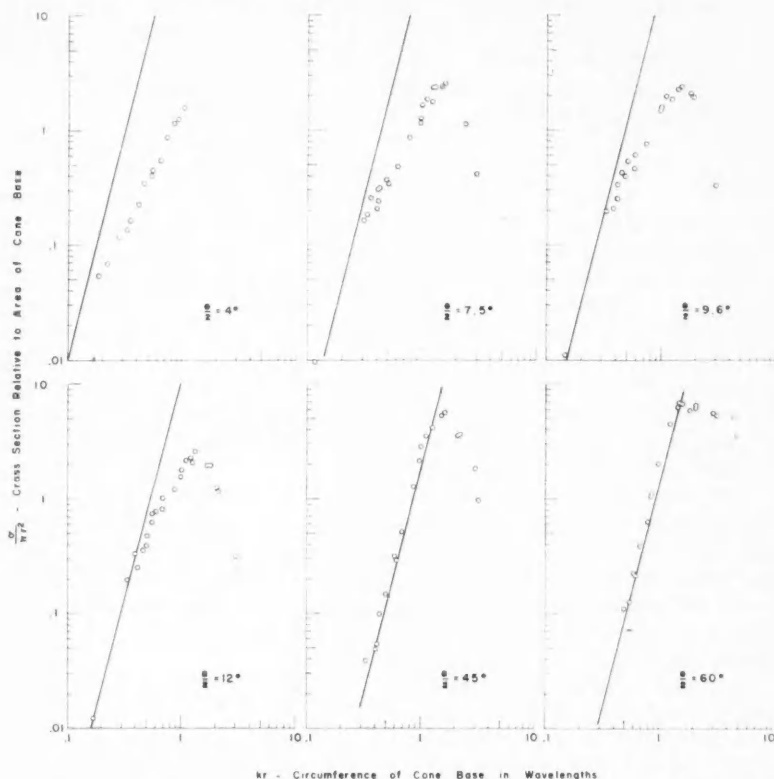


FIG. 1. Nose-on cross sections of cones with various half angles,  $\theta/2$ .  $\circ$  Experimental results; — Rayleigh theory.

The measurements were made on an indoor range, in a room lined with microwave-absorbing material. Low power, continuous wave oscillators, a microwave receiver with a sensitivity of about  $-86$  dbm, and a hybrid tee waveguide system comprised the principal components of the equipment.

All measurements were made at a distance equal to or greater than  $2D^2/\lambda$ , where  $D$  is the maximum dimension of the horn aperture or of the cone, whichever is greater. Calibration spheres were chosen so that their cross sections approximated those of the cones. Measurement procedures were as follows: With no target, the return from the background and the polyfoam

support cylinder was balanced out with the waveguide tuners. The return was then recorded for one or two spheres, for four or five cones, and then for the test spheres again as each was placed in position. If the system went out of balance, or if the second reading on the test spheres differed significantly from the first reading, the data would be discarded. The cones were not rotated, but repeated measurements, made after carefully repositioning the models on the support cylinder, were consistent. The points that appear on the accompanying curves represent the average of at least three, and usually as many as six or eight, separate readings. Before averaging, the values generally agreed to within  $\pm 1/2$  db.

The agreement obtained between X-band and S-band data was very satisfactory. The agreement between our results and those given in Keys and Primich (1959), where the values of apex angle and  $kr$  in the two sets of data overlap, was most gratifying.

It is interesting to note that, over the wide range of apex angles covered by the data, the location of the first maximum varies very slowly with cone angle.

#### ACKNOWLEDGMENT

We wish to thank Keys and Primich for making available to us the results of their experiments over the past several years. These data have been of great value in refining our viewpoint. Though this paper dwells on some theoretical disagreements between Keys and Primich (1959) and Siegel (1958), it should be emphasized that the main features are in good agreement.

- ANDREJEWSKI, W. 1952. Dissertation, Technische Hochschule (Aachen).  
HONDA, J., SILVER, S., and CLAPP, F. 1956. International Scientific Radio Union, Washington, D.C.  
KEYS, J. E. and PRIMICH, R. I. 1959. Can. J. Phys. **37**, 521.  
KOUYOUMJIAN, R. 1956. Appl. Sci. Research, B, **6**, 165.  
SIEGEL, K. M. *et al.* 1956. Transactions, IRE-PGAP, AP-4, 266.  
SIEGEL, K. M. 1958. Appl. Sci. Research, B, **7**, 293.  
WESTON, V. H. 1957. International Scientific Radio Union, XIIth General Assembly, Colorado.

RECEIVED FEBRUARY 5, 1959.  
THE RADIATION LABORATORY,  
DEPARTMENT OF ELECTRICAL ENGINEERING,  
THE UNIVERSITY OF MICHIGAN,  
ANN ARBOR, MICHIGAN.

## LETTERS TO THE EDITOR

*Under this heading brief reports of important discoveries in physics may be published. These reports should not exceed 600 words and, for any issue, should be submitted not later than six weeks previous to the first day of the month of issue. No proof will be sent to the authors.*

### Extension of Davydov's Theory of Molecular Crystals to Vibronic Transitions

The theory of the electronic states of molecular crystals was developed by Davydov (1948) in terms of exciton states. In these calculations (Davydov 1948; Winston 1951) only the *electronic* wave functions of the molecule were used, so that the resulting expression for the transition energies holds only for the pure electronic transition  $\nu_e$  which does not occur in the observed spectrum. Instead, one observes transitions  $\nu_e, \nu'$  with vibrational quantum numbers  $\nu', \nu''$  in the upper and lower states, respectively. It is therefore not correct to compare calculated Davydov splittings with those observed in the spectrum, unless the effect of molecular vibrations on the calculated splitting is included. This is true even for the 0,0-transition, which is the main source for observing the Davydov splitting. Simpson (1957) was the first to show how vibrational effects can be taken into account in such calculations. One of the two limiting cases which he discussed is treated here in more detail. This case applies to Davydov splittings which are small compared with the molecular vibrations.

Here the crystal energies can be calculated as first-order perturbations of the *vibronic* states of the free molecule in the same way presented by Fox and Schnepf (1955) for the *pure electronic* states. In their formulae the wave functions  $\psi_0^j, \psi_j^j$  of the ground and  $j$ th excited state of a molecule at the  $s$ th site in the crystal will be replaced by the product of these functions with the vibrational functions  $\phi_0^s, \phi_j^s$ . This yields the same eq. (6) of Fox and Schnepf (1955) for the excitation energy of a crystal state

$$(1) \quad E_{j,g}(\mathbf{K}) - E_0 = (\epsilon_j - \epsilon_0) + D_{j,g} + M_{j,g}(\mathbf{K}).$$

The first term on the right side is the excitation energy of the free molecule in its  $j$ th state including vibrational energies. The second term is independent of the wave vector  $\mathbf{K}$  and only shifts the free molecule transition whereas the third term splits it into a band of states characterized by  $\mathbf{K}$ .  $D$  and  $M$  are still given by eq. (7) and (8) of Fox and Schnepf (1955) except that the *vibronic* molecular wave functions are substituted for the *electronic* ones. The interaction operator  $V$  between any two molecules A and B can be written  $V = V_{ee} + V_{en} + V_{nn}$ , corresponding to interaction between the electrons of A and B, the electrons of A and the nuclei of B and vice versa, and between the nuclei of A and B. Only  $V_{ee}$  gives a non-zero contribution to the band-splitting term  $M$ , if the Born-Oppenheimer approximation holds. The resulting expressions for  $D$  and  $M$  can be reduced to one- and two-electron integrals through the use of the spinless electron densities  $\rho_0^{(g)}, \rho_j^{(g)}, \rho_0^{(e)}, \rho_j^{(e)}$ , which refer to the ground state, the  $j$ th excited state, and the transition  $0 \rightarrow j$  respectively. Thus the following expressions are obtained

$$(2) \quad b_{j,g} = \sum_m \sum_{\mu,\nu} |B_\nu^g|^2 \int \left( \rho_j^{(n\nu)}(1) - \rho_0^{(n\nu)}(1) \right) \times \left\{ V_{ne}(1) + \int \rho_0^{(m\mu)}(2) V_{ee}(1,2) d\tau_2 \right\} d\tau_1,$$

$$(3) \quad M_{j,g}(\mathbf{K}) = \sum_m \sum_{\mu,\nu} B_\nu^{g+} B_\mu^g e^{i\mathbf{K} \cdot (\mathbf{m}-\mathbf{n})} \int \rho_{0,j}^{(n\nu)}(1) \rho_{0,j}^{(m\mu)}(2) V_{ee}(1,2) d\tau_1 d\tau_2 \times \left( \int \phi_0^{(n\nu)} \phi_j^{(n\nu)} dQ^{(n\nu)} \right)^2.$$

From this the following conclusion can be drawn. The band shift term (2) remains unchanged by including vibrations; it is only a more condensed form of eq. (7) of Fox and Schnepf (1955). The band-splitting term (3) is the product of two factors. The first is the same term as calculated for the pure electronic transition. The second factor gives the influence of the vibrational motion of the molecules. It is equal to the square of the vibrational overlap integral between the ground and excited state (Simpson 1957). It will lead to a different band splitting for each vibronic transition. On the other hand, the order of the different components—numbered by the subscript  $g$ —will be the same for all vibronic transitions.

The electronic transition moment for the transition from the crystal ground state to the excited states can be calculated in the same way, giving

$$(4) \quad (\mathbf{R})_{j\mathbf{k},0} = \delta_{\mathbf{k},0} \sqrt{N} \sum_{\nu} B_{\nu}^{g*}(\mathbf{r}_{\nu})_{j,0} \times \int \phi_0^{(n\nu)} \phi_j^{(n\nu)} dQ^{n\nu}.$$

The first factor gives the electronic transition moment, expressed in terms of the moments  $(\mathbf{r}_{\nu})_{j,0}$  of the free molecules in one unit cell. This is multiplied by the same vibrational overlap integral, which occurred in eq. (3).

- DAVYDOV, A. S. 1948. J. Exptl. Theoret. Phys. U.S.S.R. **18**, 210.  
 FOX, D. and SCHNEPP, O. 1955. J. Chem. Phys. **23**, 767.  
 SIMPSON, W. T. and PETERSON, D. L. 1957. J. Chem. Phys. **26**, 588.  
 WINSTON, H. 1951. J. Chem. Phys. **19**, 156.

RECEIVED OCTOBER 27, 1958.  
 DEPARTMENT OF PHYSICS,  
 DUKE UNIVERSITY,  
 DURHAM, NORTH CAROLINA.

W. A. BINGEL



## THE PHYSICAL SOCIETY

MEMBERSHIP of the Society is open to all who are interested in Physics. FELLOWS pay an Entrance Fee of £1 1s. (\$3.15) and an Annual Subscription of £2 2s. (\$6.00).

STUDENTS: A candidate for Studentship must be between the ages of 18 and 26, and pays an Annual Subscription of 5s. (\$0.75).

MEETINGS: Fellows and Students may attend all Meetings of the Society including the annual Exhibition of Scientific Instruments and Apparatus.

PUBLICATIONS include the *Proceedings of the Physical Society*, published monthly, and *Reports on Progress in Physics*, published annually. Volume XXI, 1958, is now available (price £3 3s. (\$9.45)). Members are entitled to receive any of the Publications at a reduced rate.

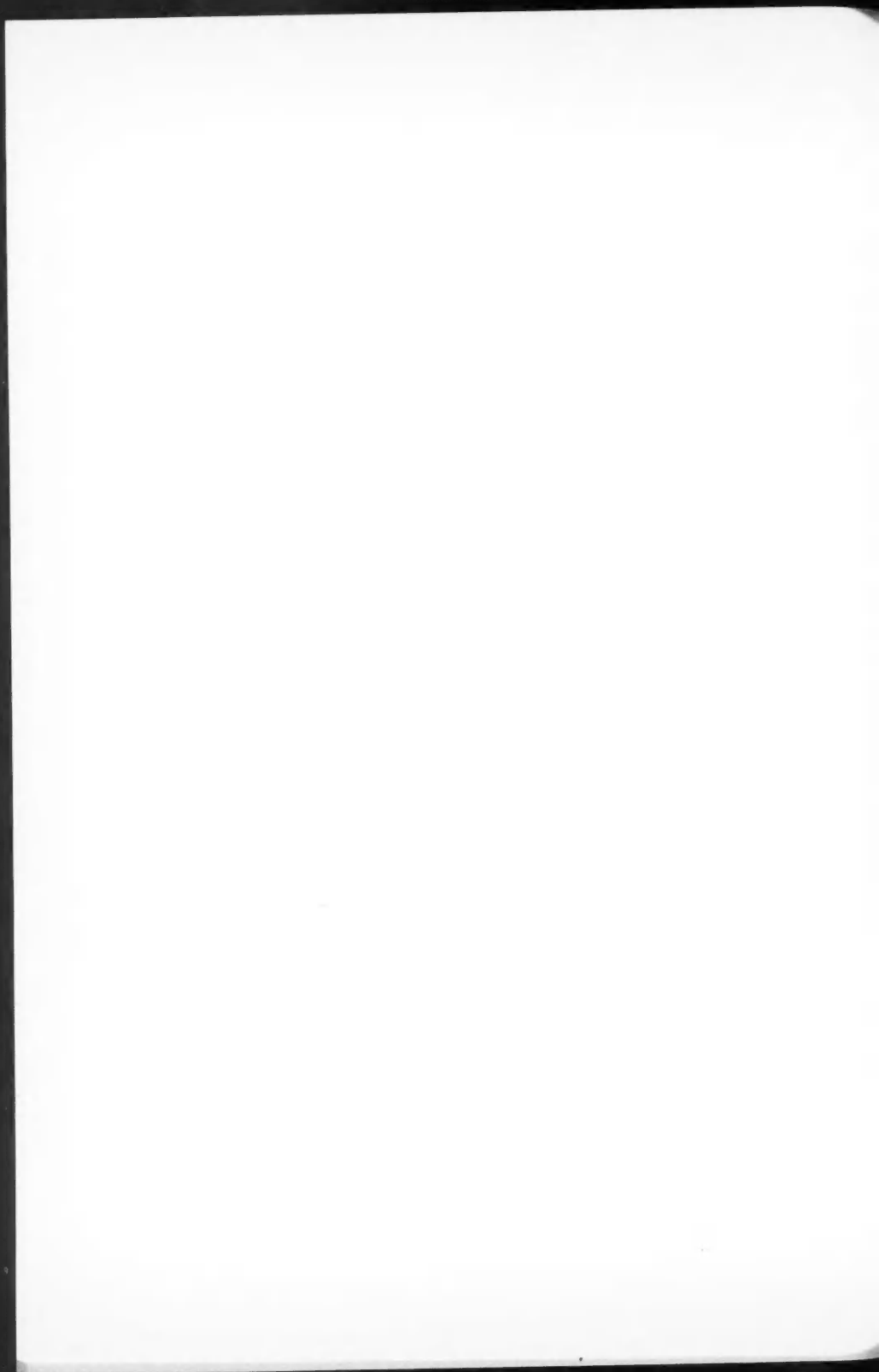
Further information can be obtained from:

THE PHYSICAL SOCIETY  
1, LOWTHER GARDENS, PRINCE CONSORT ROAD  
LONDON, S.W.7, ENGLAND









## NOTES TO CONTRIBUTORS

### *Canadian Journal of Physics*

#### MANUSCRIPTS

**General.**—Manuscripts, in English or French, should be typewritten, double spaced, on paper  $8\frac{1}{2} \times 11$  in. **The original and one copy are to be submitted.** Tables and captions for the figures should be placed at the end of the manuscript. Every sheet of the manuscript should be numbered. Style, arrangement, spelling, and abbreviations should conform to the usage of recent numbers of this journal. Greek letters or unusual signs should be written plainly or explained by marginal notes. Characters to be set in boldface type should be indicated by a wavy line below each character. Superscripts and subscripts must be legible and carefully placed. Manuscripts and illustrations should be carefully checked before they are submitted. Authors will be charged for unnecessary deviations from the usual format and for changes made in the proof that are considered excessive or unnecessary.

**Abstract.**—An abstract of not more than about 200 words, indicating the scope of the work and the principal findings, is required, except in Notes.

**References.**—References should be listed **alphabetically by authors' names**, unnumbered, and typed after the text. The form of the citations should be that used in current issues of this journal; in references to papers in periodicals, titles should not be given and only initial page numbers are required. The names of periodicals should be abbreviated in the form given in the most recent *List of Periodicals Abstracted by Chemical Abstracts*. All citations should be checked with the original articles and each one referred to in the text by the authors' names and the year.

**Tables.**—Tables should be numbered in roman numerals and each table referred to in the text. Titles should always be given but should be brief; column headings should be brief and descriptive matter in the tables confined to a minimum. Vertical rules should not be used. Numerous small tables should be avoided.

#### ILLUSTRATIONS

**General.**—All figures (including each figure of the plates) should be numbered consecutively from 1 up, in arabic numerals, and each figure referred to in the text. The author's name, title of the paper, and figure number should be written in the lower left corner of the sheets on which the illustrations appear. Captions should not be written on the illustrations.

**Line drawings.**—Drawings should be carefully made with India ink on white drawing paper, blue tracing linen, or co-ordinate paper ruled in blue only; any co-ordinate lines that are to appear in the reproduction should be ruled in black ink. Paper ruled in green, yellow, or red should not be used. All lines must be of sufficient thickness to reproduce well. Decimal points, periods, and stippled dots must be solid black circles large enough to be reduced if necessary. Letters and numerals should be neatly made, preferably with a stencil (**do NOT use typewriting**) and be of such size that the smallest lettering will be not less than 1 mm high when the figure is reduced to a suitable size. Many drawings are made too large; originals should not be more than 2 or 3 times the size of the desired reproduction. Whenever possible two or more drawings should be grouped to reduce the number of cuts required. In such groups of drawings, or in large drawings, full use of the space available should be made; the ratio of height to width should conform to that of a journal page ( $4\frac{1}{2} \times 7\frac{1}{2}$  in.), but allowance must be made for the captions. **The original drawings and one set of clear copies (e.g. small photographs) are to be submitted.**

**Photographs.**—Prints should be made on glossy paper, with strong contrasts. They should be trimmed so that essential features only are shown and mounted carefully, with rubber cement, on white cardboard, with no space between those arranged in groups. In mounting, full use of the space available should be made. **Photographs are to be submitted in duplicate; if they are to be reproduced in groups one set should be mounted, the duplicate set unmounted.**

#### REPRINTS

A total of 50 reprints of each paper, without covers, are supplied free. Additional reprints, with or without covers, may be purchased at the time of publication.

Charges for reprints are based on the number of printed pages, which may be calculated approximately by multiplying by 0.6 the number of manuscript pages (double-spaced typewritten sheets,  $8\frac{1}{2} \times 11$  in.) and including the space occupied by illustrations. Prices and instructions for ordering reprints are sent out with the galley proof.

## Contents

<i>H. R. Fickel and R. H. Tomlinson</i> —Thermal neutron absorption cross section of $\text{Xe}^{135}$ - - - - -	531
<i>Bengt Kleman and Ulla Uhler</i> —A ${}^4\Sigma\text{--}{}^6\Sigma$ transition in $\text{CrH}$ - - - - -	537
<i>K. W. Geiger</i> —Absolute standardization of radioactive neutron sources. II. The use of the $\text{F}^{19}(\alpha, n)\text{Na}^{22}$ reaction - - - - -	550
<i>M. Srirama Rao</i> —Size of irregularities in the $E$ region of the ionosphere - -	557
<i>A. G. Fenton, K. G. McCracken, D. C. Rose, and B. G. Wilson</i> —Transient decreases in cosmic ray intensity during the period October 1956 to January 1958 - - - - -	569
<i>W. J. Bratina</i> —Investigation of deformation processes in Armco iron by means of internal friction at megacycle frequencies - - - - -	579
<i>Archibald W. Smith</i> —The impedance, rectification, and electroluminescence of anodic oxide films on aluminum - - - - -	591
<i>J. P. Roalsvig, R. N. H. Haslam, and D. J. McKenzie</i> —Photoneutron cross section of $\text{Ni}^{58}$ - - - - -	607
<i>K. L. Chopra and T. S. Hutchison</i> —Study of phase propagation in superconducting aluminum by ultrasonic attenuation measurements - - -	614
<i>S. C. Loh</i> —On toroidal functions - - - - -	619
<i>G. Herzberg and L. L. Howe</i> —The Lyman bands of molecular hydrogen - -	636
<i>A. J. Ferguson and H. E. Gove</i> —Analysis of two interfering $1/2+$ levels in the disintegration of $\text{C}^{14}$ by protons - - - - -	660
Notes:	
<i>James R. Wait</i> —Radiation from a small loop immersed in a semi-infinite conducting medium - - - - -	672
<i>H. Brysk, R. E. Hiatt, V. H. Weston, and K. M. Siegel</i> —The nose-on radar cross sections of finite cones - - - - -	675
Letters to the Editor:	
<i>W. A. Bingel</i> —Extension of Davydov's theory of molecular crystals to vibronic transitions - - - - -	680

